Cosmological Parameter Estimation with QUaD CMB Polarization and Temperature Experiment

Yasin Memari

Institute for Astronomy
School of Physics and Astronomy

University of Edinburgh
Doctor of Philosophy

December 2008

“We are not to comprehend;
the secret of roses, but maybe
swimming in the incantation of roses.
Or may be looking for
the song of truth
between the morning glory,
and the century.”

Sohrab Sepehri (1928-1980)

Abstract

In this thesis we examine the theoretical origin and statistical features of the Cosmic Microwave Background radiation. We particularly focus on the CMB power spectra and cosmological parameter estimation from QUaD CMB experiment data in order to derive implications for the concordance cosmological model.

In chapter 4 we present a detailed parameter estimation analysis of the combined polarization and temperature power spectra from the second and third season observations of the QUaD experiment. QUaD has for the first time detected multiple acoustic peaks in the polarization spectrum, allowing meaningful parameter analyses from the polarization data alone. In a standard 6-parameter ΛCDM parameter estimation analysis we find the QUaD TT power spectrum to be in very good agreement with previous results. However, the QUaD polarization data shows some tension with ΛCDM model. The origin of this $1-2\sigma$ tension remains unclear, and may point to new physics, residual systematics or simple random chance. Combining polarization and temperature data we find an acceptable fit, and show that our results are dominated by the polarization signal. We combine QUaD with the five-year data from the WMAP satellite and the SDSS Luminous Red Galaxies 4th data release power spectrum, and extend our analysis to constrain the tensor-to-scalar ratio and the primordial isocurvature perturbations. Our analysis sets a benchmark for future polarization experiments.

In chapter 5 we outline and test a new semi-analytical approach for the estimation of the pseudo- temperature and polarization CMB power spectra for experiments with incomplete sky coverage. We propose a method for constructing the mode-mode coupling matrices which connect the temperature and polarization pseudo-C_ℓ's to the unbiased all-sky bandpowers in the flat sky approximation. We apply this method to the apodization masks of the QUaD CMB experiment and we show that the true underlying bandpowers can be reconstructed from the simulated QUaD-like pseudo-C_ℓ's to high precision. We further investigate the possibility of extending the proposed analytical flat sky approach to the exact calculation of the PCL covariance matrices over a large range of multipoles and we find that the numerical calculation is extremely

computationally expensive. The flat sky pseudo-C_ℓ and covariances methods presented in this chapter are still work in progress and require more testing.

Declaration

I declare that this thesis is not substantially the same as any that I have submitted for a degree or diploma or other qualification at any other University. I further state that no part of my thesis has already been or is being concurrently submitted for any such degree, diploma or other qualification.

This thesis is the outcome of my own work except where specifically indicated in the text. Some of the results in this thesis were done in collaborative work, and my contribution to each project is as follows.

- Chapter 4 was done in collaboration with the QUaD consortium particularly the parameter estimation team: Patricia Castro, Andy Taylor and Sujata Gupta. I have been responsible for developing, testing and maintaining the MCMC pipeline and have personally carried out all of the analysis runs presented in this chapter.
- The pseudo-C_ℓ method presented in chapter 5 is based on an original idea by Andy Taylor. I made significant contributions in developing the analytical formula and was responsible entirely for the numerical implementation. The results of sections 5.2 and 5.3 are entirely my contribution.

Part of this thesis is based on the following submitted scientific article:

- QUaD collaboration: P. G. Castro et al. (2009)

Yasin Memari
Edinburgh,
December 2008.

Acknowledgements

I am especially grateful to my supervisors, Andy Taylor and Patricia Castro, for their invaluable advice and supervision throughout the work of this thesis. Special thanks are due to the academic staff of the Institute for Astronomy, particularly John Peacock and Alan Heavens, for their support and encouragement. Sincere thanks to Eric Tittley for his instructions on parallel computing. Also thanks to the postgraduate students and postdoctoral fellows for the good time and delightful discussions.

Contents

List of Figures

List of Tables

Chapter 1

Introduction

Two main features today distinguish the science of cosmology from the early attempts of understanding the universe. On the one hand, today we have spectacular data from the universe which opens a new window of opportunity for probing the cosmological models and paradigms which have been only speculations until a couple of decades ago. On the other hand, today there exists a working theoretical model of the universe which can consistently explain the smooth homogeneous universe on very large scales as well as the existence of inhomogeneity and anisotropy on smaller scales. In this way today cosmologists are in a position to make testable predictions about the evolution of the cosmos.

One key principle of modern cosmology which is well-established is the idea of the expanding universe. The observations of the redshift of Type Ia supernovae have especially provided stunning results in support of this. Supernovae are very bright objects which can be used as standard candles to very large distances. By assuming that identical supernovae have equal brightness it is possible to determine the distance of the galaxies from us. On the other hand, measurement of the redshift is not difficult and yields the recessional velocity of the galaxies. In this way we can reconstruct the Hubble diagram by plotting the distance versus redshift for an ensemble of galaxies. (see Fig. 1.1) Several experiments have recently re-examined the Hubble expansion extending their observations to very high redshifts. (Riess et al., 1998; Perlmutter et al., 1999; Freedman et al., 2001) The findings of these experiments have been remarkable since it has now been discovered that not only the universe is expanding but also the rate of its expansion has increased in recent times. These observations are in favor of the dark energy dominated models in which the universe is filled with a vacuum energy or quintessence.

The *dark energy* is currently the best candidate for explaining the accelerated expansion of the universe. Around 74% of the density of the universe is estimated to have comprised

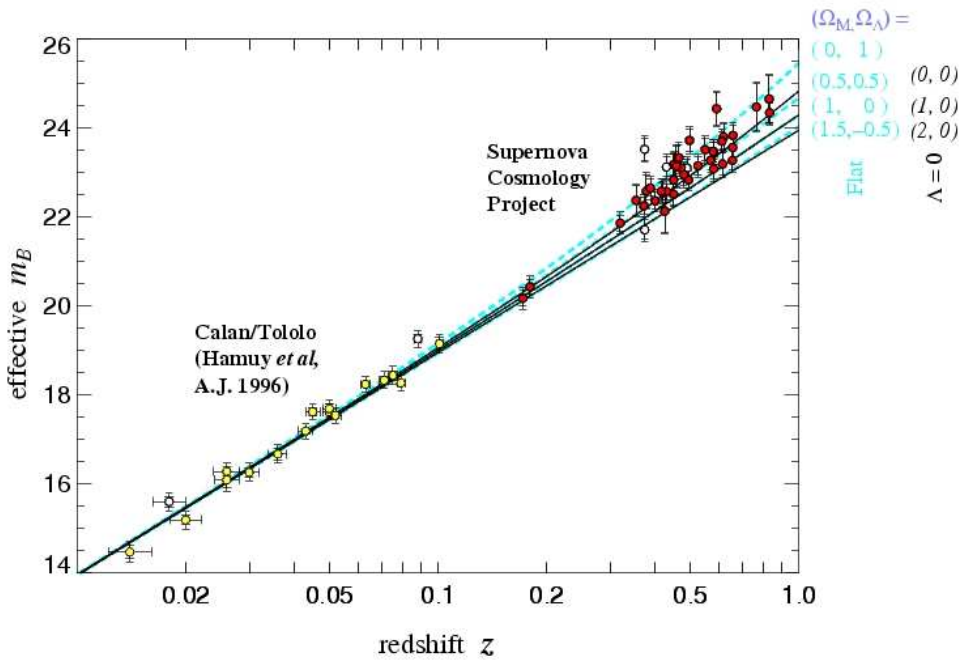

Figure 1.1: The distance-redshift relationship for 42 high-redshift Type Ia Supernovae. The effective magnitude m_B is an indicator of the distance. It is evident that the distant supernovae favor a dark energy dominated universe (dashed lines) over a matter dominated one (solid lines). (Figure from Perlmutter et al., 1999)

of this hypothetical form of energy. The dark energy is usually parameterized by an equation of state which should necessarily be negative if the universe is expanding. In such case the dark energy exerts a negative pressure on the universe which counteracts the gravitational attraction. The fate of the universe is believed to be ultimately dependent on the competition between the matter density and the dark energy content of the universe. Since the density of dark energy is assumed to be constant or relatively unchanged, whereas that of matter and radiation falls due to the expansion, the late-time accelerated expansion can be justified by the transition from matter to dark energy dominated phase. In such models the dark energy might cause the expansion to occur at even faster and faster rates eventually causing the galaxies and structures to rip apart. Alternatively the dark energy can be expected to dissipate and decay away by the expansion in which case the universe will collapse in a big crunch due to the matter gravitational attraction. Anyway, the dark energy is still a very mysterious entity and these are only speculative theories at the moment. Nevertheless, measurements of the rate of acceleration of expansion can help to answer some of these questions.

There is also significant evidence in support of the existence of the *dark matter*. Dark matter was first proposed by Zwicky (1933) to explain the 'unseen mass' in the Coma cluster of galaxies; however later it became widely accepted that to explain the rotation curve of the spiral galaxies

one has to resort to some sort of hypothetical unseen matter density. Unlike baryonic matter which interacts with electromagnetic radiation (and hence is visible), it is expected that the dark matter does not interact electromagnetically, so its existence can be inferred by its gravitational effects. The indirect evidence for dark matter comes from the rotational velocity of galaxies in clusters and the gravitational lensing. The measurements of the Cosmic Microwave Background and the large scale structure surveys require that dark matter constitutes around 21% of the density of the universe. However, although the cosmological data provides information about the distribution of dark matter in the universe, most of the evidence about the nature of the dark matter is expected to come from the particle physics experiments which aim to detect the dark matter as Weakly Interacting Massive Particles (WIMP) (see e.g. Paling, 2005). There are also alternative models of modified gravitational theories which attempt to explain that the inconsistencies regarding the missing mass arise due to the incompleteness of the present theory of gravitation. The most important of these theories at the moment is the Modified Newtonian Dynamics (MOND) which attempts to adjust the Newton's second law of motion in the limit of small accelerations (see e.g. Milgrom and Bekenstein, 1987). These are not working models however, and it is not clear whether their predictions would consistently explain the observations.

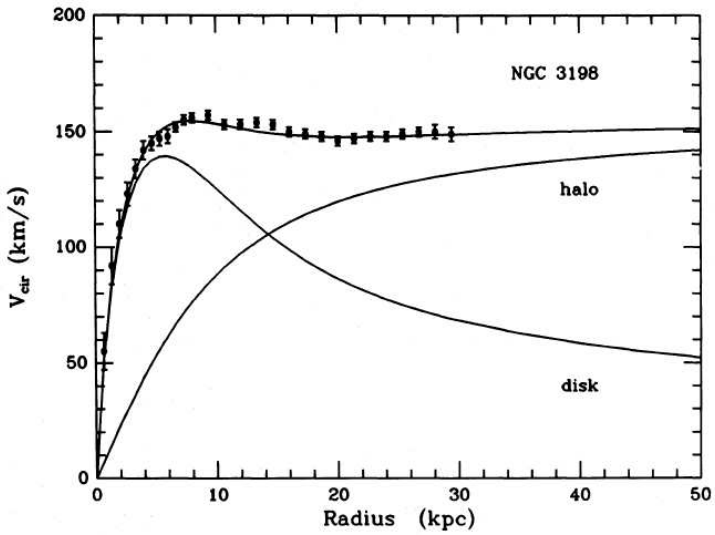

Figure 1.2: The rotational velocity curve of the spiral galaxy NGC 3198. The disk model which assumes the visible matter is concentrated in the galaxy disk predicts a velocity curve which falls by distance. However the existence of the observed flat curve can be explained by assuming a concentrated halo of dark matter in the center of the galaxy. (Figure from van Albada et al., 1985)

The origin of the baryonic matter and radiation particles on the other hand is quite well established. Today we have a consistent theory of the Big Bang Nucleosynthesis (BBN) which explains the nuclear reaction of the particles at early times when the universe was filled with a hot plasma of matter and radiation. Since the universe was in a very dense state the rapid

interaction between particles guarantees that any nucleus that forms would be immediately annihilated (hence implying also thermal equilibrium). However as the temperature falls below the nuclear binding energies the nuclei and then light elements are formed. The key parameter during nucleosynthesis is the number ratio of photons to baryons which sets the rate of the production and annihilation of the particles. From this parameter and the nuclear cross-sections, the abundances of the light elements produced by BBN can be established. Today we know that about 75% hydrogen and 25% helium were generated by the primordial nucleosynthesis. These are also consistent with the abundance values from the observations of the very distant astronomical objects which are in early stages of their evolution. Recently the WMAP measurements of the Cosmic Microwave Background anisotropies have provided strong constraints on the photon-to-baryon ratio in the early universe which can be used to make independent and consistent predictions for the abundance ratio of the light elements (see Coc et al., 2004).

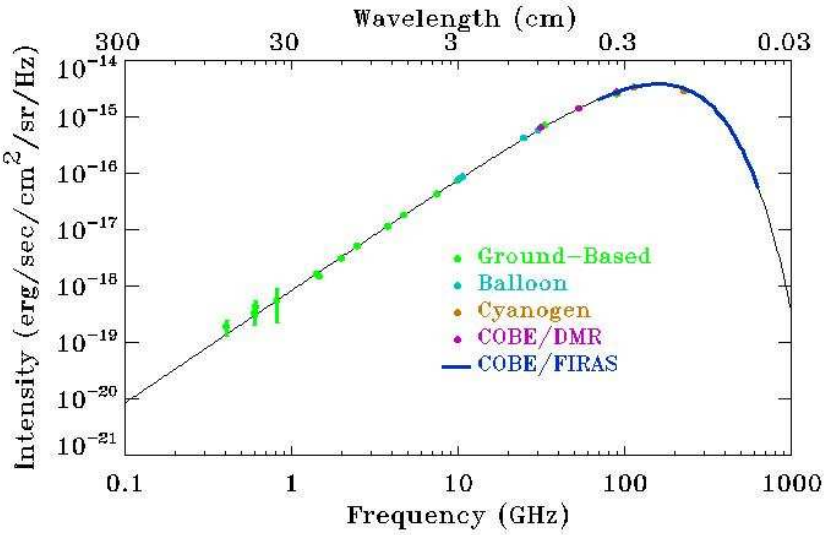

Figure 1.3: The thermal black body spectrum of the CMB measured by different experiments agrees with the theoretical prediction (solid line). (Figure courtesy of NASA)

Once the rate of the expansion overcomes the rate of the particle interactions in the primordial plasma, the corresponding species decouple from the rest of the matter and radiation and freeze out in the background. This is interesting since the study of these species today can lead to enormous information about the stage of the decoupling. Of particular interest here is the decoupling of the photons from matter at temperatures below $\simeq 10^4$K when electrons and protons bound to form hydrogen atoms, a process which is called *recombination*. In this epoch photons last scattered off the electrons and since then have freely streamed to us without having much interaction with matter. However due to the expansion of the universe the

particle number density of the photons has dropped and their wavelength has stretched giving rise to the present so-called *Cosmic Microwave Background* (CMB) radiation. Therefore the observations of the CMB photons across the sky can provide us with a snapshot from the epoch of the *last scattering* and hence the evolution of the universe.

The last scattering happened at redshift ~ 1100 when the universe was only $300,000$ years old. The crucial fact about the last scattering is that since at that time photons were in equilibrium the thermal spectrum of the CMB photons is expected to be close to a black body spectrum. The observations of the COBE FIRAS instrument provided a first measurement of this black body shape which proved revolutionary to cosmology. (Mather, 1994) For years scientists were predicting that a background radiation exists if the predominant model of the universe is the hot Big Bang. The discovery of the Planckian spectrum of the CMB (see Fig. 1.3) provided evidence for this prediction and ruled out the steady state models in which a background radiation is not physically plausible. Today we know that the CMB has a perfect blackbody spectrum of temperature $T = 2.725 \pm 0.002\text{K}$, with small temperature anisotropies of the level of one part in 10^5.

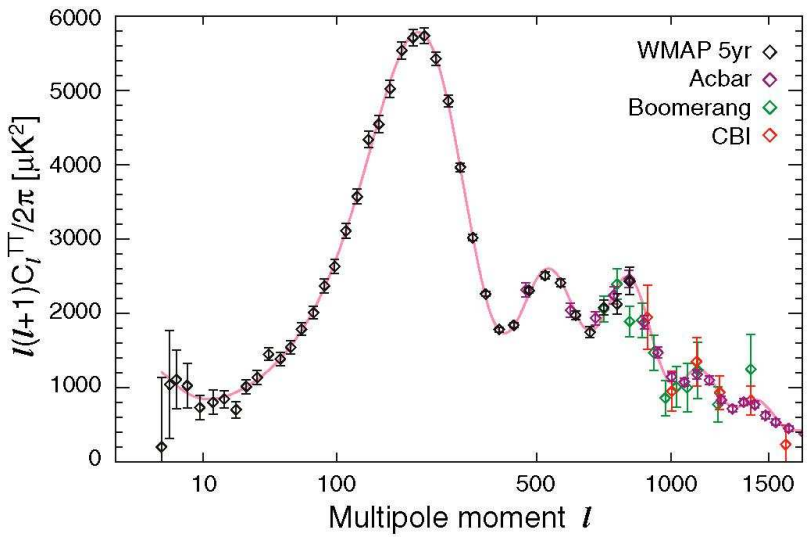

Figure 1.4: The power spectrum of the CMB temperature anisotropies measured by different experiments. (Figure courtesy of NASA and WMAP)

The COBE experiment also detected small fluctuations in the temperature of the CMB at different angles of the sky. These anisotropies are evident in the CMB angular power spectrum which represents the variance of the temperature fluctuations on the sky. (see Fig. 1.4) This observed deviation from the isotropy has had important implications for modern cosmology. The structure of the universe on very large scales is very close to homogeneous, however on smaller scales there exist inhomogeneities such as galaxies and clusters. It is widely believed that the inhomogeneity in the matter distribution and the anisotropy in the CMB have a common

origin in the perturbations in the primordial plasma of the universe. (see chapter 2) In this way high precision measurements of the fluctuations can yield enormous information about the cosmological perturbations and the evolution of the universe.

The high degree of isotropy in the CMB is also an evidence for the *cosmological principle* which postulates that the universe is homogeneous and isotropic on large scales. The fact that photons coming from different directions of the sky have the same wavelength tells us that different regions of the universe should have had almost equal temperature at the last scattering. However, as we will see in chapter 2, the dynamics of a homogeneous and isotropic universe imply that the large scales which are separated by vast distances could not have been in causal contact in the past. This seemingly acausal isotropy has long been a puzzle to cosmologists, and is called the *horizon problem*. The most promising solution to date for this problem is the inflationary scenario which we will discuss in §2.1.5. It suggests that there might have been an epoch during the early stage of evolution of the universe in which the originally causally connected regions get separated by the vast distances which we see today on large scales. However, a more important implication of inflation is that inflation provides a means for generating the primordial perturbations by predicting quantum fluctuations at the initial phase of evolution.

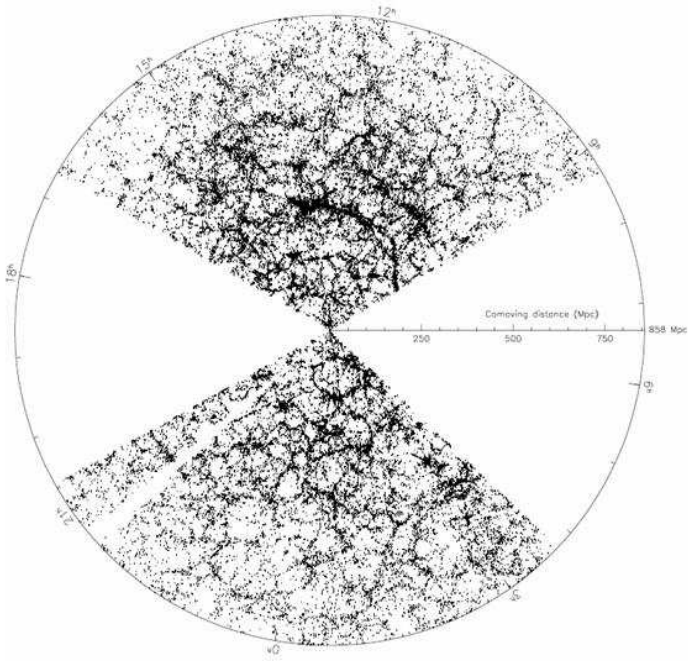

Figure 1.5: A 2d slice of the distribution of the galaxies from the spectroscopic measurements of the SDSS. (Figure courtesy of SDSS.)

The distribution of matter in the universe also provides information about the formation of large-scale structures. Over the past decade the sky surveys such as 2dF galaxy redshift survey

(2dFGRS) and the Sloan Digital Sky Survey (SDSS) have measured the position of hundreds of thousands of the galaxies. The data from these experiments confirm that galaxies are not distributed randomly, rather they lie in clusters, filaments and sheets of structures. (see Fig. 1.5) The findings of these observations are also in agreement with the results of the simulations of the growth of the cold dark matter density, the largest of which is the millennium simulation carried out by the Virgo Consortium. (Springel et al., 2005) At present the model which best explains this 'cosmic web' structure of matter is the halo model which postulates a hierarchical growth of the structure in the universe through gravitational instability.

From the observations of the large-scale structures we can construct a power spectrum for the matter densities in the universe. (see Fig. 1.6) The same mechanisms which have given rise to the radiation anisotropies of the CMB have affected the evolution of matter in the universe. Therefore observations of both matter and CMB power spectra are necessary to probe the evolution of the cosmological perturbations. To construct the matter power spectrum we should correct for the effects of the redshift space which distorts the galaxy distribution along the line of sight. Moreover there is a bias factor in the calculation of amplitude due to the fact that the dominant cold dark matter does not exactly follow the distribution of the luminous matter.

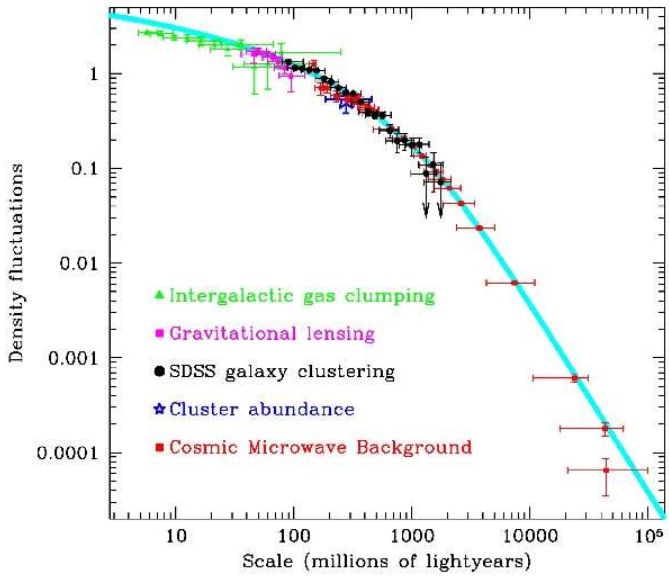

Figure 1.6: The power spectrum of density fluctuations reconstructed from different cosmological data.(Figure from Tegmark and Zaldarriaga, 2002)

In the same way we can construct a matter power spectrum from gravitational weak lensing. Gravitational weak lensing provides an indirect measurement of the mass distribution by looking at the statistical features in the distortions in shape and alignment of the galaxies due to the deflection of light by the gravitational effects. The weak lensing can especially prove effective to measure the cold dark matter power spectrum directly without introducing a bias factor.

Furthermore, observations of the Lyman-alpha forests can also be used to construct the matter power spectrum through numerical simulations. The Lyman-alpha absorption lines are observed in the spectrum of the light from distant galaxies and quasars which has travelled through the intergalactic medium. Therefore they can be used to measure the frequency, temperature and abundances in the intergalactic hydrogen clouds, hence probing the formation of structure.

Over the past couple of decades the ΛCDM model of cosmology has emerged as the model which most consistently describes the observational universe. The ΛCDM (or concordance) model postulates an isotropic and homogeneous universe which predominantly consists of dark energy that causes the accelerated expansion, and dark matter which is the main agent for structure formation. The primordial perturbations in the early universe are set by the theory of inflation and then grow by linear theory and gravitational instability into the present large scale structures. The perturbations are usually supposed to be nearly Gaussian and adiabatic and constitute an scale-independent power spectrum. The effects of different epochs and mechanisms such as recombination, reionization and gravitational lensing are well known and can be embedded into the cosmological model. In short, the numerous evidence supporting the ΛCDM model are so significant and the degrees of freedom of the model are so large that today most of the cosmology experiments are merely attempting to determine the cosmological and inflationary parameters of this model. Among these, the Cosmic Microwave Background experiments have particularly played a crucial role in providing data for precision cosmology.

In this thesis we focus on the interpretation of the CMB data and its implications for the cosmological model. The angular features of the CMB power spectra present significant information about different epochs of the universe. So in order to make accurate analysis of the CMB data it is essential to understand the underlying theory of the cosmological perturbations. Therefore in chapter 2 we first present a simple and self-contained analytical analysis of the generation of the features in the power spectrum of the CMB anisotropies and matter densities. We first discuss the implications of large scale isotropy and homogeneity and then move on to introduce the equations governing a linearly perturbed isotropic universe. In chapter 3 we first focus on the polarization of the microwave background, the mechanisms which could give rise to the CMB polarization, and the spin-weighted spherical harmonics formalism. Then in section 3.4 we give a description of the QUaD telescope which is presently in the forefront of the CMB polarization measurements. In chapter 4 we focus on the parameter estimation analysis of the QUaD polarization and temperature power spectra. We describe in detail our MCMC methodology that we adopt for CMB parameter estimation. We show with simulations that our pipeline gives unbiased results and use QUaD to constrain the standard six basic parameter ΛCDM model. We also combine QUaD with WMAP and SDSS datasets and put constraints on extended cosmological models including tensor and isocurvature perturbations. In chapter 5 we develop a new semi-analytical method for power spectrum estimation of the CMB for experiments with incomplete sky coverage. We further give details of how we implement this method to consistently recover the underlying bandpowers from QUaD-like simulations.

Chapter 2

The Cosmological Perturbations

2.1 The Unperturbed Universe

The key principle of modern cosmology is that today there exists sufficient evidence that on the average the universe is homogeneous and isotropic on the very large scales. Data from the distribution of galaxies on the sky, the symmetry of the Hubble expansion in all directions, and the isotropy of the Cosmic Microwave Background (CMB) all provide evidence that the large-scale properties of the universe seem to be isotropic around us. On the other hand, according to the Copernican Principle, humans are not expected to be privileged observers in the universe. Hence, if the universe is isotropic around us, it is also isotropic around any other observer elsewhere. Using this symmetry we can then easily show that isotropy at every point leads to homogeneity. This comes from the fact that the intersecting points of two spheres around two distinct observers should correspond to the same density. By using large enough spheres with different radii, this argument can be extended to the entire space, providing support for the homogeneity hypothesis. The assumption that on the average the universe is both isotropic and homogeneous is called the *cosmological principle*.

The cosmological principle is of such an importance in modern cosmology that a stronger version of it was later proposed which is today known as the *perfect* cosmological principle. According to this principle the universe not only is the same in all directions, but also is the same at all times. i.e. this hypothesis implies that the universe should appear the same to all observers throughout its history. Although initially only a speculation, the perfect cosmological principle was later formulated by Bondi and Gold (1948). By that time Hubble had already discovered the expansion of the universe. Subsequently the perfect cosmological principle together with

the Hubble discovery led Hoyle and Narlikar to develop the *steady-state* cosmology. The steady state cosmology implies the continuous creation of matter in order to maintain the density of the expanding universe constant. Later by discovering new observational features, such as the Cosmic Microwave Background, which cannot be explained in the steady state universe, this theory was abandoned. Nowadays, it is the Big Bang model that is widely accepted as the theoretical framework that best explains the universe.

The first main discovery of the modern era of cosmology was the discovery of the expanding universe. V. Slipher had measured the Doppler shifts for dozens of galaxies, and realised that with only a few exceptions, these were redshifted. Although Slipher stated that he thought the redshifting may be due to expansion of the universe, he didn't make the bold interpretation of data that Hubble made later on. By 1912, Hubble had obtained the Cepheid distances for 24 galaxies with respect to the redshifts. By that time, there existed predictions that redshift should increase with distance, however it is hard to know how much this influenced Hubble. Hubble formulated his law in the form that galaxies seem to be receding from the observer with a velocity proportional to their distance. This is the basis of the theories of the expanding universe today, which say early in the history of the universe, the distance between us and the distant galaxies was smaller. In this section we study the consequence of the expansion and the homogeneity of the universe. We first derive the spacetime metric that satisfies these conditions and then move on to study the dynamics of the universe and the theory of inflation. Our analysis of this section is very close to that of Peacock (1999) and Taylor (2004).

Before moving on, consider a distribution of galaxies that is expanding uniformly. We can define a global time coordinate for such a distribution by assuming a freely-falling fundamental observer in the gravitational field of each galaxy. According to the equivalence principle, all freely-falling observers should experience special relativity locally. Therefore, since all observers feel the same conditions, they must also measure the same proper time t. To synchronize the clocks of all these distinct observers we can exchange light signals between them. The time coordinate can then be thought of as a universal one. In this case, the proper time which is the time measured by any of these observers at rest with respect to the local distribution is called the *cosmic time*. Assuming the galaxies are comoving, we can formulate the uniform expansion of the distribution of the galaxies by the evolution of their position vectors $\mathbf{x}$:

$$\mathbf{x}(t) = R(t)\mathbf{x}(t_0), \tag{2.1}$$

where $R(t)$ is the *scale factor* of the universe at any arbitrary time, and the zero subscript refers to the reference time, which we choose to be the present time. If differentiated with respect to t, equation (2.1) leads to

$$\Delta\dot{\mathbf{x}}(t) = \dot{R}(t)\Delta\mathbf{x}(t_0) = H(t)\Delta\mathbf{x}(t), \tag{2.2}$$

where Δ refers to the interval of distance between the galaxies and $H(t) \equiv \dot{R}(t)/R(t)$ is called the *Hubble parameter*. Eq. (2.2) is an expression for the Hubble's law, $v = Hd$, that Hubble first discovered tentatively.

2.1.1 The Robertson-Walker Metric

Having shown that the universe is isotropic and homogeneous at large scales, we already have enough information to determine the metric that describes the global structure of space and time. Since the time coordinate of the universe is defined by the fundamental observer, the metric of the universe should be written like

$$c^2 d\tau^2 = c^2 dt^2 - d\sigma^2, \tag{2.3}$$

which is the proper time interval between the events in the fundamental frame of reference. In this case the only difficulty will be in finding the spatial part $d\sigma^2$ which depends on the geometry of the space. From the cosmological principle, we expect that the spatial part of the metric generally corresponds to a three-dimensional curved space which has the same degree of curvature at all places. Such a space can be either a 3-D Cartesian space, or the 3-surfaces of a hypersphere or a hyperboloid embedded in a four-dimensional Euclidean space. The curvature of a 3-D Cartesian space is zero everywhere, and its metric is well known, which in Euclidean and polar space is

$$\begin{aligned} d\sigma^2 &= dx^2 + dy^2 + dz^2 \\ &= dr^2 + r^2(d\theta^2 + \sin^2(\theta) d\phi^2), \end{aligned} \tag{2.4}$$

where r, θ and ϕ are the comoving spherical coordinates in the polar space. A 3-sphere of radius R in a four-dimensional Euclidean space is defined by $x^2 + y^2 + z^2 + w^2 = R^2$, or $r^2 + w^2 = R^2$, so that $wdw = -rdr$, implying $dw^2 = r^2 dr^2/(R^2 - r^2)$. The metric can therefore be written in the form

$$d\sigma^2 = \frac{r^2 dr^2}{(R^2 - r^2)} + dx^2 + dy^2 + dz^2. \tag{2.5}$$

The R parameter is arbitrary and determines the Gaussian curvature of the space $k = 1/R^2$. Now we can substitute Eq. (2.4) into Eq. (2.5) to transform to 3-D polar coordinate. We will obtain

$$d\sigma^2 = \frac{dr^2}{(1 - r^2/R^2)} + r^2(d\theta^2 + \sin^2(\theta) d\phi^2). \tag{2.6}$$

This is the metric for a 3-surface of positive constant curvature embedded in a four-dimensional Euclidean space. Now we need to find the metric of a 3-hyperbola of negative constant curvature embedded in a four-dimensional Euclidean space. This is straightforward since such a surface is defined by $x^2 + y^2 + z^2 - w^2 = -R^2$, so that if we just equivalently let $r \to ir$ in Eq. (2.6), while keeping x, y, z real, we can quickly obtain

$$d\sigma^2 = \frac{dr^2}{(1 + r^2/R^2)} + r^2(d\theta^2 + \sin^2(\theta) d\phi^2). \tag{2.7}$$

This is the metric of an isotropic universe with negative curvature $k = -1/R^2$, which could be equivalently expressed by an imaginary radius of curvature iR. The flat universe is also the one for which the radius of curvature is equal to infinity. Furthermore, even though the flat, open and closed universes are all unbound spaces, only the former two universes are infinite. This is

because the closed space described by Eq. (2.6) is identical to the surface of a sphere, in which travellers who set off a journey along the trajectory of fixed θ and ϕ will eventually return to their starting point. Having obtained the spatial part of the isotropic universe $d\sigma^2$, we can now put Eqs. (2.4), (2.6) and (2.7) back into Eq. (2.3) to obtain

$$c^2 d\tau^2 = c^2 dt^2 - \left[\frac{dr^2}{(1-kr^2)} + r^2(d\theta^2 + \sin^2(\theta) d\phi^2)\right], \tag{2.8}$$

where $k = 1$ for closed, $k = 0$ for flat, and $k = -1$ for open universes, since it is the sign of the curvature constant k that defines the geometry. We can now decompose distances into a time product of a time-dependent scale factor $R(t)$ and a time-independent term which depends on the comoving coordinate r. Hence we replace r by $R(t)\mathcal{S}_k(r)$ in Eq. (2.8), which results in

$$c^2 d\tau^2 = c^2 dt^2 - R^2(t)\big[dr^2 + \mathcal{S}_k^2(r) d\psi^2\big], \tag{2.9}$$

where

$$\mathcal{S}_k(r) = \begin{cases} \sin r & (k=1) \\ \sinh r & (k=-1) \\ r & (k=0), \end{cases}$$

where $d\psi^2 = d\theta^2 + \sin^2(\theta) d\phi^2$ is the angular part of the metric. The metric in Eq. (2.9) is called the *Robertson-Walker* metric, which governs an isotropic and hence homogeneous universe with any given geometry. The immediate consequence of this is the determination of propagation of light in cosmology. Since photons travel on null geodesics of zero proper time, the radial equation of motion for photons is

$$r(t) = \int \frac{c dt'}{R(t')}, \tag{2.10}$$

where the integration is taken from the time of emission, t_e, to the time of observation, t_o, of the photons. Since r is a comoving quantity any delay in emission and therefore absorption of the photons does not alter the integral, so we should have $dt_e/dt_o = R(t_e)/R(t_o)$. This says that the events that we see at large separations time-dilute depending on the amount of the expansion of the universe since the photons were emitted. Writing this condition in terms of the frequency, we have

$$\frac{\nu_{emit}}{\nu_{obs}} \equiv 1 + z = \frac{R(t_{obs})}{R(t_{emit})}. \tag{2.11}$$

This equality gives us the global definition for redshift z. Astronomers measure the redshift by the shift of spectral lines. At small separations, the recessional velocity of galaxies, $v = Hd$, gives the so-called Doppler shift $z \simeq \frac{v}{c}$. However, on larger separations the proper redshift is actually the accumulation of a series of infinitesimal Doppler shifts as the photon passes from observer to observer. For large separations, a common approach is to use the special relativistic Doppler shift $1 + z = \sqrt{\frac{1+v/c}{1-v/c}}$, but this method is misleading since it is only valid in a universe with zero mass density. Therefore, on universal scales, we always have to stick with the global definition of redshift, i.e. Eq. (2.11). One can always take the time of observation at the present epoch, so Eq. (2.11) can be written as $a(t) = (1+z)^{-1}$, where $a(t) \equiv R(t)/R_0$ is the dimensionless scale factor which we take to be unity at present.

2.1.2 Dynamics of the Expansion

To understand the history of the universe, we must determine the evolution of the scale factor $R(t)$ with the cosmological time t. General Relativity links the evolution of the scale of the universe to its energy content. However, in this subsection we want to avoid GR and only use simple quasi-Newtonian arguments instead.

There is a theorem in GR, known as Birkhoff's theorem, that states: a spherically symmetric gravitational field in an empty space is always described by the Schwarzschild metric, i.e. the metric generated in empty space by a point mass. This theorem also has an analogue in Newtonian gravitation that reads: the gravity of a spherical body appears to act from a central point mass, and the gravitational field inside a spherical shell vanishes. This says that the motion of a point at the edge of an imaginary sphere of radius $R(t)r$, with a constant and arbitrary r, can be influenced only by the interior mass. We can then immediately write down the equation of conservation of energy $(\dot{R}r)^2/2 - GM/(Rr) = \text{Const}$. Here $M = \frac{4}{3}\pi(Rr)^3\rho$ is the total mass inside the sphere. In GR, this equation arises from the Einstein's equations for the unperturbed Robertson-Walker metric. To find the constant in the conservation equation we do require General Relativity which leads to (see §2.3.2)

$$\dot{R}^2 - \frac{8\pi G}{3}\rho R^2 = -kc^2. \tag{2.12}$$

This equation is called the *Friedmann's equation*. Although the constant on the right comes solely from GR, Newtonian approach can lead to some clues that the constant should depend on the spatial curvature. Assume we hold the local observables H and ρ fixed, but increase R to infinity. This assumption corresponds to a flat universe limit. As the scale factor goes to infinity the geometry becomes indistinguishable from that of the Euclidean space. The conservation energy could be written as $H^2r^2/2 - 4\pi r^3\rho/3 = \text{Const}/R^2$. In this form the right hand side which is the total energy is effectively zero while the left hand side is not. Therefore the constant should be proportional to the curvature $k = 0$. For an open universe we can have a similar Newtonian argument by considering that such a universe evolves towards the limit of undecelerated expansion until $\dot{R}$ becomes a constant which implies that all particles move at a constant velocity. It can be shown that this constant velocity is just equal to the speed of light, implying $R = ct$ for this model; in which case the potential energy becomes negligible compared to the total and kinetic energy, thus proving the $k = -1$ case.

The Friedmann's equation (2.12) reveals that there is a direct connection between the density of the universe and its global geometry. For a given rate of expansion, the density for which the spatial curvature is zero is called the *critical density*

$$\rho_c = \frac{3H^2}{8\pi G}. \tag{2.13}$$

A universe with such a density is a spatially flat universe, even though it is still a curved space-time. Whereas, a universe with a higher (lower) density will be spatially closed (open). We see that the critical density only depends on the rate at which the universe is expanding. It is

common to define a dimensionless *density parameter* as the ratio of density to critical density:

$$\Omega \equiv \frac{\rho}{\rho_c} = \frac{8\pi G\rho}{3H^2}. \tag{2.14}$$

Using this definition, we can obtain the scale factor of the universe at any time by writing the Friedmann equation as

$$R = \frac{c}{H}\left[\frac{\Omega - 1}{k}\right]^{-1/2}. \tag{2.15}$$

This equation shows that the Hubble constant sets the scale factor which becomes infinitely large as Ω approaches unity. In a powerful approximate model, the energy content of the universe can always be divided into pressureless matter, radiation and vacuum energy

$$\Omega = \Omega_m a^{-3} + \Omega_r a^{-4} + \Omega_v, \tag{2.16}$$

where Ω_m, Ω_r and Ω_v refer to the values of density at 'present time'. The a^{-3} coefficient for Ω_m has been introduced because the number density of the matter particles is diluted by the expansion ($\rho_m \propto R^{-3}$), while the energy density of radiation photons decreases by a further power of a, due to the fact that the CMB photons are also redshifted by the expansion of the universe (hence $\rho_r \propto R^{-4}$). The vacuum energy density is always constant in the history of the universe, so no coefficient follows Ω_v in Eq (2.16). Substituting Eq. (2.16) in Eq. (2.15), we will have

$$\frac{kc^2}{H^2R^2} = \Omega_m(a) + \Omega_r(a) + \Omega_v(a) - 1. \tag{2.17}$$

From this relation a flat $k = 0$ universe requires $\sum \Omega_i = 1$ at all times. Alternatively, we can substitute $\rho(a)$ from Eq (2.14) into the Friedmann's equation $H^2 = 8\pi G\rho/3 - kc^2/R^2$ which leads to

$$H^2(a) = H_0^2[\Omega_v + \Omega_m a^{-3} + \Omega_r a^{-4} - (\Omega - 1)a^{-2}]. \tag{2.18}$$

An important result from this equation is the comoving distance-redshift relation. For a photon we have $Rdr = cdt = cdR/\dot{R}$, which using the relations $\dot{R} = HR$ and $R = R_0/(1+z)$ leads to

$$\begin{aligned} R_0 dr &= \frac{c}{H(z)}dz \\ &= \frac{c}{H_0}\left[(1-\Omega)(1+z)^2 + \Omega_v + \Omega_m(1+z)^3 + \Omega_r(1+z)^4\right]^{-1/2}dz. \end{aligned} \tag{2.19}$$

Integrating over this equation we can determine the comoving distance of an object along the line of sight using the redshift of the photons coming from that object. Now using the expression for $H(a)$ from Eq. (2.15), the time-dependence of the total density parameter can be obtained as follows

$$\Omega(a) - 1 = \frac{\Omega - 1}{1 - \Omega + \Omega_v a^2 + \Omega_m a^{-1} + \Omega_r a^{-2}}. \tag{2.20}$$

This equation is important since it tells us that at high redshifts all universes will tend to look like a flat $\Omega = 1$ model. It also implies that, if at present $\Omega \neq 1$, in the distant past the density parameter could only differ by a tiny amount from unity. This is called the *flatness problem* which says that for the universe to evolve to its present status the density and the rate of

the expansion should have been finely tuned in the early universe. The inflationary scenario proposes a solution for this by postulating an initial phase of acceleratory expansion in the early universe. (see §2.1.5)

2.1.3 Matter and Radiation Domination

From the observed temperature of the Cosmic Microwave Background and the assumptions for that of the neutrinos, the total density of the radiation today is negligible to a good approximation. So we can consider the present universe as matter-dominated. However, since the energy density of matter particles scales as R^{-3}, while that of relativistic particles scales as R^{-4} there must have been a time when the densities in matter and radiation were equal, with radiation dominating proceeding to this time. To see how the Friedmann equation operates, it is therefore convenient to solve it first for the case when the pressureless matter is the only constituent of the universe, then go on to the case when the universe is dominated by the relativistic particles.

Consider a universe that solely consists of matter particles. It makes the problem simpler if we write the derivatives with respect to the *conformal time* defined by $d\eta \equiv cdt/R(t)$. The matter dominated Friedmann equation becomes:

$$(c/R)^2 R'^2 = \dot{R}^2 = \frac{8\pi G}{3}\rho_0 R_0^3 R^{-1} - kc^2, \tag{2.21}$$

where we have used $\rho = \big(R/R_0\big)^{-3}\rho_0$ and prime refers to the derivatives with respect to η.

i) For the case when $k = 0$ the solution is straightforward: we have $\dot{R} \propto R^{-1/2}$, which integrates to

$$R \propto t^{2/3}, \qquad \text{(MD)} \tag{2.22}$$

This $\Omega = 1$ matter-only universe is often termed the *Einstein-de Sitter* model. Eq. (2.22) implies that the expansion of an Einstein-de Sitter universe lasts an indefinite time into the future. In this model the comoving geometry is Euclidean, and there is no natural curvature scale, i.e. $k = 0$. However, the importance of this model actually arises since it is an unstable state for the universe. As we have seen earlier in Eq. (2.20), given a slight perturbation, the universe will evolve away from $\Omega = 1$. In practice, the properties of a flat model can usually be obtained by taking the limit $\Omega \to 1$ for either open or closed universes with $k = \pm 1$.

ii) For an open or closed universe Eq. (2.21) gives $R'^2 = \frac{8\pi G}{3c^2}\rho_0 R_0^3 R - kR^2$, or

$$\big(R/R_*\big)'^2 = 2\big(R/R_*\big) - k\big(R/R_*\big)^2, \qquad k = \pm 1 \tag{2.23}$$

where $R_* = 4\pi G\rho_0 R_0^3/3c^2$. We now claim that the solution to this equation is

$$R = kR_*[1 - \mathcal{C}_k(\eta)], \tag{2.24}$$

$$ct = kR_*[\eta - \mathcal{S}_k(\eta)], \tag{2.25}$$

where $\mathcal{C}_k \equiv \sqrt{1 - k\mathcal{S}_k^2}$. Hence $\mathcal{C}_k$ means cos if $k = +1$ and cosh if $k = -1$. To check that this solution works, use

$$\dot{R} = \frac{dR/d\eta}{dt/d\eta} = \frac{ck\mathcal{S}_k(\eta)}{1 - \mathcal{C}_k(\eta)}. \tag{2.26}$$

Substituting $\mathcal{S}_k^2 = k^{-1}(1-\mathcal{C}_k^2) = k^{-1}(1-\mathcal{C}_k)(1+\mathcal{C}_k)$ and simplifying the result we obtain

$$\dot{R}^2 = 2c^2k^2\frac{R_*}{R} - kc^2, \qquad k = \pm 1 \tag{2.27}$$

which, after substituting R_* in it, leads to the Friedmann's equation (2.12).

Fig. 2.1 shows the time dependence of the scale factor for open, closed and critical matter-dominated models. For a closed universe a big crunch is expected, as the universe ceases to expand and collapses after some times. This is because there is a relation between the density of the universe, its geometry and its eventual fate. Since the total energy ($-kc^2$) for a closed universe ($k = 1$) is negative, the universe does not expand fast enough to reach the 'escape velocity', therefore it must fall back onto itself. On the other hand, an open universe ($k = -1$) with positive total energy ($-kc^2$) has an expansion rate that exceeds the escape velocity, so such a universe will expand forever. In Fig. 2.1 we see that, as t approaches to zero, the scale of the universe in all models decreases to zero, so they all predict a singularity in the early universe. However since such a singularity causes the density to diverge to infinity, the assumption of having pressureless material dominating the early universe will prove wrong. Nevertheless, the basic conclusion about the existence of a singularity still holds in an expanding universe. We also see that a flat model is a good approximation to early phases of the universe.

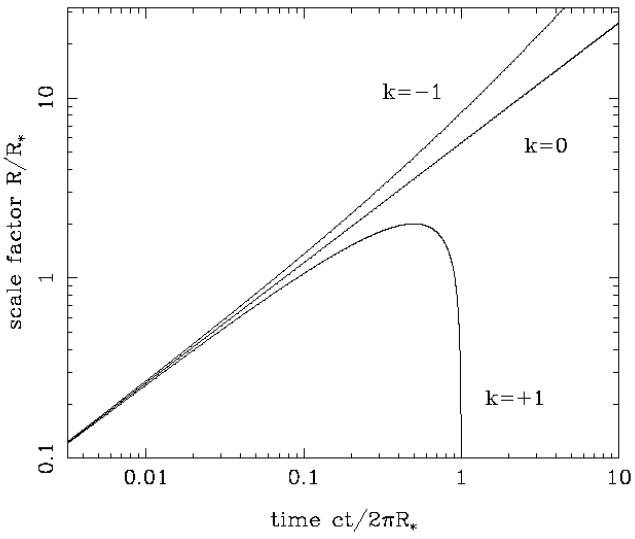

Figure 2.1: The time dependence of the scale factor for flat ($k = 0$), closed ($k = 1$) and open ($k = -1$) matter-dominated universes.

To derive the results for the radiation-dominated phase, where $\rho_r R^2 \propto R^{-2}$. consider that in this limit in the Friedmann's equation $\dot{R}^2 - 8\pi G\rho R^2/3 = -kc^2$, the potential term completely overwhelms the curvature term. So if we neglect the curvature in the radiation era, we have $\dot{R} \propto R^{-1}$, which has a power law solution

$$R \propto t^{1/2}, \qquad \text{(RD)} \tag{2.28}$$

Substituting this result into the Friedmann's equation with negligible curvature, leads to $t = \sqrt{3/32\pi G\rho}$. We could apply the same procedure to the Einstein-de Sitter model by feeding Eq. (2.22) back into Eq. (2.21), which would result in $t = 1/\sqrt{6\pi G\rho}$ which is valid for a flat matter dominated universe. Therefore since the two time scales have the same dependence on G and ρ and only differ in coefficients, we can conclude that the age of the universe is always of the order $(G\rho)^{-1/2}$.

2.1.4 Einstein's Static Universe

The significant problem regarding the expanding universe is that of the stability and fate of the mass in space. Gravitation requires all massive particles attract each other and eventually collapse, making the universe unstable. This is evident through Poisson's equation: $\nabla^2\phi = 4\pi G\rho$. Since the density of the isotropic universe is constant everywhere, this leads to solutions in the form $\phi \propto r^2$, so the gravitational acceleration should be proportional to the distance ($\nabla\phi \propto r$) which causes the mass to collapse. Einstein knew this problem, and he proposed a Poisson equation in the form

$$\nabla^2\phi + \lambda\phi = 4\pi G\rho, \tag{2.29}$$

hence introducing a new constant in nature, which is called the *cosmological constant*. Eq. (2.29) can be written in the form $\nabla^2\phi = 4\pi G(\rho - \rho_{rep})$, so we can interpret it as if a repulsive density $\rho_{rep} = \lambda\phi/4\pi G$ exists in nature which acts against the effect of the gravitational attraction. This repulsive density would have to be an isotropic property of the empty space and have a constant magnitude to cancel the gravitational acceleration. However, it can be easily shown that the Einstein's static universe actually does not work, and must either expand or contract. This is easy to understand if we imagine we introduce a little extra matter is some part of the universe. Since the vacuum energy is constant it cannot compensate for the additional gravitational attraction so the space should contract. Therefore Einstein's static universe is unstable.

Nevertheless, it turns out that the concept of the vacuum energy is of significant importance in modern cosmology. For a vacuum with non-zero energy density to have a negative-pressure, the equation of state would have to be of the form

$$p_v = -\rho_v c^2. \tag{2.30}$$

Indeed, a positive vacuum energy will act to cause a large-scale repulsion in the universe. This is evident through the equation

$$\ddot{R} = -\frac{4\pi GR}{3c^2}\big(\rho c^2 + 3p\big), \tag{2.31}$$

which can be obtained by substituting the conservation of energy relation: $d(\rho c^2 R^3) = -pd(R^3)$ into the time derivative of the Friedmann's equation (2.12). For a positive vacuum energy $\rho_v c^2 + 3p_v$ is negative, so that $\ddot{R}$ is positive. Hence, the cosmological constant can be thought

of what caused the expansion. In effect, the work done by the vacuum pressure to expand the universe is just sufficient to maintain the vacuum energy density constant. So vacuum acts as a supply of unlimited energy to inflate the universe to a required size.

The Einstein's static universe was first studied by de Sitter and named after him. A *de Sitter space* is a universe completely dominated by the cosmological constant, hence it is the limit of unstable expansion in which all the ordinary matter and radiation get redshifted away by the expansion. Consider the Friedmann's Eq. (2.12): $\dot{R}^2 - 8\pi G\rho R^2/3 = -kc^2$. Since the vacuum energy density is constant and R increases without limit, the two terms on the left hand side will eventually cancel each other. Thus, even if $k \neq 0$, the density of the universe will only infinitesimally differ from the critical value, so this establishes that we can just set $k = 0$ to solve the equation, in which case we have

$$R \propto \exp Ht, \qquad H = \sqrt{\frac{8\pi G\rho_v}{3}}. \tag{2.32}$$

This behavior is reminiscent of the steady-state universe, in which the universe appears the same to all observers at all times. For these models the perfect cosmological principle implies that the Hubble parameter should be always constant, so the steady-state model necessarily undergoes exponential expansion $R \propto \exp Ht$, the same as for de Sitter universe. In this sense, the de Sitter space can be considered as a steady-state universe because it contains a constant vacuum energy density which implies an infinite age for the universe and no big bang singularity. However, de Sitter space is not a particularly useful model because it does not account for matter density.

2.1.5 The Inflationary Universe

The inflationary scenario postulates an initial phase of rapid expansion in the history of the universe. The theory of inflation was first proposed to resolve the flatness and horizon problem of the cosmology. In short, these problems can be expressed in two questions: 1) why is the density of the observable universe so close to the critical density? and 2) Why is the universe nearly homogeneous and isotropic on large scales, even though there has been no time in the past during which these scales were causally connected? However, the theory of inflation was later turned out to be important because of its prediction of the quantum fluctuations in the spacetime metric which can be thought of as the seeds of the structure in the universe.

To describe the horizon problem recall that information cannot be communicated with speeds more than the speed of light. Therefore, at any given time t in the history of the universe, a *comoving horizon* distance can be defined by

$$\eta = \int_0^t \frac{dt'}{a(t')} = \int_0^a d\ln a' \frac{1}{a'H'}, \tag{2.33}$$

which represents the maximum (comoving) distance that light could have travelled since the Big Bang. Therefore particles separated by the comoving horizon could have never been in

contact with each other in the past. In Eq. (2.33) we have taken the speed of light $c = 1$, a convention which we will use in the rest of this thesis. From Eq. (2.33) we can further define the *comoving Hubble radius* $(aH)^{-1}$ which sets a scale for the particles beyond which they cannot communicate today but may come in contact in the future.

The comoving distances are the ones observed by the observers which are moving with the Hubble flow. These are unchanged quantities which are fixed and do not evolve with time. However, the so-called *physical* distances, which are the proper distances that we truly measure in the universe, are not fixed. The physical scales can be obtained by multiplying the comoving scales with the scale factor $a(t)$, therefore accounting for the expansion of the universe at any time. The Friedmann's equation for a flat universe implies that the 'physical' Hubble radius in different epochs obeys

$$R_H \equiv H^{-1} \propto \rho^{-1/2} \propto \begin{cases} a^2 & (RD) \\ a^{3/2} & (MD). \end{cases}$$

Therefore, since the rate of increase of the physical sizes which is $\propto a$ is smaller than that of the Hubble radius there should have been a time in the past where the perturbations corresponding to the present large scale structures could not communicate. (see Fig. 2.2 left) This is the basis of the Horizon problem.

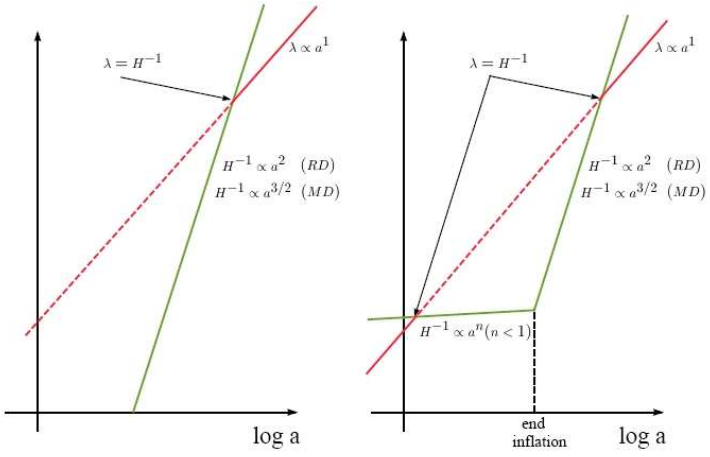

Figure 2.2: The evolution of the physical scales (red) with respect to the Hubble radius (green) with (right) and without (left) assuming an epoch of inflation. (Figure from Kolb, 1999)

The theory of inflation resolves the horizon problem by postulating an early epoch in which the Hubble radius is constant. (see Fig. 2.2 right) This can be envisaged as a period where the comoving Hubble radius shrinks rapidly so that all the comoving scales which were initially in causal contact lose communication. Since H is constant in this period the relation $da/dt = Ha$ requires a rapid exponential growth of the scale factor

$$a(t) = a_i e^{H(t-t_i)}, \qquad t_i < t < t_e \tag{2.34}$$

where $\ddot{a} > 0$. The beginning t_i and the end time t_e of inflation is often set by the number of

e-folds of expansion required so that the large scales go under horizon when inflation starts. In this sense, inflation can handle the flatness problem elegantly. Consider that from Eq. (2.15) with constant H we have $\Omega - 1 \propto a^{-2}$. The hypothesis of the adiabatic expansion of the universe tells us that to have a universe close to the critical density today, at the beginning of the radiation-dominated phase (or at the end of inflation) we should have had $|\Omega - 1| \sim 10^{-60}$. Therefore during inflation

$$\frac{|\Omega - 1|_{t=t_f}}{|\Omega - 1|_{t=t_i}} = \Big(\frac{a_i}{a_f}\Big)^2 = e^{-2N}, \tag{2.35}$$

where $N = \ln[H(t_e - t_i)]$. Now taking $|\Omega - 1|_{t=t_i}$ to have the arbitrary value of unity we can show that inflation solves the flatness problem if $N \gtrsim 70$.

Given that the dynamics of the universe determine its expansion, we can obtain more information about the characteristics of the dominant component during inflation by considering Eq. (2.31)

$$\frac{1}{a}\frac{d^2a}{dt^2} = -\frac{4\pi G}{3}(\rho + 3p). \tag{2.36}$$

This equation also arises from directly solving the time-time and space-space components of the Einstein equations (see §2.3.2). Since during inflation $d^2a/dt^2 > 0$ Eq. (2.36) implies

$$p < -\frac{\rho}{3}. \tag{2.37}$$

Therefore during inflation the pressure of the dominant component should be negative. In field theory, one candidate which satisfies this condition is the scalar field $\phi(\vec{x}, t)$ which we call *inflaton*. For a scalar field the Lagrangian density has the usual form of kinetic minus potential energy $\mathcal{L} = \frac{1}{2}\partial_\mu\phi\partial^\mu\phi - V(\phi)$, while its energy momentum tensor is of the form $T_{\mu\nu} = \partial_\mu\phi\partial_\nu\phi - g_{\mu\nu}\mathcal{L}$. Under the isotropy and homogeneity condition we have $T_{\mu\nu} = \mathrm{diag}(\rho, p, p, p)$ in which case the corresponding time-time and space-space components of the energy-momentum tensor read

$$\rho_\phi = \frac{1}{2}\dot{\phi}^2 + V(\phi) + \frac{1}{2a^2}\big(\nabla\phi\big)^2, \tag{2.38}$$

$$p_\phi = \frac{1}{2}\dot{\phi}^2 - V(\phi) - \frac{1}{6a^2}\big(\nabla\phi\big)^2. \tag{2.39}$$

Furthermore the equation of motion of the scalar field comes from the energy-momentum conservation ($T^{\mu\nu}_{;\nu} = 0$) which gives

$$\ddot{\phi} + 3H\dot{\phi} - \frac{1}{a^2}\nabla^2\phi + \frac{dV}{d\phi} = 0. \tag{2.40}$$

Now we can assume that the inflaton field is close to homogeneous with a zero order space-independent term $\phi^{(0)}(t)$ and a first-order quantum perturbation $\delta\phi(\vec{x}, t)$. Therefore, substituting $\phi(\vec{x}, t) = \phi^{(0)}(t) + \delta\phi(\vec{x}, t)$ into Eqs. (2.38) and (2.39) leads to $\rho = \dot{\phi}^2/2 + V(\Phi)$ and $\rho = \dot{\phi}^2/2 - V(\Phi)$ which imply if the potential term is much larger than the kinetic term, i.e.

$$V(\phi) \gg \dot{\phi}^2, \tag{2.41}$$

we will have $p_\phi \simeq -\rho_\phi$, or negative pressure. This means that the condition of inflation can be satisfied by a scalar field which 'slowly' rolls down a potential energy hill.

The fact that the kinetic energy of the inflaton should be very small is the basis of the *slow-roll approximation*. In models of inflation often the scalar field is capable of giving rise to rapid expansion only if this condition applies. Furthermore we can neglect the term $\ddot{\phi}$ in Eq. (2.40) since it is small compared to the other terms. Therefore, to zero order we have

$$3H\dot{\phi} = -\frac{dV}{d\phi}. \tag{2.42}$$

It is also useful to define the slow-roll parameters ϵ and η by

$$\epsilon \equiv \frac{1}{16\pi G}\Big(\frac{V'}{V}\Big)^2 \ll 1, \tag{2.43}$$

$$\eta \equiv \frac{1}{8\pi G}\Big(\frac{V''}{V}\Big) \ll 1. \tag{2.44}$$

Both these quantities are small since Eqs. (2.41) and (2.42) imply $(V')^2/V \ll H^2$ and $V'' \ll H^2$. As soon as the conditions in Eqs. (2.43) and (2.44) fail inflation comes to the end.

The strength of the theory of inflation is in its prediction of the primordial perturbations. Inflation predicts that the quantum fluctuations in the inflaton field can serve as the seeds of inhomogeneity in the universe. These are often best described in the Fourier space: Suppose χ corresponds to the fluctuations in the spacetime metric. The Fourier transform reads $\delta_\chi(\vec{k}) = \sum \delta_\chi(\vec{x}) e^{i\vec{k}\cdot\vec{x}}$. In linear theory we assume each mode of the perturbation behaves independently. Furthermore we can take the mean value of each mode equal to zero i.e. $\langle \delta_\chi(\vec{k}) \rangle = 0$. Therefore the perturbations can be expressed as a combination of independent Fourier modes with random phases. This means that the fluctuations should be Gaussian, so they can be totally characterized by the power spectrum

$$P(k) \equiv |\delta_\chi(\vec{k})|^2. \tag{2.45}$$

The shape of the power spectrum is often considered as scale-invariant. This is due to our expectation that the evolution of the universe should look the same on different scales. This resembles a fractal shape which appears the same to all observers which live on it. Defining a dimensionless power spectrum by $\Delta^2(k) \propto k^3 P(k)$ this implies that for a scale-free spectrum $\Delta^2(k)$ is constant. The simplest theories of inflation predict a scalar and tensor power spectrum of the primordial perturbations of the form (see Riotto, 2002)

$$\Delta^2_\Phi(k) = \frac{G}{2\epsilon}\Big(\frac{H}{2\pi}\Big)^2\Big(\frac{k}{aH}\Big)^{n_S-1} \equiv A_S^2\Big(\frac{k}{aH}\Big)^{n_S-1}, \tag{2.46}$$

$$\Delta^2_h(k) = 8G\Big(\frac{H}{2\pi}\Big)^2\Big(\frac{k}{aH}\Big)^{n_T} \equiv A_T^2\Big(\frac{k}{aH}\Big)^{n_T}, \tag{2.47}$$

where the indices Φ and h represent the curvature and tensor perturbations respectively (see §2.1.6). Here A_S and A_T define the amplitude of the primordial scalar and tensor perturbations, while n is the spectral index which quantifies the amount of deviation (or tilt) from the scale-invariance. Therefore for scale-invariant power spectra we should have $n_S = 1$ and $n_T = 0$.

Bartolo et al. (2001) show that at the time when a given mode k crosses the horizon $(aH)^{-1}$ the primordial power spectra are given by

$$\Delta^2_\Phi(k) \simeq \frac{1}{(2\pi)^2}\Big(\frac{H^2}{\dot\phi}\Big)^2\Big|_{k=aH}, \tag{2.48}$$

$$\Delta^2_h(k) \simeq \frac{16G}{\pi}H^2\Big|_{k=aH}. \tag{2.49}$$

Substituting these into Eqs. (2.46) and (2.47) we can calculate the spectral indices in terms of the slow-roll parameters

$$n_S - 1 = \frac{d\ln\Delta^2_\Phi}{d\ln k} = \frac{d}{d\ln k}\big[\ln H^4 - \ln\dot\phi^2\big], \tag{2.50}$$

$$n_T = \frac{d\ln\Delta^2_h}{d\ln k} = \frac{d\ln H^2}{d\ln k}. \tag{2.51}$$

Using the facts that $(d\ln H)/(d\ln k) = -\epsilon$ and $(d\ln\dot\phi)/(d\ln k) = \epsilon - \eta$ (see Riotto, 2002), these equations lead to the *consistency relations*

$$n_S = 1 + 2\eta - 6\epsilon, \tag{2.52}$$

$$n_T = -2\epsilon. \tag{2.53}$$

These are important relations since they give us a mechanism to probe the slow-roll parameters by determining the expected tilt from the observations.

Another way to probe the inflation is through the tensor-to-scalar amplitude ratio which we define by

$$r \equiv \frac{\frac{1}{100}A_T^2}{\frac{4}{25}A_S^2} = \frac{8G\Big(\frac{H}{2\pi}\Big)^2}{16\frac{G}{2\epsilon}\Big(\frac{H}{2\pi}\Big)^2} = \epsilon. \tag{2.54}$$

Eq. (2.53) then gives $r = -n_T/2$. This relation is the basis of one-field inflation theories. We will see in chapter 3 how high precision observations of the CMB, and particularly that of the polarization B-mode can enable us to put constraints on the tensor-to-scalar ratio parameter and hence the energy scale of the inflation.

2.1.6 Quantifying Inhomogeneity

Today the theory which best explains the evolution of structure and inhomogeneity in the universe is the perturbation theory. The linear theory of perturbation is based on introducing first order fluctuations in the metric of spacetime and then studying the evolution of these perturbations as the universe goes through different epochs. Since the universe is believed to be homogeneous to a very good approximation the perturbation theory always leads to the results of the unperturbed universe on very large scales, however it also leads to additional first-order terms which explain the inhomogeneities and anisotropies.

To introduce fluctuations in the metric there is always the question of how to do. This leads us to the concept of gauge freedom which is a consequence of the general relativity. It arises from

the fact that coordinate systems are not unique, as a result what we call density perturbation in one coordinate system is not necessarily a density fluctuation in another coordinate. This non-universality in the definition of the fluctuations has also caused confusions over the gauge freedom. Lifshitz (1946) adopted the synchronous gauge while Bardeen (1980) proposed gauge-invariant quantities to tackle the issues related to the synchronous gauge. Although it is possible to invent gauge-invariant formalisms, here we want to avoid this approach in order to take advantage of the gauge freedom for our discussion since some gauges lead to results which give simple physical interpretation.

For example a widely used gauge in perturbation theory is the *synchronous gauge*. In this gauge the perturbations to the spatially 'flat' FRW metric are characterized by (see Ma and Bertschinger, 1995)

$$c^2 d\tau^2 = c^2 dt^2 - a^2(t)\Big[(\delta_{ij} + h_{ij})dx^i dx^j\Big], \tag{2.55}$$

where the metric perturbation h_{ij} can be decomposed into a trace part $h \equiv h_{ii}$ and a traceless part $h_{ij} = h\delta_{ij}/3 + h^{\parallel}_{ij} + h^{\perp}_{ij} + h^{T}_{ij}$, where, by definition, the divergences of $h^{\parallel}_{ij}$ and $h^{\perp}_{ij}$ are longitudinal and transverse, respectively, and h^{T}_{ij} is transverse, satisfying

$$\epsilon_{ijk}\partial_j\partial_l h^{\parallel}_{lk} = 0, \qquad \partial_i\partial_j h^{\perp}_{ij} = 0, \qquad \partial_i h^{T}_{ij} = 0. \tag{2.56}$$

A disadvantage of the synchronous gauge is that as the choice of the initial hypersurfaces is arbitrary in the synchronous gauge, any point in the spacetime can have several different coordinate labels. This is due to the fact that since the coordinate systems are defined by freely falling observers the trajectory of different observers may intersect, hence giving rise to singularity. Furthermore, the synchronous gauge is not a particularly convenient gauge as it only leads to complicated interpretations of the evolution of the fluctuations. In spite of these disadvantages, the synchronous gauge is today a standard framework for perturbation theory.

A convenient gauge that we want to use here is the *conformal Newtonian gauge*. The conformal Newtonian gauge is a simple gauge which is only characterized by diagonal elements:

$$c^2 d\tau^2 = (1 + 2\Psi)c^2 dt^2 - a^2(t)\Big[(1 + 2\Phi)\delta_{ij}dx^i dx^j\Big]. \tag{2.57}$$

Here Ψ and Φ are two scalar potentials. The advantage of working in this gauge is that the metric tensor is diagonal, so the calculations are easy and lead to simple geodesic equations. Moreover, in the Newtonian limit Ψ and Φ here play the role of the Newtonian gravitational potential and the spacetime curvature potential respectively and thus lead to simple physical interpretation. These scalar fields are also identical to the gauge invariant variables proposed by Bardeen (1980). However, a disadvantage of the conformal Newtonian gauge written in the form (2.57) is that it is restricted to scalar perturbations and does not account for vector perturbations and gravity waves. Nonetheless, it is possible to generalize this gauge to account for these other degrees of freedom. In the rest of this chapter we employ the Newtonian gauge formalism in the flat universe to derive the equations of the evolution of fluctuations.

2.2 The Boltzmann Equation for Photons

In this section we present an equation which describes the evolution of the probability distribution function of the electrons in the early universe. Gravity is the most important factor that determines the evolution of the distribution function of the photons along their geodesics. However, photons are also affected by Compton scattering of the electrons that should also be taken into account. The equation which describes the dynamics of this photon-electron gas is the *Boltzmann equation*

$$\frac{df}{dt} = C[f]. \tag{2.58}$$

Here $f(x,p)$ is the probability distribution function of photons where $x^\mu = (t, \mathbf{x})$ and $p^\mu = (p^0, p^i)$ are the 4-position and 4-momentum of the photons in the spacetime.[1] The right hand side is the collision term which governs the rate of change of the photon inhomogeneity due to interaction with electrons. A number of textbooks and papers have worked out the Boltzmann equation for photons in the early universe. Here we follow the Newtonian gauge notation solution presented in Dodelson (2003) and Hu (1995) which give an easy and comprehensible derivation.

2.2.1 The Collisionless Boltzmann Equation

Assuming a collisionless case for the moment, the left hand side of the Boltzmann equation (2.58) reduces to

$$\frac{df}{dt} = \frac{\partial f}{\partial x^\mu}\frac{dx^\mu}{dt} + \frac{\partial f}{\partial p^\mu}\frac{dp^\mu}{dt} = 0. \tag{2.59}$$

This collisionless Boltzmann equation can be interpreted as a conservation equation for photon density along its trajectory. In order to determine the gravitational effects in this equation we have to evaluate the time derivatives of the photon momentum in Eq. (2.59). Here we adopt the conformal Newtonian gauge for a flat universe where the metric takes the form

$$\begin{aligned} g_{00} &= -[1 + 2\Psi(\mathbf{x}, t)], \\ g_{0i} &= 0, \\ g_{ij} &= a^2[1 + 2\Phi(\mathbf{x}, t)]\delta_{ij}. \end{aligned} \tag{2.60}$$

The momentum of the photons along their trajectory is given by $p^2 = p_i p^i$. Since photons are massless particles we have $p_\mu p^\mu = 0$ which, to first order in perturbation terms, leads to $p^0 = (1 - \Psi)p$ and $p^i = \frac{p(1-\Phi)}{a}\hat{p}^i$ where $\hat{p}^i$ is the unit vector along the direction of propagation. Substituting these momentum terms in Eq. (2.59) we will have

$$\begin{aligned} \frac{df}{dt} &= \frac{\partial f}{\partial t} + \frac{\partial f}{\partial x^i}\frac{p^i}{p^0} + \frac{\partial f}{\partial p}\frac{dp}{dt} + \frac{\partial f}{\partial \hat{p}^i}\frac{d\hat{p}^i}{dt} \\ &= \frac{\partial f}{\partial t} + \frac{\partial f}{\partial x^i}\frac{\hat{p}^i}{a}(1 - \Phi + \Psi) + \frac{\partial f}{\partial p}\frac{dp}{dt}, \end{aligned} \tag{2.61}$$

[1] Here we define $i, j, .. = (1, 2, 3)$ and the Latin symbols $\mu, \nu, .. = (0, 1, 2, 3)$.

where we have also used the relation $p^i/p^0 = dx^i/dt$ and have dropped the quadratic terms in the potentials. In equation (2.61) the gravitational effects are introduced through the time dependence of the momentum. Hence we need to evaluate an expression for dp/dt in terms of the metric perturbations. In order to do this we need to examine the geodesic equation which relates the photon trajectory to the spacetime metric. The geodesic equation for the photons is given by

$$\frac{d^2x^\mu}{d\lambda^2} + \Gamma^\mu_{\alpha\beta}\frac{dx^\alpha}{d\lambda}\frac{dx^\beta}{d\lambda} = 0, \tag{2.62}$$

where the Christoffel symbol $\Gamma^\mu_{\alpha\beta}$ is defined by

$$\Gamma^\mu_{\alpha\beta} \equiv \frac{1}{2}g^{\mu\delta}\Big(\frac{\partial g_{\delta\alpha}}{\partial x^\beta} + \frac{\partial g_{\delta\beta}}{\partial x^\alpha} - \frac{\partial g_{\alpha\beta}}{\partial x^\delta}\Big). \tag{2.63}$$

In Eq. (2.62) the affine parameter λ parameterizes the trajectory of photons. We can always choose λ such that $p^0 = \frac{dx^0}{d\lambda} = \frac{dt}{d\lambda}$. In this way we can write the time component of the geodesic equation in the form

$$\frac{d}{dt}[p(1-\Psi)] = -\Gamma^0_{\alpha\beta}\frac{p^\alpha p^\beta}{p}(1+\Psi). \tag{2.64}$$

Now from equation (2.63) the product $\Gamma^0_{\alpha\beta}p^\alpha p^\beta/p$ can be written as

$$\Gamma^0_{\alpha\beta}\frac{p^\alpha p^\beta}{p} = \frac{-1}{1+2\Psi}\Big[2\frac{\partial g_{0\alpha}}{\partial x^\beta} - \frac{\partial g_{\alpha\beta}}{\partial t}\Big]\frac{p^\alpha p^\beta}{p}, \tag{2.65}$$

where we have used the fact that $p^\alpha p^\beta$ is symmetric with respect to changing α and β. Now calculating and simplifying the metric terms up to first order results in

$$\Gamma^0_{\alpha\beta}\frac{p^\alpha p^\beta}{p} = (-1+2\Psi)\left[-\frac{\partial\Psi}{\partial t}p - 2\frac{\partial\Psi}{\partial x^i}\frac{p\hat{p}^i}{a} - p\Big(\frac{\partial\Phi}{\partial t} + H\Big)\right]. \tag{2.66}$$

Now substituting Eq. (2.66) in Eq. (2.64) and collecting terms we will have

$$\frac{1}{p}\frac{dp}{dt} = -H - \frac{\partial\Phi}{\partial t} - \frac{\partial\Psi}{\partial x^i}\frac{\hat{p}^i}{a}. \tag{2.67}$$

This equation is interesting as it describes the conservation of the photon momentum as it travels through the gravitational potential fields. The first term on the right states that the photon loses energy due to the Hubble expansion. The second term accounts for the energy loss due to a growing potential well. As the photon travels through an overdense region ($\Phi > 0$ and $\Psi < 0$) it first gains energy and then loses energy. But if the potential well is deepening as the photon travels through it ($\partial\Phi/\partial t > 0$), it becomes more difficult for the photon to escape the well, hence acquiring a net redshift. Finally, the third term ($\hat{p}^i\partial\Psi/\partial x^i$) accounts for the blueshift and redshift of the photon when it enters and leaves the potential well.

Now, having evaluated the gravitational redshift and dilation effects on the photon momentum, we can substitute the time component of the geodesic equation (2.67) into the Boltzmann equation (2.61). Then the Boltzmann equation for the photons can be written as

$$\frac{df}{dt} = \frac{\partial f}{\partial t} + \frac{\hat{p}^i}{a}\frac{\partial f}{\partial x^i} - p\frac{\partial f}{\partial p}\Big[H + \frac{\partial\Phi}{\partial t} + \frac{\hat{p}^i}{a}\frac{\partial\Psi}{\partial x^i}\Big]. \tag{2.68}$$

This equation contains all the information about the effect of gravity on the photon distribution function. Photons are bosons so that they have Bose-Einstein distributions. We write the perturbed Bose-Einstein distribution as

$$f(\mathbf{x},\mathbf{p},t)=\left[\exp\left\{\frac{p}{T(t)[1+\Theta(\mathbf{x},\hat{p},t)]}\right\}-1\right]^{-1}. \tag{2.69}$$

Here T is the zero order homogeneous temperature whereas $\Theta = \delta T/T$ represents the anisotropies to first order. We are interested to write the perturbed distribution function in terms of the zero-order Bose-Einstein distribution which does not include anisotropies, i.e. $f^{(0)} \equiv \left[\exp\left(\frac{p}{T}\right)-1\right]^{-1}$. So we can Taylor expand equation (2.69) to get

$$\begin{aligned} f &\simeq \left[\exp\left(\frac{p}{T}\right)-1\right]^{-1}+\frac{p\Theta\exp(\frac{p}{T})}{T\left[\exp(\frac{p}{T})-1\right]^2} \\ &= f^{(0)}-p\Theta\frac{\partial f^{(0)}}{\partial p}. \end{aligned} \tag{2.70}$$

Substituting the expansion terms in Eq. (2.70) into Eq. (2.68) the zero order collisionless Boltzmann equation gives

$$\left.\frac{df}{dt}\right|_{\text{zero order}}=\frac{\partial f^{(0)}}{\partial t}-Hp\frac{\partial f^{(0)}}{\partial p}=0. \tag{2.71}$$

Here we have ignored all terms with Ψ, Φ or Θ. Writing the time derivative term in the form $\partial f^{(0)}/\partial t = \left(\partial f^{(0)}/\partial T\right)\left(dT/dt\right)$ and using the fact that $T\partial f^{(0)}/\partial T = -p\partial f^{(0)}/\partial p$, the zero-order equation (2.71) leads to

$$\left[-\frac{1}{T}\frac{dT}{dt}-\frac{1}{a}\frac{da}{dt}\right]\frac{\partial f^{(0)}}{\partial p}=0. \tag{2.72}$$

Therefore $dT/T = -da/a$ or $T \propto 1/a$. This verifies our earlier expectation that the temperature of photons falls by the expansion of the universe.

To write a Boltzmann equation for the anisotropies Θ we have to keep the terms up to first order in the potentials. We can show that the first order collisionless Boltzmann equation can be written as

$$\left.\frac{df}{dt}\right|_{\text{first order}}=-p\frac{\partial f^{(0)}}{\partial p}\left[\frac{\partial\Theta}{\partial t}+\frac{\hat{p}^i}{a}\frac{\partial\Theta}{\partial x^i}+\frac{\partial\Phi}{\partial t}+\frac{\hat{p}^i}{a}\frac{\partial\Psi}{\partial x^i}\right]. \tag{2.73}$$

To obtain this equation we have made use of equation (2.68). This equation is what we were after. It describes the evolution of the temperature anisotropies of the photons. It incorporates the free streaming terms (the first two terms) as well as the terms accounting for the effects of gravity. However the collision terms for the Compton scattering of electrons are still missing which we will derive in the next subsection.

2.2.2 The Compton Scattering

The Compton scattering between electrons and photons $e^-(\mathbf{q})+\gamma(\mathbf{p}) \leftrightarrow e^-(\mathbf{q}')+\gamma(\mathbf{p}')$ is the major particle interaction that affects the photons. It is also the main factor that thermalizes

the photons in the early universe as a result of exchange of energy with electrons. To formulate the effect of Compton scattering on the photon distribution function $f(\mathbf{p})$ we need to sum over all possible phase space momenta $(\mathbf{q}, \mathbf{q}', \mathbf{p}')$ by which the photon and electron can exchange energy. The collision term for this mechanism is given by

$$\begin{aligned} C[f(\mathbf{p})] &= \frac{1}{E(p)} \int \frac{d^3q}{(2\pi)^3 2E_e(q)} \int \frac{d^3q'}{(2\pi)^3 2E_e(q')} \int \frac{d^3p'}{(2\pi)^3 2E_e(p')} (2\pi)^4 |M|^2 \\ &\quad \times \delta^3(\mathbf{p} + \mathbf{q} - \mathbf{p}' - \mathbf{q}') \delta[E(p) + E_e(q) - E(p') - E_e(q')] \\ &\quad \times \Big\{ g(\mathbf{x}, \mathbf{q}', t) f(\mathbf{x}, \mathbf{p}', t) - g(\mathbf{x}, \mathbf{q}, t) f(\mathbf{x}, \mathbf{p}, t) \Big\}. \end{aligned} \tag{2.74}$$

This equation determines the effect of the energy exchange due to the scattering on the photon distribution function. Here the amplitude $|M|^2 = 8\pi\sigma_T m_e^2$ is the Lorentz invariant matrix element where σ_T is the Thomson cross-section. In Eq. (2.74), $f(\mathbf{x}, \mathbf{p}, t)$ is the distribution function of photons, while $g(\mathbf{x}, \mathbf{q}, t)$ is that for the electrons.[2] Here $f(\mathbf{x}, \mathbf{p}, t) \frac{d^3p}{(2\pi)^3}$ represents the number density of photons with momenta between p and $p + dp$. In this way the product $g(\mathbf{x}, \mathbf{q}, t) f(\mathbf{x}, \mathbf{p}, t)$ represents the rate of the forward Compton scattering while $g(\mathbf{x}, \mathbf{q}', t) f(\mathbf{x}, \mathbf{p}', t)$ represents the rate of the inverse Compton scattering. In this equation we have neglected the Pauli blocking terms which arise due to the fact that more than one electron cannot occupy the same element of the space since we assume the density of electrons is low. The energy terms in Eq. (2.74) are $E(p) = p$ for photons and $E_e(q) = m_e + q^2/(2m_e)$ for electrons. Substituting these into equation (2.74) and integrating over $\mathbf{q}'$ we will have

$$\begin{aligned} C[f(\mathbf{p})] &= \frac{\pi}{4m_e^2 p} \int d^3q \frac{g(\mathbf{q})}{(2\pi)^3} \int \frac{d^3p'}{(2\pi)^3 p'} |M|^2 \\ &\quad \times \left\{ \delta(p - p') + \frac{(\mathbf{p} - \mathbf{p}') \cdot \mathbf{q}}{m_e} \frac{\partial \delta(p - p')}{\partial p'} \right\} \{ f(\mathbf{p}') - f(\mathbf{p}) \}. \end{aligned} \tag{2.75}$$

Here we have substituted $E_e = m_e$ for the energy factors in the denominators as the kinetic energy of electrons is negligible compared to their mass. Furthermore we have assumed that before and after the collision the electron energy (q, q') is negligible compared to the photon energy q. In this way the terms in the large brackets in equation (2.75) are just the Taylor expansion of the Delta function $\delta[p + E_e(q) - p' - E_e(\mathbf{q} + \mathbf{p} - \mathbf{p}')]$ up to first order in p', when $p' \simeq p$. Now if we evaluate the $\mathbf{q}$ integral the first term in the brackets gives the free electron density n_e whereas the second term which depends on $\mathbf{q}/m_e$ gives $n_e \mathbf{v}_b$ where v_b is the bulk velocity of electrons. With these assumptions the collision term takes the form

$$\begin{aligned} C[f(\mathbf{p})] &= \frac{n_e \sigma_T}{4\pi p} \int_0^\infty dp' p' \int d\Omega' \left\{ \delta(p - p') + (\mathbf{p} - \mathbf{p}') \cdot \mathbf{v}_b \frac{\partial \delta(p - p')}{\partial p'} \right\} \\ &\quad \times \left\{ f^{(0)}(\mathbf{p}') - f^{(0)}(\mathbf{p}) - p' \frac{\partial f^{(0)}}{\partial p'} \Theta(\hat{p}') + p \frac{\partial f^{(0)}}{\partial p} \Theta(\hat{p}) \right\}, \end{aligned} \tag{2.76}$$

where we have used Eq. (2.70) for the expansion of the photon distribution function. In subsection 2.4.1 we will see that on superhorizon scales adiabatic conditions imply that all

[2]Electrons are fermions, thus they obey Fermi-Dirac distribution $g = \left[\exp\left(\frac{E}{T}\right) + 1 \right]^{-1}$ where we have neglected the chemical potential.

different particle species have a common velocity field. But as the modes enter the horizon velocities start to evolve differently. Nevertheless during the epoch before recombination where photons are tightly coupled to electrons we can assume that the velocity field of the photons is equal to the bulk velocity. Now we know that the angular integral of the anisotropies over all sky results in the monopole function of the temperatures i.e. $\Theta_0 \equiv (4\pi)^{-1}\int d\Omega'\Theta(\hat{p})$. Moreover the solid angle integral over $\mathbf{p}'\cdot\mathbf{v}_b$ is zero as $\mathbf{v}_b$ is a fixed vector. Therefore equation (2.76) leads to

$$\begin{aligned} C[f(\mathbf{p})] &= \frac{n_e\sigma_T}{p}\int_0^\infty dp'p'\Big[\delta(p-p')\Big(-p'\frac{\partial f^{(0)}}{\partial p'}\Theta_0 + p\frac{\partial f^{(0)}}{\partial p}\Theta(\hat{p})\Big) \\ &\quad + \mathbf{p}\cdot\mathbf{v}_b\frac{\partial\delta(p-p')}{\partial p'}\big(f^{(0)}(p') - f^{(0)}(p)\big)\Big]. \end{aligned} \tag{2.77}$$

Here we have neglected the first-order parts of the distribution function when they multiply the bulk velocity. The above equation can be easily solved by parts to give

$$C[f(\mathbf{p})] = -p\frac{\partial f^{(0)}}{\partial p}n_e\sigma_T[\Theta_0 - \Theta(\hat{p}) + \hat{p}\cdot\mathbf{v}_b]. \tag{2.78}$$

Substituting Eq. (2.78) in Eq. (2.73) and the collisional Boltzmann equation for photons can be written as

$$\frac{\partial\Theta}{\partial t} + \frac{\hat{p}^i}{a}\frac{\partial\Theta}{\partial x^i} + \frac{\partial\Phi}{\partial t} + \frac{\hat{p}^i}{a}\frac{\partial\Psi}{\partial x^i} = n_e\sigma_T[\Theta_0 - \Theta + \hat{p}\cdot\mathbf{v}_b]. \tag{2.79}$$

In linear theory it is generally easier to write the equations in the Fourier space. It turns out that in the Fourier space each mode of the perturbation evolves independently i.e. the wavenumbers obey a set of uncoupled equations. This is particularly true for the CMB anisotropies which are small and stay in the linear regime up to the present time. Therefore we can expand the temperature anisotropies in the Fourier space as

$$\Theta(\mathbf{x},\eta) = \int\frac{d^3k}{(2\pi)^3}e^{i\mathbf{k}\cdot\mathbf{x}}\Theta(k,\mu,\eta). \tag{2.80}$$

Here $\mu \equiv \hat{k}.\mathbf{p}$ describes the direction of the propagation of the photons $\hat{p}$ along the temperature gradients $\hat{k}$. Now in the Fourier space derivatives become $\nabla \to i\mathbf{k}$. Also, assuming the velocity filed is irrotational, only the component of the velocity parallel to the wavevector is important, so $\mathbf{v}_b = -iv_b\hat{k}$. Therefore, in terms of the Fourier modes the Boltzmann equation (2.79) will take the form

$$\dot{\Theta} + ik\mu\Theta + \dot{\Phi} + ik\mu\Psi = -\dot{\tau}\big[\Theta_0 - \Theta - i\mu v_b\big], \tag{2.81}$$

where now the overdots represent derivatives with respect to the conformal time η. Furthermore we have defined τ which is the *optical depth*

$$\tau(\eta) \equiv \int_\eta^{\eta_0} d\eta' n_e\sigma_T a, \tag{2.82}$$

such that $\dot{\tau} \equiv -n_e\sigma_T a$. The optical depth can be interpreted as a measure of transparency of the universe. At early times, when the density of free electrons is high, the optical depth is very large ($\tau \gg 1$) so that the high rate of the Compton scattering causes the photons and the

electrons to be tightly coupled to each other. However, as the electron density falls due to the expansion of the universe, the optical depth becomes very small ($\tau = 0$) since the mean free path of photons is now larger. Indeed if τ had remained large after the recombination, most of the angular scale features of the CMB photons would have been erased by the Compton scattering. We will study the tightly coupled limit and the free streaming of the photons after recombination in subsection 2.5.2. Before closing this section, it is also useful to define the multipole moments of the temperature fluctuations. The Legendre polynomials $\mathcal{P}_\ell(\mu)$ give a complete and orthogonal set of functions on the interval $-1 \leq \mu \leq 1$. The first few Legendre polynomials are

$$\mathcal{P}_0(\mu) = 1, \quad \mathcal{P}_1(\mu) = \mu, \quad \mathcal{P}_2(\mu) = \frac{1}{2}(3\mu^2 - 1), \quad ... \tag{2.83}$$

We can expand the temperature in terms of the Legendre functions as

$$\Theta_\ell(k, \eta) \equiv \frac{1}{(-i)^\ell} \int_{-1}^{1} \frac{d\mu}{2} \mathcal{P}_l(\mu) \Theta(k, \mu, \eta), \tag{2.84}$$

which gives the ℓ-th multipole moment of the temperature anisotropy. In this notation the Fourier space anisotropies can be recovered from the multipoles by

$$\Theta(k, \mu, \eta) = \sum_{\ell=0}^{\infty} (-i)^\ell (2\ell + 1) \mathcal{P}_\ell(\mu) \Theta_l(k, \eta). \tag{2.85}$$

We will see in the subsequent sections that it is generally easier to represent the radiation anisotropies in terms of the multipole moments. It will turn out that only the first few multipoles are significant before recombination, moreover we will show that the multipole moments are directly related to the angular scale anisotropies on the sky.

2.3 Perturbation Theory for Multicomponent Fluid

The theory of structure formation is based on the growth of perturbations due to gravitational instability. The theory assumes that the primordial scalar perturbations grow into clusters of galaxies due to self-gravity. The early stages of this process occurs when the amplitudes of the perturbations are very small. As a result a perturbation theory can be treated by linear theory. Nevertheless, the existence of different particle species makes the evolution of the fluctuations complicated. These particle species are photons, baryons, neutrinos and the dark matter which interact differently and have different equations of state. One important factor that couples the evolution equation of these species is that they are all affected by gravity which is determined by the spacetime metric, whereas the metric itself which determines the gravity is also affected by each component. Moreover as we have seen before, photons interact with free electrons through Compton scattering whereas the electrons themselves are coupled to the protons by Coulomb scattering. We will see in section 2.5 that this results in a single photon-baryon fluid before recombination. This coupling process between photons and baryons is especially interesting as it is responsible for the oscillatory features that we observe in the angular power spectrum of

the microwave background. In this section we present the set of coupled equations that govern the evolution of the different species. These arise from the energy momentum conservation equations in a perturbed Friedmann-Robertson-Walker universe where the equations are also related to the metric fluctuations through the Einstein's equation. Our analysis here is close to that of Hu (1995) and Dodelson (2003).

2.3.1 Conservation Equations

The conservation of the energy-momentum tensor describes the evolution of the energy density and velocity of a perfect fluid, whereas the Einstein equation relates the curvature of the space time to the perturbations. In this subsection we derive the conservation equations for the perturbed universe and leave the Einstein equations for the next subsection. To begin with, we first need to calculate the Christoffel symbols in Eq. (2.63) for the flat conformal Newtonian gauge Eq. (2.60). Up to first order these will turn out to be

$$\Gamma^0_{00} = \frac{1}{2}g^{00}\frac{\partial g_{00}}{\partial t} = \frac{\partial \Psi}{\partial t}, \tag{2.86}$$

$$\Gamma^0_{0i} = \Gamma^0_{i0} = \frac{1}{2}g^{00}\frac{\partial g_{00}}{\partial x^i} = \frac{\partial \Psi}{\partial x^i} = ik_i\Psi, \tag{2.87}$$

$$\Gamma^i_{00} = -\frac{1}{2}g^{ii}\frac{\partial g_{00}}{\partial x^i} = \frac{ik^i}{a^2}\Psi, \tag{2.88}$$

$$\Gamma^0_{ij} = -\frac{1}{2}g^{00}\frac{\partial g_{ij}}{\partial t} = \Big[H + 2H(\Phi - \Psi) + \frac{\partial \Phi}{\partial t}\Big]a^2\delta_{ij}, \tag{2.89}$$

$$\Gamma^i_{0j} = \Gamma^i_{j0} = \frac{1}{2}g^{ii}\frac{\partial g_{ii}}{\partial t}\delta_{ij} = \Big[H + \frac{\partial \Phi}{\partial t}\Big]\delta_{ij}, \tag{2.90}$$

$$\Gamma^i_{jk} = \frac{1}{2}g^{i\alpha}\Big(\frac{\partial g_{\alpha k}}{\partial x^j} + \frac{\partial g_{j\alpha}}{\partial x^k} - \frac{\partial g_{jk}}{\partial x^\alpha}\Big) = i\Phi\big[k_k\delta_{ij} + k_j\delta_{ik} - k_i\delta_{jk}\big]. \tag{2.91}$$

The energy-momentum tensor of a perfect fluid in its rest-frame is given by $T^{\mu\nu} = \mathrm{diag}(\rho, p, p, p)$, where ρ and p are the energy density and pressure of the fluid measured by an observer at rest with the fluid. We can carry out a Lorentz transformation to write the general energy-momentum tensor in the form

$$T^{\mu\nu} = (\rho + p)U^\mu U^\nu - pg^{\mu\nu}, \tag{2.92}$$

where now $U^\mu \equiv dx^\mu/dt$ is the 4-velocity of the fluid. This general form of the energy-momentum tensor can also be obtained by the manifest covariance technique since $T^{\mu\nu}$ reduces to its diagonal form in the rest-frame. Now, assuming first order perturbations in the energy density and pressure, we consider $\rho \to \rho + \delta\rho$ and $p \to p + \delta p$. Then to first order the perturbed energy-momentum tensor takes the form

$$\begin{aligned} T^0_0 &= -(\rho + \delta\rho), \\ T^0_i &= (\rho + p)v_i = -T^i_0, \\ T^i_j &= (p + \delta p)\delta_{ij} + \Sigma^j_i, \end{aligned} \tag{2.93}$$

where $v^i \equiv dx^i/dx^0$ and Σ^j_i is the anisotropic sheer perturbation which is often negligible in the early universe. The equation for the conservation of the energy-momentum tensor is given by

$$T^{\mu\nu}_{;\mu} = \partial_\mu T^{\mu\nu} + \Gamma^\nu_{\alpha\beta} T^{\alpha\beta} + \Gamma^\alpha_{\alpha\beta} T^{\nu\beta} = 0. \tag{2.94}$$

The zero component of this equation guarantees the conservation of the energy density while the space component gives the momentum conservation equation. Taking $\nu = 0$, the time component of equation (2.94) becomes

$$T^{\mu 0}_{;\mu} = \partial_0 T^{00} + \partial_i T^{i0} + \Gamma^0_{00} T^{00} + \Gamma^0_{ij} T^{ij} + \Gamma^i_{i0} T^{00} + \Gamma^i_{ij} T^{0j} = 0, \tag{2.95}$$

where to first order in Ψ, Φ, $\delta\rho$ and δp we have

$$\begin{aligned}
T^{00} &= g^{00} T^0_0 = (1 + \delta_x - 2\Psi)\rho, \\
T^{i0} &= g^{00} T^i_0 = (1+\omega)\rho v_i, \\
T^{ij} &= g^{ik} T^j_k = (p + \delta p - 2\Phi p)\frac{\delta_{ij}}{a^2}, \\
\partial_0 T^{00} &= \Big(\frac{\partial \delta_x}{\partial t} - 2\frac{\partial \Psi}{\partial t}\Big)\rho + (1 + \delta_x - 2\Psi)\frac{\partial \rho}{\partial t}, \\
\partial_i T^{i0} &= i k^j v_j (1+\omega)\rho, \\
\Gamma^0_{00} T^{00} &= \frac{\partial \Psi}{\partial t}(1 + \delta_x - 2\Psi)\rho, \\
\Gamma^0_{ij} T^{ij} &= 3\Big[H\big(1 + \frac{\delta p}{p} - 2\Psi\big) + \frac{\partial \Phi}{\partial t}\Big]\rho\omega, \\
\Gamma^i_{i0} T^{00} &= 3\Big[H(1 + \delta_x - 2\Psi) + \frac{\partial \Phi}{\partial t}\Big]\rho, \\
\Gamma^i_{ij} T^{0j} &= i k^j v_j \Phi (1+\omega)\rho.
\end{aligned} \tag{2.96}$$

Here we have used $\delta_{ij}\delta^{ij} = 3$ and $\delta_x \equiv \delta\rho/\rho$ and have defined $\omega_x \equiv p/\rho$ to be the equation of state of the fluid. Now to zero order in perturbations Ψ, Φ, $\delta\rho$, δp and v_i we have

$$\frac{1}{\rho}\frac{\partial \rho}{\partial t} = -3\frac{1}{a}\frac{\partial a}{\partial t}(1+\omega). \tag{2.97}$$

This equation is what we were already expecting. For a constant ω equation (2.97) gives $\rho \propto a^{-3(1+\omega)}$. Therefore, e.g. for the radiation we have $\omega_r = \frac{1}{3}$, which leads to $\rho_r \propto a^{-4}$ and for the matter we get $\rho_m \propto a^{-3}$ since $\omega_m = 0$. The first order terms of equation (2.95) give

$$\begin{aligned}
(\delta_x - 2\Psi)\frac{\partial \rho}{\partial t} + \rho\frac{\partial \delta_x}{\partial t} + 3\Big[H\big(\frac{\delta p}{p} - 2\Psi\big) + \frac{\partial \Phi}{\partial t}\Big]\rho\omega \\
+ 3\Big[H(\delta_x - 2\Psi) + \frac{\partial \Phi}{\partial t}\Big]\rho + i(1+\omega)\rho k^j v_j = 0.
\end{aligned} \tag{2.98}$$

Now in this equation if we substitute the zero order result of Eq. (2.97) we will have

$$\dot{\delta_x} = -(1+\omega)\big(k v_x + 3\dot{\Phi}\big) - 3\frac{\dot{a}}{a}\Big(\frac{\delta p}{\delta \rho} - \omega\Big)\delta_x. \tag{2.99}$$

Note that $H = \frac{1}{a}\frac{da}{dt} = \dot{a}/a^2$. Here overdots again denote derivatives with respect to the conformal time and v_x is the velocity of the fluid species in the comoving frame. Eq. (2.99)

represents a *continuity equation* for the perturbations in a single fluid. The second term in the bracket corresponds to the fluctuation in the equation of state i.e. $\delta\omega = \frac{p+\delta p}{\rho+\delta\rho} - \omega = (\frac{\delta p}{\delta\rho} - \omega)\delta_x$. This term is generally zero for the non-relativistic fluids in the early universe as we often keep the equation of state constant. The term $3\dot{\Phi}$ in the right hand side accounts for the stretching of the space. Recall that, from Eq. (2.60), the factor responsible for the spatial stretching of the the metric is $a\sqrt{1+2\Phi} \approx a(1+\Phi)$. Considering that the number density of the particles dilutes by a factor $n_x \approx [a(1+\Phi)]^{-3} \approx a^{-3}(1-3\Phi)$, we arrive at $\delta n_x/n_x = -3\delta a/a - 3\delta\Phi$, which is just what we expect from the zero order and first order continuity equation (2.97) and (2.99).

Now let us calculate the space component of the energy-momentum conservation. Take $\nu = i$, equation (2.94) leads to

$$\begin{aligned}\Gamma^{\mu i}_{;\mu} &= \partial_0 T^{0i} + \partial_j T^{ji} + \Gamma^i_{00}T^{00} + 2\Gamma^i_{0j}T^{0j} + \Gamma^j_{j0}T^{0i} \\ &+ \Gamma^0_{00}T^{0i} + \Gamma^j_{jk}T^{0k} + \Gamma^0_{0k}T^{ik}, \end{aligned} \tag{2.100}$$

where

$$\begin{aligned} T^{0i} &= g^{ii}T^0_i = \frac{1}{a^2}(1+\omega)\rho v_i, \\ \partial_0 T^{0i} &= \Big[(1+\omega)\Big(\frac{\partial v_i}{\partial t} + (\frac{1}{\rho}\frac{\partial\rho}{\partial t} - \frac{2}{a}\frac{\partial a}{\partial t})v_i\Big) + \frac{\partial\omega}{\partial t}v_i\Big]\frac{\rho}{a^2}, \\ \partial_j T^{ij} &= ik^i\omega\frac{\rho}{a^2}\Big(-\frac{\delta p}{p} + \frac{2}{3}\Pi\Big), \\ \Gamma^i_{00}T^{00} &= \frac{ik^i\Psi}{a^2}(\rho + \delta\rho - 2\Psi\rho), \\ \Gamma^i_{0j}T^{0j} &= \Gamma^0_{00}T^{0i} = H(1+\omega)\frac{\rho v_i}{a^2}, \\ \Gamma^j_{j0}T^{0i} &= 3H(1+\omega)\frac{\rho v_i}{a^2}, \\ \Gamma^j_{jk}T^{0k} &= 3\Phi(1+\omega)ik^k\frac{\rho v_k}{a^2}, \\ \Gamma^0_{0k}T^{ik} &= \frac{ik^i\Psi}{a^2}(p + \delta p - 2\Phi p), \end{aligned} \tag{2.101}$$

where Π is the anisotropic stress which is related to Σ^j_i. To first order equation (2.100) leads to

$$\begin{aligned}(1+\omega)\Big[(\frac{1}{\rho}\frac{\partial\rho}{\partial t} - \frac{2}{a}\frac{\partial a}{\partial t})v_i + ik^i\Psi\Big] + \Big[-\frac{\delta p}{p} + \frac{2}{3}\Pi\Big]ik^i\omega \\ + (1+\omega)\frac{\partial v_i}{\partial t} + \frac{\partial\omega}{\partial t}v_i + 6H(1+\omega)v_i = 0. \end{aligned} \tag{2.102}$$

Now multiplying by ik^i and substituting from Eq. (2.97) we will have

$$\dot{v_x} = -\frac{\dot{a}}{a}(1-3\omega)v_x - \frac{\dot{\omega}}{1+\omega}v_x + \frac{\delta p/\delta\rho}{1+\omega}k\delta_x - \frac{2}{3}\frac{\omega}{1+\omega}k\Pi + k\Psi. \tag{2.103}$$

This equation is called the *Euler equation* which describes the conservation of the momentum of the fluid. The time derivative of the equation of state in the Euler equation (2.103) is given by

$$\begin{aligned}\dot{\omega} &= \frac{\dot{\rho}}{\rho}\Big(\frac{\dot{p}}{\dot{\rho}} - \omega\Big) \\ &= -3H(1+\omega)(c_s^2 - \omega), \end{aligned} \tag{2.104}$$

where $c_s \equiv \sqrt{\dot{p}/\dot{\rho}}$ is the speed of sound in the fluid. To get the second equality of Eq. (2.104) we have substituted from equation (2.97). For a single component fluid we usually expect the equation of state to be constant. However, when the fluid is composed of different species with different equations of state whose number densities do not fluctuate together $\dot{\omega}$ generally is not zero. We will discuss the different types of the primordial perturbations in subsection 2.4.1.

In the early universe the non-relativistic particles that can be treated as an ideal fluid are baryons and cold dark matter (CDM) particles. For these particles it is not necessary to solve the Boltzmann equation in the phase space. Instead, we can simply calculate their corresponding fluid equations and then, by analogy with the Boltzmann equation, account for the interaction terms which arise due to the momentum exchange in the Compton scattering process. This approach will lead to the same result which can be obtained by solving the relativistic Boltzmann equations. The cold dark matter and baryon particles are pressureless so for these components we can assume $\omega = \dot{\omega} = \delta p/\delta\rho \simeq 0$. The cold dark matter particles are collisionless particles so from Eqs. (2.99) and (2.103) we immediately have

$$\dot{\delta}_c = -kv_c - 3\dot{\Phi}, \tag{2.105}$$

$$\dot{v}_c = -\frac{\dot{a}}{a}v_c + k\Psi, \tag{2.106}$$

where δ_c and v_c are the density and velocity of the CDM perturbations. The equations governing the evolution of the baryon perturbations are essentially the same as these in the absence of coupling to photons. However, additional terms have to be added to Eqs. (2.105) and (2.106) to account for the Compton scattering before recombination. The conservation of momentum for the total photon-baryon fluid gives

$$\rho_b \delta v_b = (\rho_\gamma + p_\gamma)\delta v_\gamma = \frac{4}{3}\rho_\gamma \delta v_\gamma. \tag{2.107}$$

Therefore equations (2.105), (2.106) and (2.107) imply (see Dodelson, 2003)

$$\dot{\delta}_b = -kv_b - 3\dot{\Phi}, \tag{2.108}$$

$$\dot{v}_b = -\frac{\dot{a}}{a}v_b + k\Psi + \dot{\tau}(v_b - 3v_\gamma)/R, \tag{2.109}$$

where R is the photon-baryon momentum density ratio $R = 3\rho_b/4\rho_\gamma$. Here the third term in equation (2.109) accounts for the transfer of momentum between photons and baryons in the Compton scattering. For an actual derivation of this equation see section 2.6 of Valiviita (2005). We will see in subsection 2.5.1 that the peculiar velocity of the photons with respect to the background represents a Doppler effect in the temperature anisotropies i.e. $\Theta(k) = -i\vec{v}_\gamma \cdot \vec{r}$. Multiplying with $\int d\mu/(-2i)$ and integrating, this relation leads to $\Theta_1 = v_\gamma$, which is a good approximation before recombination.

Neutrinos, on the other hand, are relativistic massless particles which cannot be treated as a fluid. As a result the evolution equations which govern the neutrino perturbations can be only obtained by solving the Boltzmann equations. However, the solution to the Boltzmann equation for neutrinos is similar to what we found in the last section. The neutrinos are Fermions but

their distribution function, up to first order, expands the same as in Eq. (2.70). Moreover, they are weakly interacting particles and do not experience the Compton scattering. So the Boltzmann equation for neutrinos can be found immediately by substituting $\Theta \to \mathcal{N}, \dot{\tau} \to 0$ in equation (2.81) where $\mathcal{N}(k, \mu, \eta)$ is the neutrino temperature perturbation. Thus

$$\dot{\mathcal{N}} + ik\mu\mathcal{N} + \dot{\Phi} + ik\mu\Psi = 0. \tag{2.110}$$

2.3.2 Einstein Equations

Until now we have determined the equations which govern the evolution of the perturbations of different species. These are written in terms of the gravitational potentials which themselves evolve due to the evolution of matter and radiation densities. Therefore to complete the set of equations of the previous subsection we also need to determine the evolution of the metric perturbations. The equation which relates the spacetime metric to the energy momentum tensor is the Einstein equation

$$G^{\mu}_{\nu} \equiv g^{\mu\alpha}\Big(R_{\alpha\nu} - \frac{1}{2}g_{\alpha\nu}R\Big) = 8\pi G T^{\mu}_{\nu}. \tag{2.111}$$

where $R_{\mu\nu}$ and R are the Ricci curvature tensor and scalar given by $R_{\mu\nu} = \Gamma^{\alpha}_{\mu\nu,\alpha} - \Gamma^{\alpha}_{\mu\alpha,\nu} + \Gamma^{\alpha}_{\beta\alpha}\Gamma^{\beta}_{\mu\nu} - \Gamma^{\alpha}_{\beta\nu}\Gamma^{\beta}_{\mu\alpha}$ and $R = g^{\mu\nu}R_{\mu\nu}$ respectively. Here we can also assume that the total energy-momentum tensor of the species has the form of Eq. (2.93). Although this assumption is not exactly true it leads to correct results. As photons and neutrinos are relativistic particles their energy-momentum tensor is not of the form of that of a perfect fluid. For radiation we have to work with the distribution functions. Using the perturbed distribution function Eq. (2.70) it is possible to show that for photons $T^0_0 = -\rho_\gamma(1 + 4\Theta_0)$ and likewise for neutrinos $T^0_0 = -\rho_\nu(1 + 4\mathcal{N}_0)$. However we can also get the same relations by assuming $T^0_0 = -\rho_r(1 + \delta_r)$ for radiation, because $\delta\rho_r/\rho_r = 4\delta T/T$ since $\rho_r \propto T^4$, hence justifying the use of Eq. (2.93). Likewise it can be shown that the space-space component of the energy momentum tensor for radiation is related to the quadrupole moment which resembles an anisotropic stress term (see Dodelson, 2003).

Now using the expressions for the Christoffel symbols Eqs. (2.86-2.91) we can write the time-time and space-space part of the Ricci tensor as

$$R_{00} = -\frac{3}{a}\frac{d^2a}{dt^2} + 3H\Big(\frac{\partial\Psi}{\partial t} - 2\frac{\partial\Phi}{\partial t}\Big) + \frac{1}{a^2}\frac{\partial^2\Psi}{\partial x^i\partial x^i} - 3\frac{\partial^2\Phi}{\partial t^2}, \tag{2.112}$$

$$\begin{aligned} R_{ij} &= \delta_{ij}\Big[3\Big(2a^2H^2 + a\frac{d^2a}{dt^2}\Big)(1 + 2\Phi - 2\Psi) + a^2H\Big(6\frac{\partial\Phi}{\partial t} - \frac{\partial\Psi}{\partial t}\Big) \\ &+ a^2\frac{\partial^2\Phi}{\partial t^2} - \frac{\partial^2\Phi}{\partial x^k\partial x^k}\Big] - \frac{\partial^2(\Phi + \Psi)}{\partial x^i\partial x^j}, \end{aligned} \tag{2.113}$$

which lead to

$$\begin{aligned} R &= (6 - 12\Psi)\Big(H^2 + \frac{1}{a}\frac{d^2a}{dt^2}\Big) - 6H\Big(\frac{\partial\Psi}{\partial t} - 4\frac{\partial\Phi}{\partial t}\Big) \\ &+ 6\frac{\partial^2\Phi}{\partial t^2} - \frac{2}{a^2}\Big(\frac{\partial^2\Psi}{\partial x^i\partial x^i} + 2\frac{\partial^2\Phi}{\partial x^i\partial x^i}\Big). \end{aligned} \tag{2.114}$$

From Eqs. (2.93), (2.111), (2.112) and (2.114) we see that zero-order terms of the time-time component of the Einstein equation leads to the Friedmann equation $3H^2 = 8\pi G\rho_T$ for a flat universe, as we had expected before. Here ρ_T is the total density of matter and radiation. Using the zero-order continuity equation (2.97) we can write the Friedmann equation in this form

$$\Big(\frac{\dot{a}}{a^2}\Big)^2 = \frac{8\pi G}{3}\Big[\rho_r\big|_{a=1}a^{-4} + \rho_m\big|_{a=1}a^{-3} + \rho_v\Big], \tag{2.115}$$

where we have assumed the vacuum density is constant. For a radiation dominated universe the first term in the bracket is considerable whereas for matter dominated epoch we can drop all terms in the bracket but the second term. Therefore equation (2.115) leads to

$$\frac{\dot{a}}{a} = \begin{cases} 1/\eta & \text{RD} \\ 2/\eta & \text{MD.} \end{cases}$$

Hence in a radiation dominated universe we expect $a \propto \eta$ while in a matter dominated universe we have $a \propto \eta^2$. This is an interesting result which we will use in the next section.

To first order Eqs. (2.111), (2.112) and (2.114) give $\delta G^0_0 = -6H\partial\Phi/\partial t + 6\Psi H^2 - 2k^2\Phi/a^2$ where we have substituted the derivatives with ik. This leads to the first order Einstein equation

$$k^2\Phi + 3\frac{\dot{a}}{a}\Big(\dot{\Phi} - \Psi\frac{\dot{a}}{a}\Big) = 4\pi G a^2[\rho_c\delta_c + \rho_b\delta_b + 4\rho_\gamma\Theta_0 + 4\rho_\nu\mathcal{N}_0], \tag{2.116}$$

where we have written the derivatives with respect to the conformal time. The above equations resemble a generalized Poisson equation for a perturbed expanding and isotropic universe. In a universe which is not expanding or when the scales are within the horizon $k\eta \gg 1$ equation (2.116) reduces to the ordinary Poisson equation of the Newtonian theory.

The calculation of the space-space component of the equation (2.111) is not straightforward. However knowing that G^i_j is of the form $G^i_j = A\delta^i_j + k_ik_j(\Phi+\Psi)/a^2$ makes the calculation much simpler. Multiplying G^i_j by the projection operator $\hat{k}_i\cdot\hat{k}^j - \frac{1}{3}\delta^i_j$ kills all the terms proportional to δ^i_j and leaves $\hat{k}_i\cdot\hat{k}^j - \frac{1}{3}\delta^i_jG^i_j = 2k^2(\Phi+\Psi)/3a^2$. It is possible to show that the right hand side of equation (2.111) can be written in terms of the total anisotropic stress Π_T (see Valiviita, 1999). In this way the space-space component of the first order Einstein equation takes the form

$$k^2(\Phi+\Psi) = -8\pi G a^2 p_T\Pi_T. \tag{2.117}$$

The above equation shows that when the anisotropic stress is negligible we can put $\Psi = -\Phi$. In fact the anisotropic stress is only considerable well before recombination, therefore for most of the history of the universe we can neglect it.

The Einstein equations (2.116) and (2.117) contain all the necessary information about the evolution of the metric perturbations. The rest of the components of the Einstein equation do not add any new information, therefore we do not derive them here. However, some combinations of the Einstein equations are rather useful for simplifying the calculations. For example it can be shown that the time-time component of the Einstein equation combined with its time-space component gives (see Dodelson, 2003)

$$k^2\Phi = 4\pi G a^2\Big[\rho_m\delta_m + 4\rho_r\Theta_{r,0} + \frac{3aH}{k}\big(\rho_m v_m + 4\rho_r\Theta_{r,1}\big)\Big], \tag{2.118}$$

where e.g. $\rho_m\delta_m \equiv \rho_c\delta_c + \rho_b\delta_b$ and $\rho_r\Theta_{r,0} \equiv \rho_\gamma\Theta_0 + \rho_\nu\mathcal{N}_0$. This equation will turn out to be useful in subsection 2.4.4.

2.4 Power Spectrum of Matter Perturbations

As we saw in §2.1.5, the theory of inflaton provides a mechanism for producing perturbations in the early universe. These inflation induced perturbations i.e. $\delta\phi$ later evolve through quantum mechanisms to give rise to the metric and the energy-momentum tensor perturbations. We learnt that the particle horizon shrinks during inflation so that soon after inflation all the scales are larger than the horizon scale. Hence we expect that the wavelength of the perturbations k^{-1} should be initially larger than the comoving horizon η, so these modes are not affected by causal physics. As the universe evolves the comoving horizon grows and the super-horizon perturbations eventually enter the horizon scales. In this section we study the evolution of the matter perturbations through the horizon crossing transition. We first set up the initial conditions of the super-horizon scales in the Newtonian gauge in §2.4.1. Then we move on to study the evolution of the potentials during the transition from radiation to matter dominated phase in subsections 2.4.2 and 2.4.3. Here we especially focus on the evolution of the matter fluctuations which produce most of the present observable structures. The result of this analysis will lead us to the calculation of a matter transfer function in §2.4.4 which determines the shape of the power spectrum of matter densities.

Before moving on, it is important to bear in mind that to study the evolution of the perturbations one has to consider the full set of equations presented in sections 2.2 and 2.3. These are Boltzmann equations for photons and neutrinos and continuity and Euler equations for cold dark matter and baryon particles. These set of equations are all coupled to each other through the gravitational effects and scattering processes which make it complicated to reach exact analytical solutions. Indeed there exists no exact analytic solution yet which can explain the evolution of the density perturbations up to the present time. Hence the easiest way to solve these equations is to use computers (see Ma and Bertschinger, 1995). Nevertheless, we can still make analytical implications about the perturbations by solving the equations in some certain limits and approximations. In this section we follow the analytical analysis presented in Hu and Sugiyama (1996) and Dodelson (2003).

2.4.1 Initial Super-horizon Solution

We start with setting up the initial conditions for the perturbations. Since the modes start to evolve when they are still larger than the horizon scale, a good approximation is $k\eta \ll 1$. In this limit since the modes are not affected by causal mechanisms, the universe should look smooth and uniform, therefore the radiation anisotropies can be totally characterized by a monopole. We can further assume that matter density (ρ_b, ρ_c) is negligible compared to the radiation density (ρ_γ, ρ_ν) since the universe is in its radiation dominated phase, in which case we have

$\dot{a}/a = 1/\eta$. In these limits we can immediately write Eqs. (2.81), (2.110), (2.105), (2.108) and (2.116) in the form

$$\dot{\Theta}_0 + \dot{\Phi} = 0 \quad , \quad \dot{\mathcal{N}_0} + \dot{\Phi} = 0 \tag{2.119}$$

$$\dot{\delta}_c = -3\dot{\Phi} \quad , \quad \dot{\delta}_b = -3\dot{\Phi} \tag{2.120}$$

$$3\big(\frac{\dot{a}}{a}\big)\Big(\dot{\Phi}\eta + \Phi\Big) = 16\pi G a^2(\rho_\gamma \Theta_0 + \rho_\nu \mathcal{N}_0), \tag{2.121}$$

where again we have substituted $\Phi = -\Psi$ as we neglect the anisotropic stress Π in equation (2.117). Substituting the Friedmann equation in equation (2.121) we will have

$$\eta\dot{\Phi} + \Phi = 2\Big[\frac{\rho - \rho_\nu}{\rho}\Theta_0 + \frac{\rho_\nu}{\rho}\mathcal{N}_0\Big]. \tag{2.122}$$

Differentiating with respect to η and using Eqs. (2.119) yield

$$\eta\ddot{\Phi} + 4\dot{\Phi} = 0. \tag{2.123}$$

The above equation has simple solutions in the form $\Phi = \eta^p$ with $p = -3$ for the decaying mode and $p = 0$ for the normal mode. One approximation that we can make here is to assume that $\Theta_0 = \mathcal{N}_0$. This is generally true at early stages when photons and neutrinos are not indistinguishable. This is because it is most likely that the radiation perturbations in photon and neutrino species have been generated in a similar way. So, with this assumption, equation (2.122) with a non-decaying solution for potential reduces to

$$\Phi(k, \eta) = 2\Theta_0(k, \eta), \tag{2.124}$$

which is only applicable in early times.

Now before moving on, we need to introduce the different types of the primordial perturbations. These are called adiabatic and isocurvature perturbations. Adiabatic perturbations correspond to the condition that the particle number ratio of the different species do not vary spatially i.e.

$$\delta\Big(\frac{n_A}{n_B}\Big) = 0, \quad \text{(adiabatic)} \tag{2.125}$$

As a result all the particles share a common comoving velocity field, so they can be characterized by a single uniform equation of state which can fluctuate spatially. In this way for adiabatic modes we will have a total energy density which is not constant

$$\sum_i \delta\rho_i \neq 0, \quad \text{(adiabatic)} \tag{2.126}$$

where the sum is over different species. Isocurvature perturbations correspond to the case where the abundance ratio of the particles can fluctuate spatially in such a way that there is no initial curvature perturbation ($\Phi = 0$). Therefore the total energy density for isocurvature perturbations is fixed.

$$\sum_i \delta\rho_i = 0, \quad \text{(isocurvature)} \tag{2.127}$$

We can also define the entropy perturbation for each species. This is defined by the fluctuations in the number density of the particles e.g.

$$S = \frac{\delta(n_i/n_\gamma)}{(n_i/n_\gamma)} = \frac{\delta n_i}{n_i} - \frac{\delta n_\gamma}{n_\gamma} = \delta_i - \frac{3}{4}\delta_\gamma, \tag{2.128}$$

where from section 2.3.2 $\delta_\gamma = 4\Theta_0$. Here we have taken the photons to be the base particles with respect to which we measure the abundance ratio fluctuations. Also we have written the relations $\rho_r \propto a^{-4}$ and $n_r \propto a^{-3}$ in the form $n_r \propto \rho_r^{3/4}$. Often a general primordial perturbation can be considered as a combination of the adiabatic and isocurvature modes. For example we can assume that the abundance ratio is fixed for photons, neutrinos and baryons i.e.

$$\frac{\delta n_\gamma}{n_\gamma} = \frac{\delta n_\nu}{n_\nu} = \frac{\delta n_b}{n_b}, \tag{2.129}$$

and it is only the cold dark matter species which has a non-zero entropy perturbation. In this way we will have one adiabatic mode and a cold dark matter isocurvature mode. Then Eqs. (2.119) and (2.120) imply that $\dot{\delta}_c = 3\dot{\Theta}_0$ or

$$\delta_c(k,\eta) = 3\Theta_0(k,\eta) + S, \quad \text{(CDM isocurvature)} \tag{2.130}$$

where the constant of integration comes from equation (2.128). We should remember that this equation is only valid at early times when the modes are outside the horizon. For a pure adiabatic case the entropy perturbation S in the above equation is zero and we expect

$$\delta_c = \delta_b = \frac{3}{4}\delta_\gamma = \frac{3}{4}\delta_\nu = 3\Theta_0. \tag{2.131}$$

2.4.2 Large Scale Solution

Having determined the initial conditions of the perturbations, we can now study the evolution of the density perturbations. For the purpose of studying the evolution of matter densities the Einstein equation plays an important role since it relates the density perturbations to the potential field. Therefore we often try to solve the potential equations and then utilize the results to find a solution for the density perturbations. Moreover for the rest of this section we consider the limit where baryon density is small. Indeed, for most of the history of the universe, the cold dark matter is the dominant factor in the evolution of the matter densities. Except before recombination epoch, which we will analyze in subsection 2.5.2, baryon densities merely mirror the evolution of the cold dark matter densities. Therefore we ignore the baryons here which will help simplify the equations.

Here we divide the discussion in two parts: (i) In this subsection we study the evolution of the superhorizon scales and we show that for these modes the potential drops slightly by about 10% as the universe goes from radiation to matter dominated. (ii) In the next subsection we will show that the potential of the small scale modes decays after crossing the horizon in the radiation dominated phase and shows oscillatory behaviors before becoming constant again in the matter-dominated phase.

With the above assumptions, on superhorizon scales the Einstein equation (2.116) takes form

$$3\frac{\dot{a}}{a}\Big(\dot{\Phi}+\frac{\dot{a}}{a}\Phi\Big)=4\pi G a^2(\rho_c\delta_c+4\rho_\gamma\Theta_0+4\rho_\nu\mathcal{N}_0). \tag{2.132}$$

Here we assume adiabatic conditions $\Theta_0=\mathcal{N}_0=\delta_c/3$ on large scales (see §2.4.1). At this stage we also introduce the quantity $y\equiv a/a_{eq}=\rho_c/\rho_r$, where a_{eq} is the scale factor at the epoch of matter-radiation equality and $\rho_r=\rho_\gamma+\rho_\nu$. It is generally useful to investigate the evolution in terms of y which is directly measurable. In this way we can write Eq. (2.132) in the form

$$3H^2\big(y\Phi'+\Phi\big)=4\pi G\rho_c\delta_c\Big(1+\frac{4}{3y}\Big), \tag{2.133}$$

where prime denotes derivative with respect to y. Here we have used $\frac{d}{d\eta}=aHy\frac{d}{dy}$ to get the above equation. Now we can substitute the Friedmann equation in this form $3H^2=8\pi G\rho=8\pi G\rho_c(1+y)/y$ into the Einstein equation. This leads to

$$y\Phi'+\Phi=\frac{3y+4}{6(y+1)}\delta_c. \tag{2.134}$$

Differentiating both sides with respect to y gives

$$y\Phi''+2\Phi'=\frac{-1}{6(y+1)^2}\delta_c+\frac{3y+4}{6(y+1)}\delta_c'. \tag{2.135}$$

Now substituting for δ_c from equation (2.134) and setting δ_c' equal to $-3\Phi'$, due to Eq. (2.120) which is valid on large scales, we obtain

$$\Phi''+\frac{21y^2+54y+32}{2y(y+1)(3y+4)}\Phi'+\frac{\Phi}{y(y+1)(3y+4)}=0. \tag{2.136}$$

This equation has been solved analytically by Kodama and Sasaki (1984). They show that the solution of Eq. (2.136) is

$$\Phi(y)=\frac{\Phi(0)}{10y^3}\Big[16\sqrt{1+y}+9y^3+2y^2-8y-16\Big]. \tag{2.137}$$

This expression gives the evolution of the potential when the modes are larger than the horizon. Fig. 2.3 ($k=0.001$ h Mpc^{-1}) shows a pictorial representation of this solution. We see that the potential starts with a value equal to $\Phi(0)$ and decays a little while the universe goes through radiation to matter domination transition. The amount of decay is measurable by considering a large value for y in equation (2.137). At large y, the y^3 term dominates which leads to $\Phi\rightarrow\frac{9}{10}\Phi(0)$. Therefore we should expect a drop of 10% in the large scale potentials during their transition. Well into the matter dominated universe, the modes gradually enter the horizon. As a result, in this limit equation (2.137) should not apply any more. However the Poisson's equation $k^2\Phi=4\pi G a^2\rho\delta_{tot}$ which is a good approximation in the matter domination implies that the rate of the expansion is just enough to cancel the rate of the growth of the overdensities. This is because in this limit the continuity and Euler equations (2.105) and (2.106) lead to $\delta_{tot}\sim-(k\eta)v_{tot}$ and $v_{tot}\sim(k\eta)\Psi_i$ which give $\delta_{tot}\sim-(k\eta)^2\Psi_i$. Since in the matter dominated universe $a^2\rho\sim a^{-1}\propto\eta^{-2}$ Poisson's equation implies $\Psi\sim-(k\eta)^{-2}\delta_{tot}\sim\Psi_i$ i.e. the potential does not evolve in the matter-dominated universe.

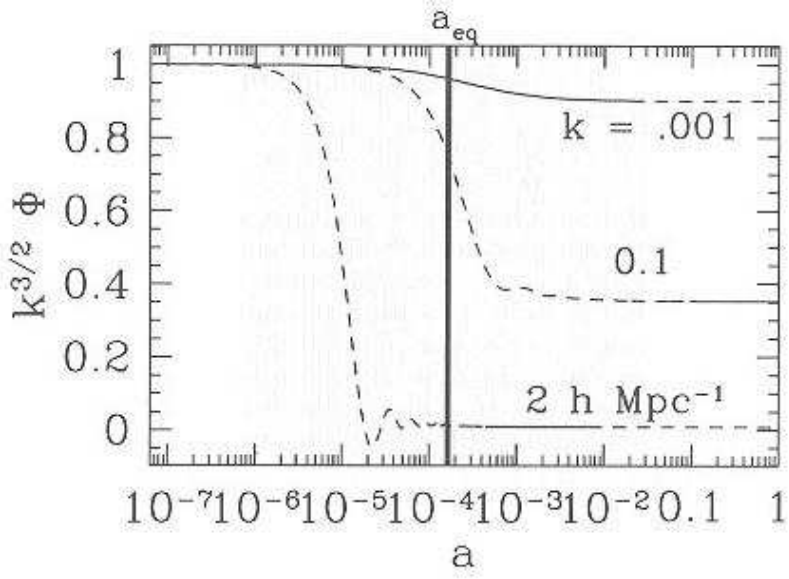

Figure 2.3: The evolution of the curvature potential during radiation and matter dominated epochs. The dashed lines represent the phase when the modes are subhorizon. The very large scale modes ($k = 0.001$ h Mpc^{-1}) enter the horizon very late during the matter domination so they only experience a small drop in their amplitude. The small scales ($k = 0.1, 2$ h Mpc^{-1}) cross the horizon in the radiation-dominated epoch so their amplitude decays significantly and also shows oscillatory features. (Figure from Dodelson, 2003)

Note that Fig. 2.3 also shows the analytic result for the small scales ($k = 0.1, 2$ h Mpc^{-1}). As we see in the figure, these modes experience a large drop in their potential before they go through a phase of damped oscillation. However, remember that for these scales Eq. (2.137) is not a valid solution since the small scale perturbations enter the horizon much earlier. In the next subsection we will derive an analytical solution for small scale potentials which will explain the large drop in the potential that we see in Fig. 2.3. In subsection 2.4.4 we will use these information to match the small scale solutions to the large scale solutions.

2.4.3 Small Scale Solution

We saw in the last section that the evolution of the large scale potential can be determined by the Einstein equation assuming that the baryon density is negligible and that the dominant multipole moment of radiation is the monopole. The analysis of the small scale potential is similar except the fact that the modes enter the horizon during the radiation dominated epoch. As a result radiation fluctuations now play the dominant role in the evolution of the potential. Moreover well after horizon crossing and before recombination the radiation modes have developed a dipole moment which we cannot neglect when radiation density is dominant. Hence the radiation is now characterized by two moments $\Theta_{r,0}$ and $\Theta_{r,1}$ where again r subscript

refers to both photons' and neutrinos' multipoles. Now the evolution equations for radiation species are the non-collisional Boltzmann equation for the case where we neglect the baryon densities. Multiplying equation (2.81) by $(d\mu/2)\mathcal{P}_0(\mu)$ and integrating from $\mu = -1$ to 1 we will have

$$\dot{\Theta}_{r,0} + k\Theta_{r,1} = -\dot{\Phi}. \tag{2.138}$$

To get this equation we have used the relations (2.83). To obtain a differential equation for dipole moments we multiply the Boltzmann equation by $(d\mu/2)\mathcal{P}_1(\mu)$ and then integrate over μ. The calculation is straightforward leading to

$$\dot{\Theta}_{r,1} - \frac{k}{3}\Theta_{r,0} = \frac{k}{3}\Psi = -\frac{k}{3}\Phi. \tag{2.139}$$

Now to examine the evolution of the potentials we utilize the Einstein equation (2.118) for the case when we ignore the matter components. Eq. (2.118) leads to

$$\Phi = \frac{6}{k^2\eta^2}\Big[\Theta_{r,0} + \frac{3}{k\eta}\Theta_{r,1}\Big]. \tag{2.140}$$

Note that to get this equation we have used $3H^2 = 8\pi G\rho_r$ and $aH = 1/\eta$ which are valid during the radiation domination. Substituting the monopole $\Theta_{r,0}$ form Einstein equation (2.140) into equations (2.138) and (2.139) we can show that

$$-\frac{3}{k\eta^2}\dot{\Theta}_{r,1} + \Big(\frac{3}{k\eta^2} + k\Big)\Theta_{r,1} = -\Big(1 + \frac{1}{6}k^2\eta^2\Big)\dot{\Phi} - \frac{1}{3}k^2\eta\Phi, \tag{2.141}$$

$$\dot{\Theta}_{r,1} + \frac{1}{\eta}\Phi_{r,1} = \Big(\frac{-k}{3} + \frac{1}{18}k^3\eta^2\Big)\Phi. \tag{2.142}$$

Now substituting Eq. (2.142) into (2.141) in order to eliminate the derivative $\dot{\Theta}_{r,1}$ we get

$$\frac{6}{k\eta^2}\Theta_{r,1}\Big[\frac{k^2\eta^2}{6} + 1\Big] = -\dot{\Phi}\Big[1 + \frac{k^2\eta^2}{6}\Big] + \Phi\Big[\frac{-3}{k\eta}\Big(\frac{k}{3} - \frac{k^3\eta^2}{18}\Big) - \frac{k^2\eta}{3}\Phi\Big], \tag{2.143}$$

or

$$\dot{\Phi} + \frac{1}{\eta}\Phi = \frac{-6}{k\eta^2}\Theta_{r,1}. \tag{2.144}$$

We can further differentiate this equation. This will lead to two radiation terms $\Theta_{r,1}$ and $\dot{\Theta}_{r,1}$ on the right hand side which can be eliminated by substituting from Eqs. (2.142) and (2.144). The result of the calculation will be

$$\ddot{\Phi} + \frac{4}{\eta}\dot{\Phi} + \frac{k^2}{3}\Phi = 0. \tag{2.145}$$

This is a second order equation which governs the evolution of the small scale potentials during the radiation dominated epoch. Dodelson (2003) shows that a solution for equation (2.145) valid for small η is given by

$$\Phi = 3\Phi(0)\Big[\frac{\sin(k\eta/\sqrt{3}) - (k\eta/\sqrt{3})\cos(k\eta/\sqrt{3})}{(k\eta/\sqrt{3})^3}\Big]. \tag{2.146}$$

It is evident that the $\eta \to 0$ limit of this equation gives $\Phi(0)$. This equation leads to some remarkable results. One notable result is that as the modes enter the horizon the amplitude

of the potentials start to decay by η^{-2} (see Fig. 2.3). This decay is also evident in equation (2.140). This is because during the radiation dominated epoch the radiation itself is not able to grow as it gets suppressed by the pressure. On the other hand, the matter density cannot grow unimpeded by pressure from the dominant radiation. As a result the total density perturbation does not evolve, hence the relativistic Poisson equation implies that the potential should decay. However, as the potential decays, it sets up oscillations in the matter-radiation fluid. We should expect the monopole $\Theta_{r,0}$ to oscillate due to the growth in matter and radiation perturbations offsetting each other. This will also give rise to the oscillatory features in the gravitational potential which are noticeable after the potential decay. Fig. 2.3 shows the analytical solution of equation (2.146) for modes $k = 0.1, 2$ h Mpc^{-1}. Now we have two equations (2.137) and (2.146) which describe the evolution of the potential function on small and large scales. However we still need a procedure that links the two solutions and also be valid on intermediate scales. In the next subsection we will present a fitting formula which matches the two results together in one single transfer function.

2.4.4 Matter Transfer Function

Having established the evolution of the potentials in the previous subsections 2.4.2 and 2.4.3 we now move on to study the evolution of the small scale cold dark matter density. Although the dark matter is initially subdominant in the universe its rate of growth is faster than that of the radiation, so it eventually becomes the dominant species. The evolution of the cold dark matter is given by the continuity and Euler equations (2.108) and (2.109). It is easy to show that these equations imply

$$\ddot{\delta}_c + \frac{\dot{a}}{a}\dot{\delta}_c = \mathcal{S}(k,\eta), \tag{2.147}$$

where the source term is

$$\mathcal{S} = -k^2\Psi - 3\ddot{\Phi} - 3\frac{\dot{a}}{a}\dot{\Phi}. \tag{2.148}$$

During the radiation-dominated epoch we know $\dot{a}/a = 1/\eta$. But since we are probing the small scale modes which are within the horizon we can expect $k\eta \gg 1$. Therefore the last term of the source term is negligible. It is easy to show that two solutions of the homogeneous equation (with $\mathcal{S} = 0$) are $s_1 \equiv \delta_c = 1$ and $s_2 \equiv \delta_c = \ln(a)$ (or $s_2 \equiv \ln(\eta)$). Given these homogeneous solutions we can construct a particular solution for Eq. (2.147) by the Green's methods which says that the integral of $[s_1(a)s_2(a') - s_1(a')s_2(a)]/[\dot{s}_1(a')s_2(a') - s_1(a')\dot{s}_2(a')]$ weighted by the source term $\mathcal{S} = k^2\Phi - 3\ddot{\Phi}$ is a particular solution. Therefore

$$\delta_c = C_1 + C_2\ln(a) - \int_0^\eta \mathcal{S}(k,\eta')[\ln(a') - \ln(a)]\frac{a'}{\dot{a}'}d\eta'. \tag{2.149}$$

Now adiabatic conditions imply that $C_1 = \delta_c(k, \eta = 0) = 3\Theta_0$ and $C_2 = 0$. Also the source function depends on the potential which is dominant only during horizon crossing epoch. As we have seen in subsection 2.4.3, the potentials decay to zero after the mode enters the horizon. So we can expect that at large η the first term in the integral is a constant and the second

term is proportional to $\ln(a)$. In fact, Hu and Sugiyama (1996) show that at large η when the potentials have decayed to zero the cold dark matter density grows logarithmically by

$$\delta_c \simeq I_1 \Phi(0) \ln\Big(I_2 \frac{a}{a_H}\Big), \qquad (RD) \tag{2.150}$$

where a_H is the scale factor at Hubble crossing which depends on the wavenumber. The constants I_1 and I_2 can be obtained numerically by setting the above equation equal to Eq. (2.149). For the case when $\rho_\gamma = \rho_\nu$, Hu and Sugiyama (1996) show that the numerical method gives $I_1 = 9.76$ and $I_2 = 0.45$.

To describe the evolution of matter when the universe is matter dominated it is easier to work with the equality-normalized scale factor $y \equiv a/a_{eq}$. Again noting the fact that $\frac{d}{d\eta} = aHy\frac{d}{dy}$ and $\frac{d^2}{d\eta^2} = a^2H^2y^2\frac{d^2}{dy2} + \frac{a^2H^2y^2}{2(1+y)}\frac{d}{dy}$ we can easily write Eq. (2.147) in the form

$$\delta_c'' + \frac{2+3y}{2y(1+y)}\delta_c' = \frac{-k^2}{a^2H^2y^2}\Psi, \tag{2.151}$$

where again prime refers to derivative with respect to y. In this equation we have only considered the first term of the source function of Eq. (2.148). Other potential terms are negligible for small scales due to the condition $k\eta \gg 1$. In this limit where $\dot{a}/a = 2/\eta$ is negligible the Einstein equation (2.116) gives

$$k^2\Phi = \frac{3y}{2(y+1)}a^2H^2\delta_c, \tag{2.152}$$

where again we have used the fact $8\pi G\rho_c = 3H^2y/(1+y)$. Assuming zero anisotropic stress ($\Phi = -\Psi$) we can substitute the Einstein equation (2.152) into equation (2.151). This leads to a second-order equation for the sub-horizon cold dark matter densities

$$\delta_c'' + \frac{2+3y}{2y(y+1)}\delta_c' - \frac{3}{2y(y+1)}\delta_c = 0. \tag{2.153}$$

This equation is known as the *Meszaros equation*. The answers to this equation have been worked out in Padmanabhan (1993). The solutions of equation (2.153) correspond to a growing and a decaying mode given respectively by

$$U_1(y) = \frac{2}{3} + y, \tag{2.154}$$

$$U_2(y) = \big(\frac{2}{3} + y\big)\ln\Big[\frac{\sqrt{1+y}+1}{\sqrt{1+y}-1}\Big] - 2\sqrt{1+y}. \tag{2.155}$$

Therefore the general solution for δ_c is given by

$$\delta_c = C_1U_1(y) + C_2U_2(y), \qquad (MD) \tag{2.156}$$

which is valid for the sub-horizon modes in the matter dominated phase. Now having determined the evolution equations for the dark matter densities in both radiation and matter domination, we need to fit the two results into one equation valid in both regimes. To do so we put the two solutions (2.150) and (2.156) and their derivatives equal to each other at some intermediate

matching epoch a_m well into the radiation domination which satisfies $a_H \ll a_m \ll a_{eq}$. Here a_H is the scale factor when the modes enter the horizon. We will have

$$I_1\Phi(0)\ln\Big(I_2\frac{y_m}{y_H}\Big) = C_1U_1\Big(\frac{a_m}{a_{eq}}\Big) + C_2U_2\Big(\frac{a_m}{a_{eq}}\Big), \tag{2.157}$$

$$\frac{I_1\Phi(0)}{y_m} = C_1U_1'\Big(\frac{a_m}{a_{eq}}\Big) + C_2U_2'\Big(\frac{a_m}{a_{eq}}\Big). \tag{2.158}$$

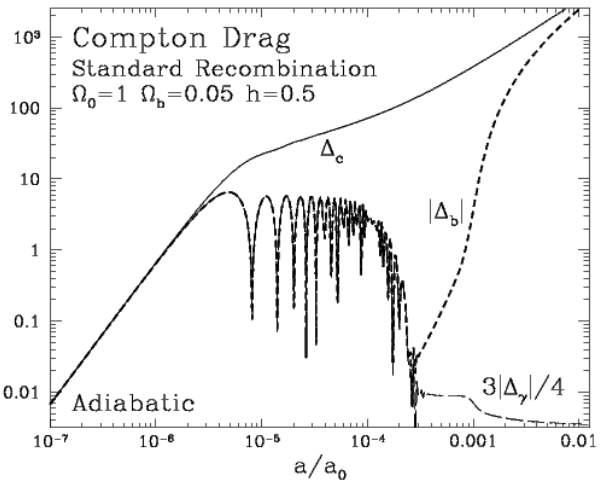

Figure 2.4: The evolution of CDM, baryon and photon density. Before radiation-matter equality, the evolution of baryons is determined by their tight-coupling to the photons. After recombination, baryons escape from the Compton drag and fall into the gravitational wells of the CDM particles which are the dominant species. (Figure from Hu, 1995)

To derive C_1 from these we multiply the first equation by $U_2'(y_m)$ and the second by $U_2(y_m)$, then subtract the two equations. Likewise to get C_2 we multiply the first equation by $U_1'(y_m)$ and the second by $U_1'(y_m)$, then we subtract them from each other. We can further use the small limit of y_m since $y_m \ll 1$, which gives $U_1(y_m) \to 2/3$, $U_2(y_m) \to (2/3)\ln(4/y_m) - 2$, $U_1'(y_m) \to 1$ and $U_2'(y_m) \to (-2/3y_m) + \ln(4/y_m)$. With these assumptions we can show that

$$C_1 = \frac{-9}{4}I_1\Phi(0)\Big[\frac{-2}{3}\ln\Big(I_2\frac{y_m}{y_H}\Big) - \frac{2}{3}\ln\Big(\frac{4}{y_m}\Big) + 2\Big], \tag{2.159}$$

$$C_2 = \frac{9}{4}I_1\Phi(0)\Big[\ln\Big(I_2\frac{y_m}{y_H}\Big)y_m - \frac{2}{3}\Big]. \tag{2.160}$$

With C_1 and C_2 determined by the above equations, equation (2.156) gives an approximate solution for the evolution of the sub-horizon scales in both radiation and matter dominated epoch. However, we are often interested in the power spectrum of matter densities at late times. At late times ($a \gg a_{eq}$) the decaying mode should have fallen to zero i.e. $U_2 \to 0$. Hence an approximate solution for the small-scale cold dark matter density at late times is given by

$$\delta_c = \frac{3I_1\Phi(0)a}{2a_{eq}}\ln\Big[\frac{4I_2e^{-3}a_{eq}}{a_H}\Big], \qquad a \gg a_{eq} \tag{2.161}$$

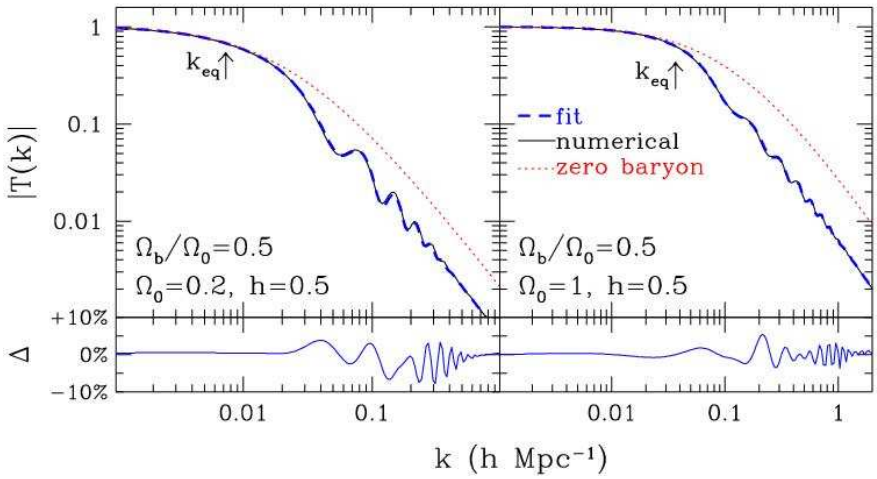

Figure 2.5: The matter transfer function from numerical results and fitting methods. The dotted lines represent the no baryon case. Note the baryon wiggles are clear in the figure and they are enhanced when the total density is smaller. (Figure from Eisenstein and Hu, 1998)

Also remember that at late times the Poisson equation gives an appropriate relation for the gravitational potentials. The equation implies for a matter dominated universe we have

$$\Phi = \frac{4\pi G\rho_m a^2 \delta_m}{k^2}, \qquad a \gg a_{eq} \tag{2.162}$$

Substituting the relations $\rho_m/\rho_0 = \Omega_m a^3$ and $3H_0^2 = 8\pi G\rho_0$ into the Poisson's equation we will have

$$\Phi(k) = \frac{3H_0^2\Omega_m}{2k^2 a}\delta_c, \qquad a \gg a_{eq} \tag{2.163}$$

We have also substituted δ_c for δ_m because the cold dark matter is the dominant constituent to the matter density. We now define a transfer function by writing the late time gravitational potential in the form

$$\Phi(k) \equiv \frac{9}{10}\Phi(0)T(k)\frac{D(a)}{a}. \tag{2.164}$$

Here $T(k)$ is the *transfer function* of matter which relates the late time density fluctuations to the primordial gravitational potential set after inflation. Therefore, the transfer function encapsulates all the information about the horizon-crossing as well as the scale factor of radiation-matter equality. The factor 9/10 has appeared in the definition above due to our expectation from subsection 2.4.2, because we want to normalize the transfer function to unity on large scales. (see Fig. 2.5) The function $D(a)$ is called the *growth function* which determines the scale-independent growth of the perturbations at late times. For a flat matter-dominated universe which we consider here the growth function is $D(a) = a$. But this is not the case for a dark energy or curvature dominated universe which have recently received great attention. Now

we can get the transfer function by substituting Eq. (2.161) into Eq. (2.163) and comparing with equation (2.164). We will have

$$T(k) = \frac{5I_1\Omega_m H_0^2}{2k^2 a_{eq}} \ln\Big[\frac{4I_2 e^{-3} a_{eq}}{a_H}\Big]. \tag{2.165}$$

In practice we can define a transfer function for each species of matter and radiation, however since after recombination baryons simply fall into the potential wells of the cold dark matter and mirror its evolution (see Fig. 2.4), we can call the above the 'matter' transfer function. The power spectrum of the density fluctuations is defined by

$$\langle \delta(\mathbf{k})\delta^*(\mathbf{k}')\rangle = (2\pi)^3 P(k)\delta^3(\mathbf{k}-\mathbf{k}'). \tag{2.166}$$

Substituting from equations (2.161) and (2.165) we will have

$$P(k) = \frac{4k^4 a^2 T^2(k)}{25 H_0^4 \Omega_m^2} P_\Phi. \tag{2.167}$$

where P_Φ is the primordial power spectrum of equation (2.46) set by the inflation. Figure 2.6 shows the power spectrum of matter densities in the linear regime for two flat cosmological models. On large scales where the transfer function is unity the power spectrum is scaled with $P \propto k$. This also corresponds to the scale-invariant signature of the primordial fluctuations. The turn-over in the graphs is due to the fact that the small scale potential decays significantly since it enters the horizon in the radiation dominated epoch (recall Fig. 2.3). Furthermore as we go to higher wave numbers we should expect a bigger drop in amplitude since these are the modes which have entered the horizon even earlier so they have been more suppressed. An interesting feature in Fig. 2.6 is that when we add more cold dark matter particles the turn-over shifts to smaller scales. This is because more mass in the universe means an earlier radiation-matter equality in which the small scale potential decays less since the period of transition is shorter. In Fig. 2.6 we also see small baryonic wiggles in the power spectrum. These share the same origin with the acoustic oscillations in the CMB power spectrum, so along the turn-over wave number, baryonic wiggles provide important source of information for cosmological parameter estimation.

2.5 Anisotropies of the Microwave Background

In this section we present a conceptually simple analysis of the mechanisms that have given rise to the features in the CMB temperature power spectrum. Since perturbations to the CMB photons are very small and remain uniform we can treat them by linear theory on almost all scales. In analogy with the previous section, here we give analytical solutions to the CMB anisotropies in different limits and approximations. One approach that we take here is that we consider the fact that before recombination baryons and photons are tightly coupled to each other by Compton scattering, whereas neutrinos and cold dark matter are coupled to these only gravitationally. It's therefore easier to study a single tightly-coupled photon-baryon fluid and

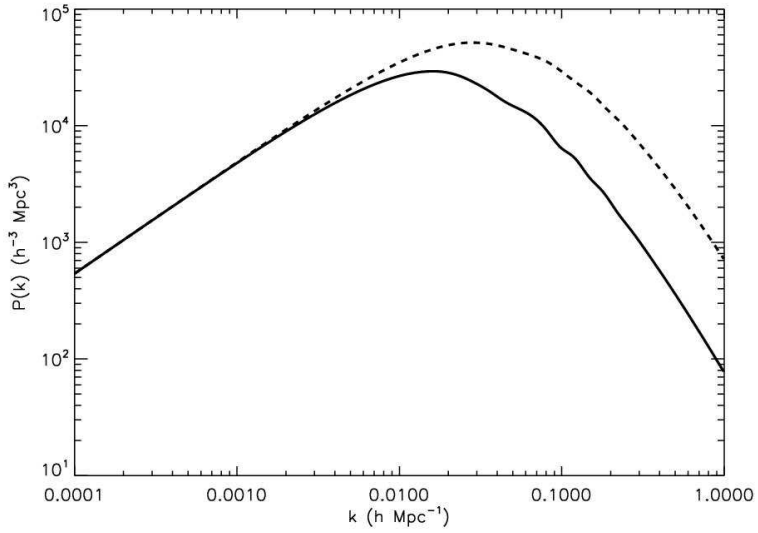

Figure 2.6: The matter power spectra calculated by CAMB for a flat model with $h = 0.73$, $\Omega_b h^2 = 0.02229$ and $\Omega_c h^2 = 0.10541$ (solid), and for the same model with twice as much cold dark matter density (dashed).

then account for the gravitational field of the other species. As we will see in subsection 2.5.2 this interpretation will lead to a simple analytical solution of a damped, driven oscillator in which the gravitational potential acts as a driving force while the photon pressure acts as a restoring force. For large scales which have been superhorizon during the epoch before recombination the analysis is much simpler. These perturbations are believed to have generated from the initial conditions of the universe and have been only affected by gravitational fields. We will verify the solution for these in subsection 2.5.1. After recombination photons free stream to us, so they do not interact with matter densities, therefore in a simplistic case we only need to account for the effect of the geometry of the universe and the projection of the CMB anisotropies from the last scattering surface to the present time. We will discuss this and derive the corresponding formula for the present time CMB multipoles in subsection 2.5.4.

For the purpose of this section it is useful to introduce a new form of the Boltzmann equation. This arises from multiplying equation (2.81) by $\mathcal{P}_\ell(\mu)$ and integrating over μ. It is easy to show that the Boltzmann equation can be decomposed into the multipole form

$$\dot{\Theta}_0 = -k\Theta_1 - \dot{\Phi}, \tag{2.168}$$

$$\dot{\Theta}_1 = \frac{k}{3}\Big(\Theta_0 + \Psi\Big) + \dot{\tau}\Big(\Theta_1 - \frac{v_b}{3}\Big), \tag{2.169}$$

$$\dot{\Theta}_\ell = \frac{k\ell}{2\ell+1}\Theta_{\ell-1} - \frac{k(\ell+1)}{2\ell+1}\Theta_{\ell+1} + \dot{\tau}\Theta_\ell, \quad (\ell > 1). \tag{2.170}$$

One way to solve this Boltzmann hierarchy is to utilize a computer to solve the above set of equations all together to determine each multipole moment. However, the numerical compu-

tation of these up to $\ell \sim 3000$ (which we often need) will turn out to be extremely CPU time consuming. An alternative and much simpler way to solve this hierarchy is to keep in mind that multipoles higher than $l = 2$ are only significant after recombination. As we have already seen, on superhorizon scales, radiation monopole Θ_0 totally characterizes the anisotropy - since physical mechanisms have not affected these modes yet, the radiation can be considered as fully uniform. After the modes enter the horizon the relative velocity of the photons with respect to the background can give rise to Doppler effects which induce a dipole Θ_1 in the photon temperature on the last scattering surface. However the tight coupling of the photons to electrons does not allow the multipoles higher than quadrupole to grow at recombination. Therefore, for the purpose of this section we only consider that only the monopole and dipole are significant. In subsections 2.5.1, 2.5.2 and 2.5.3 we will see that this assumption leads us to some interesting results for the monopole and dipole at the last scattering. In subsection 2.5.4 we will study the line of sight method which implies that the present anisotropies can be obtained from the monopole and dipole at recombination by integrating along the line of path of the photons from the last scattering. We will see that after the last scattering epoch the monopole and the dipole spread into higher order multipoles to make up the power spectra of the CMB temperature anisotropies that we see today. In the next chapter we will study the effect of the subdominant quadrupole moments at the last scattering surface where we will show that they will give rise to the polarization which is of significant interest today for CMB experiments.

2.5.1 Large Scale Anisotropies

In this section we present the large scale anisotropy solutions at the epoch of the last scattering surface. Here it is important to first identify the different sources of the primordial temperature anisotropies. Well before recombination the rate of the Compton scattering was too high for anisotropies to form. Therefore most of the primary CMB anisotropies have a primordial origin or have been generated during the recombination epoch. For a photon travelling through the epoch of recombination three different factors determine its temperature: i) The initial conditions of the universe determine the intrinsic temperature of the photon at the last scattering surface ii) The photon which last scatters when it is in a potential well experiences a gravitational redshift as it climbs up the potential. iii) The peculiar velocity of the photons $\vec{v}_\gamma$ along the direction of observation at the last scattering surface causes a Doppler shift. These effects can be characterized as

$$\frac{\Delta T}{T}(\vec{n}) = \left[\Theta_0 + \Psi - \vec{n} \cdot \vec{v}_\gamma\right]_{\eta=\eta_*}, \tag{2.171}$$

where $\vec{n}$ is a unit vector in the direction of the line of sight and η_* denotes conformal time at the epoch of the last scattering. Here we call the quantity $\Theta_0 + \Psi$ the *effective temperature*. We are especially interested to characterize the anisotropies in terms of the effective temperature as this is the quantity which oscillates in the tight-coupling limit and gives the observed temperature fluctuations on the sky. Moreover because of the appearance of Ψ in the effective temperature

large scale cold spots in the CMB should actually be perceived as overdense regions on the last scattering. This is because an overdense region which corresponds to a deeper potential well (or a larger negative value for Ψ) induces a bigger gravitational redshift on a photon which is climbing out of the well. Therefore an overdensity (underdensity) leads to a bigger (smaller) decrease in the energy of the travelling photon, hence a cold (hot) spot in the CMB. However, although this kind of analogy is being widely used today, there are other factors such as the Integrated Sachs Wolfe effect which break this assumption.

On very large scales physical interactions are irrelevant so the peculiar velocity can be assumed uniformly zero everywhere and we are left with $\frac{\Delta T}{T} = \Theta_0 + \Psi$. From equation (2.119) for superhorizon modes we have

$$\Theta_0(\eta) = -\Phi(\eta) + \text{Const.} \tag{2.172}$$

where the constant can be determined by the initial conditions. For adiabatic perturbations equation (2.124) implies $\Theta_0(0) = \Phi(0)/2$. Substituting into equation (2.172) gives the constant to be equal to $3\Phi(0)/2$. Now we make the assumption that the last scattering happens in the epoch of the matter domination. With this assumption, the discussion of subsection 2.4.2 implies $\Phi(\eta_*) = \frac{9}{10}\Phi(0)$. Using these values equation (2.172) gives

$$\begin{aligned} \big[\Theta_0 + \Psi\big](k, \eta_*) &= \Big[-\Phi(k, \eta_*) + \frac{5}{3}\Phi(k, \eta_*)\Big] + \Psi(k, \eta_*) \\ &= \frac{1}{3}\Psi(k, \eta_*), \qquad \text{(adiabatic)} \end{aligned} \tag{2.173}$$

where we have considered $\Phi \simeq -\Psi$. This is the well known *Sachs-Wolfe effect* which gives the large scale temperature anisotropies. Here we should note that this result is not precise since the last scattering does not occur in a fully matter dominated universe. Nevertheless the true results which depend on the distance to the last scattering surface and the dynamics of the universe are not so different from this approximate one. For isocurvature perturbations the initial potential vanishes $\Phi(0) = \Theta_0(0) = 0$ which implies the constant in equation (2.172) is zero. This leads to the Sachs-Wolfe effect for the isocurvature perturbations

$$\big[\Theta_0 + \Psi\big](k, \eta_*) = 2\Psi(k, \eta_*), \qquad \text{(isocurvature)} \tag{2.174}$$

Another source of anisotropy which is dominant on large scales is the *Integrated Sachs-Wolfe* (ISW) effect. The ISW effect is a secondary effect due to the evolution of the potential wells after recombination. A photon which comes from the last scattering surface gains a net gravitational blueshift when it travels through a decaying potential well $\Psi < 0, \dot{\Phi} < 0$. This is because as the photon falls in to the well it experiences a blueshift which is larger than the redshift that it suffers when it emerges back. Furthermore general relativity implies that the time-dilation effect due to the contraction of space is analogous to another blueshift effect. Therefore the total effect, which is almost twice the gravitational effect, is a differential effect $(\dot{\Psi} - \dot{\Phi})\delta\eta$ which should be integrated along the line of sight. We will calculate the contribution of the ISW effect to the anisotropies in subsection 2.5.4.

2.5.2 Tightly Coupled Approximation

The evolution of the temperature fluctuations which enter the horizon before recombination is given by the dynamics of the photon-baryon fluid. Before recombination the rate of the Compton scattering is so high that photons and electrons can be considered as tightly coupled to each other at small scales. In this subsection we will see that in this limit the competition between gravitational compression and photon pressure sets up acoustic oscillations in the photon-baryon fluid. In the next subsection we will see that this assumption breaks up for the scales which are smaller than the diffusion length of the photons in which case the oscillations get damped by the photon diffusion.

The equations which govern the anisotropies before recombination are the Boltzmann equations for photons, Eqs. (2.168-2.169), and continuity and Euler equations for baryons (2.108), (2.109). The discussion at the beginning of this section implies that at recombination we can ignore all multipoles except Θ_0 and Θ_1. Therefore we can write these equations as

$$\dot{\Theta}_0 = -k\Theta_1 - \dot{\Phi}, \tag{2.175}$$

$$3\Theta_1 - v_b = \dot{\tau}^{-1}\Big[3\dot{\Theta}_1 - k(\Theta_0 + \Psi)\Big], \tag{2.176}$$

$$\dot{\delta}_b = -kv_b - 3\dot{\Phi}, \tag{2.177}$$

$$\dot{v}_b = \frac{-\dot{a}}{a}v_b + k\Psi + \dot{\tau}(v_b - 3v_\gamma)/R, \tag{2.178}$$

where recall $v_\gamma = \Theta_1$. The tightly coupled limit implies that $\dot{\tau}^{-1}$ is very small. Therefore to zero order in $\dot{\tau}^{-1}$ we can ignore the term on the right hand side of equation (2.176) which leads to

$$v_b^{(0)} = 3\Theta_1 = 3v_\gamma. \tag{2.179}$$

Now we can substitute this equation into the Euler equation (2.178) to find an expression for the baryon velocity up to the first order. This will give

$$v_b^{(1)} = 3\Theta_1 + 3\dot{\tau}^{-1}R\Big(\dot{\Theta}_1 + \frac{\dot{a}}{a}\Theta_1 - \frac{k}{3}\Psi\Big). \tag{2.180}$$

In this equation we can show that $\frac{\dot{a}}{a}R$ is equal to $\dot{R}$ where $R = \frac{3}{4}\frac{\rho_b}{\rho_\gamma}$. This is because

$$\dot{R} = \frac{3}{4}\Big[\frac{\dot{\rho}_b}{\rho_\gamma} - \frac{\dot{\rho_\gamma}}{\rho_\gamma}\frac{\rho_b}{\rho_\gamma}\Big] = R\Big(\frac{\dot{\rho}_b}{\rho_b} - \frac{\dot{\rho}_\gamma}{\rho_\gamma}\frac{\rho_b}{\rho_b}\Big) = -3R\frac{\dot{a}}{a} + 3R\frac{\dot{a}}{a}\big(1 + \frac{1}{3}\big) = \frac{\dot{a}}{a}R, \tag{2.181}$$

where we have used the zero order continuity equation (2.97). Now we can feed back this result and equation (2.180) into equation (2.176). It is easy to show that this will lead to

$$\dot{\Theta}_1 + \frac{\dot{R}}{R+1}\Theta_1 - \frac{k}{3(R+1)}\Theta_0 - k\frac{\Psi}{3} = 0. \tag{2.182}$$

Now, using equation (2.175), we can write the dipole in terms of the monopole i.e. $\Theta_1 = \frac{-1}{k}\dot{\Theta}_0 - \frac{1}{k}\dot{\Phi}$ and $\dot{\Theta}_1 = \frac{-1}{k}\ddot{\Theta}_0 - \frac{1}{k}\ddot{\Phi}$. Substituting these into equation (2.182) leads to

$$\ddot{\Theta}_0 + \frac{\dot{R}}{1+R}\dot{\Theta}_0 + \frac{k^2\Theta_0}{3(R+1)} = -\frac{k^2}{3}\Psi - \frac{\dot{R}}{1+R}\dot{\Phi} - \ddot{\Phi}, \tag{2.183}$$

or

$$\Big\{\frac{d^2}{d\eta^2}+\frac{\dot{R}}{1+R}\frac{d}{d\eta}+k^2c_s^2\Big\}[\Theta_0+\Phi]=F, \tag{2.184}$$

where $c_s=\sqrt{\frac{1}{3(R+1)}}$ is the sound speed in the photon baryon fluid[3] and

$$F=\frac{k^2}{3}(3c_s^2\Phi-\Psi). \tag{2.185}$$

Note that the second order equation (2.184) is an equation for a damped oscillator driven by the forcing function F. The term $k^2\Psi$ corresponds to the gravitational infall which tends to increase the anisotropies; while the term $k^2c_s^2\Theta_0$ represents the photon pressure which counters the gravity, therefore setting up acoustic oscillations in the fluid. For a constant sound speed ($\dot{R}=0$) and no driving force ($F=0$) the equation reduces to that of a harmonic oscillator with constant frequency $\omega=kc_s$. It is obvious that in this limit adding more baryons results in a smaller angular frequency or more spacing between the acoustic peaks. To solve the equation (2.184) we can first work out the homogeneous solutions. This is done in the WKB approximation by considering that the damping term is small compared to the pressure term. This is a valid approximation for small scales or for the case when R is small. In this limit, Hu and Sugiyama (1995a) show that assuming a solution of the form $s=A\exp(iu(\eta))$ results in the two fundamental solutions

$$s(\eta)=(1+R)^{-1/4}\exp\big\{\pm ikr_s(\eta)\big\}, \tag{2.186}$$

where $r_s(\eta)\equiv\int_0^\eta d\eta' c_s(\eta')$ is the *sound horizon*. A particular solution of Eq. (2.184) can be obtained by Green's method. Valiviita (2005) shows that this will lead to the final solution

$$\begin{aligned}[1+R]^{1/4}[\Theta_0(\eta)+\Phi(\eta)] &= C_1\cos(kr_s)+C_2\sin(kr_s)\\ &+\frac{\sqrt{3}}{k}\int_0^\eta d\eta'[1+R(\eta')]^{3/4}\sin[kr_s(\eta)-kr_s(\eta')]F(\eta'),\end{aligned} \tag{2.187}$$

where we have used the approximation $c_s\simeq 1/\sqrt{3}$ which is valid in the limit $R\to 0$. The constants C_1 and C_2 are determined by the initial conditions. Assuming that in early times Θ_0 and Φ are both constant the initial conditions for equation (2.187) and its derivative imply $C_1=\Theta_0(0)+\Phi(0)$ and $C_2=0$. To find an expression for the dipole we can substitute Eq. (2.187) into Eq. (2.175). This will lead to an expression for Θ_1 which is out of phase with Θ_0.

Note that equation (2.187) applies only before recombination when photons and electrons are tightly coupled to each other. This will result in a series of zeros and extrema ($k_n=n\pi/r_s$) for the effective monopole temperature on the surface of the last scattering which is then projected on the angular power spectrum of anisotropies on the sky. Those wavenumbers which reach positive or negative extrema in the monopole at the last scattering ($n=0,2,4,..$) yield 'peaks'

[3]The square of sound speed in the single photon-baryon fluid is given by

$$c_s^2\equiv\frac{\dot{p}_\gamma}{\dot{\rho}_\gamma+\dot{\rho}_b}=\frac{\omega_\gamma}{1+\dot{\rho}_b/\dot{\rho}_\gamma}=\frac{1/3}{1+(\rho_b/\rho_\gamma)(1/(1+\omega_\gamma))}=\frac{1}{3(1+R)},$$

where in the third equality we have used the continuity equation $\frac{\dot{\rho}_x}{\rho_x}=-3(1+\omega_x)\frac{\dot{a}}{a}$.

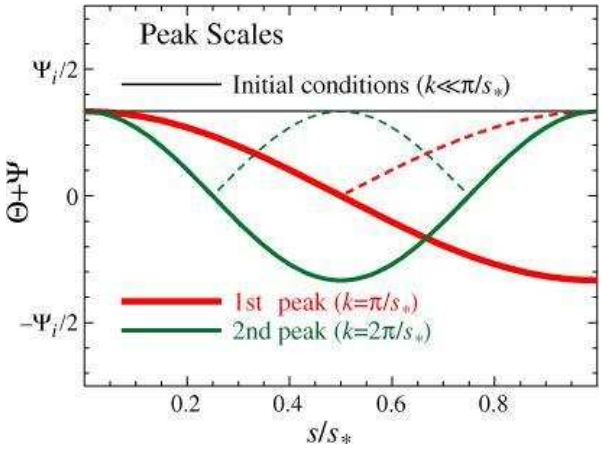

Figure 2.7: The effective temperature of the photons at the recombination epoch. The first peak corresponds to the wave number which completes half an oscillation by the last scattering, whereas the second peaks corresponds to a full oscillation. (Figure from Hu and Dodelson, 2002)

in the CMB power spectrum. (see Fig. 2.7) These are compressional or rarefactional acoustic modes in the potential wells, which respectively correspond to overdensity or underdensity of the photons and baryons at recombination. However, the modes which are caught at their zero monopole at the last scattering ($n = 1, 3, 5, ..$) give rise to very small anisotropies or 'troughs' in the CMB power spectrum. One important remark is that if we add more baryons to the fluid only the compressional phases grow since it becomes harder for pressure to resist the larger gravity. This makes the overdense peaks (every other peak) to grow in amplitude, whereas the underdense peaks may even shrink a little since they are now less underdense. This discrepancy between the magnitude of the alternating peaks in the temperature power spectrum is a good measure of the baryon loading at recombination.

2.5.3 Photon Diffusion Damping

The fate of the anisotropies on very small scales is determined by the diffusion damping of the photons. It arises from the fact that, on very small scales, the photons are not exactly tightly coupled to the electrons. On these scales photons random walk through baryons carrying energy between hot and cold regions. To account for the photon diffusion we will have to solve the anisotropy equations in the previous subsection up to first order in $\dot{\tau}^{-1}$. In this limit the solutions for the monopole and dipole will turn out to be the same as that of a damped acoustic oscillator. However, there will arise new terms due to the exponential damping of the anisotropies. To begin with, let us find an expression for v_b up to the second order. This can be found by feeding back the first order equation (2.180) into the Euler equation (2.178). The result will comprise many terms, however if we consider that on very small scales the potentials and the baryon to photon energy momentum ratio are very slowly varying (i.e. $\dot{\Phi}$, $\dot{\Psi}$ and $\dot{R}$ are

zero) we will have

$$v_b^{(2)} = 3\Theta_1 + \dot{\tau}^{-1}R\Big[3\dot{\Theta}_1 + \frac{d}{d\eta}\big(3\dot{\tau}^{-1}R(\dot{\Theta}_1 - \frac{k}{3}\Psi)\big) - k\Psi\Big]. \tag{2.188}$$

Using the fact that $\frac{d}{d\eta} = -\dot{\tau}^{-2}\ddot{\tau} \simeq 2\dot{\tau}^{-1}\frac{\dot{a}}{a}$ since $\dot{\tau} \propto n_e a \propto a^{-2}$; we can further simplify equation (2.188) to get

$$v_b^{(2)} = 3\Theta_1 + 3\dot{\tau}^{-1}R\Big(\dot{\Theta}_1 - \frac{k}{3}\Psi\Big) + 3\dot{\tau}^{-2}R^2\ddot{\Theta}_1. \tag{2.189}$$

Now in analogy with the solution in subsection 2.5.2 assume to second order

$$\Theta_0^{(2)}, \Theta_1^{(2)} \propto e^{i\int_0^\eta \omega(\eta')d\eta'}, \tag{2.190}$$

where $\omega(\eta)$ is the quantity to be determined. Substituting this into equation (2.189) we will have

$$v_b^{(2)} = 3\Theta_1 + \dot{\tau}^{-1}R(3i\omega\Theta_1 - k\Psi) - 3\dot{\tau}^{(-2)}R^2\Theta_1. \tag{2.191}$$

Substituting this equation in Eq. (2.176) leads to

$$i\omega(1+R)\Theta_1 = \frac{k}{3}\big(\Theta_0 + (1+R)\Psi\big) - \dot{\tau}^{-1}R^2\omega^2\Theta_1. \tag{2.192}$$

Now if we differentiate the above equation and ignore the terms containing $\dot{R}$ and $\dot{\Psi}$ we arrive at

$$i\omega(1+R)\dot{\Theta}_1 = \frac{k}{3}\dot{\Theta}_0 - \dot{\tau}^{-1}R^2\omega^2\dot{\Theta}_1. \tag{2.193}$$

Substituting $\dot{\Theta}_1 = i\omega\Theta_1$ and $\dot{\Theta}_0 = -k\Theta_1$ in equation (2.193) yields an equation for ω

$$(1+R)\omega^2 = \frac{k^2}{3} + i\dot{\tau}^{-1}R^2\omega^3. \tag{2.194}$$

Since we are looking for a small correction to the zero order angular frequency we can expect $\omega = kc_s + \delta\omega$. Therefore assuming that $\omega^3 = \omega\omega^2 \approx \omega(kc_s)^2$ equation (2.194) leads to

$$\omega^2 + \frac{-i\dot{\tau}^{(-1)}k^2R^2}{3(1+R)^2}\omega + \frac{-k^2}{3(1+R)} = 0. \tag{2.195}$$

The answers to this quadratic equation in the case when we neglect the $\dot{\tau}^{-2}$ term is given by

$$\omega = \pm kc_s + \frac{i}{6}k^2\dot{\tau}^{-1}\frac{R^2}{(1+R)^2}. \tag{2.196}$$

Therefore our approximate solutions for the monopole and dipole including corrections for the diffusion damping are

$$\Theta_0(\eta), \Theta_1(\eta) \propto \exp\big\{\pm ikr_s(\eta)\big\}\exp\Big\{-\frac{k^2}{k_D^2}\Big\}, \tag{2.197}$$

where k_D is the damping wavenumber given by

$$\frac{1}{k_D^2} \equiv \frac{1}{6}\int_0^\eta \dot{\tau}^{-1}(\eta')\frac{R^2(\eta')}{[1+R(\eta')]^2}d\eta'. \tag{2.198}$$

The photon diffusion mixes the hot and cold regions and therefore wipes out the anisotropies if the damping scale k_D^{-1} exceeds the scale of the perturbations k^{-1}. An important thing to

notice is that the diffusion damping is especially sensitive to the reionization history (through $\dot{\tau}$) as well as the baryon density R. If the last scattering occurs quite late diffusion damping can totally erase the acoustic peaks. This can happen in models with early reionization for which the damping scale can be much larger which makes the photon diffusion to continue until later times.

2.5.4 Line of Sight Integration

Having determined the anisotropies at the last scattering we now introduce a powerful formalism which projects the monopole and dipole on the last scattering on to the multipole moments of the present day CMB temperature fluctuations. This method is based on integrating the fluctuations along the line of sight from early times to the present η_0. Consider the Boltzmann equation (2.81) which is valid at all times. We can write this equation in the form

$$[\dot{\Theta}+\dot{\Psi}]+(ik\mu-\dot{\tau})[\Theta+\Psi]=[\dot{\Psi}-\dot{\Phi}]-\dot{\tau}\big\{[\Theta_0+\Psi]-i\mu v_b\big\}. \tag{2.199}$$

The theory of ordinary differential equations suggests that a first order equation of the form $y'+p(x)y=q(x)$ has the solution $y(x)=\int_{x_0}^{x}u(t)q(t)dt$ where $u(x)\equiv\exp[\int_{x_0}^{x}p(t)dt]$ is called the integrating factor. With this formula an integrating factor for equation (2.199) is

$$u(\eta)=\exp\Big\{\int_{\eta}^{\eta_0}[ik\mu-\dot{\tau}(\eta')]d\eta'\Big\}=e^{ik\mu(\eta_0-\eta)}e^{-\tau(\eta,\eta_0)}, \tag{2.200}$$

where $\tau(\eta,\eta_0)=\int_{\eta}^{\eta_0}\dot{\tau}(\eta')d\eta'$ is the optical depth from η to the present. Armed with this knowledge, we can construct a solution for equation (2.199). We will have

$$[\Theta+\Psi](k,\mu,\eta_0)=\int_0^{\eta_0}\Big\{\dot{\Psi}-\dot{\Phi}-\dot{\tau}(\Theta_0+\Psi-i\mu v_b)\Big\}e^{ik\mu(\eta_0-\eta)}e^{-\tau(\eta,\eta_0)}d\eta. \tag{2.201}$$

Now we represent the position of the photon at time η by $\vec{x}=\chi\hat{n}\equiv(\eta_0-\eta)\hat{n}$ where $\hat{n}$ is the unit vector pointing along the line of sight. With this notation $e^{ik\mu(\eta_0-\eta)}=e^{i\vec{k}\cdot\vec{x}(\eta)}$. Moreover we will have $\frac{d}{d\eta}e^{i\vec{k}\cdot\vec{x}(\eta)}=-ik\mu e^{i\vec{k}\cdot\vec{x}(\eta)}$. Substituting these relations in equation (2.201) we arrive at

$$[\Theta+\Psi](k,\mu,\eta_0)=\int_0^{\eta_0}\Big\{\big[\dot{\Psi}-\dot{\Phi}-\dot{\tau}(\Theta_0+\Psi)\big]e^{i\vec{k}\cdot\vec{x}(\eta)}-\frac{1}{k}v_b\dot{\tau}\frac{d}{d\eta}\big[e^{i\vec{k}\cdot\vec{x}(\eta)}\big]\Big\}e^{-\tau(\eta,\eta_0)}d\eta. \tag{2.202}$$

Here we can expand the exponent function $e^{i\vec{k}\cdot\vec{x}}$ as (see Jackson, 1975)

$$e^{i\vec{k}\cdot\vec{x}}=4\pi\sum_{\ell}\sum_{m=-\ell}^{\ell}i^{\ell}j_{\ell}(k\chi)Y_{\ell m}(\theta,\phi)Y^{*}_{\ell m}(\theta_k,\phi_k). \tag{2.203}$$

Using the relations $4\pi\sum_m Y_{\ell m}(\theta,\phi)Y^{*}_{\ell m}=(2\ell+1)\mathcal{P}_{\ell}(-\mu)$ and $\mathcal{P}_{\ell}(-\mu)=(-1)^{\ell}\mathcal{P}_{\ell}(\mu)$ the above equation gives

$$e^{i\vec{k}\cdot\vec{x}}=\sum_{\ell}(-i)^{\ell}(2\ell+1)j_{\ell}(k\chi)\mathcal{P}_{\ell}(\mu). \tag{2.204}$$

Now writing the left hand side of equation (2.202) in terms of the multipole expansion (2.85) and substituting Eq. (2.204) in the right hand side we will have

$$\sum_\ell (-i)^\ell (2\ell+1)\mathcal{P}_\ell(\mu)[\Theta+\Psi]_\ell(k,\mu,\eta_0) = \sum_\ell (-i)^\ell (2\ell+1)\mathcal{P}_\ell(\mu) \times \int_0^{\eta_0} \Big\{ \big[\dot\Psi - \dot\Phi - \dot\tau(\Theta_0+\Psi)\big] j_\ell(k\chi) - \frac{1}{k} v_b \dot\tau \frac{d}{d\eta}\big[j_\ell(k\chi)\big] \Big\} e^{-\tau(\eta,\eta_0)} d\eta. \tag{2.205}$$

In this equation we expect that the multipoles Ψ_ℓ are zero since the potential is not a function of the direction (i.e. μ). Moreover, with our knowledge about the optical depth before and after recombination we can make guesses about the shape of the exponent term on the right hand side. The optical depth before recombination is very large i.e. $\tau(\eta,\eta_0) \to \infty$ for $\eta < \eta_*$. After recombination there is almost no Compton scattering, therefore $\tau(\eta,\eta_0) = 0$ for $\eta > \eta_*$. This means that the term $\dot\tau e^{-\tau}$ is zero before and after recombination. Furthermore we know that $\int_0^{\eta_0} \dot\tau(\eta) e^{-\tau(\eta,\eta_0)} d\eta = -\int_0^{\eta_0} \frac{d}{d\eta} e^{-\tau(\eta,\eta_0)} d\eta = -e^{-\tau(\eta,\eta_0)}\Big|_\infty^0 = -1$. In this case it is obvious that the function $g \equiv -\dot\tau e^{-\tau}$ has the properties of a Dirac delta function, whereas the exponent $e^{-\tau}$ should be a step function. i.e.

$$e^{-\tau(\eta,\eta_0)} \to \theta(\eta-\eta_*), \qquad -\dot\tau e^{-\tau(\eta,\eta_0)} \to \delta(\eta-\eta_*) \tag{2.206}$$

The function g is called the *visibility function* which gives the probability of a photon being last scattered between η and $\eta + d\eta$. The fact that it approximately corresponds to the Dirac delta function $\delta(\eta-\eta_*)$ means that most of the last scattering occurs at the recombination η_*. Substituting the relations (2.206) into the equation (2.205) each of the the terms on the right is given by

$$\Theta_\ell^{\rm Monopole}(\eta_0,k) = [\Theta_0+\Psi](\eta_*,k) j_\ell[k(\eta_0-\eta_*)], \tag{2.207}$$

$$\Theta_\ell^{\rm Dipole}(\eta_0,k) = 3\Theta_1(\eta_*,k)\Big[j_{\ell-1}[k(\eta_0-\eta_*)] - \frac{(\ell+1) j_\ell[k(\eta_0-\eta_*)]}{k(\eta_0-\eta_*)}\Big], \tag{2.208}$$

$$\Theta_\ell^{\rm ISW}(\eta_0,k) = \int_{\eta_*}^{\eta_0} d\eta [\dot\Psi - \dot\Phi](\eta,k) j_\ell[k(\eta_0-\eta)], \tag{2.209}$$

where we have used $dj_\ell(x)/dx = j_{\ell-1}(x) - (\ell+1)j_\ell(x)/x$ and also $v_b = 3\Theta_1$ from equation (2.179). The relations (2.207-2.209) give the three main contributions to the present multipoles $\Theta_\ell(\eta_0)$. The monopole term arises from the intrinsic temperature fluctuations and the gravitational redshift due to the climbing up of the photons from the potential wells at the last scattering. As we saw in subsection 2.5.1 on large scales this is determined by the Sachs-Wolfe effect which gives us a means for the study of the initial perturbations. The dipole term in equation (2.208) arises from the Doppler effect due to the velocity field of the photons. Therefore the CMB photons look warmer if their velocity points towards us at the last scattering. Equation (2.209) represents the contribution from the Integrated Sachs-Wolfe effect. Time varying potentials give rise to time dilation and gravitational effect which contribute to the temperature after recombination. All these features can be observed today in the temperature anisotropy spectrum of the CMB (see Fig. 2.8).

On the sky, the temperature fluctuations can be expanded in terms of the spherical harmonics as

$$\Theta(\hat{n}) = \sum_{\ell m} a_{\ell m} Y_{\ell m}(\hat{n}), \tag{2.210}$$

where

$$a_{\ell m} = \int d\hat{n} Y^*_{\ell m}(\hat{n})\Theta(\hat{n}). \tag{2.211}$$

If the fluctuations are Gaussian all the information in the CMB is characterized in the angular power spectrum which is defined by

$$\langle a_{\ell m} a^*_{\ell' m'} \rangle = \delta_{\ell\ell'}\delta_{mm'} C_\ell. \tag{2.212}$$

Therefore, transforming to the Fourier space and then expanding with respect to the Legendre functions the power spectrum is given by

$$\begin{aligned} C_\ell &= \langle a_{\ell m} a^*_{\ell m} \rangle \\ &= \int \frac{d^3k}{(2\pi)^3} \int \frac{d^3k'}{(2\pi)^3} e^{i(\vec{k}-\vec{k}')\cdot\vec{x}} \int d\hat{n} Y^*_{\ell m}(\hat{n}) \int d\hat{n'} Y_{\ell m}(\hat{n'}) \langle \Theta(k)\Theta^*(k') \rangle \\ &= \int \frac{d^3k}{(2\pi)^3} \sum_{\ell',\ell''} (-i)^{\ell'} (+i)^{\ell''} (2\ell'+1)(2\ell''+1) \langle \Theta_{\ell'}(k)\Theta^*_{\ell''}(k) \rangle \\ &\quad \times \int d\hat{n} Y^*_{\ell m}(\hat{n'}) \mathcal{P}_{\ell'}(\mu) \int d\hat{n'} Y_{\ell m}(\hat{n'}) \mathcal{P}_{\ell''}(\mu'), \end{aligned} \tag{2.213}$$

where we have used the fact that $\int d^3x e^{i(\vec{k}-\vec{k}')\cdot\vec{x}} = (2\pi)^3\delta^3(\vec{k}-\vec{k'})$. The last two integrals in equation (2.213) are nonzero only if $\ell' = \ell$ and $\ell'' = \ell$, in which case they are equal to $4\pi Y_{\ell m}(\hat{k})/(2\ell+1)$ (see Dodelson, 2003). Splitting the integral over d^3k to radial and angular parts we will have

$$C_\ell = \frac{2}{\pi} \int_0^\infty \frac{dk}{k} k^3 \left|\Theta_\ell(\eta_0, k)\right|^2, \tag{2.214}$$

where we have used $\int d\hat{k} |Y_{\ell m}(\hat{k})|^2 = 1$ since the spherical harmonics constitute an orthonormal set of functions on the sphere. The equation (2.214) relates the present day multipoles of the temperature fluctuations from Eqs. (2.207-2.209) to the CMB power spectrum on the sky. Therefore we now have an analytical scheme which relates the evolution of the perturbations to the angular power spectrum measured on the sky. (see Fig. 2.8)

On very small scales we can adopt the flat sky approximation in which case the spherical harmonics expansion becomes Fourier transformation. In this limit the angular scales on the sky correspond to $\theta = 2\pi/\ell$. The appearance of the Bessel function in equation (2.207) is related to the assumption that we have considered a flat geometry for the universe. For the case of open or closed universes j_ℓ should be replaced by ultra-spherical Bessel functions. By the way, note that the Bessel function provides us with a one-to-one relationship between k and ℓ. The function $j_\ell(x)$ generally peaks at $x \approx \ell$, which implies that from equation (2.207) we should expect $\ell \approx kD_*$ where $D_* \equiv \eta_0 - \eta_*$ is the comoving distance to the recombination. This relates the angular scale features on the CMB sky maps to the wavenumbers on the last scattering surface. For example, this relation implies that the acoustic peaks in the anisotropy

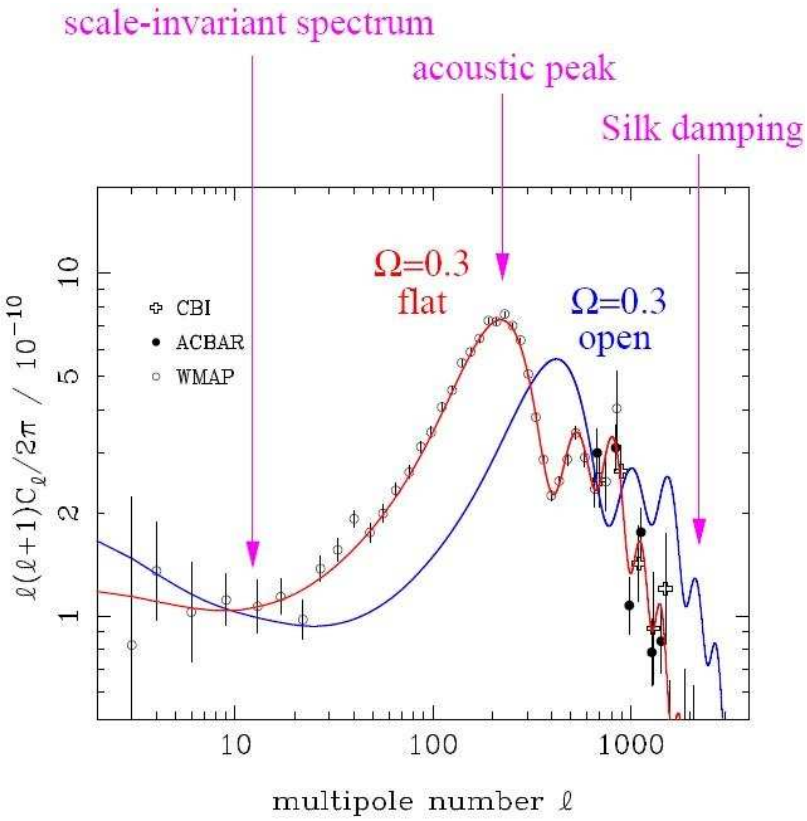

Figure 2.8: The angular power spectrum of CMB temperature fluctuations in units of $\mu\mathrm{K}^2$. The theoretical spectra (solid lines) correspond to the cosmological parameters $(n, \Omega_m, \Omega_b, h) = (1, 0.3, 0.05, 0.65)$, with $\Omega_v = 1 - \Omega_m$ for the flat model and $\Omega_v = 0$ for the open model. In an open universe the angular distance to the last scattering is larger, so wavenumbers at the recombination correspond to smaller angular scales $\theta \propto \ell^{-1}$. Therefore the acoustic peaks are shifted towards higher multipole moments. (Figure from Peacock, 2007)

spectrum are located at $\ell = n\Delta\ell \approx n\pi D_*/r_*$ (see subsection 2.5.2) For a matter dominated universe $\eta \propto a^{1/2} = (1+z)^{(-1/2)}$ leads to $r_*/D_* \approx \eta_*/\eta_0 \approx 1/\sqrt{1000} \approx 1/30 \approx 2^\circ$, which is equivalent to $\ell_1 \approx 200$ for the first acoustic peak.

One important remark here is that the power spectrum of the CMB anisotropies on the sky starts at $\ell = 2$ rather than $\ell = 0$. This is because the monopole term is zero due to our definition $\Theta_0 = (4\pi)^{-1} \int d\Omega' \Theta(\hat{n}) = \langle \Theta(\hat{n}) \rangle \approx 0$. The monopole is an important source of information, however its value cannot be exactly determined because we simply do not know whether the temperature of the photons we observe locally is the same as the average temperature all over the universe. This is an example of the cosmic variance which we will discuss in the next chapter. The dipole moment on the other hand is affected by the Doppler effect due to the motion of our own reference frame with respect to the background. This is a significant source of contamination to the CMB, which although can be useful for determining our own velocity

in the cluster, is often discarded from the CMB power spectra. Before closing this section, note that we have plotted $\ell(\ell+1)C_\ell/(2\pi)$ (rather than C_ℓ) in Fig. 2.8 This is because the correlation between temperature fluctuations at different angles is

$$\begin{aligned}\langle\Theta(\hat{n}_1)\Theta(\hat{n}_2)\rangle &= \sum_{\ell m}\sum_{\ell' m'}\langle a_{\ell m}a^*_{\ell' m'}\rangle Y_{\ell m}(\hat{n}_1)Y^*_{\ell' m'}(\hat{n}_2) \\ &= \sum_{\ell}\frac{2\ell+1}{4\pi}C_\ell\mathcal{P}_\ell(\cos\theta). \end{aligned} \tag{2.215}$$

Here we have used the spherical harmonics' addition theorem

$$\mathcal{P}_\ell(\cos\theta) = \frac{4\pi}{2\ell+1}\sum_{m=-\ell}^{\ell} Y_{\ell m}(\hat{n}_1)Y^*_{\ell m}(\hat{n}_2), \tag{2.216}$$

where θ is the angular separation between $\hat{n}_1$ and $\hat{n}_2$. In this way, from Eq. (2.215), variance of the fluctuations evaluates to

$$\langle|\Theta|^2\rangle = \sum_{\ell}\frac{2\ell+1}{4\pi}C_\ell \approx \int\frac{\ell(\ell+1)}{2\pi}C_\ell d\ln\ell, \tag{2.217}$$

which means that $\ell(\ell+1)C_\ell/(2\pi)$, which is plotted, is the power per logarithmic interval. We will particularly focus on the statistics of the CMB temperature and polarization fields in the next chapter where we introduce the power spectrum estimators and their covariances.

Chapter 3

The Cosmic Microwave Background

The discovery of the cosmic microwave background in 1965 by Penzias and Wilson was a major achievement for modern cosmology. The timing of the discovery was ironic, since by that time theoretical predictions had made it clear that a background radiation should exist in an expanding universe. From Eq. (2.11), we see that the frequency of photons scales as $1/R$ which means that the wavelength of the photons scales with the size of the universe R. On the other hand, thinking of quantum mechanics, the momentum of the photons is inversely proportional to their de Broglie wavelength. Therefore, as the energy of the photons decreases their wavelength should stretch with the expansion, resembling standing waves trapped in a box. Arguments like this paved the way for cosmologists to rule out the steady state model in favor of the Big Bang upon Penzias and Wilson discovery of CMB long before the black body spectrum was discovered by the COBE FIRAS instrument.

Over the past decade accurate measurements of the CMB anisotropies have played a crucial role in constraining the cosmological models. The large-angle Sachs-Wolfe effect, multiple acoustic oscillations and the Silk damping tail in the temperature power spectrum have now been confirmed by a range of experiments from the largest angular scales down to angular scales of a few arcminutes (see e.g. Dunkley et al., 2008; Reichardt et al., 2008). Another prediction of cosmology is that the CMB photons should be polarized due to Thomson scattering by free electrons of the local quadrupole in the radiation field at the last scattering surface. The CMB polarization originates from the velocity fields at recombination, which are anti-correlated with the density fields which have generated the temperature anisotropies. Therefore the detection of anti-correlated polarization is a crucial consistency check of the standard model, in which case, it can be also used to break degeneracies between the cosmological parameters. Nevertheless, the CMB polarization is very small (at the 10% level) and the polarized foregrounds are poorly

known, so it is generally much more difficult to measure the polarization. Polarization has been first detected by the ground-breaking DASI experiment (Kovac et al., 2002), and later verified by several experiments at a wide range of angular scales. (Barkats et al., 2005; Readhead et al., 2004; Montroy et al., 2006; Sievers et al., 2007; Page et al., 2007; Bischoff et al., 2008; Nolta et al., 2008) QUaD is the latest of these experiments which has detected multiple acoustic peaks in the polarization of the CMB. (QUaD collaboration: C. Pryke et al., 2008)

In this chapter we study the origin of the polarization and the statistics of the CMB fluctuations. In section 3.1 we first introduce the Thomson scattering which generates polarization from quadrupole anisotropies at the last scattering. We then go on to examine the spin-weighted spherical harmonics expansion of the linear Stokes parameters in section 3.2. We analyze the statistics of the angular power spectra in section 3.3 and explain how different mechanisms contribute to the polarization spectra. In section 3.4 we describe the QUaD CMB experiment survey and give a short description of the process of map-making and power spectrum estimation used for QUaD data. We will finally present the combined measured QUaD polarization and temperature power spectra which we will utilize for cosmological parameter estimation.

3.1 Polarization from Thomson Scattering

In this section we discuss the Thomson scattering of photons at recombination and explain how it generates polarization from quadrupole radiation anisotropies. Our analysis here is very close to Dodelson (2003) and Kosowsky (1996).

The CMB polarization originates from re-scattering of the primordial photons on the hot electron gas on their way to us. Imagine an electron which is at rest in the origin. This electron is accelerated by an incoming plane wave of radiation with wave vector $\vec{k}_i$ and re-radiates an outgoing wave along $\vec{k}_s$. The Compton scattering implies that any incoming radiation transverse to the outgoing direction passes through unimpeded, whereas the radiation parallel to the outgoing direction will stop. Such a process in which the photon energy remains unchanged is called *Thomson scattering*. The plane spanned by $\vec{k}_i$ and $\vec{k}_s$ is called the scattering plane, and the cross-section for the outgoing photons is proportional to $|\hat{k}_i \cdot \hat{k}_s|^2$. Thus the scattered radiation intensity peaks in the direction normal to the incident polarization.

Now imagine the incoming plane wave is travelling along the x axis towards the origin, with its corresponding electric and magnetic fields oscillating in the y-z plane. If the intensity along the two transverse directions y and z is equal, then the light is unpolarized. This ray then scatters off an electron at the origin and gets deflected into all directions. The Thomson scattering can then guarantee that the outgoing radiation observed in the $+\hat{z}$ direction has a linear polarization pattern. This is due to the fact that none of the incoming intensity along the outgoing direction (z-axis) gets transmitted. The intensity along the y-axis is the only component of the polarization that passes through unimpeded in the $+\hat{z}$ direction. Hence the outgoing radiation is polarized in the y-direction if observed along the z axis. Obviously, this

result is for one single incoming ray and if we generalize to radiation incident from all directions we realise that producing polarization will not be as easy.

Imagine an unpolarized incoming isotropic radiation (monopole) incident from all directions on an electron. Figure 3.1 (left) is a simple representation of this situation where incoming rays from only two directions, the $+\hat{x}$ and $+\hat{y}$ directions, have been depicted. We are interested in the polarization of outgoing photons in the $\hat{z}$ direction. The intensity of the outgoing ray along the x-axis comes from the radiation incident from the $\hat{y}$ direction, while the outgoing y-intensity comes from the radiation from the x-axis. Since the incoming amplitudes from both directions have equal intensity for an isotropic radiation, the outgoing radiation along the x and y axes will turn out to have equal intensities, leading to an unpolarized outgoing radiation along the $\hat{z}$ direction. Hence, isotropic radiation does not produce polarization.

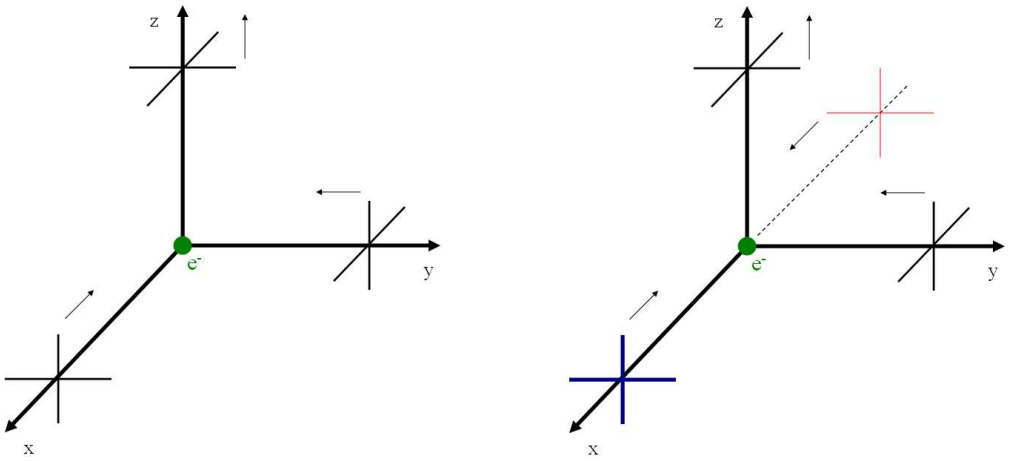

Figure 3.1: Thomson scattering of incoming isotropic (left) and dipole (right) radiation. Here black lines denote radiation with average intensity. Blue (thick) lines show incoming radiation that is hotter than average intensity and red (thin) lines represent radiation that is colder that average. The net result for both isotropic and dipole radiation is outgoing unpolarized light.

Incoming dipole radiation also produces no polarization. The simplest example of a dipole is the case when the incoming radiation is hotter than average from the $+\hat{x}$ direction and colder than average from $-\hat{x}$ direction. Figure 3.1 (right) shows such a situation. Here the outgoing intensity along the x-axis comes from the $\pm\hat{y}$ incident radiations which have the average temperature. The two rays from the $\pm\hat{x}$ directions also produce an outgoing intensity that is neither hot nor cold along the y-axis because it is just equal to the average intensity of the incoming rays along the $\pm\hat{x}$ direction. Since these have the same average intensity the intensity of the outgoing wave along x and y axes are equal. Hence the net result is outgoing unpolarized radiation.

To produce polarized radiation, the incident radiation field should actually possess a quadrupole variation in intensity or temperature. This happens when the average incoming

radiation from the $\hat{y}$ direction is hotter (colder) than it is along the $\hat{x}$ direction. Figure 3.2 illustrates such a case where the incident radiation along the x-axis is hotter than it is in the y direction. Therefore, the intensity of the outgoing radiation is greater along the y-axis than along the x-axis. Thus, the outgoing radiation is polarized for a quadrupole radiation. Furthermore, since the scattering cross-section of the Thomson scattering is quadratic, we do not proceed to study the effect of larger multipoles.

In reality, a quadrupole anisotropy of the photon flux at one point on the last scattering surface, when the universe is still ionized, can generate polarization in the cosmic background radiation. Before recombination, the high electron density means that the mean free path of the photons is too small to produce a quadrupole; however after the recombination the electron density is too low for significant Thomson scattering to occur. Therefore, unlike temperature fluctuations, polarization can only be produced during a short period around recombination, which means that the amplitude of the polarization is expected to be smaller than the temperature anisotropies. Also, although late re-ionization, which is due to the process of early star formation, enhances the polarization at large scales, it does not alter the conclusion that the polarization signal is small.

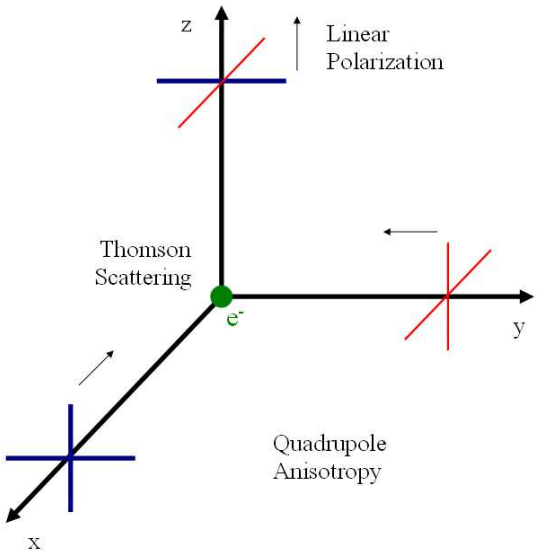

Figure 3.2: Thomson scattering of radiation with a quadrupole anisotropy generates linear polarization. Blue colors (thick lines) represent hot and red colors (thin lines) cold radiation.

The quadrupole anisotropy of the photon flux in the last scattering epoch can arise from the velocity gradients of the density fluctuations. In the photon-baryon fluid rest frame, the fluid is accelerated towards the cold spot, or decelerated towards a hot spot. In the former case, the velocity of neighboring particles tends to diverge radially from and converge transversely to the scattering point. In the latter case, the velocity of neighboring particles tends to converge

radially to and diverge transversely from the scattering point. We see the patterns produced by these processes in Fig. 3.3. Then the Doppler shift induces a quadrupole flux anisotropy around the last scattering point, leading to radial polarization in the first case and to transverse polarization in the second case. This mechanism or any known secondary effect does not produce any circular polarization, so from now on we set the circular components of the polarization equal to zero.

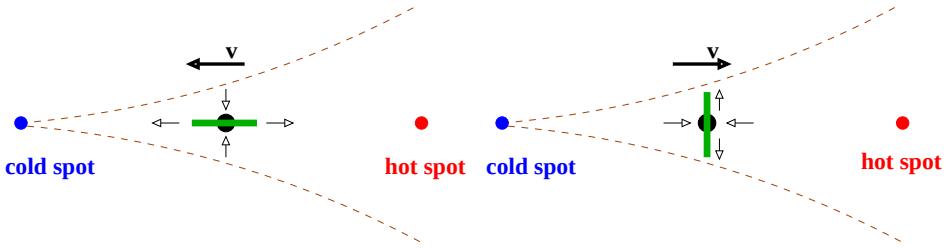

Figure 3.3: Generation of the local quadrupole anisotropies in the photon flux on the last scattering surface. The velocity gradients generate radially correlated polarization around cold spots (left) and tangentially correlated polarization around hot spots (right). (Figure from Kaplan et al., 2003)

Having described how polarization is generated by Thomson scattering, we now need to quantify this discussion in terms of the Stokes' parameters. Any incoherent and linearly polarized radiation can be parameterized by its intensity as well as two quantities Q and U which depend on the components of the intensity function. The Stokes parameter Q is positive (negative) if the fluctuations are larger (smaller) along the x axis relative to the y axis, while U is positive (negative) if the fluctuations are larger (smaller) along the diagonal direction at 45° angle relative to the diagonal direction at $-45°$. In this way it is easy to calculate Q and U by summing over all incident rays which generate such anisotropies.

First, define the polarization vectors for the outgoing beam of light so that $\hat{\epsilon}_1$ is perpendicular to the scattering plane and $\hat{\epsilon}_2$ is in the scattering plane. (Figure 3.4) The Thomson scattering cross-section for an incident wave with linear polarization $\hat{\epsilon}'$ into a scattered wave with linear polarization $\hat{\epsilon}$ is given by

$$\frac{d\sigma}{d\Omega_{n'}} = \frac{3\sigma_T}{8\pi}|\hat{\epsilon}' \cdot \hat{\epsilon}|^2, \tag{3.1}$$

where σ_T is the total Thomson cross section and $d\Omega_{n'}$ is the differential solid angle in the direction of the incoming ray $\hat{n}'$. Consider first an unpolarized incident plane wave of intensity I', so $Q' = U' = 0$. The Q polarization of the outgoing wave is the difference between the cross-section for photons polarized in the $\hat{\epsilon}_1$ and $\hat{\epsilon}_2$ directions. Hence, we have

$$Q = \frac{3\sigma_T}{8\pi}\left(\sum_{j=1}^{2}|\hat{\epsilon}_1 \cdot \hat{\epsilon}'_j(\hat{n}')|^2 - \sum_{j=1}^{2}|\hat{\epsilon}_2 \cdot \hat{\epsilon}'_j(\hat{n}')|^2\right). \tag{3.2}$$

Without loss of generality, we can choose the $\hat{z}$ axis to be along the propagation direction of the scattered light. So we can choose the two outgoing polarization axes as $\hat{\epsilon}_1 = \hat{x}$ and $\hat{\epsilon}_2 = \hat{y}$.

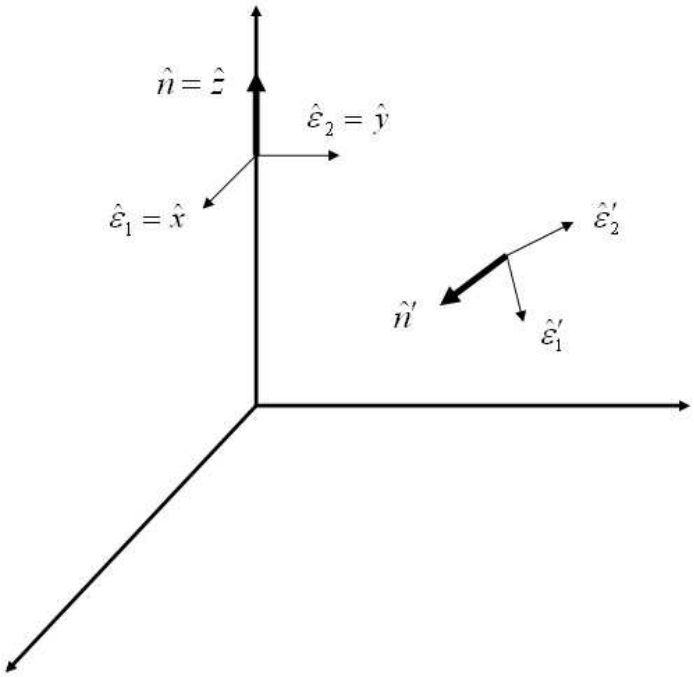

Figure 3.4: Incoming and outgoing polarization vectors for Thomson scattering of a light beam.

Integrating over all $\hat{n}'$ directions, Eq. (3.2) leads to

$$Q(\hat{z}) = \int d\Omega_{n'} I'(\hat{n}') \sum_{j=1}^{2} \left(|\hat{x} \cdot \hat{\epsilon}'_j(\hat{n}')|^2 - |\hat{y} \cdot \hat{\epsilon}'_j(\hat{n}')|^2 \right). \tag{3.3}$$

To take the dot product in Eq. (3.3), we express $\hat{\epsilon}'_1$ and $\hat{\epsilon}'_2$ in terms of their Cartesian coordinates:

$$\hat{\epsilon}'_1(\theta', \phi') = (\cos\theta' \cos\phi', \cos\theta' \sin\phi', -\sin\theta'), \tag{3.4}$$

$$\hat{\epsilon}'_2(\theta', \phi') = (-\sin\phi', \cos\phi', 0). \tag{3.5}$$

Now, the dot products become trivial, and we find

$$\begin{aligned} Q(\hat{z}) &= \int d\Omega_{n'} I'(\hat{n}') \Big[(\cos^2\theta' \cos^2\phi' + \sin^2\phi') - (\cos^2\theta' \sin^2\phi' - \cos^2\phi') \Big] \\ &= \int d\Omega_{n'} I'(\hat{n}') \Big[(\cos^2\phi' - \sin^2\phi')(\cos^2\theta' - 1) \Big] \\ &= -\int d\Omega_{n'} I'(\hat{n}') \sin^2\theta' \cos(2\phi'). \end{aligned} \tag{3.6}$$

In the same way we can derive the corresponding expression for $U(\hat{z})$. The U-component of the polarization is proportional to the difference between the cross-section for outgoing photons polarized in the $(\hat{x} + \hat{y})/\sqrt{2}$ and $(\hat{x} - \hat{y})/\sqrt{2}$ directions. It is then straightforward to derive the

U-component as follows

$$\begin{aligned} U(\hat{z}) &= \int d\Omega_{n'} I'(\hat{n}') \sum_{j=1}^{2} \left(\left| \left(\frac{\hat{x}+\hat{y}}{\sqrt{2}} \right) \cdot \hat{\epsilon}'_j(\hat{n}') \right|^2 - \left| \left(\frac{\hat{x}-\hat{y}}{\sqrt{2}} \right) \cdot \hat{\epsilon}'_j(\hat{n}') \right|^2 \right) \\ &= \frac{1}{2} \int d\Omega_{n'} I'(\hat{n}') \Big[|(\cos\theta' \cos\phi' + \cos\theta' \sin\phi')|^2 + |(-\sin\phi' + \cos\phi')|^2 \\ &\qquad - |(\cos\theta' \cos\phi' - \cos\theta' \sin\phi')|^2 - |(-\sin\phi' - \cos\phi')|^2 \Big] \\ &= \frac{1}{2} \int d\Omega_{n'} I'(\hat{n}') \Big[(\cos^2\theta' - 1)(1 + \sin 2\phi') + (1 - \cos^2\theta')(1 - \sin 2\phi') \Big] \\ &= -\int d\Omega_{n'} I'(\hat{n}') \sin^2\theta' \sin(2\phi'). \end{aligned} \tag{3.7}$$

Eqs. (3.6) and (3.7) imply that Q and U are defined by the integration over $\cos(2\phi')$ and $\sin(2\phi')$ components of the incident intensity field respectively. Here we define the polarization in the direction $\hat{z}$ by (see §3.2)

$$Q(\hat{z}) - iU(\hat{z}) = -\frac{3\sigma_T}{8\pi} \int d\Omega_{n'} \sin^2\theta' e^{2i\phi'} I'(\theta', \phi'). \tag{3.8}$$

We will elaborate on this definition in the next section where we describe its rotation properties as well. We now further expand the incident intensity by spherical harmonics

$$I'(\theta', \phi') = \sum_{lm} a'_{lm} Y_{lm}(\theta', \phi'). \tag{3.9}$$

Using the orthonormality of the Y_{lm} and considering that the integrand in Eq. (3.8) is proportional to $Y_{22}(\theta', \phi') = \sqrt{15/32\pi} e^{2i\phi'} \sin^2\theta'$, Eqs. (3.8) and (3.9) lead to

$$(Q - iU)(\hat{z}) = \frac{3\sigma_T}{2\pi} \sqrt{\frac{2\pi}{15}} a'_{22}. \tag{3.10}$$

Thus, polarization is generated along the outgoing $\hat{z}$-axis provided that the quadrupole component a'_{22} of the incoming radiation is non-zero. To determine the outgoing polarization in a direction making an angle β with the z-axis, the same incoming radiation $I'(\hat{z})$ field must be expanded in the new coordinate system

$$I'(\hat{z}) = \widetilde{I}'(\hat{n}_{\rm rot}) = \sum_{lm} \tilde{a}'_{lm} Y_{lm}(\hat{n}_{\rm rot}), \tag{3.11}$$

where tilde refers to the quantities in the frame $\hat{n}_{rot} = R(\beta)\hat{z}$. The rotated multipole coefficients are

$$\begin{aligned} \tilde{a}'_{lm} &= \int d\hat{n}_{\rm rot} Y^*_{lm}(\hat{n}_{\rm rot}) \widetilde{I}'(\hat{n}_{\rm rot}) \\ &= \int d(R(\beta)\hat{z}) Y^*_{lm}(R(\beta)\hat{z}) I'(\hat{z}) \\ &= \sum_{m'=-m}^{m} \mathcal{D}^{l*}_{m'm}(R(\beta)) \int d\hat{z} Y^*_{lm'}(\hat{z}) I'(\hat{z}) \\ &= \sum_{m'=-m}^{m} \mathcal{D}^{l*}_{mm'}(R(\beta)) a'_{lm'}, \end{aligned} \tag{3.12}$$

where $\mathcal{D}^l_{mm'}$ is the Wigner D-symbol. We see that only a^*_{2m} components of incident radiation contribute to $\tilde{a}'_{22}$ which generates the polarization in the $\hat{n}_{rot}$ direction. Hence the polarization in the new direction is

$$(Q - iU)(\hat{n}_{\rm rot}) = \frac{3\sigma_T}{2\pi}\sqrt{\frac{2\pi}{15}}\sum_{m=-2}^{2}\mathcal{D}^{2*}_{2m}(R(\beta))a'_{2m}. \tag{3.13}$$

Thus, we see that Thomson scattering transfers the quadrupole moments a_{2m} of the incident radiation field at the last scattering surface into polarization in the microwave background. We will investigate the observational implications of this definition of the polarization in the rest of this chapter.

3.2 Spin-weighted Spherical Harmonics Formalism

The CMB radiation is completely characterized by its temperature anisotropy and polarization at each direction in the sky. The temperature anisotropy of the CMB is a scalar field, so it is invariant under rotation (spin-0)[1] and has zero parity. Hence it can be expanded by the usual spherical harmonics $Y_{lm}(\hat{n})$ on the celestial sphere

$$T(\hat{n}) = \sum_{lm} T_{lm}Y_{lm}(\hat{n}), \tag{3.14}$$

where

$$T_{lm} = \int d\Omega Y^*_{lm}(\hat{n})T(\hat{n}). \tag{3.15}$$

Here $\hat{n} = (\theta, \phi)$ is the unit vector along the line of sight. The polarization of the CMB is described by the electromagnetic field $\vec{\epsilon}$, which is orthogonal to its direction of propagation $\vec{k}$. A general radiation is an incoherent superposition of waves with the same wave vector $\vec{k}$ and different frequencies. Choosing two basis vectors $\hat{x}$ and $\hat{y}$ orthogonal to $\hat{k}$, all statistical information is encoded in the 'coherence matrix' $\mathbf{C}$:

$$\mathbf{C} = \begin{pmatrix} \langle|\epsilon_x|^2\rangle & \langle\epsilon_x\epsilon_y^*\rangle \\ \langle\epsilon_y\epsilon_x^*\rangle & \langle|\epsilon_y|^2\rangle \end{pmatrix} = \frac{1}{2}\begin{pmatrix} I+Q & U-iV \\ U+iV & I-Q \end{pmatrix},$$

where the averages are over a range of frequencies. The quantities I, Q, U and V are all real and called the *Stokes parameters*. The I parameter measures the radiation intensity. The other parameters describe the polarization state. It can be shown that $I^2 \geqslant Q^2 + U^2 + V^2$, and because of this property, it is always possible to decompose an observed radiation (I, Q, U, V) into two components: one completely unpolarized with $\big(I-(Q^2+U^2+V^2)^{1/2}, 0, 0, 0\big)$, and one elliptically polarized with $\big((Q^2 + U^2 + V^2)^{1/2}, Q, U, V\big)$. Therefore, the parameters Q and U measure the linear polarization, i.e. the orientation of the ellipse relative to the x-axis via the polarization angle

$$\chi = \frac{1}{2}\tan^{-1}\frac{U}{Q}, \tag{3.16}$$

[1] A spin-s function is defined as one which transforms as ${}_sf'(\theta,\phi) = e^{-is\psi}\ {}_sf(\theta,\phi)$ under rotation of the reference frame by an angle ψ.

and the polarization amplitude

$$\vec{P} = (Q^2 + U^2)^{1/2}\hat{\chi}, \tag{3.17}$$

with $\hat{\chi}$ representing the unit vector in the direction of the polarization. Note that Q and U parameters depend on the reference frame since

$$Q = \langle|\epsilon_x|^2\rangle - \langle|\epsilon_y|^2\rangle, \tag{3.18}$$

$$U = \langle\epsilon_x\epsilon_y^*\rangle + \langle\epsilon_y\epsilon_x^*\rangle. \tag{3.19}$$

It is easy to show that under rotation of the reference frame $(\hat{x}, \hat{y})$ by an angle ψ (around $\hat{n}$) i.e. when $\epsilon'_x = \cos\psi\epsilon_x + \sin\psi\epsilon_y$ and $\epsilon'_y = -\sin\psi\epsilon_x + \cos\psi\epsilon_y$, the Stokes parameters (Q, U) rotate by an angle 2ψ

$$Q' = Q\cos(2\psi) + U\sin(2\psi), \tag{3.20}$$

$$U' = -Q\sin(2\psi) + U\cos(2\psi). \tag{3.21}$$

Therefore, from these quantities we can construct two spin-2 objects $Q \pm iU$ which satisfy the transformation relation

$$(Q \pm iU)'(\hat{n}) = e^{\mp 2i\psi}(Q \pm iU)(\hat{n}). \tag{3.22}$$

From this equation we can also see that under rotation the amplitude in Eq. (3.17) remains invariant and the polarization angle in Eq. (3.16) transforms $\chi \to \chi - \psi$. (Kosowsky, 1999) The fourth Stokes parameter, V, measures the relative strength of the two linear polarization states, and is nonzero only if polarization is circularly polarized.

The polarization field of the CMB can be described by the Stokes parameters U and Q. One can conveniently combine Eqs. (3.16) and (3.17) into a single complex quantity representing the polarization in the direction $\hat{n}$ on the sky

$$P(\hat{n}) = (Q + iU)(\hat{n}). \tag{3.23}$$

From Eq. (3.22) we know that this quantity is a spin-2 object, hence unlike a scalar (spin-0) function, polarization can not be expanded by the usual spherical harmonics on the surface of a sphere. The mathematical machinery necessary to represent angular distribution of the polarization of the CMB on the celestial sphere is actually the spin-weighted harmonics ${}_sY_{lm}(\hat{n})$. These are a set of functions that form an orthonormal and complete basis on the sphere:

$$\int d\Omega\ {}_sY^*_{l'm'}(\theta,\phi)\ {}_sY_{lm}(\theta,\phi) = \delta_{l'l}\delta_{m'm}, \tag{3.24}$$

$$\sum_{l,m}\ {}_sY^*_{lm}(\theta,\phi)\ {}_sY_{lm}(\theta',\phi') = \delta(\phi-\phi')\delta(\cos\theta - \cos\theta'). \tag{3.25}$$

The parity relation for these functions is

$${}_sY_{lm} \to (-1)^l\ {}_{-s}Y_{lm}. \tag{3.26}$$

There also exists a pair of raising $\eth$ and lowering $\bar{\eth}$ operators, respectively, which raise and lower the spin-weight of a function as

$$(\eth\ {}_sf)' = e^{-i(s+1)\psi}(\eth\ {}_sf), \tag{3.27}$$

$$(\bar{\eth}\ {}_sf)' = e^{-i(s-1)\psi}(\bar{\eth}\ {}_sf), \tag{3.28}$$

where the prime refers to a quantity in a frame rotated ψ from the original frame. The explicit form of these operators is

$$\eth\ {}_sf(\theta,\phi) = -\sin^s(\theta)\left[\partial_\theta + \frac{i}{\sin\theta}\partial_\phi\right]\sin^{-s}(\theta)\ {}_sf(\theta,\phi), \tag{3.29}$$

$$\bar{\eth}\ {}_sf(\theta,\phi) = -\sin^{-s}(\theta)\left[\partial_\theta - \frac{i}{\sin\theta}\partial_\phi\right]\sin^{s}(\theta)\ {}_sf(\theta,\phi). \tag{3.30}$$

Using the raising and lowering operators, one can relate the spin-s spherical harmonics and the usual spherical harmonics by

$${}_sY_{lm} = \left[\frac{(l-s)!}{(l+s)!}\right]^{1/2}\eth^s\ Y_{lm}, \tag{3.31}$$

for $0 \leq s \leq l$, and

$${}_sY_{lm} = \left[\frac{(l+s)!}{(l-s)!}\right]^{1/2}(-1)^s\bar{\eth}^{-s}\ Y_{lm}, \tag{3.32}$$

for $-l \leq s \leq 0$. Hence, using these, we can obtain (see Lin and Wandelt, 2006)

$${}_{\pm2}Y_{lm} = \left[\frac{(l-s)!}{(l+s)!}\right]^{1/2}\left[\partial_\theta^2 - \cot\theta\ \partial_\theta \pm \frac{2i}{\sin\theta}(\partial_\theta - \cot\theta)\partial_\phi - \frac{1}{\sin^2\theta}\partial_\phi^2\right]Y_{lm}. \tag{3.33}$$

Other useful properties of the spin-weighted spherical harmonics include

$$\begin{aligned}
{}_sY^*_{lm} &= (-1)^{m+s}\ {}_{-s}Y_{l-m},\\
\eth\ {}_sY_{lm} &= [(l-s)(l+s+1)]^{1/2}\ {}_{s+1}Y_{lm},\\
\bar{\eth}\ {}_sY_{lm} &= -[(l+s)(l-s+1)]^{1/2}\ {}_{s-1}Y_{lm},\\
\bar{\eth}\,\eth\ {}_sY_{lm} &= -(l-s)(l+s+1)\ {}_sY_{lm}.
\end{aligned} \tag{3.34}$$

We now can expand the polarization (3.23) and its complex conjugate by the spin-2 spherical harmonics (3.33) in the form

$$(Q \pm iU)(\hat{n}) = \sum_{lm}(E_{lm} \pm iB_{lm})\ {}_{\pm2}Y_{lm}(\hat{n}), \tag{3.35}$$

where the real and imaginary parts of the expansion components have been separated since Q and U are real parameters. With the help of the spin raising and lowering operators, together

with Eq. (3.34), we obtain

$$\begin{aligned}
\eth^{\,2}(Q-iU)(\hat{n}) &= \sum_{lm}(E_{lm}-iB_{lm})\,\eth\,\eth\;{}_{-2}Y_{lm}(\hat{n}) \\
&= \sum_{lm}(E_{lm}-iB_{lm})\,\eth\left(\sqrt{(l+2)(l-1)}^{\,2}\;{}_{-1}Y_{lm}(\hat{n})\right) \\
&= \sum_{lm}\left[\frac{(l+2)!}{(l-2)!}\right]^{1/2}(E_{lm}-iB_{lm})\;Y_{lm}(\hat{n}), \\
\bar{\eth}^{\,2}(Q+iU)(\hat{n}) &= \sum_{lm}\left[\frac{(l+2)!}{(l-2)!}\right]^{1/2}(E_{lm}+iB_{lm})\;Y_{lm}(\hat{n}).
\end{aligned} \tag{3.36}$$

From these, the expansion coefficients can be found by using the orthonormality of spin-0 & -2 spherical harmonics:

$$\begin{aligned}
E_{lm}+iB_{lm} &= \int d\Omega\;{}_{2}Y^{*}_{lm}(\hat{n})(Q+iU)(\hat{n}) \\
&= \left[\frac{(l-2)!}{(l+2)!}\right]^{1/2}\int d\Omega Y^{*}_{lm}(\hat{n})\,\bar{\eth}^{\,2}(Q+iU)(\hat{n}), \\
E_{lm}-iB_{lm} &= \int d\Omega\;{}_{-2}Y^{*}_{lm}(\hat{n})(Q-iU)(\hat{n}) \\
&= \left[\frac{(l-2)!}{(l+2)!}\right]^{1/2}\int d\Omega Y^{*}_{lm}(\hat{n})\,\eth^{\,2}(Q-iU)(\hat{n}).
\end{aligned} \tag{3.37}$$

From Eqs. (3.37) it is clear that E_{lm} and B_{lm} are scalar spin-0 quantities. Furthermore, we can write these in the form

$$\begin{aligned}
E_{lm} &= \frac{1}{2}\left[\frac{(l-2)!}{(l+2)!}\right]^{1/2}\int d\Omega Y^{*}_{lm}(\hat{n})\Big(\bar{\eth}^{\,2}(Q+iU)(\hat{n})+\eth^{\,2}(Q-iU)(\hat{n})\Big), \\
B_{lm} &= \frac{-i}{2}\left[\frac{(l-2)!}{(l+2)!}\right]^{1/2}\int d\Omega Y^{*}_{lm}(\hat{n})\Big(\bar{\eth}^{\,2}(Q+iU)(\hat{n})-\eth^{\,2}(Q-iU)(\hat{n})\Big).
\end{aligned} \tag{3.38}$$

Using the above equations it is now easy to show that E_{lm} and B_{lm} have distinct parities. Let us consider the space inversion where we reverse the sign of the x-coordinate, but leave the other coordinates unchanged. In spherical notation this amounts to $r \to r$, $\theta \to \theta$ and $\phi \to \phi + \pi$ (therefore $\partial_{\theta'} = \partial_\theta$ and $\partial_{\phi'} = -\partial_\phi$). Let $\hat{n} = (\theta, \phi)$ and $\hat{n}' = (\theta', \phi')$ refer to the same physical direction in the original and space-inversed frames, respectively. From the definition of the Stokes parameters, Eqs. (3.18) and (3.19), we therefore expect that under this transformation $Q'(\hat{n}') = Q(\hat{n})$ and $U'(\hat{n}') = -U(\hat{n})$. So Q has even parity, while U has odd parity. Now using Eqs. (3.29) and (3.30) and considering that $(Q+iU)'(\hat{n}') = (Q-iU)(\hat{n})$, we have

$$\begin{aligned}
\bar{\eth}\,(Q+iU)'(\hat{n}') &= \frac{-1}{\sin^2\theta'}\Big(\partial_{\theta'}-\frac{i}{\sin\theta'}\partial_{\phi'}\Big)\sin^2\theta'(Q+iU)'(\hat{n}') \\
&= -\sin^{-2}\theta\Big(\partial_\theta+\frac{i}{\sin\theta}\partial_\phi\Big)\sin^2\theta(Q-iU)(\hat{n}) \\
&= \eth\,(Q-iU)(\hat{n}),
\end{aligned} \tag{3.39}$$

and likewise

$$\bar{\eth}^{\,2}(Q+iU)'(\hat{n}') = \eth^{\,2}(Q-iU)(\hat{n}). \tag{3.40}$$

Substituting Eq. (3.40) into Eq. (3.37), we will have $E'_{lm} = E_{lm}$ and $B'_{lm} = -B_{lm}$. Therefore E and B have even and odd parities respectively. It is useful to define two rotationally invariant quantities in real space. Using Eqs. (3.36), these are defined by

$$\begin{aligned}
\tilde{E}(\hat{n}) &\equiv \frac{1}{2}\Big[\bar{\eth}^{\,2}(Q+iU) + \eth^{\,2}(Q-iU)\Big] \\
&= \sum_{lm}\left[\frac{(l+2)!}{(l-2)!}\right]^{1/2} E_{lm}Y_{lm}(\hat{n}) = \sum_{lm}\tilde{E}_{lm}Y_{lm}(\hat{n}), \\
\tilde{B}(\hat{n}) &\equiv -\frac{i}{2}\Big[\bar{\eth}^{\,2}(Q+iU) - \eth^{\,2}(Q-iU)\Big] \\
&= \sum_{lm}\left[\frac{(l+2)!}{(l-2)!}\right]^{1/2} B_{lm}Y_{lm}(\hat{n}) = \sum_{lm}\tilde{B}_{lm}Y_{lm}(\hat{n}),
\end{aligned} \tag{3.41}$$

where $\tilde{E}_{lm} = \left[\frac{(l+2)!}{(l-2)!}\right]^{1/2} E_{lm}$ and $\tilde{B}_{lm} = \left[\frac{(l+2)!}{(l-2)!}\right]^{1/2} B_{lm}$. Under parity transformation the pattern of $E(\hat{n})$ on the sky remains the same, while that of $B(\hat{n})$ changes sign. Thus E and B can be thought of as the electric (i.e. 'gradient' or curl-free) and magnetic (i.e. 'curl' or divergence-free) modes of the polarization function. Typical E or B type polarization patterns are shown in figure 3.5. It has become conventional to express the polarization anisotropies in terms of E and B modes which do not depend on the coordinate system, rather than the Stokes parameters Q and U which do.

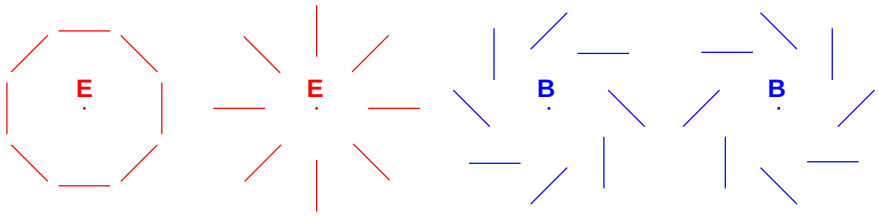

Figure 3.5: Typical E or B type polarization patterns. The electric and magnetic modes of the polarization are distinguished by their behavior under reflection. (Figure from Kaplan et al., 2003)

3.3 The Angular Power Spectra

To characterize the statistics of the CMB perturbations we introduce the power spectra of temperature and polarization anisotropies. Since the primordial perturbations are expected to be Gaussian to a high degree of accuracy and since linear theory is the highly accurate approximation to the evolution of these perturbations until last scattering, the small anisotropies of the temperature and polarization in the CMB are expected to follow Gaussian statistics. Therefore the expansion components in Eqs. (3.14) and (3.35) each constitutes independent Gaussian random variables with

$$\langle T_{\ell m}\rangle = \langle E_{\ell m}\rangle = \langle B_{\ell m}\rangle = 0, \tag{3.42}$$

where the statistical isotropy implies that for Gaussian distributions the correlation functions contain all the information

$$\begin{aligned}
\langle T_{\ell m} T^*_{\ell' m'} \rangle &= \delta_{\ell\ell'}\delta_{mm'} C_\ell^{TT}, \\
\langle T_{\ell m} E^*_{\ell' m'} \rangle &= \delta_{\ell\ell'}\delta_{mm'} C_\ell^{TE}, \\
\langle E_{\ell m} E^*_{\ell' m'} \rangle &= \delta_{\ell\ell'}\delta_{mm'} C_\ell^{EE}, \\
\langle B_{\ell m} B^*_{\ell' m'} \rangle &= \delta_{\ell\ell'}\delta_{mm'} C_\ell^{BB}, \\
\langle B_{\ell m} E^*_{\ell' m'} \rangle &= \langle B_{\ell m} T^*_{\ell' m'} \rangle = 0.
\end{aligned} \tag{3.43}$$

Here δ is the Kronecker symbol and the angle brackets denote ensemble average over all realizations of the sky. In this way the ensemble average of the two-point correlations corresponds to the power spectra specified by the perturbation theory, i.e. $C_\ell \equiv C_\ell^{\rm th}$. The B pattern changes sign under parity transformation, so cross-correlations between B and T or E vanish.

Figure 3.6 shows the CMB temperature and polarization power spectra. These have been generated by the CMBFAST code (Seljak and Zaldarriaga, 1996) which numerically solves the perturbation equations introduced in chapter 2. As we saw in §3.1, the CMB polarization signal primarily arises due the Thomson scattering of the photon quadrupoles during recombination. However, there are other processes which can alter the polarization after the last scattering. These are mainly the process of re-ionization of the universe and the weak gravitational lensing of the microwave background photons. At the time when the first stars and quasars were formed the universe became ionized again, in which case the condition for Thomson scattering was satisfied. During this epoch more polarization is produced in the CMB which led to an increase in the amplitude of both E and B modes. This effect is observed in the Cosmic Microwave Background as an enhancement in the polarization signal on very large scales ($l \approx 20$) because the re-ionization had to happen and end at rather low redshifts ($7 < z < 11.3$). On small scales, the polarization signal is affected by the weak gravitational lensing, which is due to the deflection of CMB photons by the gravitational potential of the large-scale structures. Weak lensing converts some E-mode polarization into B-mode since it produces curls in the polarization patterns on the sky. The weak lensing also introduces small effects in the acoustic peaks of the TT and EE spectra, which are not very considerable. Therefore, the lensing signal in the B mode can especially provide useful information about the large-scale structures, which can be used to constrain cosmological parameters such as the neutrino mass.

The decomposition of the polarization field into E and B modes is also useful for distinguishing between different sources of the anisotropies. The CMB fluctuations originate from the density and metric perturbations on the last scattering surface. The metric fluctuations are classified as scalar, vector, and tensor perturbations depending on their transformation properties under rotation. Scalar perturbations comprise the total density fluctuations. Vector contributions arise from rotational fields in the plasma which get damped by the expansion of the universe. Tensor fluctuations are primordial gravity waves which are predicted in the inflationary scenario. The factor which distinguishes the contribution from different types of the

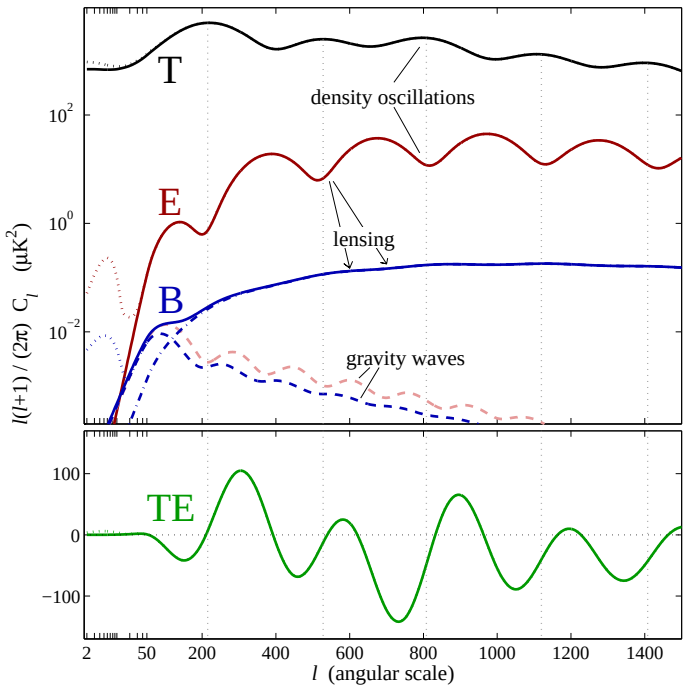

Figure 3.6: Power spectra of the temperature and polarization of the CMB. The dashed lines are the gravitational waves contribution to E and B mode polarization with tensor to scalar ratio $r = 0.1$. The dotted lines show the enhancement due to reionization. The dashed-dotted line represents the effect of the gravitational lensing in B-mode polarization. The bottom plot is the cross-correlation of the temperature anisotropies and E mode polarization. (Figure from Carlstrom et al., 2003)

perturbations is their imprints on the polarization patterns (see Hu and White, 1997). Scalar perturbations are curl-free, so can only generate the gradient component of the polarization, i.e. E mode; However, tensor perturbations can generate both E and B polarization modes. In this way, E-mode can be produced by both scalar and tensor perturbations, while large scale B-mode is primarily produced only by gravitational waves at the last scattering. Therefore, since the tensor perturbations are subdominant in the temperature spectrum, the best way to detect them is to measure them in the polarization modes, especially in B mode which is small and does not have primary contributions from scalar fluctuations. In this way the relative amplitude of the BB polarization spectrum on large scales can be a direct measure of the ratio of the tensor to scalar perturbations (see §2.1.5), and therefore can put important constraints on the energy scale of the inflation.

Since the temperature and polarization of the CMB are Gaussian, the real and imaginary parts of the complex coefficients $a^X_{\ell m}$ (for $X = T, E, B$) should also be Gaussianly-distributed

with mean zero and variance $C_\ell/2$,[2] i.e. their probability density function is given by

$$P(a_{\ell m,o}) = \frac{\exp[-a_{\ell m,o}^2/C_\ell]}{\sqrt{\pi C_\ell}}, \tag{3.44}$$

where o refers to either real or imaginary components. One can construct simple statistical estimators for the power spectra (3.43) from maps of the microwave background temperature and polarization. An unbiased estimator of the power spectrum is given by

$$\hat{C}_\ell = \frac{1}{2\ell+1}\sum_{m=-\ell}^{\ell} a_{\ell m}a_{\ell m}^*. \tag{3.45}$$

Recall that if X_i are n independent Gaussian variables with zero mean and variance σ^2, the quantity $V \equiv \sum_i^n X_i^2/\sigma^2$ has a chi-square distribution with n degrees of freedom, i.e. the probability density function of V is

$$P(V) = \frac{V^{(n-2)/2}e^{-V/2}}{2^{(n/2)}\Gamma(n/2)}. \tag{3.46}$$

Therefore, since the distribution of $a_{\ell m}$ is assumed to be Gaussian, the estimates given by Eq. (3.45) are χ_ν^2-distributed with $\nu = 2\ell+1$ degrees of freedom. It is easy to verify that substituting Eq. (3.43) results in the mean value $\langle\hat{C}_\ell\rangle = C_\ell$ for the distribution.

Note that Eq. (3.45) means that the process of power spectrum estimation is indeed variance estimation. It also implies that to construct C_ℓ we average over only $2\ell+1$ independent samples from a Gaussian distribution. This comes from the fact that the number of samplings that we can have on different angular scales on the sky is finite, a phenomenon which is called *cosmic variance*. This statistical uncertainty causes a fractional error in the calculation of C_ℓ which is proportional to $\sqrt{1/(2\ell+1)}$. To verify this factor we can calculate the standard deviation of the C_ℓ. For a full and uniform sky coverage C_ℓ's are approximately independent, therefore they should have a diagonal covariance matrix. The sampling distribution of C_ℓ is close to a Gaussian with mean square deviation

$$\begin{aligned}
\langle(\hat{C}_\ell - C_\ell)^2\rangle &= \langle\hat{C}_\ell\hat{C}_\ell\rangle - C_\ell^2 \\
&= \frac{1}{(2\ell+1)^2}\Big[\sum_{mm'} 2\langle a_{\ell m}a_{\ell m'}^*\rangle\langle a_{\ell m}^* a_{\ell m'}\rangle \\
&\quad + \langle a_{\ell m}a_{\ell m}^*\rangle\langle a_{\ell m'}a_{\ell m'}^*\rangle\Big] - C_\ell^2 \\
&= \frac{2C_\ell^2}{2\ell+1},
\end{aligned} \tag{3.47}$$

where we have used Eqs. (3.43). Note that to arrive to this relationship we have utilized the Wick's theorem for Gaussian fields

$$\langle x_1x_2x_3x_4\rangle = \langle x_1x_2\rangle\langle x_3x_4\rangle + \langle x_1x_3\rangle\langle x_2x_4\rangle + \langle x_1x_4\rangle\langle x_2x_3\rangle, \tag{3.48}$$

[2]Note that the covariance matrix of $a_{\ell m}$ is diagonal only in full sky provided that the condition of rotational invariance is also satisfied, i.e. $\langle a_{\ell_1 m_1}a_{\ell_2 m_2}^*\rangle = \sum_{m_1' m_2'}\langle a_{\ell_1 m_1'}a_{\ell_2 m_2'}^*\rangle\mathcal{D}^{\ell_1}_{m_1' m_1}\mathcal{D}^{\ell_2 *}_{m_2' m_2}$.

where x_i are normal random variables. In Eq. (3.47) we have also used the fact that $a^*_{\ell m} = (-1)^m a_{\ell -m}$ which comes from considering the reality of T, Q and U in Eqs. (3.14) and (3.35) and the first of the Eqs. (3.34). Therefore equation (3.47) implies that there is a fractional uncertainty in the measurement of the C_ℓ due to the sampling variance (Knox, 1995)

$$\frac{\sqrt{\langle (\hat{C}_\ell - C_\ell)^2 \rangle}}{C_\ell} = \sqrt{\frac{2}{2\ell + 1}}. \tag{3.49}$$

Note that this uncertainty cannot be improved by designing new survey strategies since it is intrinsic to the one-sky problem.

3.4 QUaD Polarization Experiment

QUaD[3] was a CMB telescope experiment operated from the south pole which provided polarization data at high significance. The choice of the south pole is ideally suited for CMB experiments mostly due to the high elevation and low temperature which freezes out much of the water vapor in the atmosphere, hence reducing the atmospheric emission and absorption at microwave frequencies. The QUaD instrument was a bolometric polarimeter which measured the microwave background in two frequency channels at 100GHz and 150GHz over three Austral winter seasons. The main body of the instrument consisted of a 2.6m radio telescope, a secondary optical mirror which was supported by a foam cone, and the receiver which consisted of a focal plane on which polarization-sensitive bolometers (PSB) were positioned. The choice of the foam cone was to support the axial symmetry of the instrument and to keep the temperature inside the cone warm at about $15°C$, hence protecting the components from icing and contraction issues. The telescope was installed on a mount originally used for DASI, which allowed the entire optics and the instrument to rotate around the line of sight. The instrument was further isolated by a ground-shield to protect from wind loading and excess power coming from photons reflected on the ground. For more details about the instrument see QUaD collaboration: J. Hinderks et al. (2008).

Figure 3.10 shows the QUaD detector including the focal plane and the bolometers. To measure the anisotropies the focal plane was kept at low temperatures about $250mK$. The array of 31 orthogonal PSBs which were positioned on the focal plane consisted of nineteen polarimeters operating at 150GHz and the remaining twelve operating at 100GHz. The intensity of the incoming light is proportional to the sum of the two voltages from each PSB pair. Subtracting the two voltages results in a signal which is proportional to a linear combination of the Stokes' parameters Q and U. To obtain each individual linear Stokes parameter a point in the sky has to be observed at two different angles. This corresponds to the hexagonal configuration for the PSBs which is seen in Figure 3.9. The time ordered data from each PSB and the details of the orientation of the instrument were saved and transfered through satellite

[3]QUaD stands for "QUEST and DASI". In turn, QUEST is "Q & U Extragalactic Survey Telescope". The two experiments merged to become QUaD in 2003.

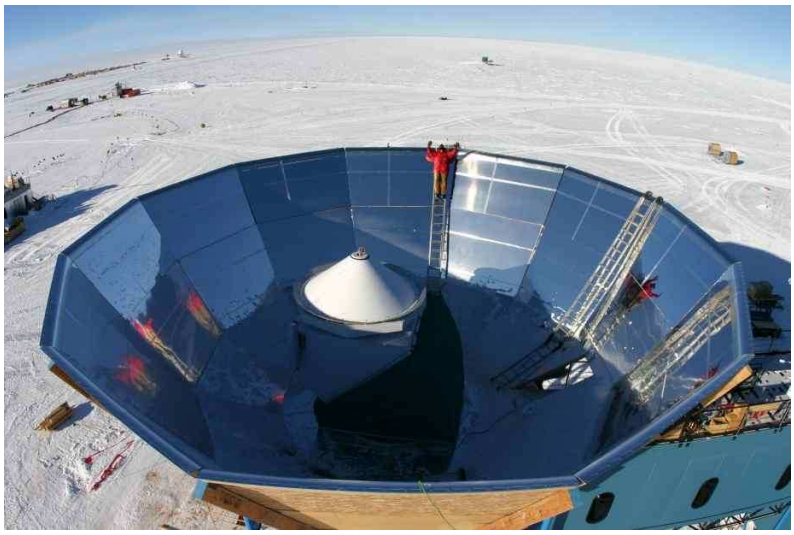

Figure 3.7: The QUaD telescope inside its ground shield at the south pole. (Figure from QUaD collaboration: J. Hinderks et al., 2008)

daily. Out of 289 days of observations, data from only 143 days was used to construct the CMB information - the rest of the data was discarded due to very bad weather conditions, high level of moon contamination or instrumental problems. This data was later calibrated and processed

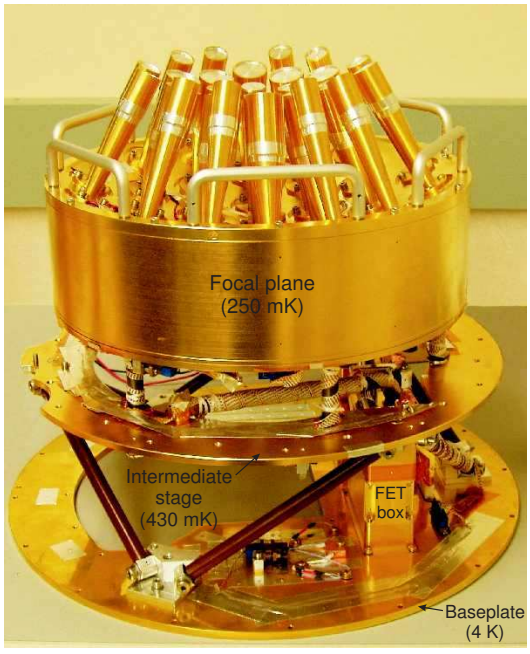

Figure 3.8: The QUaD receiver, including the orthogonal PSB feeds which are installed on the focal plane at very low temperatures. (Figure from QUaD collaboration: J. Hinderks et al., 2008)

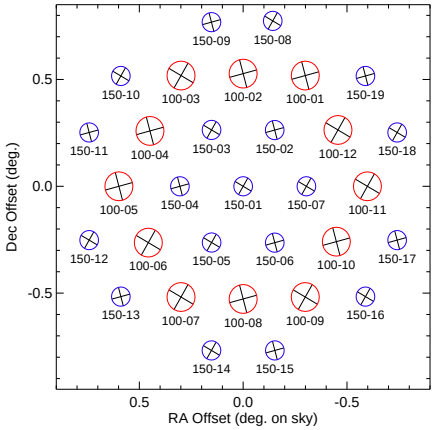

Figure 3.9: The arrangement and orientation of the of the PSBs in the QUaD receiver. (Figure from QUaD collaboration: J. Hinderks et al., 2008)

to construct temperature and polarization maps on the sky.

The QUaD PSBs which detect the optical power are similar to the ones employed in the B2K experiment (Masi et al., 2006). They consist of silicon-nitrite micromesh absorbers which are metalized only in one direction. This allows the absorber to weakly couple to one linear component of the incoming radiation polarization. The whole absorber membrane is then connected to a fixed heat sink and the temperature gradients are measured by the change in thermal conductivity. The thickness of metalization and the circular geometry of the absorber have been designed to achieve maximum impedance-matching to the coupling structure. To detect

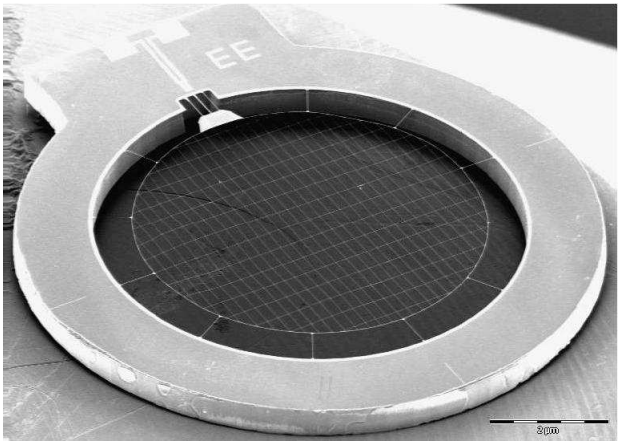

Figure 3.10: The Polarization-Sensitive Bolometers employed on QUaD. The metalized grids run from the upper left to the lower righ, and the perpendicular non-metalized grids are only for mechanical support. The thermistor on the upper left of the image measures the temperature. (Figure from QUaD collaboration: J. Hinderks et al., 2008)

both the Stokes parameters Q and U, two co-axial orthogonally-oriented PSBs are mounted in the center of a corrugated feed horn with a small separation between each other. Inside the cylindrical feeds a standing wave is established with a wavelength twice the length of the cavity. Therefore the PSBs which are located at the center can detect the maximum electric field of the incoming 100GHz and 150GHz frequency radiations depending on the length of the feed cavities. (see Jones et al. 2003 for more discussion on the design of the PSBs)

The QUaD survey area which covers about 100° squared of the sky is shown in white in Figure 3.11. The color image shows the FDS model of dust emission intensity at 150GHz. The region of the sky covered by QUaD was chosen to be free of significant dust and galaxy synchrotron contamination, although the temperature in this region is overall larger than the average CMB temperature. QUaD further detected several discrete sources, such as moon, Cen A, and a part of the galactic plane which can be used in CMB foreground studies. The point sources in QUaD survey have been useful in verifying the instrument pointing offsets of the PSB feeds and determining the beam parameters. Of particular interest is the quasar PKS 0537-441 which was observed by QUaD and used to characterize the beam uncertainty which resulted in $5.0'$ at 100GHz and $3.5'$ at 150GHz (see QUaD collaboration: J. Hinderks et al., 2008). For absolute calibration, QUaD cross-correlates the maps with the temperature maps of the Boomerang 2003 experiment (Masi et al., 2006), which results in an estimate of 5% calibration uncertainty in temperature units (see QUaD collaboration: C. Pryke et al., 2008).

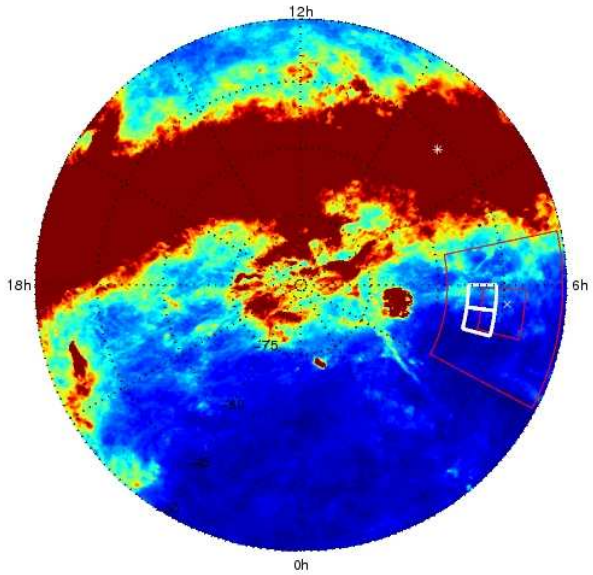

Figure 3.11: Location of QUaD lead-trail fields with respect to B03 deep and shallow regions on the FDS model image of galaxy dust emission. The white asterisk and cross represent the RCW38 galactic region and the quasar PKS 0537-441 respectively. (Figure from QUaD collaboration: C. Pryke et al., 2008)

QUaD observation strategy is based on a daily azimuth-scanning of a lead-trail field on the

sky. Every day of observation starts at the same local sidereal time and consists of two eight hour blocks, where the rest of the time is devoted to thermal stabilization of the instrument and calibration observations before and after each time block. Each hour of observation is equally dedicated to lead and trail scanning in two half-hours. During the first half-hour the telescope scans the lead field (centered at RA 5.25 h) in a set of ten half-scans back and forth over a 7.5 deg throw at constant elevation, where after each scan-set the telescope is stepped in declination by 0.02 deg. The same scanning procedure is repeated four times until the first half-hour is over, and then the pointing center moves to the trail field centered at RA 5.75 h and the exact same scanning strategy consisted of 40 half-scans is repeated. Since the scan pattern is the same on both lead and trail fields, any ground signal which is constant over the half-hours should be canceled by subtracting the lead and trail data. The lead-trail subtraction has been carried out for the second and third year QUaD to remove the significant ground pickups which are seen in the data (see QUaD collaboration: C. Pryke et al., 2008). However, an improved analysis by the QUaD collaboration: Brown et al., (in prep) is also aiming to remove the ground contamination by novel modeling of the ground template, which then results in a doubling of the covered sky area and also smaller error bars on the bandpowers.

After low level data processing and lead-trail field differencing, a third order polynomial is removed from each half-scan timestream to subtract off the bulk of atmospheric noise. Then the PSB signals are pair summed and pair differenced and co-added using the telescope pointing matrix. In co-adding the PSB signals, a weight function is applied to each half-scan to account for periods of bad weather condition. Then the pair sum data is used to produce the temperature maps, whereas the pair difference data is used with the detector angle information to construct the Stokes Q and U maps. As we will discuss later, under flat sky approximation, maps of E and B modes are then obtained by performing a rotation of the Stokes parameters in the Fourier space. The QUaD power spectra have been estimated using a standard Monte Carlo bandpower estimation analysis. Before constructing the power spectra the temperature and polarization maps are multiplied by the inverse variance apodization masks. Simulations of pure noise timestream data have been generated to construct the power spectrum for noise. Signal only maps have been produced to estimate the correction necessary for the polynomial filtering applied to the time ordered data. Signal plus noise simulations have been produced to construct the bandpower covariance matrices needed for parameter estimation analysis. For power spectrum estimation with QUaD data two separate pipelines exist which we briefly review here:

The first pipeline is based on a Master technique proposed by Hivon et al. (2002) implemented for an analytical curved sky pseudo-C_ℓ method (Brown et al., 2005). The method calculates the QUaD pseudo-C_ℓ's on the cut sky, $\tilde{C}_\ell$, using the HEALpix package, and estimates the full-sky bandpowers using

$$P_b = \sum_{b'} M^{-1}_{bb'} \sum_{\ell} P_{b'\ell} \Big(\tilde{C}_\ell - \langle \tilde{N}_\ell \rangle_{MC} \Big). \tag{3.50}$$

Here, $\langle \tilde{N}_\ell \rangle_{MC}$ is the noise power spectrum, $P_{b\ell}$ defines the binning procedure, and $M_{bb'}$ corresponds to the temperature and polarization binned mode-mode coupling matrices defined in Brown et al. (2005) which contain information about the survey geometry. We will properly study the pseudo-C_ℓ methods in chapter 5. The bandpower covariance matrices which also give the bandpower error bars are then estimated from Monte Carlo simulations of noise plus signal simulations.

The second pipeline employs a flat sky power spectrum estimation technique, and the mode mixing effects are estimated numerically. In flat sky the bandpowers are estimated by multiplying maps of Q and U Stokes' parameters by the QUaD apodization masks and transferring the results to the Fourier space in which the E and B modes can be obtained by

$$E = Q\cos 2\phi + U \sin 2\phi, \tag{3.51}$$

$$B = -Q\sin 2\phi + U \cos 2\phi, \tag{3.52}$$

where ϕ is the polar angle in the Fourier plane. Then the auto and cross spectra are obtained from the mean of the product of the modes within and between each annular bin. The noise power spectra are calculated from flat sky noise-only simulations and subtracted from the real spectra. The pipeline also corrects for the effect of the survey geometry by convolving each annulus with the Fourier transform of the apodization masks. In this case the power spectrum of the convolved annulus gives an estimate of the bandpower window function which encapsulates the information about contribution of each multipole to each bandpower. For polarization this method yields two extra bandpower window functions accounting for the mixing between EE and BB spectra. In this pipeline the filtering and beam correction is carried out by dividing the spectra by the suppression factors which result from the convolution by the beam and apodization masks. (For details see QUaD collaboration: C. Pryke et al., 2008)

The second and third season data from QUaD has been subjected to extensive processing by the second power spectrum estimation pipeline. A series of jackknife tests have shown that the level of systematic contamination is insignificant above the instrumental noise. These tests involve splitting the timestream data into two equal halves which approximately represent the same signal, and then generating maps from these data splits. If no source of contamination is present in the polarized maps constructed from either of the subsets, the difference of the two maps should only contain noise due to the finite size of the data. Thus, the power spectra constructed from the difference maps should be generally consistent with zero. The jackknife tests have been carried out for four data split strategies, namely the deck angle jackknife, scan direction jackknife, split season jackknife and focal plane jackknife, and have been proven that the data is free of significant systematics. A frequency difference test has also shown that the foreground contamination should be negligible. This is done in the same way as jackknife tests by subtracting the 100GHz and 150GHz frequency maps and constructing their power spectra. However, it particularly points at foreground polarized contamination since the CMB signal is itself independent of the frequency, whereas the atmospheric foregrounds are frequency-dependent. For details about the data processing and power spectrum estimation see QUaD

collaboration: C. Pryke et al. (2008).

The temperature and polarization power spectra from QUaD data have been calculated for 100GHz, 150GHz and cross-frequency, and have been combined in one set of spectra shown in Figure 3.12. These bandpowers have been estimated at 23 multipoles with bin spacing $\Delta\ell = 81$, ranging from $\ell = 164$ to the high multipole $\ell = 2026$. For the first time QUaD has detected with high precision multiple acoustic oscillations in the E-mode polarization of the CMB, which also seem to be out of phase with the temperature data and serve as another evidence for the standard model. The fact that the upper limits on the BB spectrum are very tight indicates that the systematics which can give rise to false signal in polarization have been contained. QUaD has also provided a measurement of the TT spectrum to a precision which it was not originally aimed for. The TT spectrum makes it possible to probe the consistency of QUaD with other CMB data sets, since most of the CMB experiments have measured the temperature. The polarization data is also significant enough to be used independently for parameter estimation. In the next chapter we will use the QUaD combined TT, TE, EE and BB spectra to obtain constraints on the cosmological parameters.

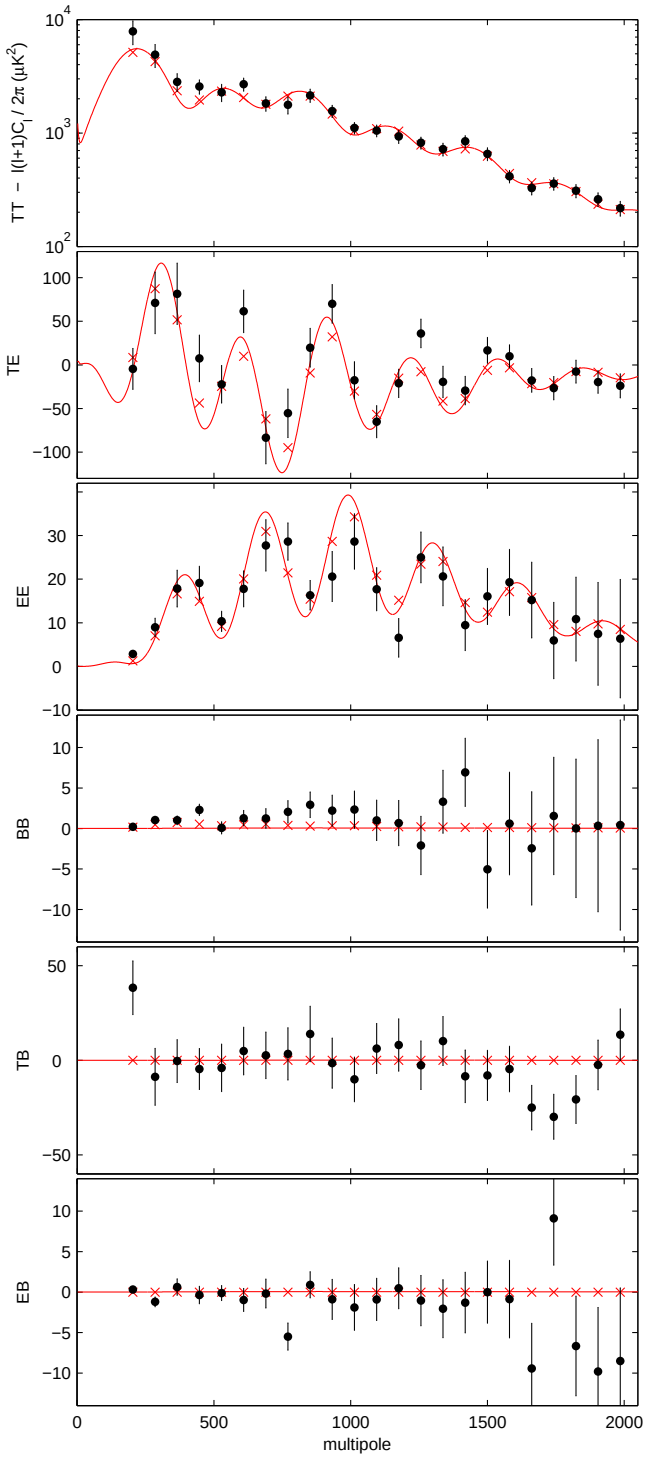

Figure 3.12: The bandpower spectra measured from the QUaD experiment data. The crosses are the QUaD bandpowers expected from the ΛCDM model which is shown as red lines. (Figure from QUaD collaboration: C. Pryke et al., 2008)

Chapter 4

Parameter Estimation from QUaD

The significance of the measurements of the CMB temperature and polarization is in their ability in determining the cosmological parameters of the standard model of cosmology. Today the CMB temperature data has provided strong evidence in favor of a ΛCDM model seeded by primordial scale-invariant adiabatic perturbations. (Spergel et al., 2003) We now have powerful constraints on the rate of the expansion of the universe, the large-scale geometry of the universe and the mean density of baryons and dark matter, the optical depth to reionization as well as the spectral index and the amplitude of the primordial scalar fluctuations set by inflation. (Dunkley et al., 2008) Despite this information we are still lacking precise constraints on the level of tensor and isocurvature fluctuations in the primordial perturbations, the density of massive neutrinos and the equation of state of the dark energy.

Observations of the linearly polarized components of the CMB will be very important for parameter estimation purposes. Since the local velocity fields giving rise to the E-mode polarization are linked to the density fields, which give rise to the temperature, full knowledge of the temperature field should be sufficient to predict the gross features of the E-mode polarization (see e.g. Jaffe, 2003). Therefore combination of the CMB temperature and polarization data can break the parameter degeneracies and provide powerful parameter constraints. In addition, information about large scale E-mode polarization is essential for gaining robust constraints on the optical depth to reionization. Furthermore a detection of primordial gravitational waves in the odd-parity B mode on large angular scales would provide a direct measurement of the energy scale of reionization. Nevertheless, our CMB database is still lacking information about the polarization power spectra down to arcminute scales, as we have for the temperature. B-mode polarization has not yet been detected and only upper limits have been determined.

The QUaD experiment is at the forefront of this small-scale polarization quest, and after

three years of observations has delivered by far the highest resolution E-mode spectrum and the tightest upper limits on the B-modes yet measured. This is a significant improvement over the first season of data results, previously reported by Ade et al. (2008). In particular, the sensitivity of QUaD has allowed us to see, for the first time, four acoustic oscillations in the E-mode spectrum and all significant oscillations in the TE spectrum to $\ell = 2000$. The overall consistency of peak phases and spacings between the temperature and QUaD EE data was shown in QUaD collaboration: C. Pryke et al. (2008). The obvious question asked here is, given this new information, how much extra insight into cosmology does the QUaD polarization and temperature spectra provide us?

In this chapter we concentrate on using the QUaD temperature and polarization power spectra alone to constrain the standard cosmological model. Based on the standard 6-parameter baseline model, we analyze the different contributions coming from each of the QUaD spectra. We also go beyond the basic 6-parameter model by combining the QUaD data with the WMAP fifth year data release and the SDSS Red Luminous Galaxies data in order to constrain the ratio of tensor to scalar modes, and any isocurvature contribution. Section 4.1 describes our parameter estimation methodology which is based on a Markov Chain Monte Carlo exploration of the likelihood space including the effect of beam and calibration marginalization. In section 4.2 we present our main results using only QUaD power spectra. In section 4.3 we combine QUaD with WMAP5 and SDSS data sets and go beyond our baseline model and analyze the tensor and isocurvature contributions. We finally present our conclusions in section 4.4.

4.1 Cosmological Parameter Estimation: Methodology

In this section we describe the data sets and the methodology chosen to estimate a set of cosmological parameters from the data. The core of the cosmological parameter estimation relies on the well-established Markov Chain Monte Carlo (MCMC) method which uses a Bayesian statistical approach to explore the likelihood shape. MCMC algorithms have become standard practice in CMB studies, and have been described in detail for example in (Lewis et al., 2002; Kosowsky et al., 2002; Dunkley et al., 2005). However, the detailed implementation can vary between analysis.

Here in subsection 4.1.1 we outline our parameter estimation method and the convergence and good-mixing criteria. In subsection 4.1.2 we justify our choice of the likelihood shape and present the QUaD data set. We then introduce the cosmological parameters and the priors in subsection 4.1.3. In subsection 4.1.4 we explain how we marginalize over the nuisance parameters (calibration and beam uncertainties). Then in subsection 4.1.5 we test our pipeline with simulations and verify that there is no bias in our analysis.

4.1.1 Markov Chain Monte Carlo

The Markov Chain Monte Carlo (MCMC) method (Metropolis et al., 1953; Gilks et al., 1995; Neal, 1993) became a mainstream tool for CMB cosmological parameter estimation studies as the dimensionality of the parameter space to explore increased, driven by higher and higher quality data. The MCMC is a method designed to efficiently explore an unknown Probability Distribution Function (PDF) by sequentially drawing samples from it according to a specific proposal probability function. The ensemble of these samples constitute a Markov Chain whose distribution corresponds to that of the unknown PDF.

We adopt the standard sampling method which is also described in Verde et al. (2003). This is essentially a uniform random walk process in the cosmological parameter space where the underlying PDF is the likelihood function of the data given the theory. The strategy is as follows:

1) Start with a set of cosmological parameters $\{\vec{p}_1\}$, compute the corresponding power spectra and C_l^{1th} and the likelihood function $\mathcal{L}_1 = \mathcal{L}(C_l|C_l^{1th})$ for that point.

2) Obtain a new set of cosmological parameters $\{\vec{p}_2\}$ by doing a random walk in parameter space. We draw the random step from Gaussian distributions with variance σ_i^2 where σ_i are the *step sizes*.

3) Compute the C_l^{2th} and its likelihood function $\mathcal{L}_2$ for the new set of the parameters $\{\vec{p}_2\}$.

4.a) If $\mathcal{L}_2/\mathcal{L}_1 \geq 1$, save the new set of cosmological parameters $\{\vec{p}_2\}$ as part of the chain, then substitute $\{\vec{p}_1\} \rightarrow \{\vec{p}_2\}$ and go to step 2.

4.b) If $\mathcal{L}_2/\mathcal{L}_1 < 1$, compare the ratio with a random number ε between 0 and 1. If $\varepsilon \geq \mathcal{L}_2/\mathcal{L}_1$, save the old set of parameters $\{\vec{p}_1\}$ as part of the chain, otherwise if $\varepsilon < \mathcal{L}_2/\mathcal{L}_1$ save the new set of cosmological parameters $\{\vec{p}_2\}$. Substitute $\{\vec{p}_1\} \rightarrow \{\vec{p}_2\}$ and go to step 2.

The MCMC is a stationary process in the sense that, after discarding a *burn-in* period, sampled Markov chains converge to stationary distributions. Therefore the outcome of the process does not usually depend on the initial point and the chain does not always converge to the maximum likelihood point. The choice of the step sizes is usually important since it sets how high or low the acceptance rate is. If the step sizes are too small, the acceptance rate may be too high, in which case the MCMC will cover only a small part of the underlying distribution, as a result we will have poor *mixing*. The same situation can happen when the step sizes are too large in which case the acceptance rate will be too small for good mixing to occur early enough. It is generally ideal to choose the step sizes to be of the order of the standard deviation of the PDF in order to gain complete mixing in a short period of time. We assess the convergence and the mixing of the MCMC chains by employing the Gelman and Rubin R-statistic (Gelman and Rubin, 1992). They advocate comparing several chain sequences drawn from different starting

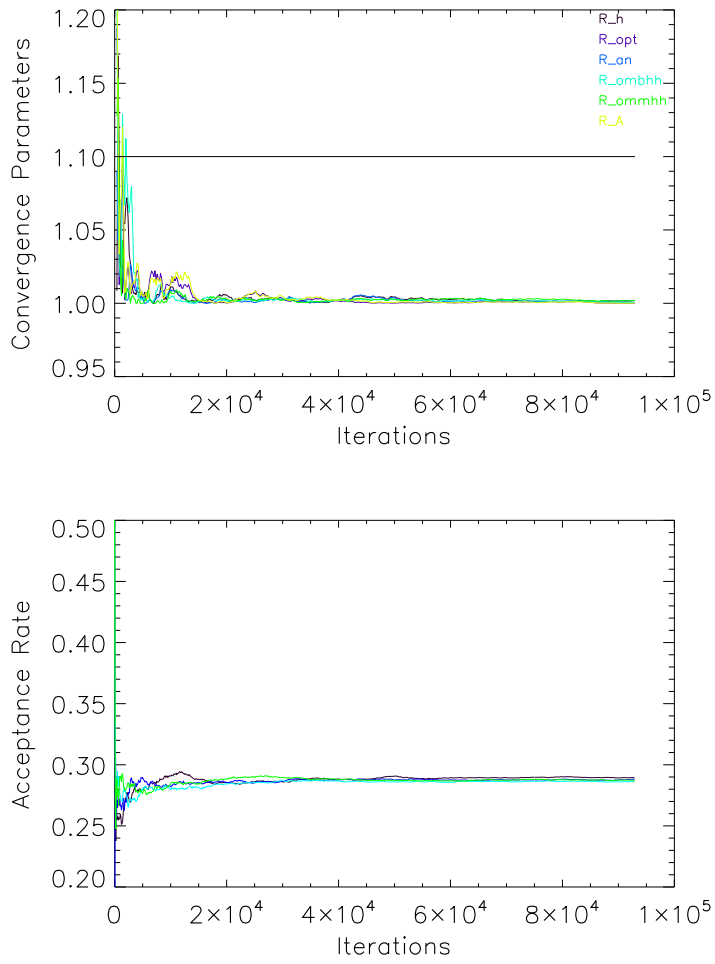

Figure 4.1: Convergence and mixing measures from the combined QUaD temperature and polarization constraints. *Top:* Gelma and Rubin statistic evolution with iteration step; *Bottom:* evolution of the acceptance rate for all the chains with iteration step.

points and checking to see that they are indistinguishable by monitoring the variance between the chains and within the chains. To describe the methodology consider M chains each of N elements: $\{y_i^j\}$ where $i = 1, \ldots, N$ and $j = 1, \ldots, M$ and y is a single parameter. We define the mean of the variance within each chain as

$$W = \frac{1}{M(N-1)} \sum_{ij} (y_i^j - \bar{y}^j)^2, \tag{4.1}$$

where $\bar{y}^j = \frac{1}{N} \sum_{i=1}^{N} y_i^j$ is the mean of each chain. We further define the variance between all chains as

$$B_n = \frac{1}{M-1} \sum_{j=1}^{M} (\bar{y}^j - \bar{y})^2, \tag{4.2}$$

where $\bar{y} = \frac{1}{NM}\sum_{ij=1}^{NM} y_i^j$ is the mean of the distribution. In this case, the R-quantity of Gelman & Rubin is defined by

$$R = \frac{B_n(1+\frac{1}{M}) + W(1-\frac{1}{N})}{W}. \tag{4.3}$$

In case the chains have converged, both the numerator and the denominator are unbiased estimates of the variance of the target distribution. However, if the chains have not converged, the numerator is an overestimate and the denominator is an underestimate of the overall variance. Therefore it is clear that R-quantities of the parameters should approach unity as we obtain better mixing between the chains. For the Gelman and Rubin parameter R, we choose the conservative condition for convergence of $R < 1.1$. We compare sets of 4 chains whose starting points are drawn from Gaussian distributions with mean equal to the fiducial WMAP 3yr bestfit model and variance equal to the square of the step sizes. As we will describe in §4.1.3, we optimize the MCMC so that the Markov chains converge in a few thousands of steps. We generate chains of around 100 000 steps long, of which we use at least 80 000 steps after cutting the burn-in and convergence period. Figure 4.1 shows the evolution of the R-parameter and the rate of convergence of the 4 chains for MCMC with QUaD temperature and polarization power spectra. We see that after some time the acceptance rates settle and the convergence parameters remain close to unity.

When we have a fair sample of the underlying distribution, the MCMC method trivializes marginalization to a simple projection of the points of the MCMC chain. The mean marginalized value of each parameter will therefore be called "the mean Best-fit model". Uncertainties on parameter values are indicated by quoting the 68% Confidence Limits (CL) of the 1-D marginalized distributions and 95% CL upper limits when the distribution is one-tailed (when the 68% CL hits the boundary on one end of the distribution). Assuming Gaussian distributions, we shall also plot 2-D marginalized parameter distributions with 68% and 95% CL's estimated from $\Delta \ln L = -2.3$ and -6.17 from the peak values. We also quote χ^2 values corresponding to our best fit model, and the Probability To Exceed (PTE), $P(>\chi^2|\nu)$, which gives the random probability to have found the measured value of χ^2 or worse by chance, for ν degrees of freedom.

4.1.2 The Likelihood and Data Set

The majority of MCMC applications are oriented towards Bayesian inference. Having made a measurement of the data-set, d, and given the prior distribution, $P(p)$, which contains all the information about the model parameters, p, Bayes' theorem updates this prior knowledge of the model to the so-called posterior distribution of p given the data d, which is defined as

$$P(p\,|\,d) \propto P(d\,|\,p)P(p). \tag{4.4}$$

$P(d\,|\,p)$ is called the likelihood of the data, d, conditional on the model parameters, p. The normalization factor in this equation is called the evidence $P(d) = \int P(d\,|\,p)P(p)dp$ which is independent of the model parameters. Our MCMC approach samples from the posterior PDF

where the data, d, consists of a vector of cosmological data and p corresponds to a vector of cosmological parameters. In our case, we take the data to be the set of observed CMB bandpower spectra $\hat{C}_b$ within a given range of multipoles. We shall need a model for $P(d\,|\,p)$, i.e. $P(\hat{C}_b\,|\,C_b^{\rm th}(p))$, and a cosmological model and a set of priors on the model parameters $P(p)$.

It is often assumed that the likelihood distribution for the difference between the measured bandpower C_ℓ's and the theoretical estimates $P(\hat{C}_b \mid C_b^{\rm th}(p))$ is Gaussian. However even if the CMB fluctuations are indeed nearly Gaussianly distributed, as predicted by the standard inflationary models, if the power spectra are binned and measured on a cut-sky, one is to expect deviations from Gaussianity, in particularly at large angular scales. In fact, the posterior $P(\hat{C}_b\,|\,C_b^{\rm th}(p))$ is well described by an "offset log-normal" distribution (see Bond et al., 1998). For completeness, the offset log-normal likelihood function has been tested for QUaD and it has turned out that the difference in the resulting parameter estimates and error bars is insignificant compared to those calculated for a Gaussian likelihood function (see QUaD collaboration: P. G. Castro et al., 2009). As a consequence we will assume that the likelihood for the bandpower C_ℓ's is well approximated by a Gaussian distribution given by

$$P(\hat{C}_b\,|\,C_b^{\rm th}) \propto \exp\left[-\frac{1}{2}\Delta C_b(p) N_{bb'}^{-1} \Delta C_{b'}^{\dagger}(p)\right], \tag{4.5}$$

where $\Delta C_b(p) = \hat{C}_b - C_b^{\rm th}(p)$, $\hat{C}_b$ are the measured QUaD binned bandpowers and $C_b^{\rm th}(p)$ are the binned theoretical power spectra which depend on the cosmological parameters, p. Here $N_{bb'} = \langle \Delta C_b \Delta C_{b'}^{\dagger} \rangle$ is the bandpower covariance matrix (BPCM) which determines the weighting scheme for contribution of each bandpower in the likelihood function. In §4.1.4 we will see that assuming a Gaussian likelihood function for QUaD parameter estimation has the added benefit that it helps to simplify the formalism of the marginalization over nuisance parameters.

The QUaD data set which we use to constrain cosmological parameters is published in QUaD collaboration: C. Pryke et al. (2008) and given in `http://find.uchicago.edu/quad/` (May 2008 - Second Release). It includes the combined 100GHz, 150GHz auto-spectra and 100/150GHz cross spectra temperature and polarization power spectra, $\hat{C}_b^{TT}$, $\hat{C}_b^{TE}$ $\hat{C}_b^{EE}$, and $\hat{C}_b^{BB}$, measured in 23 bandpowers over angular multipoles ranging from $\ell = 164,\ 245$ to $\ell = 2026$; a BPCM which has been calculated from an ensemble of 500 signal plus noise simulations of the CMB sky for QUaD; and the bandpower window functions (BPWF), which transform a smooth theoretical power spectrum into estimates for the step-wise bandpower. For details of the calculation of the BPCM and BPWFs see QUaD collaboration: C. Pryke et al. 2008.

The BPWFs determine the relative weighting that each multipole receives when we bin the theoretical spectra. We transform the theoretical spectra to predictions of the binned bandpowers by means of the definition

$$C_b^{\rm th} = \sum_\ell \frac{W_{b\ell}}{\ell} C_\ell^{\rm th}, \tag{4.6}$$

where ℓ is given up to the multipole $\ell = 2700$. In addition to BPWF for each spectrum there are also two mode-mode coupling bandpower window functions to account for mixing between

EE and BB spectra on the cut sky. The effect of this mode-mode mixing is added to equation (4.6) by introducing similar terms on the right hand side for $E \rightarrow B$ and $B \rightarrow E$ mixing.

The BPCM is estimated from QUaD-like simulations which are generated from a fixed fiducial ΛCDM model. In our analysis the BPCM remains fixed and independent of the cosmological parameters, although in principle for the likelihood analysis we should vary the covariance matrix as we move around the parameter space. However, the validity of using a fixed BPCM has been tested by carrying out MCMC test runs with a different BPCM calculated from simulations generated at the QUaD bestfit point in parameter space (see QUaD collaboration: P. G. Castro et al., 2009) and it has been found that a different covariance matrix does not lead to any distinguishable difference. In parameter estimation we only use the diagonal and the first two off-diagonal terms of the bandpower covariance matrix for TT-TT, TE-TE, EE-EE, and BB-BB covariances, and the diagonal and first off-diagonal terms in the TT-TE and TE-EE covariances, as is provided by the QUaD collaboration `http://find.uchicago.edu/quad/`. This is motivated by the need to avoid excessive off-diagonal shot noise in the BPCM, due to its estimation from finite numerical simulations, which can cause problems inverting the BPCM (see QUaD collaboration: C. Pryke et al., 2008).

4.1.3 The Standard Cosmological Model

For our Standard ΛCDM Cosmological Model we consider a spatially flat universe filled with photons, massless neutrinos, baryons, cold dark matter and dark energy in the form of a cosmological constant. Initial conditions are taken to be purely adiabatic with an initial power-law perturbation power spectrum. We parameterize our ΛCDM cosmological model with the following standard set of 6 cosmological parameters: the Hubble constant, $H_0 = 100h\mathrm{kms}^{-1}\mathrm{Mpc}^{-1}$; the matter density, $\Omega_m h^2$; the baryon density, $\Omega_b h^2$; the amplitude of scalar fluctuations, A_s; the scalar spectral index, n_s; and the optical depth, τ. We define the scalar amplitude by $\Delta^2_R(k_p) = 2.95 \times 10^{-9} A_s$, where Δ^2_R is the amplitude of the primordial curvature perturbation at a given pivot scale k_p (see Verde et al., 2003).

The rate of convergence of the Markov chain is slowed down by degeneracies between parameters, and the choice of the step size in the MCMC algorithm as the chain explores the multi-dimensional parameter space. It has become standard practice to apply a partial reparametrization of the parameter space as suggested in Kosowsky et al. (2002), and introduce the so-called physical parameters. These are

$$\omega_b = \Omega_b h^2, \tag{4.7}$$

$$\omega_v = \Omega_\Lambda h^2, \tag{4.8}$$

$$R = \frac{a_* \Omega_m}{\Omega_r}, \tag{4.9}$$

$$M = (1 + R^{-2})^{1/2} \Omega_m h^2, \tag{4.10}$$

$$\theta = \frac{r_s(a_*)}{D_A(a_*)}, \tag{4.11}$$

$$\mathcal{Z} \quad = \quad e^{-2\tau}, \tag{4.12}$$

along with the scalar perturbation amplitude, A_s, and spectral index n_s, and where $r_s(a_*)$ is the physical size of the sound horizon and θ is the angular size of the sound horizon at the surface of last scattering. The Hubble parameter, h, is found by solving these equations. This re-parametrization removes the geometrical degeneracy. As we shall assume a flat cosmology we set $\Omega_\Lambda = 1 - \Omega_m$, or $\omega_v = h^2 - \omega_b$.

To further reduce the remaining degeneracies and correlations between parameters and to optimize the step sizes, we apply a method (Tegmark et al., 2004) which consists of computing the parameter covariance matrix of the iterations of a preliminary chain, i.e. p_i where $\mathbf{p} \equiv (p_1, p_2, ...)$ is our parameter vector, in the following way: obtain $\mathbf{C} \equiv < \mathbf{p}\mathbf{p}^t > - < \mathbf{p} >< \mathbf{p} >^t$ from the chain, diagonalize it as $\mathbf{C} = \mathbf{R}\mathbf{\Lambda}\mathbf{R}^t$ such that $\mathbf{R}\mathbf{R}^t = \mathbf{R}^t\mathbf{R} = \mathbf{I}$. The transformed parameter vector $\mathbf{p'} \equiv \mathbf{\Lambda}^{-1/2}\mathbf{R}^t[\mathbf{p} - < \mathbf{p} >]$, then has the advantage of having the properties $< \mathbf{p'} >= 0$ and $< \mathbf{p'}\mathbf{p'}^t >= \mathbf{I}$. It turns out that this change of basis removes the degeneracies and the transformed parameters are orthogonal. We can then use a very simple Gaussian distributed step function with $\sigma = 1$. In fact, as shown by Dunkley et al. (2005), using instead $\sigma = (2.4^2/D)$, where D is the dimension of our parameter space, optimises the mixing and speeds-up the convergence of the chains.

We impose the following flat priors in the likelihood analysis: $0 \leq \Omega_c h^2 \leq 1$, $0 \leq \Omega_b h^2 \leq 1$, $0.005 \leq \theta \leq 0.1$, $0 \leq \tau \leq 0.8$, $0. \leq A_s \leq 2.5$ and $0 \leq n_s \leq 2$. With these priors, the partial re-parametrization of the parameter space introduces an implicit prior on the h parameter, however for consistency we explicitly take the hubble parameter prior to be in the range $0.2 \leq h \leq 1.2$. We generate the MCMC random walks in the orthogonal transformed physical parameter space and then transform back to the physical and cosmological parameter space to calculate the likelihood function. Note that the underlying prior distributions in the cosmological space are not uniform due to the parameter transformations. We have tested whether the chosen prior ranges and physical parameters could bias our parameter estimation by running our MCMC algorithm with no data. More specifically we take the likelihood function to be equal to unity which causes the acceptance rate to be 100%. The recovered 1-D distributions from the no-data analysis are uniform when they are constructed from a few hundred thousands of iterations, however as the number of parameter points increases to a few millions the underlying distributions in Figure 4.2 reveal themselves. This shows that the flat priors in transformed physical space do not in general translate into flat priors in cosmological space, which is due to the space rotations and prior boundaries. However, since this issue is significant only for very large number of MCMC steps, and because when we include the data we probe a small region of the prior distributions, we believe this not to be of strong impact on our analysis.

To generate the theoretical spectra we use the publicly available CAMB code (Lewis et al., 2000), a fast parallel Boltzmann solver based on CMBFAST (Seljak and Zaldarriaga, 1996). We took advantage of its parallel computing capabilities to speed-up our MCMC analysis. We use CAMB to calculate the theoretical CMB temperature and polarization power spectra, (C_ℓ^{TT},

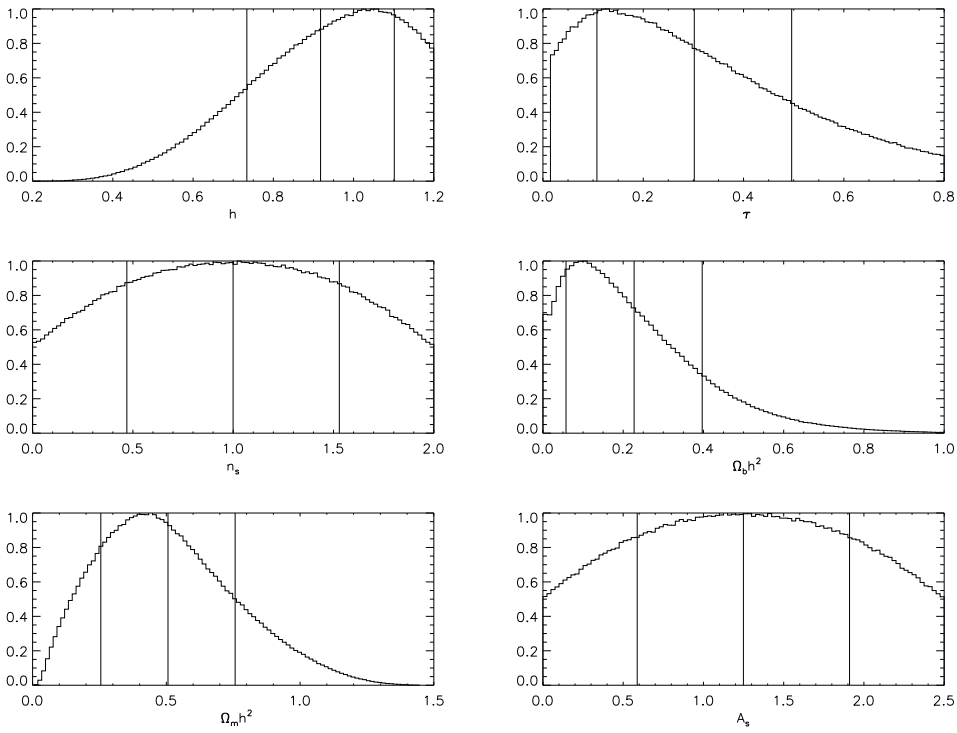

Figure 4.2: The underlying priors of the cosmological parameters from the no-data MCMC analysis. The histograms show the distribution of parameters from 4 chains each containing one million iterations. The vertical lines show the mean and 1-sigma marginalized errors. For smaller number of iterations the distributions are close to uniform.

C_ℓ^{TE}, C_ℓ^{EE}, C_ℓ^{BB}), including the effects of reionization, and gravitational lensing by foreground structure. We choose the pivot scale to be in the range of angular scales probed by QUaD. Since the angular distance to last scattering is roughly $D_*(h, \Omega_v = 0.7, \Omega_m = 0.3) \approx h^{-1}10000 Mpc^{-1}$, a conventional pivot scale of $k_p = 0.05 Mpc^{-1}$ corresponds to the multipole $\ell_p \sim D_* k_p = 714$ (for $h = 0.7$). This is well within the range of QUaD multipoles, hence from now on we adopt $k_p = 0.05 Mpc^{-1}$ for QUaD parameter estimation. When comparing our QUaD results with WMAP we regenerate WMAP best-fit values based on this pivot value using our own MCMC pipeline. This is to reassure that we are comparing the results of the same pivot scale. Anyway, we have verified that changing the pivot scale for WMAP5 data impacts mostly on the value of the amplitude parameter, A_s, which can be approximately estimated at any wavenumber by $A_s(k) = A_s(k_p)(k/k_p)^{n_s - 1}$ (see e.g. Verde et al., 2003). However, when adding QUaD data to WMAP for a combined analysis we revert to the WMAP 5yr preferred pivot scale of $k_p = 0.002 Mpc^{-1}$ since WMAP is a more robust data set.

4.1.4 Nuisance Parameters

It is becoming increasingly important to include the nuisance parameters in parameter estimation. Parameters such as calibration and beam uncertainties are not themselves important quantities in parameter determination, however their effect on other parameters has to be marginalized over in order to acquire better estimates of the bestfits which are also independent of the uncertainties. Therefore as the sensitivity and resolution of the CMB experiments are improving the effect of the nuisance parameters have to be taken into account. This is particularly true for the QUaD experiment which employs a refined beam model and calibration determination strategy (see QUaD collaboration: J. Hinderks et al., 2008; QUaD collaboration: C. Pryke et al., 2008).

An ideal way to include the effect of the nuisance parameters is to marginalize over all their possible values in the likelihood function. This will leave us with a likelihood function which is independent of the nuisance parameters. Nevertheless, including the nuisance parameters in MCMC is computationally costly, as the running time increases by a factor equal to the number of steps needed for the extra parameters to converge. To circumvent this problem, Bridle et al. (2002) devised an analytic marginalization scheme by integrating a Gaussian likelihood function over Gaussian priors for the calibration and beam uncertainty. The resulting likelihood function will have a similar shape but a different bandpower covariance matrix. This method is easy and ideal to use with MCMC since it does not add any additional free parameter. It only requires us to re-calculate the covariance matrix for each model with some additional noise terms coming from the nuisance parameters. To proceed we first introduce the exact method of marginalization over calibration/beam uncertainty and then move on to review the Bridle et al. (2002) approximation method which we use for QUaD parameter estimation.

Exact Marginalization Method

The exact marginalization requires integration over the likelihood function in the form

$$P(\mathcal{C}^o|\mathcal{C}^p,\sigma_b) \propto \int P(\mathcal{C}^o|\mathcal{C}^p,b)P(b|\sigma_b)db, \tag{4.13}$$

where $\mathcal{C}^o$ is the observed bandpower and b resembles the deviation from the predicted bandpower $\mathcal{C}^p \equiv \mathcal{C}^{\rm th}$ due to the nuisance parameter. Assuming a Gaussian likelihood function we can define the chi-squared as $\chi^2 \equiv (\mathcal{C}^o - \mathcal{C}^p)^T \mathcal{N}^{-1}(\mathcal{C}^o - \mathcal{C}^p)$ where $P(\mathcal{C}^o|\mathcal{C}^p) = -\frac{1}{2}\chi^2$. In CMB experiments one does not usually know the underlying priors of the nuisance parameters. Therefore for simplicity we assume a Gaussian prior on the distribution of the nuisance quantity b as

$$P(b|\sigma_b) = \frac{1}{(2\pi)^{1/2}\sigma_b} \exp\Big[-\frac{b^2}{2\sigma_b^2}\Big]. \tag{4.14}$$

In the case of calibration, the uncertainty multiplies the predicted bandpowers as

$$\mathcal{C}^{p\prime} = (1+c)\mathcal{C}^p, \tag{4.15}$$

where c is the unknown calibration factor which we want to marginalize over. The effect of beam uncertainty grows exponentially with multipoles as $\mathcal{C}^{p\prime} \propto \mathcal{C}^{p} \exp(\ell^2\theta_B^2)$ where θ_B is the true value of the beam size. Therefore, if we consider a Gaussian beam of width σ_b whose mean size has been misestimated to be $\theta_0 = \theta_B(1+b)$, the predicted power spectra are given by

$$\mathcal{C}^{p\prime} = \mathcal{C}^{p} \exp\Big[\ell^2(\theta_0^2 - \theta_B^2)\Big], \tag{4.16}$$

where now b is the beam nuisance parameter. This equation means that for a beam which is misestimated to be too small ($\theta_0 < \theta_B$), the predicted bandpowers will have to be smaller ($\mathcal{C}^{p\prime} < \mathcal{C}^{p}$). To marginalize over the beam and calibration uncertainty one has to substitute the new predicted bandpower $(1+c)\mathcal{C}^{\rm th} \exp\left[\ell^2(\theta_0^2 - \theta_B^2)\right]$ into equation (4.13) and integrate over the Gaussian priors (4.14). This corresponds to two additional parameters c and b in the MCMC and the effective chi-squared given by

$$\begin{aligned}\chi^2 = \Big[\big(\mathcal{C}_\ell^o - (1+c)\mathcal{C}_\ell^{\rm th} e^{\ell^2\theta_B^2(2b+b^2)}\big)\Big)^T \mathcal{N}_{\ell\ell'}^{-1} \\ \big(\mathcal{C}_{\ell'}^o - (1+c)\mathcal{C}_{\ell'}^{\rm th} e^{\ell'^2\theta_B^2(2b+b^2)}\big)\Big] + \frac{c^2}{\sigma_c^2} + \frac{b^2}{\sigma_b^2} + 2\ln(2\pi\sigma_b\sigma_c).\end{aligned} \tag{4.17}$$

We have verified that the implementation of this relation hugely slows down the convergence of the MCMC due to added new free parameters in the analysis. We will present and discuss the results in Table 4.1.

Approximate Marginalization Method

The analytic approximation method of Bridle et al. (2002) is based on assuming the predicted bandpowers are related linearly to the nuisance parameter. Using this assumption one can write

$$\mathcal{C}^{p\prime} = \mathcal{C}^{p} + b\mathcal{C}^{b}, \tag{4.18}$$

where b again quantifies the level of deviation from the expected bandpower value and $\mathcal{C}^b$ is a function which represents the effect of the nuisance parameter. In this case Bridle et al. show that the integration (4.13) for Gaussian prior (4.14) will reduce to

$$P(\mathcal{C}^o|\mathcal{C}^p, \mathcal{C}^b, \sigma_b) \propto \exp\Big[-\frac{1}{2}(\mathcal{C}^o - \mathcal{C}^p)^T \mathcal{M}^{-1}(\mathcal{C}^o - \mathcal{C}^p)\Big] \tag{4.19}$$

where the covariance matrix in this equation is given by $\mathcal{M} = \mathcal{N} + \sigma_b^2 \mathcal{C}^b \mathcal{C}^{b^T}$ and its inverse reads

$$\mathcal{M}^{-1} = \mathcal{N}^{-1} - \frac{\mathcal{N}^{-1}\mathcal{C}^b\mathcal{C}^{b^T}\mathcal{N}^{-1}}{\mathcal{C}^{b^T}\mathcal{N}^{-1}\mathcal{C}^b + \sigma_b^{-2}}. \tag{4.20}$$

This equation can also be generalized to multiple nuisance parameters.

- According to equation (4.18), a calibration uncertainty of the form $\mathcal{C}^{p\prime} = c\mathcal{C}^p$ implies $\mathcal{C}^b = \mathcal{C}^p$, $b = c - 1$ and therefore $\sigma_b = \sigma_c$. In this case the covariance matrix including the effect of marginalization over calibration uncertainty is given by substituting $\mathcal{C}^b = \mathcal{C}^p$ and $\sigma_b = \sigma_c$ in equation (4.20).

- The beam uncertainty increases exponentially for higher multipole bandpowers. The expected bandpower from equation (4.16) can be approximated by the linear relation $\mathcal{C}_\ell^{p\prime} = \mathcal{C}_\ell^p \exp[\ell^2(\theta_0^2 - \theta_B^2)] \simeq \mathcal{C}_\ell^p(1 + \ell^2(\theta_0^2 - \theta_B^2))$ which, in the notation of equation (4.18), corresponds to $b = (\theta_0^2 - \theta_B^2)$. We define the matrix $\mathcal{A} = \mathrm{diag}(\ell^2)$ in such a way that $\mathcal{C}^b = \mathcal{A}\mathcal{C}^p$ and normalize it so that $\sigma_b = 1$.

In this case the new covariance matrix including both calibration and beam uncertainty marginalization will have the form $\mathcal{O} = \mathcal{M} + \mathcal{A}\mathcal{C}^p\mathcal{C}^{pT}\mathcal{A}^T$ with $\mathcal{M} = \mathcal{N} + \sigma_c^2\mathcal{C}^p\mathcal{C}^{pT}$. The inverse of this matrix is then given by

$$\mathcal{O}^{-1} = \mathcal{M}^{-1} - \frac{\mathcal{M}^{-1}\mathcal{A}\mathcal{C}^p\mathcal{C}^{pT}\mathcal{A}^T\mathcal{M}^{-1}}{\mathcal{C}^{pT}\mathcal{A}^T\mathcal{M}^{-1}\mathcal{A}\mathcal{C}^p + 1}. \tag{4.21}$$

Substituting the calibration covariance matrix from Eq. (4.20) into Eq. (4.21) we will have

$$\begin{aligned}\chi^2 = {} & (\mathcal{C}^o - \mathcal{C}^p)^T\Big(\mathcal{N}^{-1} - \frac{\mathcal{N}^{-1}\mathcal{C}^p\mathcal{C}^{pT}\mathcal{N}^{-1}}{\mathcal{C}^{pT}\mathcal{N}^{-1}\mathcal{C}^p + \sigma_c^{-2}}\Big)(\mathcal{C}^o - \mathcal{C}^p) \\ & - (\mathcal{C}^o - \mathcal{C}^p)^T\left[\frac{\Big(\mathcal{N}^{-1} - \frac{\mathcal{N}^{-1}\mathcal{C}^p\mathcal{C}^{pT}\mathcal{N}^{-1}}{\mathcal{C}^{pT}\mathcal{N}^{-1}\mathcal{C}^p + \sigma_c^{-2}}\Big)\mathcal{A}\mathcal{C}^p\mathcal{C}^{pT}\mathcal{A}^T\Big(\mathcal{N}^{-1} - \frac{\mathcal{N}^{-1}\mathcal{C}^p\mathcal{C}^{pT}\mathcal{N}^{-1}}{\mathcal{C}^{pT}\mathcal{N}^{-1}\mathcal{C}^p + \sigma_c^{-2}}\Big)}{\mathcal{C}^{pT}\mathcal{A}^T\Big(\mathcal{N}^{-1} - \frac{\mathcal{N}^{-1}\mathcal{C}^p\mathcal{C}^{pT}\mathcal{N}^{-1}}{\mathcal{C}^{pT}\mathcal{N}^{-1}\mathcal{C}^p + \sigma_c^{-2}}\Big)\mathcal{A}\mathcal{C}^p + 1}\right](\mathcal{C}^o - \mathcal{C}^p).\end{aligned} \tag{4.22}$$

This new chi-squared contains both the effect of marginalization over beam and calibration uncertainty. One way to make it faster to operate is to calculate some of the repeatable quantities in advance. Defining the quantities

$$\begin{aligned}\mathbf{v}_o &= \mathcal{N}^{-1}\mathcal{C}^o, && (4.23)\\ \mathbf{v}_p &= \mathcal{N}^{-1}\mathcal{C}^p, && (4.24)\\ Q_a &= \mathcal{A}^T\mathcal{N}^{-1}, && (4.25)\\ Q_{aa} &= \mathcal{A}^T\mathcal{N}^{-1}\mathcal{A}, && (4.26)\\ s_{po} &= \mathcal{C}^{pT}\mathbf{v}_o = \mathcal{C}^{pT}\mathcal{N}^{-1}\mathcal{C}^o, && (4.27)\\ s_{pp} &= \mathcal{C}^{pT}\mathbf{v}_p = \mathcal{C}^{pT}\mathcal{N}^{-1}\mathcal{C}^p, && (4.28)\\ s_c &= s_{pp} + \sigma_c^{-2}, && (4.29)\end{aligned}$$

equation (4.22) will reduce to

$$\begin{aligned}\chi^2 = {} & s_{oo} - 2s_{po} + s_{pp} - \frac{1}{s_c}(s_{po} - s_{pp})^2 \\ & - \frac{\Big[\mathbf{v}_o^T - \mathbf{v}_p^T - \frac{1}{s_c}\Big(s_{po}\mathbf{v}_p^T - s_{pp}\mathbf{v}_p^T\Big)\Big]\mathcal{A}\mathcal{C}^p\mathcal{C}^{pT}\mathcal{A}\Big[\mathbf{v}_o - \mathbf{v}_p - \frac{1}{s_c}\Big(\mathbf{v}_p s_{po} - \mathbf{v}_p s_{pp}\Big)\Big]}{\mathcal{C}^{pT}Q_{aa}\mathcal{C}^p - \frac{1}{s_c}\Big(\mathcal{C}^{pT}Q_a\mathcal{C}^p \cdot \mathcal{C}^{pT}Q_a\mathcal{C}^p\Big) + 1}.\end{aligned} \tag{4.30}$$

Now defining

$$s_{ao} = \mathcal{C}^{pT} Q_a \mathcal{C}^o, \tag{4.31}$$

$$s_{ap} = \mathcal{C}^{pT} Q_a \mathcal{C}^p, \tag{4.32}$$

$$s_{pp} = \mathcal{C}^{pT} Q_{aa} \mathcal{C}^p, \tag{4.33}$$

we will have

$$\begin{aligned} \chi^2 &= s_{oo} - 2s_{po} + s_{pp} - \frac{1}{s_c}(s_{po} - s_{pp})^2 \\ &- \frac{(s_{ao} - s_{ap})^2 - \frac{2}{s_c}\Big[(s_{ao} - s_{ap}) s_{ap}(s_{po} - s_{pp})\Big] + \frac{1}{s_c^2}\Big[s_{ap}(s_{po} - s_{pp})\Big]^2}{s_{aa} - \frac{1}{s_c} s_{ap}^2 + 1}. \end{aligned} \tag{4.34}$$

Note that since the calibration uncertainty has a linear effect on the bandpowers, the above formula is exact for marginalizing over the calibration, so long as the underlying likelihood function is also Gaussian. However the beam uncertainty affects in a non-linear way, and has been linearized by expanding the exponential to first order around the true beam size, therefore this approximation should work well assuming the beam uncertainty is not too large. Note that the advantage of using the approximate chi-squared (4.34) over the the exact marginalization chi-squared (4.17) is that it does not introduce any additional varying parameter in the MCMC process, hence the convergence is faster.

In order to verify the approximative method we have compared the results of the application of the exact and approximate beam and calibration marginalization to parameter estimation with QUaD TT-TE-EE-BB spectra in Table 4.1. We do not see any significant difference in the values of the parameters of this table, however the speed-up factor which we gain by using the approximate method is around 20 which largely compensates the small differences found as compared to the exact method. Therefore for all the MCMC analysis results which we will present in this chapter we will use Bridle et al. analytical approximation method.

In this way we can modify the QUaD likelihood function of equation (4.5) to include the terms from marginalization over beam and calibration nuisance parameters. In this case the new likelihood function takes the form

$$\ln P(C_b|C_b^{\rm th}) = -\frac{1}{2}\Delta C_b \mathcal{O}^{-1}_{bb'} \Delta C^\dagger_{b'} - \frac{1}{2}{\rm Tr}\ln \mathcal{O}, \tag{4.35}$$

where

$$\mathcal{O}_{bb'} = N_{bb'} + \sigma_c^2 C_b C^\dagger_{b'} + \sigma_b^2 \ell_b^2 C_b \ell^2_{b'} C^\dagger_{b'}, \tag{4.36}$$

is the marginalized bandpower covariance matrix. The notation ℓ_b means the average multipole in a bin and C_b represents the QUaD bandpowers. The second term on rhs of equation (4.35) is the normalization factor given in the appendix of Bridle et al. (2002). In assessing the goodness-of-fit of our best-fit models, and when comparing the measured pseudo-C_ℓ's with the WMAP5 ΛCDM model we shall use the χ^2 value given by equation (4.34) or

$$\chi^2 = \Delta C_b \mathcal{O}^{-1}_{bb'} \Delta C^\dagger_{b'}. \tag{4.37}$$

Table 4.1. Tests of nuisance marginalization using QUaD TT-TE-EE-BB combined spectra.

Symbol	Exact	Bridle et al approx.
$\Omega_b h^2$	$0.0334\ ^{+0.00340}_{-0.0040}$	$0.0334\ ^{+0.004}_{-0.004}$
$\Omega_m h^2$	$0.119\ ^{+0.014}_{-0.014}$	$0.119\ ^{+0.014}_{-0.015}$
h	$0.91\ ^{+0.09}_{-0.09}$	$0.91\ ^{+0.09}_{-0.09}$
τ	< 0.57 (95 % cl)	< 0.60 (95 % cl)
A_s[a]	$1.25\ ^{+0.50}_{-0.44}$	$1.25\ ^{+0.47}_{-0.42}$
n_s[a]	$0.81\ ^{+0.08}_{-0.08}$	$0.81\ ^{+0.08}_{-0.08}$

[a]The pivot point for A_s and n_s is $k_p = 0.05$ Mpc^{-1} for both analyses.

For the parameter estimation of the QUaD combined spectra, we use an estimate of 10% fractional uncertainty on both the calibration (in power units) and the beam sizes, and we assume a nominal beam of 4.1 arcminutes. More details are found in QUaD collaboration: C. Pryke et al. (2008). Note that if the beam uncertainty is much smaller than its mean size (i.e. $\sigma_b \ll \theta_0$) then $(\theta_0^2 - \theta_B^2)$ will also be Gaussianly distributed with width $\sigma_{\theta_B^2} = 2\sigma_{\theta_B}\theta_0$ (see Bridle et al., 2002). Therefore, we perform the beam marginalization by putting the beam uncertainty equal to $\sigma_b = \sigma_{\theta_B^2} = 2\sigma_{\theta_B}\theta_0$ in radians.

4.1.5 Simulating Parameter Estimation

We test our MCMC pipeline by running it on a set of 50 simulations of the estimated QUaD TT-TE-EE-BB power spectra. These are provided by the QUaD collaboration and generated by simulating the signal and noise properties of the time-ordered data and analyzing these through the QUaD pipeline in the same way as the data (for details see QUaD collaboration: C. Pryke et al., 2008). The input cosmological model used to generate the simulations is the WMAP3 mean best-fit results from Table 2 of Spergel et al. (2007). Therefore one is expected that in average the input model should be recoverable from the MCMC analysis of an ensemble of the simulations.

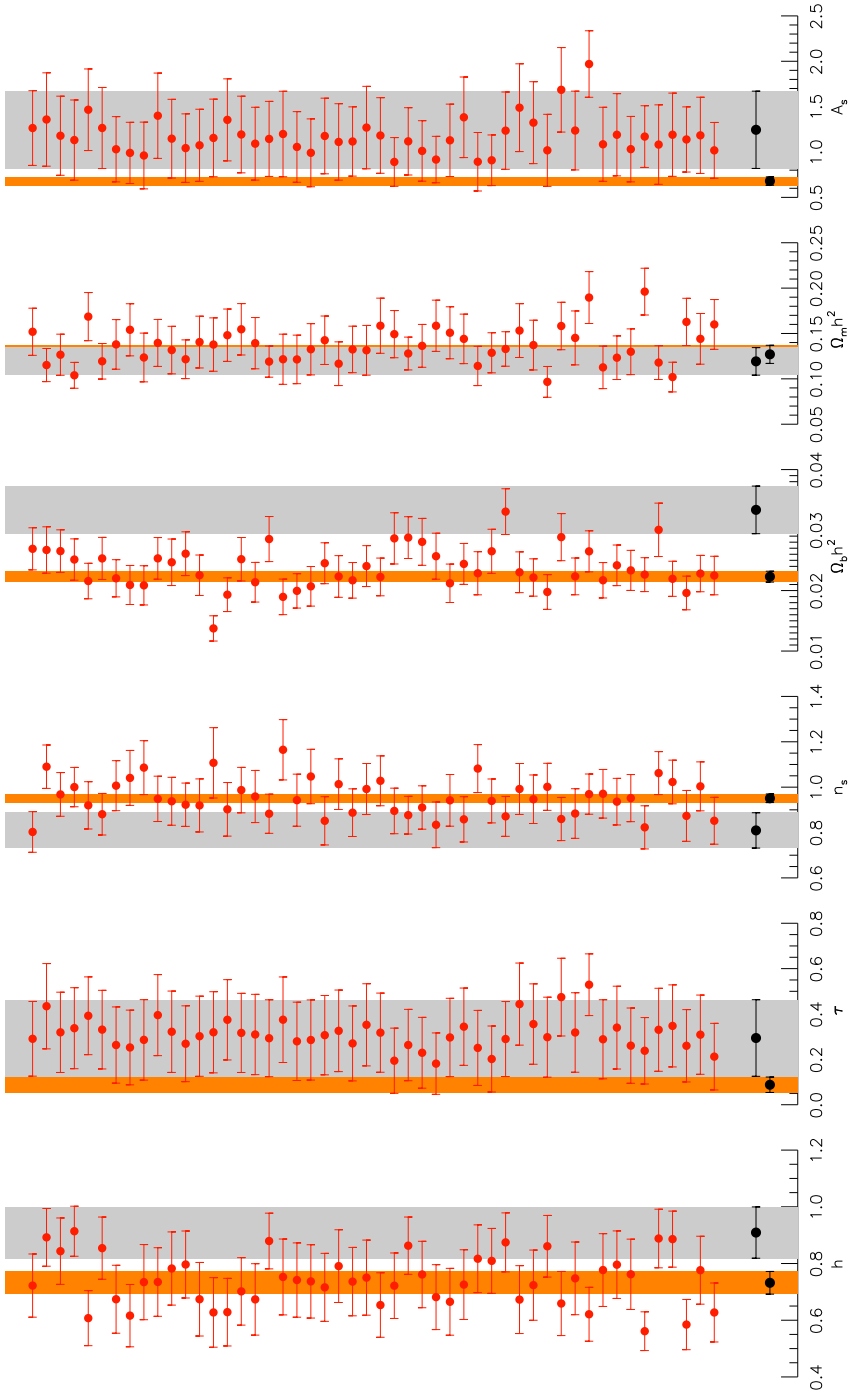

Figure 4.3: The bestfit parameters and 1 sigma errors of the MCMC analysis with 50 QUaD-like simulations. For comparison, we have also plotted the recovered bestfits for QUaD (gray band) and WMAP 3yr (orange band) which has been used to produce the simulations, all with pivot scale $k_p = 0.05 Mpc^{-1}$.

Figure 4.3 shows the parameter values and 1 sigma error bars of the bestfit models estimated from the simulations (red dots and error bars). For comparison, the QUaD bestfit values are also shown as gray bands, whereas the WMAP 3yr bestfit values from MCMC are shown as orange bands. Our recovered mean bestfit WMAP 3yr is well in agreement with the values reported in Spergel et al. (2007) paper. It is clear in this figure that the bestfit parameters and error bars from the simulations are well scattered around the WMAP bestfits, indicating that for most parameters we are not biased. However the scalar amplitude and the optical depth do appear to be biased, their values being systematically higher than the input values. We will discuss and correct the A_s and τ degeneracy which causes this bias in a little bit. However for now note that Figure 4.3 also shows that, among the 50 simulations which we have analyzed, QUaD bestfit predicts one of the least likely values for baryon density parameter. This unusually high baryon density is not due to bias in the analysis since it is exclusive to QUaD data (and one of the simulations). In section 4.2 we will probe the cause of this large baryon density and we will find that it mostly comes from the polarization spectra.

In Figure 4.4 we also plot the scatter in the values of the best-fit recovered model obtained from each one of the 50 simulations. We overplot the average values estimated from the 50

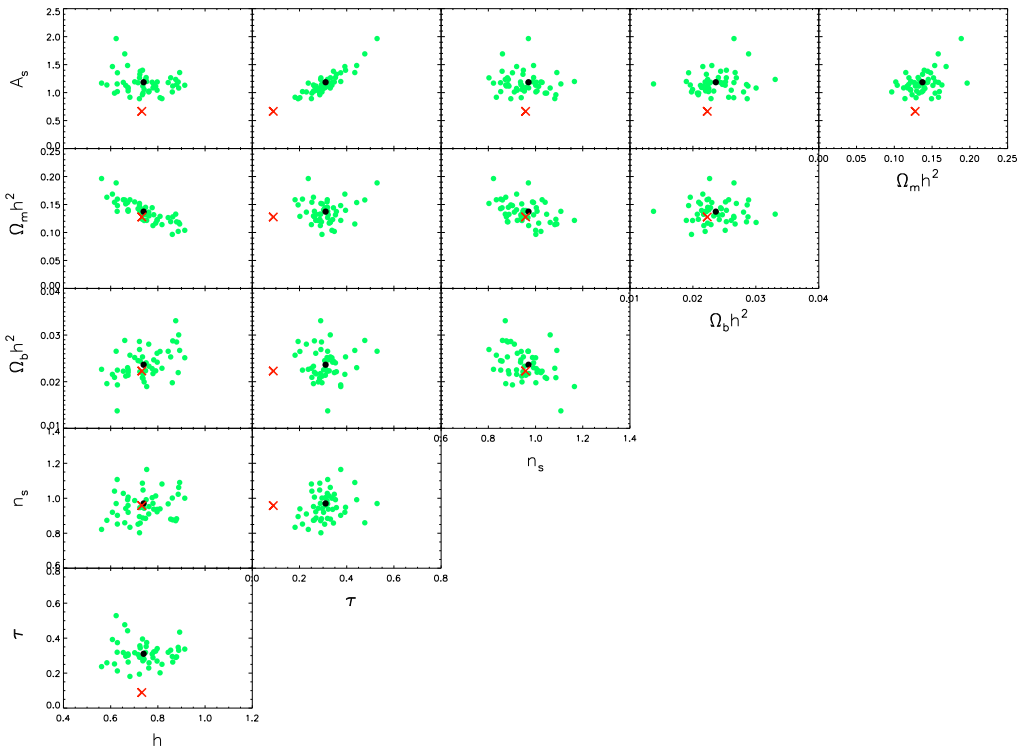

Figure 4.4: Scattered values (green) of the mean best-fit standard cosmological model obtained from 50 simulations of QUaD temperature and polarization data generated from the wmap3 best-fit model (in red crosses) from table 2 of Spergel et al. (2007). The mean over the 50 simulations is shown as dark blue points.

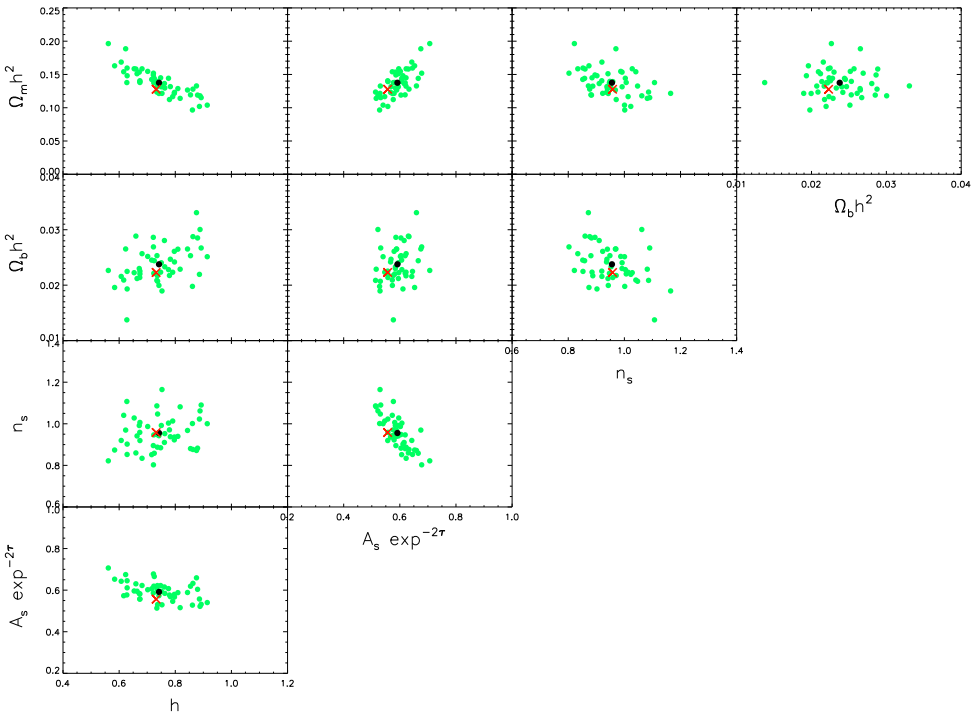

Figure 4.5: The same as Figure 4.4 but in 5 dimensions. The amplitude and baryon density have been projected on one orthogonal parameter $A_s e^{-2\tau}$ in order to break the degeneracy and the bias in the distributions.

simulations (dark blue dots), and compare them with the input WMAP3 model (red crosses). We have verified that the scatter in the simulated best-fit results is close to the size of the likelihood contours obtained for QUaD data (see §4.2), indicating that our likelihood code does not produce spurious parameter uncertainties. It is again obvious in the contours that the mean value of the parameters (except for τ and A_s) matches the input WMAP model. The bias in τ and A_s appears to be largely due to the large degeneracy between the amplitude and the optical depth which is seen in the $A_s - \tau$ contours. In the range of scales probed by QUaD these two parameters are completely degenerate, as they both affect the overall amplitude of power spectra. In our case, this degeneracy also arises marginally due to the prior ranges allowed for the parameters. To break this degeneracy we would require large-scale polarization measurements probing the re-ionization bumps at lower ℓ-modes. Therefore we conclude that due to the priors and the large degeneracy between A_s and τ, we cannot constrain these two parameters independently.

To rectify the bias seen in the scatter of A_s and τ we find that reducing our parameter space to 5D in which A_s and τ are combined into one single parameter removes the degeneracy and the observed bias. We project the A_s and τ values of all the MCMC points on a plane orthogonal to the line of degeneracy to construct one single parameter $A_s e^{-2\tau}$. This new

parameter encapsulates the correlation information by which A_s and τ compensate the effect of each other on the power spectra. Therefore, any two set of values of amplitude and optical depth which give the same equal $A_s e^{-2\tau}$ would leave the power spectra almost unchanged, as long as we are not loosing points at the boundaries. Figure 4.5 shows the contours for the new 5D parameter space constructed from the original simulation runs. In this new parameter space the bias is lifted and the mean of all simulations recovers the WMAP model. Henceforth, due to lack of constraining power on A_s and τ, without any loss of information we will be showing the combined parameter $A_s e^{-2\tau}$ for QUaD only analysis.

4.2 Results: Basic 5-Parameter Constraints from QUaD

In this section we will present various sets of combinations of the QUaD data in order to understand the new information each spectra brings into parameter estimation. The combinations we use are the temperature spectrum on its own (TT), all polarization spectra together (TE, EE and BB), the cross temperature-E mode polarization spectra on its own (TE), the pure polarization spectra together (EE and BB), and finally all temperature and polarization spectra combined (TT, TE, EE and BB).

The QUaD data set includes the highest quality polarization spectra measured so far, and it is worth exploring what such a data set can achieve by itself. We will later explore QUaD data in combination with other data sets.

In this section we apply our MCMC likelihood analysis to estimate cosmological parameters in a standard 6-parameter analysis, with the parameter-sets then projected to 5D space parameterized by: h, $\Omega_m h^2$, $\Omega_b h^2$, $A_s e^{-2\tau}$, n_s. The pivot scale used here is $k_p = 0.05\text{Mpc}^{-1}$.

In the following sections we present our parameter likelihood estimation for the QUaD temperature spectrum on its own (subsection 4.2.1), the polarization spectra on their own (subsection 4.2.2), and all the spectra combined (subsection 4.2.3). All of our QUaD only bestfit results are summarized in Table 4.2. Figure 4.6 shows the corresponding 2-D marginalized contour projections of the likelihood in the 5-parameter space. For comparison we have also shown the results of our MCMC runs for WMAP 5yr data set.

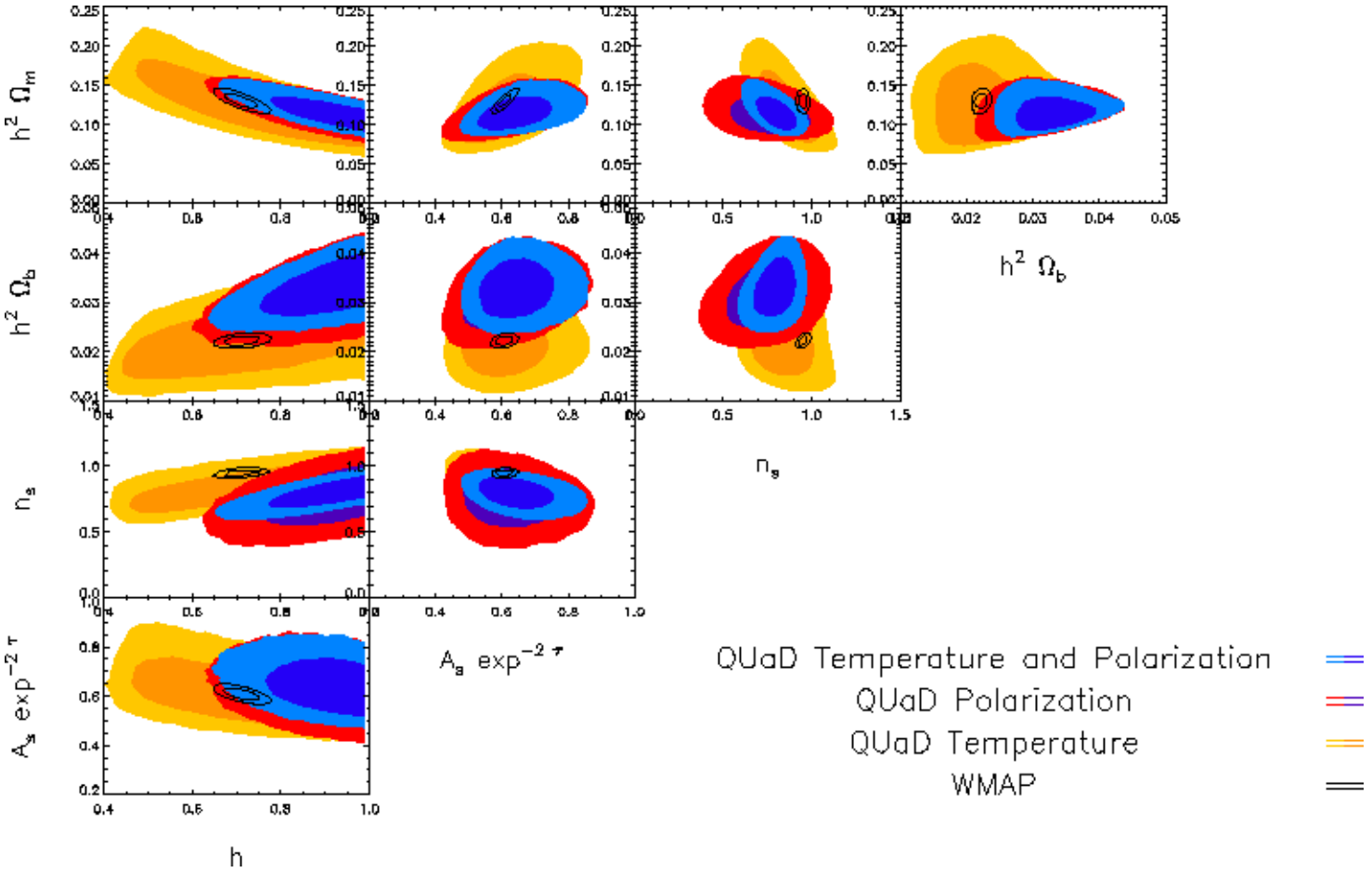

Figure 4.6: 2-D projected basic parameter likelihood surfaces with two-parameter 1- and 2-sigma contours for QUaD only constraints using the $TT/TE/EE/BB$ data set (TP: the blue contours), using the $TE/EE/BB$ data set (P: the red & magenta contours) and using the TT spectrum (T: the yellow & orange contours) versus the WMAP5 constraints (black non-filled contours). Pivot scale used is $k_p = 0.05$ Mpc^{-1}.

Table 4.2. Basic cosmological mean parameter constraints using QUaD bandpower spectra for various data combinations.

Symbol	Q08 $TT/TE/EE/BB$	Q08 $TE/EE/BB$	Q08 TT	Q08 TE	Q08 EE/BB	WMAP5
$\Omega_b h^2$	$0.0334\ ^{+0.0039}_{-0.0040}$	0.0319 ± 0.0046	$0.0242\ ^{+0.0058}_{-0.0057}$	0.0398 ± 0.0051	$0.0366\ ^{+0.0159}_{-0.0161}$	$0.02261\ ^{+0.00062}_{-0.00063}$
$\Omega_m h^2$	$0.119\ ^{+0.014}_{-0.015}$	0.117 ± 0.017	$0.133\ ^{+0.035}_{-0.033}$	0.149 ± 0.025	$0.155\ ^{+0.034}_{-0.035}$	$0.1329\ ^{+0.0064}_{-0.0065}$
h	0.91 ± 0.09	0.90 ± 0.10	$0.75\ ^{+0.17}_{-0.18}$	0.87 ± 0.11	0.77 ± 0.18	$0.717\ ^{+0.026}_{-0.027}$
$A_s e^{-2\tau}$ [a]	0.66 ± 0.08	0.63 ± 0.09	$0.64\ ^{+0.09}_{-0.10}$	0.63 ± 0.13	0.79 ± 0.21	$0.614\ ^{+0.017}_{-0.018}$
n_s [a]	0.809 ± 0.078	0.766 ± 0.152	$0.848\ ^{+0.117}_{-0.121}$	$1.337\ ^{+0.259}_{-0.254}$	$0.534\ ^{+0.155}_{-0.161}$	0.967 ± 0.015
$\chi^2(\nu)$ [b]	88.60 (86)	74.78 (63)	12.73 (17)	19.67 (17)	33.16 (40)	
PTE: $P(\geq \chi^2 \vert \nu)$	40.26%	14.72%	75.38%	29.14%	76.94%	
$\chi^2(WMAP5 \vert Q08)$ [c]	108.63 (92)	86.99 (69)	14.48 (23)	31.44 (23)	41.62 (46)	
$PTE(WMAP5 \vert Q08)$	11.36%	7.07%	91.24%	11.24%	65.60%	

[a] The pivot point for A_s and n_s is $k_p = 0.05$ Mpc^{-1} for both the QUaD data and WMAP5 data.

[b] χ^2 for the 6-parameter mean recovered model against QUaD data, with the number of degrees of freedom in brackets.

[c] χ^2 for WMAP5 mean recovered model given the QUaD data set, with the number of degrees of freedom in brackets.

4.2.1 QUaD temperature analysis (TT)

In this section we show the best-fit parameters obtained by using only our temperature data (TT) over a range of multipoles from $\ell = 164$ to $\ell = 2026$. Applying a 5-parameter estimation analysis to the temperature data alone is an important consistency test for QUaD, as all parameter constraints prior to QUaD are based almost exclusively on CMB temperature spectra due to its extensive angular coverage and high quality as compared to the polarization. In particular, the WMAP satellite measured the temperature power spectra to unprecedented accuracy. The basic parameters fits to WMAP data are then mostly constrained by the temperature spectrum, with the exception of the reionization optical depth constraint which hugely benefits from the large angular scales E-mode measurement by WMAP. (Dunkley et al., 2008)

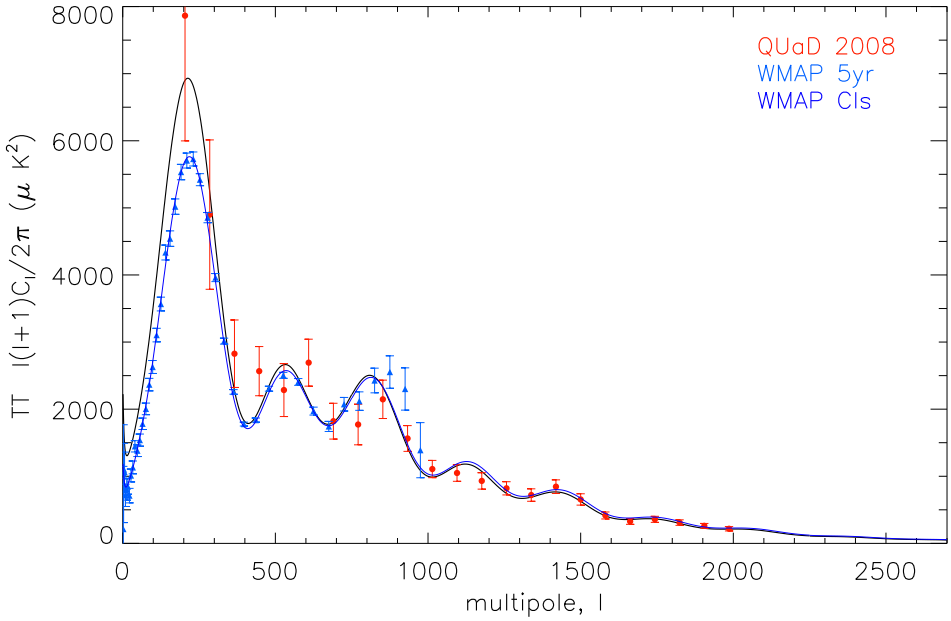

Figure 4.7: The best fit cosmological model from the temperature-only (TT) power spectrum (black line, with values from Table 4.2 plotted against the combined QUaD TT data bandpower spectra shown as red points with error bars. The blue data points are WMAP5 power spectra data, and the blue line shows the WMAP5 best fit model.

Figure 4.6 shows the 2-D contour projections of the likelihood function in our 5-parameter space from our analysis of the QUaD TT spectra. From this plot we can immediately see that the QUaD temperature spectrum is in very good agreement with the results from the WMAP5 experiment, with the WMAP5 results all lying within the 1-sigma contours. Looking at the Table 4.2 this scenario is confirmed. In fact we have verified that all of the TT best fit parameter values are consistent with WMAP5, not only in the 5D projected space but also in the 6 dimensions. However, since we do not believe QUaD has constraining power on A_s and τ

individually we do not show their mean values. Figure 4.7 shows the TT best fit cosmological model compared with the QUaD data points, and the WMAP5 best fit model. To generate the best-fit spectra we have assumed the WMAP 5yr bestfit value of $\tau = 0.087$ for the optical depth (Dunkley et al., 2008), which corresponds to an Amplitude of $A_s = 0.76$, given our $A_s e^{-2\tau}$ constraint.

The χ^2 of the temperature-only best fit model is $\chi^2 = 12.73$ for $\nu = 17$ degrees of freedom, where we expect a theoretical chi-squared value of $\chi^2 = 17 \pm 5.83$. When substituting into a cumulative χ^2-distribution with ν-degrees of freedom we find the Probability To Exceed (PTE) the measured QUaD χ^2 by chance, $P(> \chi^2|\nu)$, is 75.38%. We can also compare the χ^2-statistics for the WMAP5 best fit model to the QUaD data. This yields a χ^2 of 14.48 for 23 degrees of freedom, which gives a PTE of 91.24%. All of these statistics verify the QUaD temperature power spectrum is compatible with the results from WMAP5. This consistency is a non-trivial test of QUaD data, since the overlap of scales measured by QUaD and WMAP5 is only in the range $\ell = 164$ to $\ell = 950$, while the QUaD data extends to $\ell = 2026$ with good signal-to-noise.

4.2.2 QUaD polarization analysis (TE, EE and BB)

In this subsection we show the best-fit parameters obtained by using different combinations of the QUaD polarization bandpower spectra. This is the first time such a polarization study can be done to constrain cosmological parameters, and is only possible because of the resolution power of QUaD in the TE and EE polarization power spectra.

QUaD TE, EE and BB-polarization analysis (TE/EE/BB)

We begin by analyzing the full polarization data set which consists of the TE, EE, and BB bandpower spectra (TE/EE/BB). We have plotted the best fit TE/EE/BB spectra model along with the QUaD data in figure 4.8. Figure 4.6 shows the 2-D contour projections of the likelihood function in the 5-parameter space from our analysis. The first thing to notice is that the parameter constraints from the polarization data are comparable with our temperature data, although tighter than the temperature constraints for the majority of the parameters. We also can see there is a noticeable shift in some of the parameter values and likelihood contours. While the matter density, $\Omega_m h^2$, and the parameter $A_s e^{-2\tau}$ agree well with WMAP5 within the 68% regions, the Hubble parameter, h, is pushed higher and the spectral index, n_s is pushed lower. The most significant effect, however, is on the baryon density parameter, $\Omega_b h^2 = 0.0319 \pm 0.0046$, which is pushed higher compared to $\Omega_b h^2 = 0.02261 \pm 0.00062$ from WMAP5. It is therefore interesting to investigate this discrepancy further by analyzing the polarization data in more detail, which we will in the rest of this subsection. Note that polarization constraints have substantially improved (by between 30% to 50%) as compared to the first season TE/EE/BB data constraints of Ade et al. (2008), and by up to 50% as compared to the Boomerang "B03pol" polarization analysis of MacTavish et al. (2006).

The χ^2 of the best fit model listed in the Table 4.2 against the QUaD TE/EE/BB data is 74.78 for 63 degrees of freedom. For this case the expected theoretical chi-squared is $\chi^2 = 63 \pm 11.22$. The probability to exceed the measured QUaD χ^2 by chance, $P(> \chi^2|\nu)$, is 14.72%. The χ^2 of the WMAP5 best fit model compared with the QUaD TE/EE/BB spectra is $\chi^2 = 86.99$ for 69 degrees of freedom, which gives a Probability To Exceed this by chance of 7.07%.

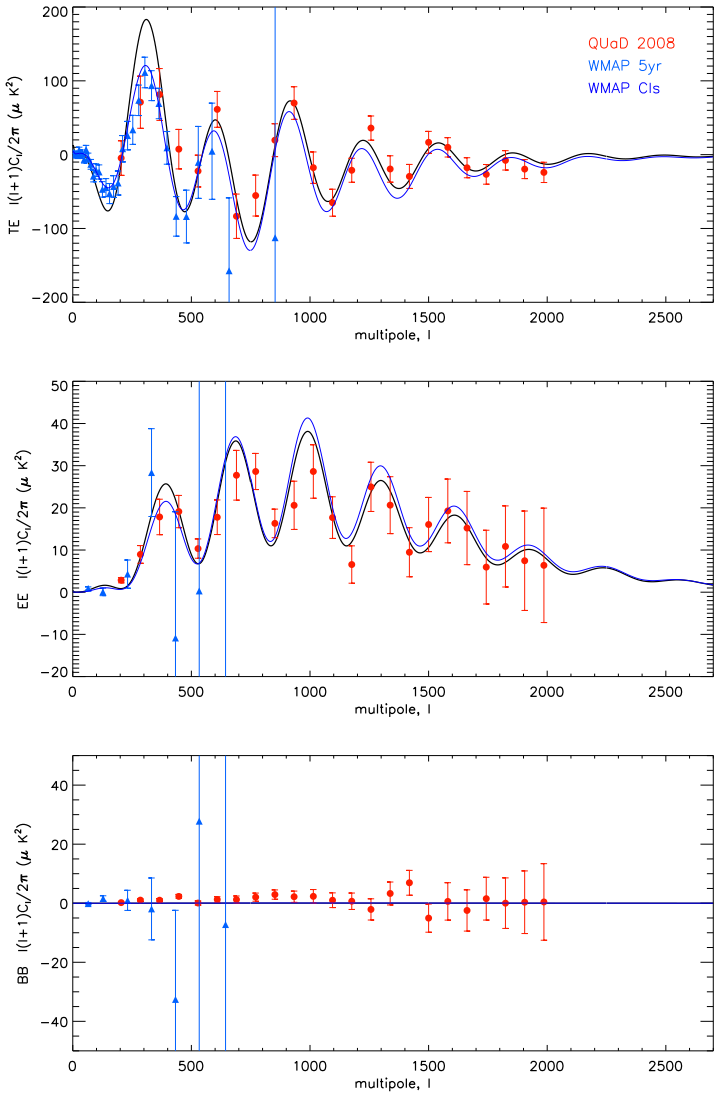

Figure 4.8: Combined QUaD TE/EE/BB data power spectra shown as red points with error bars. The blue data points are WMAP 5th year power spectra data. The blue line shows the WMAP5 best-fit model, and the black line shows our TE/EE/BB best fit model, with values in Table 4.2. For the mean recovered model, we assumed the WMAP5 best-fit value for the optical depth ($\tau = 0.087$), which corresponds to an Amplitude of $A_s = 0.75$, given our $A_s e^{-2\tau}$ constraint.

QUaD TE-polarization analysis (TE)

We continue our analysis by investigating the TE bandpower spectrum alone. As can be seen in the Table 4.2 and Figure 4.12, although the TE spectrum represents a small fraction of the total data constraining power it has the single greatest influence on the estimation of $\Omega_b h^2$. Clearly we are losing constraining power and most parameters are prior driven, but surprisingly we obtain constraints on $\Omega_b h^2$ and $\Omega_m h^2$ that are not influenced by our choice of priors. Figure 4.9 shows the 2-D projected likelihood surface for the ($\Omega_b h^2$,$\Omega_m h^2$) parameter space. We also overplot the TT only contours and show the results from WMAP5 and from BBN constraints. We clearly see that the contours for TE spectrum are tighter than those from TT, however they offset the constraints of the BBN and WMAP 5yr.

Figure 4.10 shows the TE QUaD bandpower spectrum data versus its best fit model and WMAP5 full data set best fit model. This figure visually illustrates the best fit model power spectra difference between the two data sets in terms of height and location of the peaks. The main reason for the higher baryon density parameter seems to be larger acoustic oscillations at higher multipoles in QUaD *TE*. This can be explained by the fact that increasing baryons results in more Thomson scattering and a suppression of the diffusion damping, which in turn lead to an enhancement of the small scale peaks as well as a shift to higher multipoles, resulting also in a slight degeneracy with h. The origin of this source of tension with ΛCDM is unclear, but could be due to a new physical mechanism, residual systematics or random chance.

The χ^2 of the best fit model listed in Table 4.2 against the QUaD TE data is 19.67 for 17

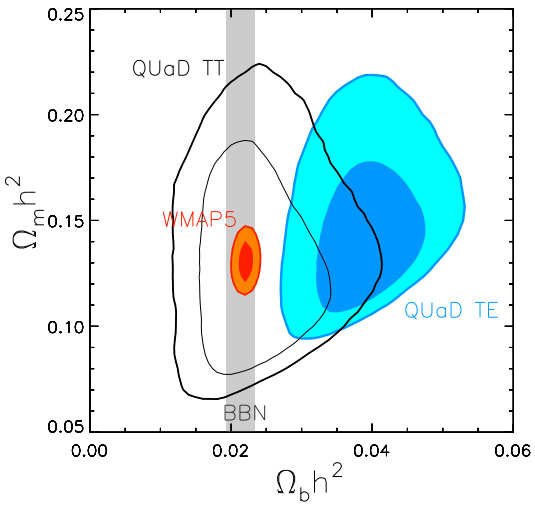

Figure 4.9: 2-D marginalized contours of the parameters $\Omega_b h^2$ versus $\Omega_m h^2$ obtained from QUaD *TE* data only. Also plotted are the contours from QUaD *TT* data only, the results from WMAP5, and the BBN constraint of $\Omega_b h^2 = 0.0214 \pm 0.002$ from Kirkman et al. (2003).

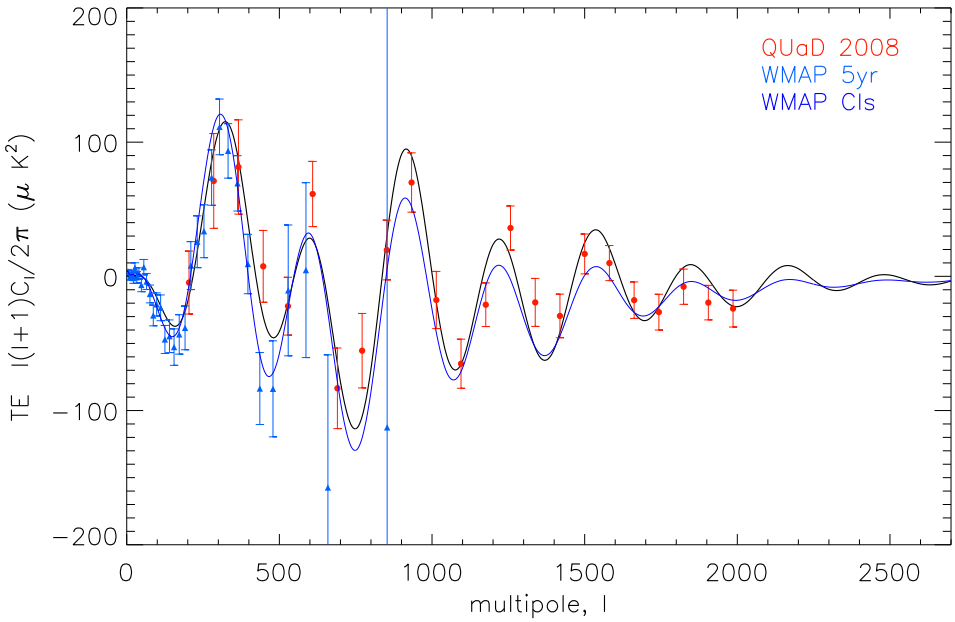

Figure 4.10: Plot of the QUaD TE data bandpower spectrum (in red) versus QUaD TE best fit model (black) and WMAP5 best fit model (blue). For the mean recovered model, we assumed the WMAP5 best-fit value for the optical depth ($\tau = 0.087$), which corresponds to an Amplitude of $A_s = 0.75$, given our $A_s e^{-2\tau}$ constraint.

degrees of freedom, giving a probability to exceed this by chance of $P(> \chi^2|\nu) = 29.14\%$. The χ^2 of the WMAP5 best fit model against the QUaD TE data is $\chi^2 = 31.44$ for 23 degrees of freedom, which gives a probability to exceed by chance of 11.24%.

QUaD EE and BB-polarization analysis (EE/BB)

In this section we present our E-mode and B-mode data set study (EE/BB). As expected the EE and the BB bandpower spectra provide very little information on parameters. They do however have an unusual feature. Table 4.2 and Figure 4.12 show the parameter constraints from EE/BB analysis. The preferred range of scalar spectral index values is low ($n_s = 0.534\ ^{+0.155}_{-0.161}$), which points at small tension with the WMAP5, although the contours overlap slightly in 2-sigma region. The origin of this tension seems to lie in the lower than expected amplitude of the third and fourth acoustic oscillations in the EE power spectrum detected by QUaD. Since we have taken the pivot scale to be at $k_p = 0.05 Mpc^{-1}$, increasing the spectral index results in an enhancement of the amplitude of the wavenumbers bigger than $\ell_p \sim 714$ relative to the large-scale amplitude. This means that QUaD TE data should favor a smaller spectral index to explain the relatively low amplitude of the detected acoustic peaks. This feature can also be seen in the best-fit spectra of the EE/BB analysis which are plotted in Figure 4.11. It is

evident that the best-fit spectrum (solid line) is tilted a little towards the small scales to fit the QUaD EE bandpowers.

The χ^2 of the best fit model listed in the Table 4.2 to the QUaD EE/BB data is 33.16 for 40 degrees of freedom, giving a probability to exceed by chance of $P(> \chi^2|\nu) = 76.94\%$. The χ^2 for the WMAP5 best fit model compared with our EE/BB polarization spectra is $\chi^2 = 41.62$ for 46 degrees of freedom, which gives a probability to exceed this by chance of 65.60% for the EE/BB data set. So although TT and TE share the majority of the constraining power, the EE and BB spectra exert an influence in combination with the remaining spectra by restricting the n_s-range to low values.

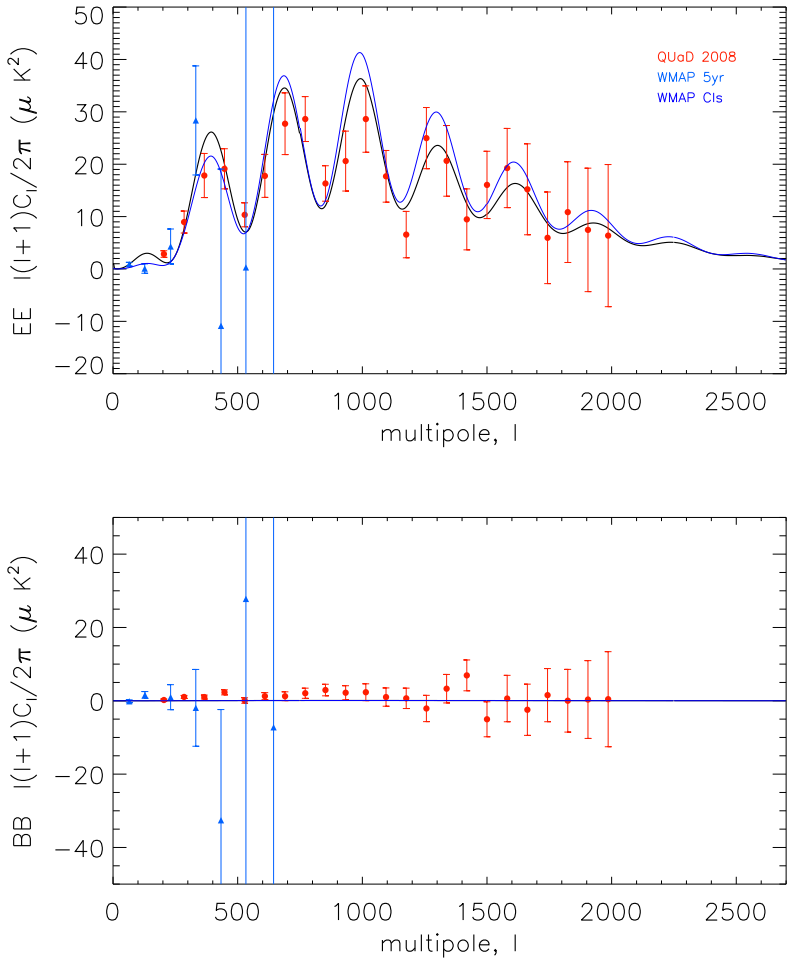

Figure 4.11: Plot of the QUaD EE and BB bandpower spectra (in red) versus QUaD EE/BB best fit model (black) and WMAP5 best fit model (blue). For the mean recovered model, we assumed the WMAP5 best-fit value for the optical depth ($\tau = 0.087$), which corresponds to an Amplitude of $A_s = 0.94$, given our $A_s e^{-2\tau}$ constraint.

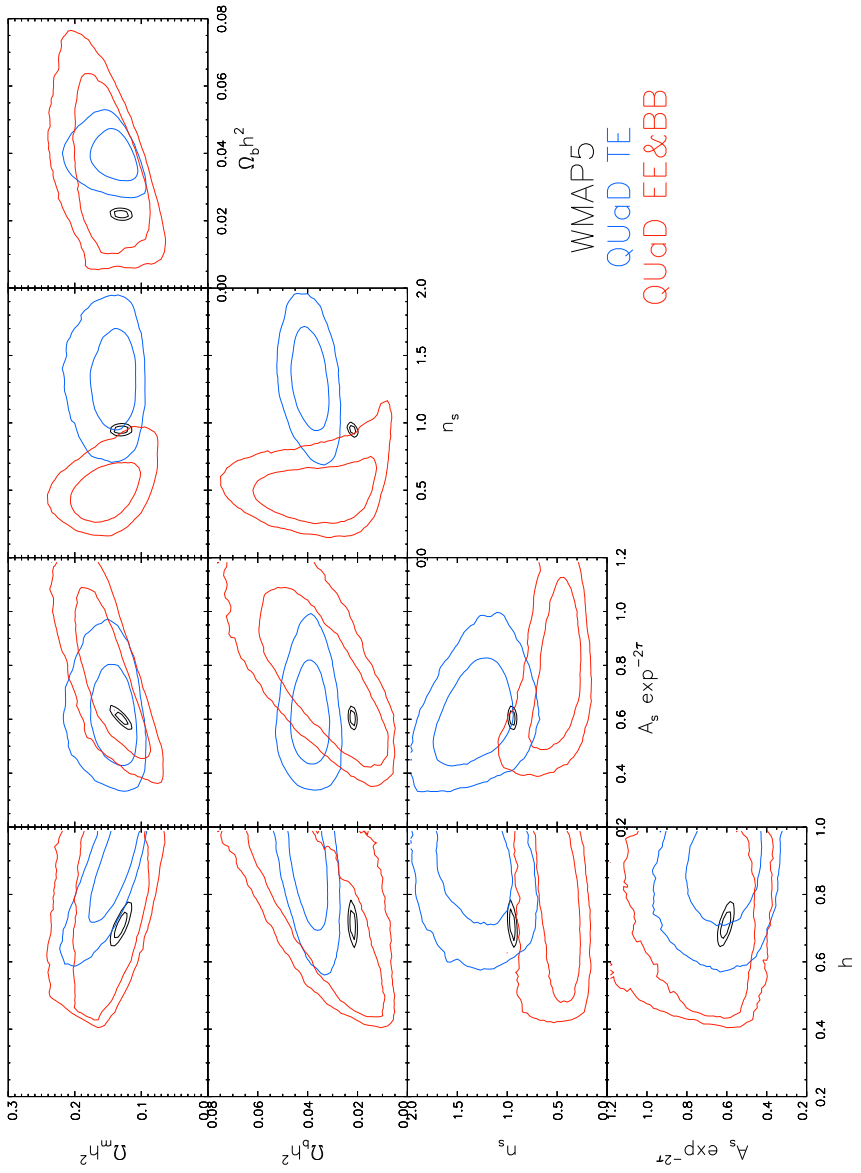

Figure 4.12: 2-D projected basic parameter 1-sigma and 2-sigma likelihood contours for QUaD only constraints, using the QUaD *TE* (blue contours) and the QUaD *EE/BB* data set (red contours) versus the WMAP5 constraints (black contours). Pivot scale used is $k_p = 0.05$ Mpc^{-1}.

4.2.3 Combined polarization and temperature analysis (TT/TE/EE/BB)

In this section we present the best fit standard parameters to the full second and third season QUaD data sets, ie the temperature and all the polarization bandpower spectra (TT/TE/EE/BB). We have introduced these parameter constraints informally in subsections 4.1.4 and 4.1.5.

From Figure 4.6 we can see the constraining strength of the polarization data versus the temperature data when used in combination. The polarization data clearly dominates the combined temperature and polarization data set. Just as in the TE/EE/BB constraints, the 68% confidence regions of matter density, $\Omega_m h^2$ and $A_s e^{-2\tau}$ parameter enclose the WMAP5 results, however the Hubble parameter, h, is pushed higher and the spectral index, n_s is pushed lower, influenced by the EE/BB contribution. The stronger effect is again on the baryon density parameter, $\Omega_b h^2$, which is pushed higher influenced by the polarization data, in particular the TE spectrum. Compared to the Big Bang Nucleosynthesis (BBN) value of $\Omega_b h^2 = 0.0214 \pm 0.002$ (Kirkman et al., 2003) we are more than 2-σ away. Figure 4.13 shows a comparison between our TT/TE/EE/BB best fit model spectra and the WMAP5 best fit spectra.

The χ^2 of the QUaD TT/TE/EE/BB best fit model listed in the Table 4.2 compared to the QUaD data is 88.60, with 86 degrees of freedom giving a probability to exceed this by chance of 40.26%. The χ^2 for the WMAP5 best fit model compared with the measured QUaD TT/TE/EE/BB power spectra is 108.63 with 92 degrees of freedom which gives a probability to exceed this by chance of 11.36%.

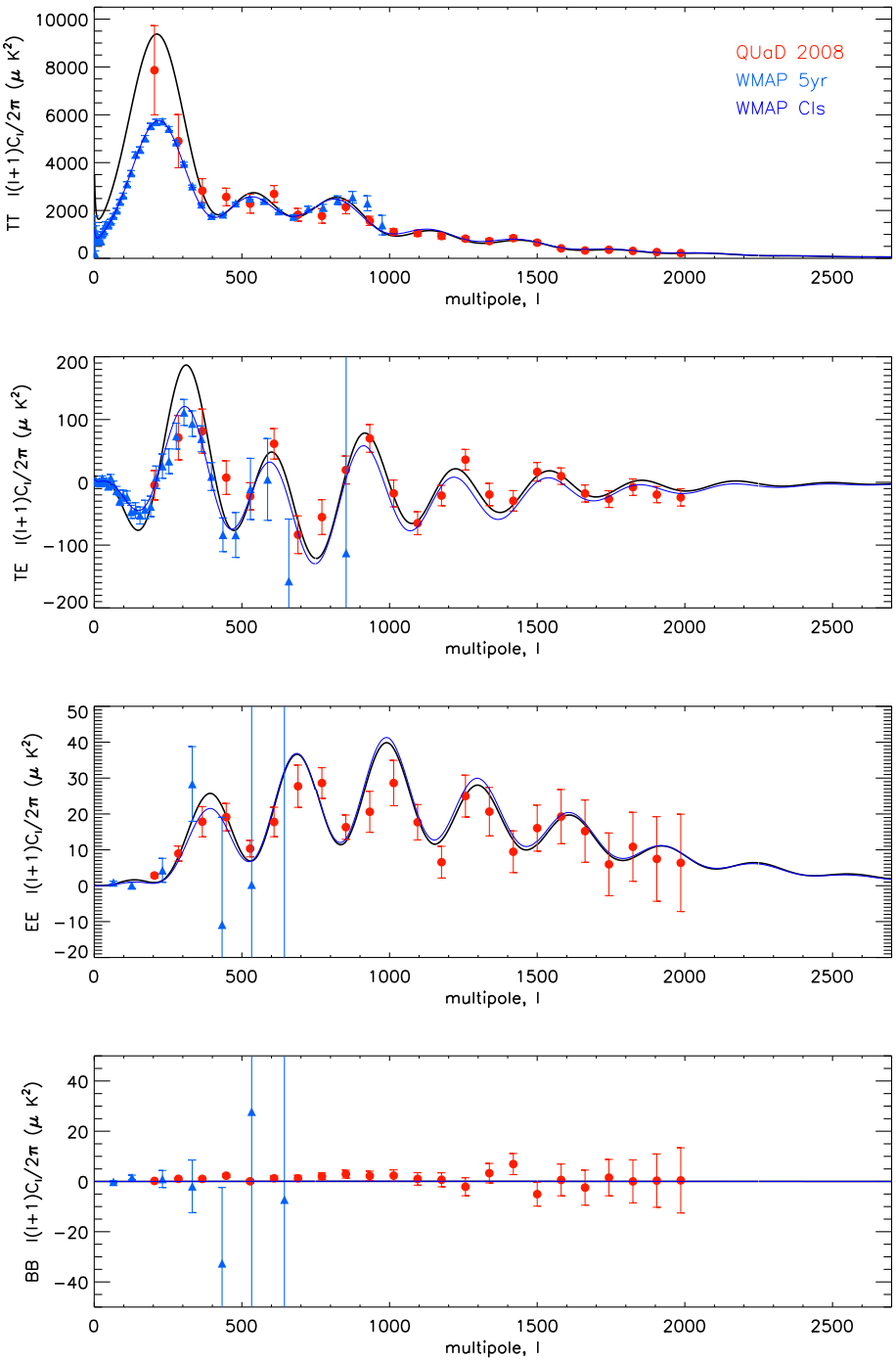

Figure 4.13: Combined QUaD TT/TE/EE/BB data power spectra shown as red points with error bars. The blue data points are WMAP5 power spectra data. The blue line shows the WMAP5 best fit model, while the black line shows our TT/TE/EE/BB best fit model with values given in Table 4.2. For the mean recovered model, we assumed the WMAP5 best-fit value for the optical depth ($\tau = 0.087$), which corresponds to an Amplitude of $A_s = 0.78$, given our $A_s e^{-2\tau}$ constraint.

4.3 Results: Combining QUaD with other data sets

In this section we combine the QUaD data set with other cosmological probes to assess the overall constraints on the cosmological parameters. Here we combine QUaD with the most comprehensive set of CMB data available, the WMAP 5-year data release, and the Sloan Digital Sky Survey (SDSS: Tegmark et al. 2006) Luminous Red Galaxies (LRG) data set, the largest ongoing large-scale structure survey. In subsection 4.3.1 we will provide the 6 basic parameter constraints from QUaD combined with these data sets. In subsection 4.3.2 we go beyond the 6 basic parameters and include the tensor-to-scalar ratio, the isocurvature perturbations and a quantity which parametrizes the gravitational lensing contribution in the MCMC analysis. This extended analysis is only feasible for QUaD combined with other data sets, since QUaD alone does not provide sufficient constraining power.

As before, for WMAP 5-year temperature and polarization data set (TT, TE, EE, BB) we use the publicly available WMAP5 likelihood code on the LAMBDA website and their methodology (Dunkley et al., 2008), however we do not include the Sunyaev Zel'dovich (SZ) marginalization (Sunyaev and Zel'dovich, 1972). The SDSS LRG matter power spectrum is measured over wavenumbers $0.01h\mathrm{Mpc}^{-1} < k < 0.2h\mathrm{Mpc}^{-1}$. The onset of nonlinear corrections is present for Fourier wavenumbers $k > 0.07h\mathrm{Mpc}^{-1}$. For our analysis we remove all Fourier modes above this value so that we do not have to consider any nonlinear correction. We marginalize over the amplitude of the galaxy power spectrum which removes any dependence on the galaxy bias parameter, b_g, and linear redshift-space distortion. We shall assume the WMAP5 and QUaD (and SDSS) data sets are independent, since the QUaD data only covers a small fraction of the WMAP5 sky, and the overlap in angular wavenumber is only partial. Therefore we simply add the chi-squared values of all data sets to gain the overall constraints. To optimally estimate the amplitude parameter, A_s, we choose the pivot scale which lies within the range of the angular scales. Since the preferred choice for WMAP 5yr and SDSS is the pivot scale $k_p = 0.002\mathrm{Mpc}^{-1}$ and they provide most of the constraining power we shall use this pivot scale in this section.

4.3.1 The Basic 6-parameter Constraints

The QUaD TT/TE/EE/BB power spectra data has little impact on the baseline 6-parameter fit when combined with WMAP5. This is perhaps unsurprising, given the accuracy of the WMAP5 measurement of the first acoustic peak in the temperature power spectrum, and the low-ℓ power in TT and TE. The impact it does have is to tighten the error bars on parameters determined from the relative heights of acoustic peaks, on the baryon density, $\Omega_b h^2$, and the matter density $\Omega_m h^2$, as QUaD data adds a substantial amount of well-defined peak information at high-ℓ. The improvements obtained can be seen in Table 4.3 and Figure 4.15. The 1-D marginalized distributions are shown in Figure. 4.14. Note that the WMAP5 values presented in Table 4.3 were obtained using our MCMC analysis pipeline with $k_p = 0.002$ Mpc^{-1} and no SZ

Table 4.3. Basic mean parameters for QUaD $TT/TE/EE/BB$, SDSS LRG and WMAP5 data.

Symbol	Q08+WMAP5	Q08+WMAP5+SDSS	WMAP5
$\Omega_b h^2$	$0.02233\ ^{+0.00055}_{-0.00057}$	$0.02235\ ^{+0.00051}_{-0.00058}$	$0.02259\ ^{+0.00061}_{-0.00062}$
$\Omega_m h^2$	0.1266 ± 0.0060	$0.1266\ ^{+0.0038}_{-0.0039}$	0.1329 ± 0.0065
h	0.733 ± 0.027	0.731 ± 0.019	$0.715\ ^{+0.027}_{-0.026}$
τ	0.087 ± 0.017	0.087 ± 0.016	0.087 ± 0.017
A_s[a]	0.805 ± 0.038	$0.806\ ^{+0.032}_{-0.033}$	0.816 ± 0.039
n_s[a]	$0.960\ ^{+0.014}_{-0.013}$	$0.960\ ^{+0.014}_{-0.012}$	$0.966\ ^{+0.014}_{-0.015}$

[a]The pivot point for A_s and n_s is $k_p = 0.002$ Mpc^{-1} for QUaD, WMAP5 and SDSS LRG data.

marginalization, for a fair comparison. When we add the SDSS LRG and WMAP5 data to the QUaD data we see an improvement compared to the just QUaD and WMAP5 combination, as expected. This improvement is mostly due to the extra constraining power on $\Omega_m h^2$ and $\Omega_b h^2$ coming from the break-scale in the SDSS LRG galaxy power spectrum, and the baryon acoustic oscillations (BAO's). However the QUaD data still reduces the error bars of $\Omega_b h^2$.

4.3.2 Beyond the Standard 6-Parameter Model

In this section we will extend our analysis of the QUaD temperature and polarization data set beyond the standard 6 parameters to include parameters which can also affect the nature of structure formation in the Early Universe. We focus on two models which polarization data may help to constrain; tensor, or gravitational wave, modes, measured in the power spectra by the tensor-to-scalar ratio parameter, r, and isocurvature modes. We will further investigate the constraints on the gravitational lensing from QUaD.

Tensor-to-Scalar Ratio, r

The simplest inflation scenarios generically produce a background of scalar and tensor perturbations due to quantum excitations during accelerated expansion. The power spectrum of these perturbations is often assumed to have power-law dependence on the wavenumber, k, with

$$\Delta_S^2(k) = A_S^2 \Big(\frac{k}{k_p}\Big)^{n_s - 1}, \tag{4.38}$$

$$\Delta_T^2(k) = A_T^2 \Big(\frac{k}{k_p}\Big)^{n_t}. \tag{4.39}$$

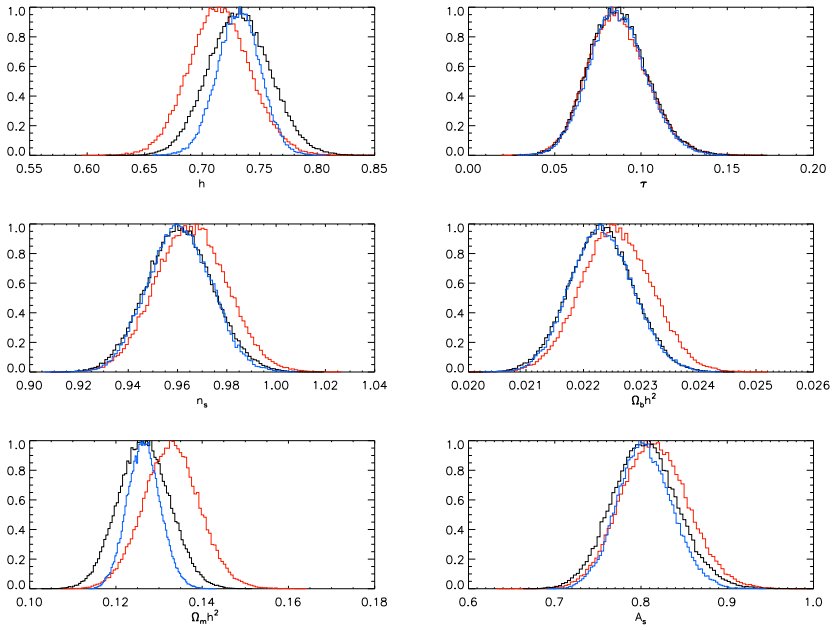

Figure 4.14: 1D marginalized distributions for 6-parameters model from QUaD combined with WMAP5 (black), combined with WMAP5 and SDSS (blue), as compared to WMAP5 only constraints (red).

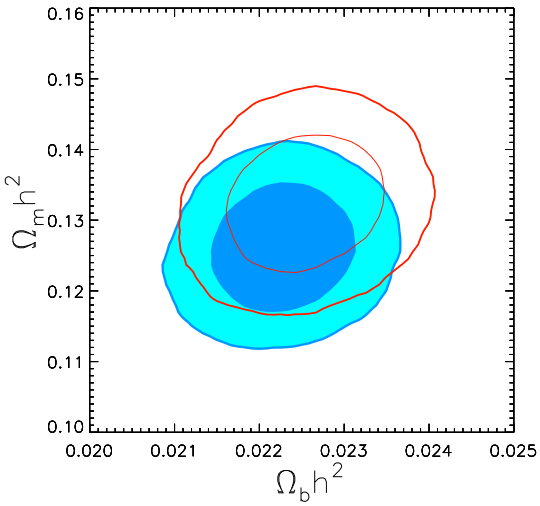

Figure 4.15: 2D marginalized contours for $\Omega_m h^2$ versus $\Omega_b h^2$ of WMAP5 only (red contours) and WMAP5 combined with QUaD TT/TE/EE/BB full data set (blue filled contours).

The simplest slow-roll models of inflation predict the amplitude of the scalar and tensor perturbations and the ratio of the amplitudes:

$$A_S^2 = \frac{32}{75 m_p^4}\frac{V}{\epsilon}, \tag{4.40}$$

Table 4.4. Tensor-to-scalar ratio constraints QUaD TT/TE/EE/BB data, WMAP5 and SDSS LRG.

Symbol	Q08+WMAP5	Q08+WMAP5+SDSS	WMAP5
$\Omega_b h^2$	$0.02298\ ^{+0.00072}_{-0.00073}$	$0.02297\ ^{+0.00068}_{-0.00071}$	$0.02334\ ^{+0.00077}_{-0.00080}$
$\Omega_m h^2$	$0.1217\ ^{+0.00655}_{-0.00667}$	$0.1249\ ^{+0.0038}_{-0.0037}$	$0.1281\ ^{+0.0069}_{-0.0070}$
h	$0.767\ ^{+0.037}_{-0.036}$	$0.753\ ^{+0.022}_{-0.023}$	$0.751\ ^{+0.036}_{-0.035}$
τ	0.090 ± 0.017	$0.089\ ^{+0.017}_{-0.017}$	0.091 ± 0.018
A_s[a]	0.743 ± 0.054	0.756 ± 0.044	0.751 ± 0.054
n_s[a]	$0.986\ ^{+0.019}_{-0.022}$	$0.982\ ^{+0.020}_{-0.019}$	$0.991\ ^{+0.022}_{-0.021}$
r (95 % cl)	< 0.45	< 0.38	< 0.44

[a]The pivot point for A_s and n_s is $k_p = 0.002$ Mpc^{-1} for QUaD, WMAP and SDSS data.

$$A_T^2 = \frac{32}{75 m_p^4} V, \tag{4.41}$$

$$r = \frac{A_T^2}{A_S^2} = \epsilon, \tag{4.42}$$

where V is the potential of the inflaton and ϵ is the logarithmic slope of the potential, and $m_p = \sqrt{\hbar c/G}$ is the Planck mass. (remember §2.1.5) Tensor modes contribute to all of the CMB power spectra at large angles, dropping off rapidly at high-multipole, allowing the tensor-to-scalar ratio, r, to be measured. Most significantly, as we saw in section 3.3, the tensor background will give rise to odd-parity B-modes in the CMB polarization, providing the most direct measurement of gravitational waves and the potential field amplitude, V. However, the gravitational wave B-modes may be masked by the effect of gravitational lensing by foreground structure transforming E-modes into B-modes. These lensed B-modes dominate the BB-power spectrum at high-multipole, peaking at around $0.025 \mu K^2$ at $\ell = 1000$.

The tensor-scalar ratio can be used to measure the shape of the inflationary potential (Lucchin and Matarrese, 1985; Stewart and Lyth, 1993; Terrero-Escalante et al., 2002; Terrero-Escalante, 2003). A large measurement of r would rule out many inflationary models, whereas a value of $r \simeq 0.1$ is favored by several scenarios. A measurement of the large angular scales r parameter is therefore the final frontier for CMB physics, as it will provide an important direct test of the early universe scenarios. The current 95% upper confidence limit on r (without including running of the spectral index and isocurvature modes) obtained from WMAP5 alone is $r < 0.43$. In combinations with other small-scale CMB data sets (Boomerang + CBI + VSA + ACBAR 2006) this drops to $r < 0.36$, and finally combined with LSS data (2dFGRS and SDSS) and supernova data the strongest constraint is $r < 0.20$ (Dunkley et al., 2008).

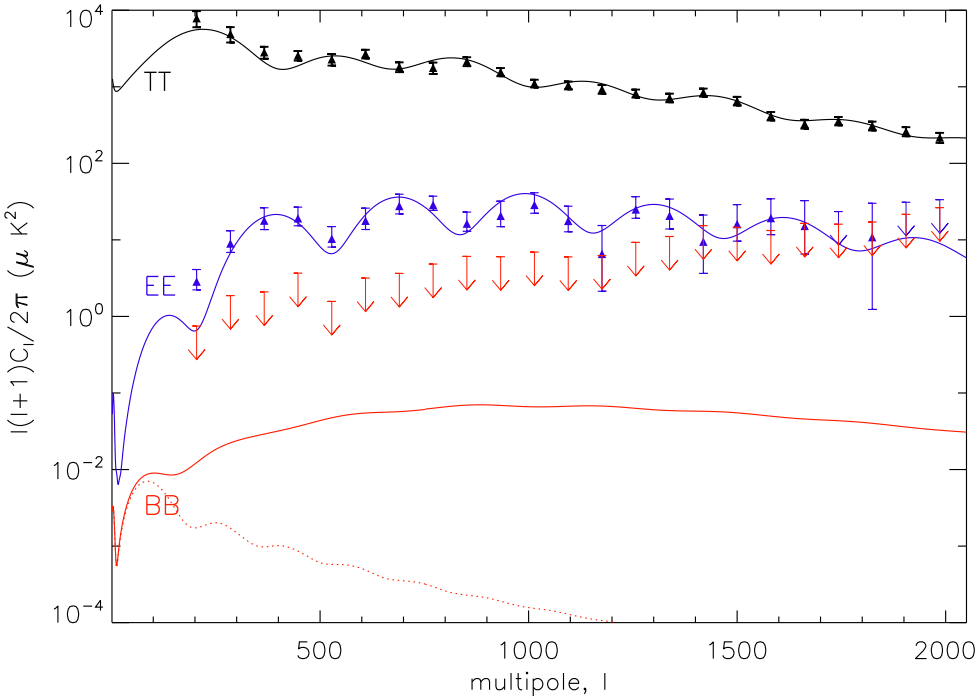

Figure 4.16: The QUaD power spectra (data points). Solid lines include gravitational lensing for a WMAP5 standard cosmological model. Dotted line represents the gravitational waves contribution to the BB spectrum ($r = 0.1$).

Despite the fact that the QUaD data sets the strongest upper limits on the BB mode over a wide range of angular scales, it does not constrain the larger angular scales ($\ell \approx 100$) where a gravitational waves signal may be present. Likewise, it does not provide meaningful constraining power on the expected gravitational lensing signal in the BB spectrum, which peaks at $\ell \approx 1000$, as can be seen in Figure 4.16. However through the measurement of TT, TE and EE at high-ℓ, combined with the low-ℓ constraints from WMAP5, QUaD may be of help in constraining r.

In order to investigate whether we are able to improve on the present constraints on a tensor contribution, we add WMAP5 first and then WMAP5 together with the SDSS LRG data to the QUaD combined bandpower spectra. Unfortunately, we are not able to tighten the r constraints as compared to our WMAP5 only best fit upper limit value, $r < 0.44$, although we do not weaken them significantly, showing we have low systematics. This is largely to be expected due to the absence of low multipole information from QUaD and the high quality of WMAP5 data at this range, and the fact that r contributes only as an extra source of magnitude at lower angular scales. The full results are presented in Table 4.4.

When we add the SDSS LRG data set to the QUaD and WMAP5 data sets we do see an improvement of the majority of the parameters' error bars. In particular we do see an improvement of the tensor contribution constraint. We now obtain $r < 0.38$ at 95% confidence,

compared to $r < 0.45$ when using WMAP5 and QUaD data, hence concluding that SDSS data provides better constraining power than QUaD.

Isocurvature Modes

Adiabatic perturbations are the simplest, but not only, relativistically covariant perturbations possible. A Universe with multiple particle species opens up the possibility that they have not always been in thermal equilibrium with radiation. Relative perturbations between the different species, which do not conserve entropy, becomes possible.

Theoretical predictions of isocurvature modes and their evolution, and the role of CMB polarization observations in constraining them, has been an active field over the past few years (Kawasaki and Sekiguchi, 2007; Keskitalo et al., 2007; Bean et al., 2006; Beltran et al., 2004; Moodley et al., 2004) among many others. Pure isocurvature perturbations have been ruled out (Stompor et al., 1996; Langlois and Riazuelo, 2000; Enqvist et al., 2000; Amendola et al., 2002) although the presence of a subdominant isocurvature fraction has been claimed (Keskitalo et al., 2007). Observationally, isocurvature modes have a phase difference from adiabatic modes, which provides a distinct signature.

We can completely characterize the primordial perturbations by one adiabatic and several isocurvature components. The adiabatic component is given by the associated curvature perturbation $\mathcal{R}$ corresponding to an initial overdensity $\delta = \delta\rho/\rho$. The non-adiabatic components are given by entropy perturbations $\mathcal{S}_x = \delta_x - (3/4)\delta_\gamma$ between photons and a different species, x. These correspond to four possible non-decaying isocurvature modes: a baryon density isocurvature (BI) mode, a cold dark matter density isocurvature (CI) mode, a neutrino density isocurvature (NDI) mode and a neutrino velocity isocurvature (NVI) mode. Bucher et al. (2000) have presented a thorough analysis of these components.

Under these assumptions, the total angular power spectra of the CMB are determined by integrating over the correlation function of the different primordial modes

$$C_\ell^{ij} = \sum_{xy} \int_0^\infty \frac{dk}{k} \mathcal{C}_{xy}(k) \Theta_\ell^i(k) \Theta_\ell^j(k). \tag{4.43}$$

Here Θ_ℓ is the photon transfer function and the labels i, j represent the temperature T and polarization (E and B) modes of the CMB. The primordial spectrum in this equation is given by the correlation function $\mathcal{C}_{xy} = \langle A_x(k) A_y(-k) \rangle$ which is a 5 by 5 real, symmetric matrix that represents the most general power spectrum of the primordial perturbations (see Bucher et al., 2000). Here x and y label different adiabatic and isocurvature modes with amplitude A at wavenumber k.

After the inflationary epoch when the scales are well outside the horizon the curvature perturbation remains constant. In contrast, the entropy perturbations may evolve at superhorizon scales and they may also seed curvature perturbations. The transition of the perturbations

from the epoch of inflation to the early radiation dominated era is given by

$$\begin{pmatrix} \mathcal{R}_{rad} \\ \mathcal{S}_{rad} \end{pmatrix} = \begin{pmatrix} 1 & T_{\mathcal{RS}} \\ 0 & T_{\mathcal{SS}} \end{pmatrix} \begin{pmatrix} \mathcal{R}_i \\ \mathcal{S}_i \end{pmatrix}.$$

Here the index i refers to well after inflation when the perturbations have been generated. The transfer function $T_{\mathcal{RR}} = 1$ is determined by the conservation of curvature perturbation for purely adiabatic perturbations, whereas $T_{\mathcal{SR}} = 0$ guarantees that adiabatic perturbations cannot give rise to entropy perturbations. If we assume the scale-dependence of the perturbations has a power-law form, the auto-correlation and cross-correlation of the perturbations are determined by

$$\mathcal{C}_{\mathcal{RR}}(k) = A_{\mathcal{R}}^2 \left(\frac{k}{k_0}\right)^{n_{ad1}-1} + A_{\mathcal{S}}^2 \left(\frac{k}{k_0}\right)^{n_{ad2}-1}, \tag{4.44}$$

$$\mathcal{C}_{\mathcal{SS}}(k) = B^2 \left(\frac{k}{k_0}\right)^{n_{iso}-1}, \tag{4.45}$$

$$\mathcal{C}_{\mathcal{SR}}(k) = A_{\mathcal{S}} B \left(\frac{k}{k_0}\right)^{n_{cor}-1}. \tag{4.46}$$

Here the spectral index of the correlated mode is defined by $n_{cor} = (n_{ad2} + n_{iso})/2$. Therefore in this way the most general form of the total CMB power spectra with one adiabatic and one isocurvature mode is given by

$$C_\ell^{ij} = A_{\mathcal{R}}^2 C_\ell^{ij,ad1} + A_{\mathcal{S}}^2 C_\ell^{ij,ad2} + B^2 C_\ell^{ij,iso} + A_{\mathcal{S}} B C_\ell^{ij,cor}. \tag{4.47}$$

The spectra $C_\ell^{ij,ad1}$ and $C_\ell^{ij,ad2}$ are generated from pure adiabatic perturbations (they are essentially the same except their spectral indices being different); likewise $C_\ell^{ij,iso}$ is generated from pure isocurvature perturbations.

In this analysis we shall assume there is no correlation between adiabatic and isocurvature modes. For simplicity we will also consider the adiabatic mode and one isocurvature mode at a time. Therefore we parameterize the contribution of the adiabatic and isocurvature modes to the total temperature and polarization power spectra by

$$C_\ell^X = A_s^2 \left[(1-\alpha)\hat{C}_\ell^{X,\mathrm{Ad}} + \alpha \hat{C}_\ell^{X,\mathrm{Iso}}\right], \tag{4.48}$$

where α is the isocurvature fraction. The adiabatic spectra, $\hat{C}_\ell^{X,\mathrm{Ad}}$, and the isocurvature spectra, $\hat{C}_\ell^{X,\mathrm{Iso}}$, are defined with unit amplitude.

We analyze the QUaD $TT/TE/EE/BB$ power spectra combined with WMAP5, and combined with the WMAP5 plus the SDSS LRG data. The shape of the galaxy power spectrum is sensitive to an isocurvature contribution, and has been used in the past to improve on isocurvature constraints (e.g. Beltran et al., 2004, 2005; Crotty et al., 2003). The results we obtain are given in Table 4.5 for the CDMI mode, in Table 4.6 for the NDI mode and in Table 4.7 for the NVI mode.

Our analysis shows an improvement in the isocurvature contribution when we add the QUaD data to the WMAP5 data, from $\alpha_{\mathrm{cdmi}} < 0.21$ to $\alpha_{\mathrm{cdmi}} < 0.19$ where we quote 95% confidence

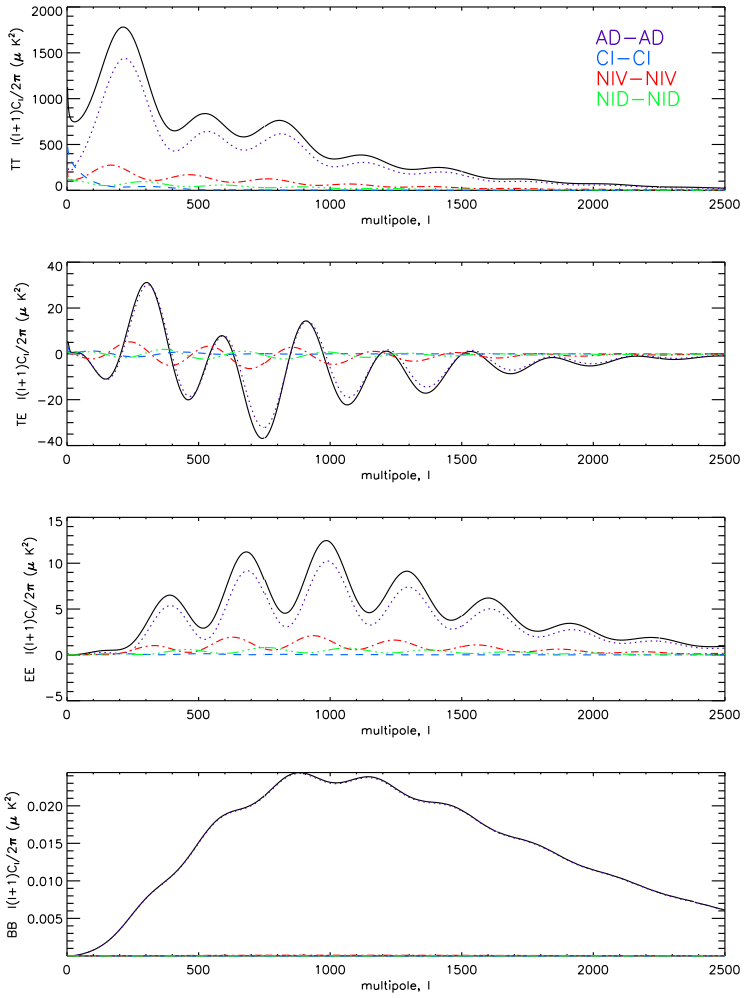

Figure 4.17: Figure shows the auto-correlation power spectra of the adiabatic (dotted), CDM (dashed) isocurvature, neutrino velocity (dot-dashed) and neutrino density (dot-dot-dashed) isocurvature modes for the case when they each equally contribute (25%) to the total primordial perturbation. The solid lines represent the superposition spectra of the different modes. The baryon isocurvature mode has not been considered here its spectra are essentially similar to the CDM isocurvature mode but a factor of Ω_c/Ω_b smaller in amplitude.

limits. In addition we find an improvement on the $\Omega_b h^2$ and $\Omega_m h^2$ error bars. There is a similar improvement for the neutrino density isocurvature constraints: we go from $\alpha_{\rm ndi} < 0.38$ to $\alpha_{\rm ndi} < 0.37$. For the neutrino velocity isocurvature there is no improvement, the constraint staying at $\alpha_{\rm nvi} < 0.27$.

We can further improve on these results by adding the SDSS LRG data. The cold dark matter constraint becomes $\alpha_{\rm cdmi} < 0.11$ (95 % confidence limit). We find the largest improvement when we add in the SDSS data is for the neutrino density isocurvature mode, $\alpha_{\rm ndi} < 0.26$, while the smallest improvement is for the neutrino velocity isocurvature mode, $\alpha_{\rm nvi} < 0.23$.

Table 4.5. CDM Isocurvature mean parameter constraints for QUaD $TT/TE/EE/BB$, WMAP5 and SDSS LRG data.

Symbol	Q08+WMAP5	Q08+WMAP5+SDSS	WMAP5
$\Omega_b h^2$	$0.02312\ ^{+0.00080}_{-0.00081}$	0.02280 ± 0.00070	$0.02362\ ^{+0.00096}_{-0.00094}$
$\Omega_m h^2$	$0.1214\ ^{+0.0067}_{-0.0068}$	$0.1256\ ^{+0.0038}_{-0.0037}$	$0.1279\ ^{+0.0072}_{-0.0071}$
h	0.773 ± 0.039	0.746 ± 0.022	0.759 ± 0.041
τ	0.087 ± 0.017	$0.084\ ^{+0.016}_{-0.016}$	0.087 ± 0.017
A_s[a]	0.786 ± 0.037	$0.797\ ^{+0.031}_{-0.030}$	0.789 ± 0.038
n_s[a]	0.987 ± 0.023	$0.976\ ^{+0.018}_{-0.017}$	$0.998\ ^{+0.027}_{-0.026}$
$\alpha_{\rm cdmi}$ (95 % cl)	< 0.19	< 0.11	< 0.21

[a]The pivot point for A_s and n_s for all isocurvature constraints is $k_p = 0.002$ Mpc^{-1} for QUaD, WMAP and SDSS data.

Table 4.6. NDI Isocurvature mean parameter constraints for QUaD $TT/TE/EE/BB$, WMAP5 and SDSS LRG data.

Symbol	Q08+WMAP5	Q08+WMAP5+SDSS	WMAP5
$\Omega_b h^2$	0.02370 ± 0.00110	0.02300 ± 0.00080	$0.02410\ ^{+0.00130}_{-0.00120}$
$\Omega_m h^2$	$0.1200\ ^{+0.0073}_{-0.0072}$	0.1261 ± 0.0039	$0.1270\ ^{+0.0075}_{-0.0077}$
h	0.800 ± 0.030	$0.751\ ^{+0.027}_{-0.025}$	$0.780\ ^{+0.058}_{-0.055}$
τ	0.090 ± 0.017	0.085 ± 0.016	0.090 ± 0.017
A_s	0.869 ± 0.058	$0.855\ ^{+0.053}_{-0.051}$	0.872 ± 0.059
n_s	$0.995\ ^{+0.0271}_{-0.0252}$	$0.976\ ^{+0.020}_{-0.017}$	$1.003\ ^{+0.031}_{-0.030}$
$\alpha_{\rm ndi}$ (95 % cl)	< 0.37	< 0.26	< 0.38

Table 4.7. NVI Isocurvature mean parameter constraints for QUaD $TT/TE/EE/BB$, WMAP5 and SDSS LRG data.

Symbol	Q08+WMAP5	Q08+WMAP5+SDSS	WMAP5
$\Omega_b h^2$	0.02350 ± 0.00090	$0.02339\ ^{+0.00080}_{-0.00070}$	0.02390 ± 0.00100
$\Omega_m h^2$	0.1260 ± 0.0060	0.1277 ± 0.0040	0.1330 ± 0.0063
h	0.745 ± 0.029	0.734 ± 0.018	$0.728\ ^{+0.027}_{-0.028}$
τ	0.088 ± 0.017	$0.087\ ^{+0.016}_{-0.015}$	0.089 ± 0.018
A_s	$0.851\ ^{+0.048}_{-0.047}$	$0.854\ ^{+0.044}_{-0.045}$	0.859 ± 0.048
n_s	$0.980\ ^{+0.017}_{-0.018}$	$0.978\ ^{+0.015}_{-0.014}$	$0.988\ ^{+0.019}_{-0.018}$
$\alpha_{\rm nvi}(95\%cl)$	< 0.27	< 0.23	< 0.27

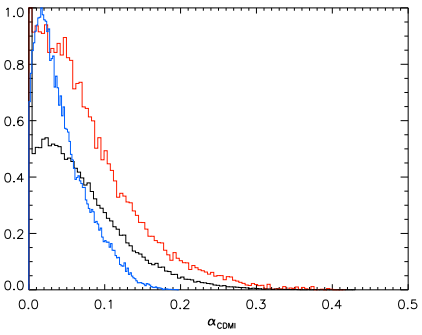

(a) CDM

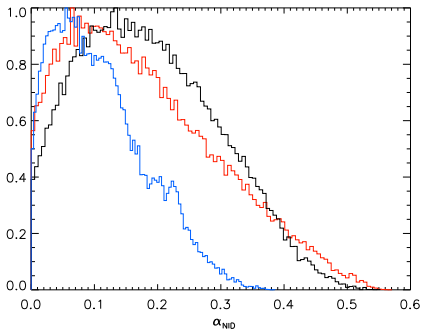

(b) NDI

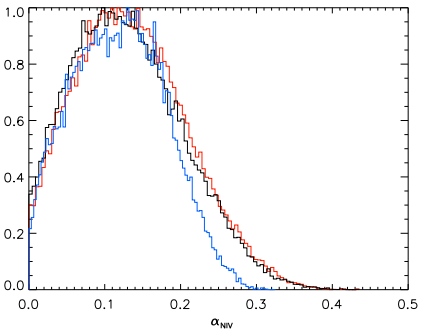

(c) NVI

Figure 4.18: 1D marginalized distributions for isocurvature constraints from QUaD combined with WMAP5 (black), combined with WMAP5 and SDSS (blue), as compared to WMAP5 only constraints (red).

Table 4.8. Gravitational lensing constraints from QUaD TT-TE-EE-BB combined spectra and WMAP 5yr.

Symbol	Q08+WMAP5	WMAP5
$\Omega_b h^2$	$0.02234\ ^{+0.00056}_{-0.00058}$	$0.02273\ ^{+0.00064}_{-0.00063}$
$\Omega_m h^2$	0.1262 ± 0.0060	0.1332 ± 0.0065
h	$0.734\ ^{+0.028}_{-0.027}$	0.746 ± 0.022
τ	0.087 ± 0.017	0.088 ± 0.017
A_s[a]	0.803 ± 0.038	$0.812\ ^{+0.039}_{-0.038}$
n_s[a]	$0.961\ ^{+0.014}_{-0.013}$	$0.969\ ^{+0.014}_{-0.015}$
$q_{\rm lens}$	$1.10\ ^{+0.63}_{-0.62}$	$1.53\ ^{+0.65}_{-0.69}$

[a]The pivot point for A_s and n_s is $k_p = 0.002$ Mpc^{-1} for both QUaD and WMAP data.

Gravitational Lensing, $q_{\rm lens}$

In this section we use the QUaD and WMAP5 data sets to put constraints on the level of gravitational lensing in the CMB. The effect of the gravitational lensing is very small on the CMB power spectra and it is only significant in the B mode polarization. QUaD also only provides upper limits on the BB spectrum, however its high precision data for TT, TE and EE spectra can help to constrain the gravitational lensing. We parameterize the gravitational lensing effect by defining the total power spectra as

$$C_\ell^X = \hat{C}_\ell^{X,\rm Unlensed} + q_{\rm lens}(\hat{C}_\ell^{X,\rm Lensed} - \hat{C}_\ell^{X,\rm Unlensed}), \tag{4.49}$$

where the superscripts 'Lensed' and 'Unlensed' refer to spectra calculated with and without assuming gravitational lensing effect. The $q_{\rm lens}$ is the parameter which we want to constrain. Hence, a value of $q_{\rm lens} = 1$ is expected for a cosmological model which favors the gravitational lensing. We have added $q_{\rm lens}$ as an extra parameter in the MCMC analysis and have used WMAP5 data only and in combination with QUaD to constrain this parameter. The results are shown in Table 4.8. We find that adding QUaD pushes the $q_{\rm lens}$ bestfit value towards unity, form 1.53 for WMAP5 only, to 1.10 for WMAP5 in combination with QUaD. There is also a slight improvement in the 1 sigma error bars of the parameters. This result is impressive since it means that QUaD data is consistent with the standard ΛCDM model. The improvement which we see in the bestfit $q_{\rm lens}$ value is due to the fact that WMAP is only robust on large scales, while QUaD 2008 data probes a wide range of multipoles and particularly the small scales where the gravitational lensing is most important.

4.4 Conclusions

We have presented a cosmological parameter estimation analysis using the QUaD temperature and polarization combined 100GHz, 150GHz and 100/150GHz bandpower spectra, $\hat{C}_\ell^{TT}$, $\hat{C}_\ell^{EE}$, $\hat{C}_\ell^{BB}$ and $\hat{C}_\ell^{TE}$, each power spectrum measured in 23 bandpower over angular multipoles from $\ell = 164$ to $\ell = 2026$) from Season 2 and 3 of the QUaD survey. The QUaD data set is the first CMB polarization data set to detect the anticipated acoustic oscillations in the EE-power spectra and so the first to provide meaningful constraints on cosmological parameters from CMB polarization alone.

We have developed an MCMC maximum likelihood analysis, with analytic marginalization over nuisance parameters, and used it to constrain the standard 6-parameter flat ΛCDM model. We have verified our statistics by running an ensemble of simulations and we concluded that our methodology is unbiased and overall recovers the input WMAP 3yr model from the simulations. However, the constraining power from QUaD alone is not sufficient to determine the highly degenerate scalar amplitude and optical depth parameters independently. As a result we projected these two parameters on one combined parameter $A_s e^{-2\tau}$ which we determine without any bias.

We find our temperature data is in good agreement with the results from WMAP5. Our polarization data is also in agreement, but the baryon density is marginally higher, which seems to originate from the TE data. A χ^2 analysis shows there is a 11.36% probability of the QUaD bandpowers arising by chance, assuming the ΛCDM with WMAP5-parameters model is correct. The combined TE/EE/BB χ^2 fit with this model yields 7.07% probability for QUaD to arise by chance. This shows that, while we find tension with WMAP5 parameters, the level of disagreement is not significant. It will be interesting to see if this trend continues in future polarization experiments.

We also combined QUaD with WMAP 5yr and SDSS data sets and extended our parameter analysis to include a tensor-to-scalar ratio parameter, isocurvature fractions and the gravitational lensing contribution. We found that QUaD marginally increases the WMAP5 95% upper limit on the tensor-to-scalar ratio, however the discrepancy is not significant to point at large systematics. We also found that QUaD reduces the 95% constraint on the fractional cold dark matter isocurvature mode, $r_{\rm cdmi}$, from < 0.21 for WMAP5 alone to < 0.19, an improvement of 6%. The neutrino density and velocity isocurvature mode constraints are nearly unaffected by adding QUaD. However, we found that all the upper limits drop significantly when we add SDSS data. We also defined a quantity, $q_{\rm lens}$, to parameterize the gravitational lensing contribution in the CMB, and we found that adding QUaD substantially improves the gravitational lensing constraint, making it more consistent with the expectations from the ΛCDM model.

Chapter 5

A Flat-Sky Pseudo-C_ℓ Approach

The angular power spectra have become the conventional way of compacting the information in the CMB. The power spectra not only are useful since they encapsulate the scale-dependent features of the CMB which can be probed directly by the linear cosmological theory, but also since they have proved to be advantageous for the purpose of parameter estimation (see §4). Without the power spectra one has to resort to the CMB sky maps in order to infer information about the cosmological parameters. This approach can be extremely slow and not feasible for mega-pixel maps. In this way the power spectrum analysis has become the standard way of representing the CMB anisotropies, especially since the fluctuations are supposed to be highly Gaussian.

To estimate the power spectra there have developed two main methods. The traditional way of calculating the C_ℓ is based on the maximum likelihood analysis of the observed time ordered data or pixelized maps on the sky. Given a data vector $\mathbf{x}$ of size $N_{\rm pix}$ one can define a likelihood function of the form

$$\mathcal{L}(C_\ell|\mathbf{x}) = \frac{\exp\big(-\frac{1}{2}\mathbf{x}^T C^{-1}\mathbf{x}\big)}{(2\pi)^{N_{\rm pix}/2}|C|^{1/2}}, \tag{5.1}$$

which assumes Gaussian errors on $\mathbf{x}$. Here the covariance matrix C is

$$C_{ij} = \langle x_i x_j\rangle = S_{ij}(C_\ell) + N_{ij}. \tag{5.2}$$

Here S is the signal matrix which is a function of C_ℓ, while N is the noise matrix. Then an estimator of the power spectrum is defined by the C_ℓ which maximizes the likelihood function (5.1). For a complete sky coverage it turns out that the estimators (3.45) are the maximum likelihood estimators for C_ℓ. However, for incomplete sky coverage, which is almost always

the case, we should specifically maximize the likelihood (5.1) to construct the C_ℓ. Brute force methods in combination with analytical approximations can be applied to the maximum likelihood estimators in order to investigate large ensembles of possible spectra (see e.g. Bond et al., 1998). However, although this method can be very optimal in determining the C_ℓ, it requires the inversion of $N_{\rm pix} \times N_{\rm pix}$ covariance matrices which is prohibitively slow and impractical for maps of large pixel number.

An alternative method of constructing estimators for C_ℓ is the pseudo-C_ℓ (or PCL) methods. These are the variants of the same estimators of Eq. (3.45) which are defined on the region of sky which is covered by the experiment. So they are biased since they are extracted from incomplete data. The pseudo-C_ℓ methods have been discussed in Wandelt et al. (2000) who also examined the statistics of the estimators as well as their applications to parameter estimation. Although these methods lead to results which are sub-optimal to those of maximum likelihood estimators they are fast and flexible. They can be applied to any type of CMB experiment with any survey geometry or noise pattern. Variants of the pseudo-C_ℓ estimators can be proposed to account for the effect of the incomplete sky coverage in order to recover the true underlying power spectra (see e.g. Hivon et al., 2002). In short, PCL-based methods and particularly their hybrid use with maximum likelihood methods (Efstathiou, 2004, 2006) are presently the best available methods for the power spectrum estimation of the CMB data.

In this chapter we will propose a new promising semi-analytical method for the pseudo-C_ℓ estimators in the flat sky approximation and will investigate the implications of these for the recovery of the unbiased bandpowers and the calculation of the PCL covariances. In section 5.1 we outline the analytical formula that we use to construct the mode-mode coupling matrices in the flat sky limit. We explain in detail in section 5.2 how we implement this method to recover the unbiased bandpowers from QUaD-like simulations. In section 5.3 we extend the flat sky approach to the power spectra covariances estimation and explain how we attempt to calculate the exact covariance matrices numerically.

5.1 Pseudo-C_ℓ Estimators in Flat-Sky

The PCL methods are presently the fastest optimal method available for power spectrum estimation. For an experiment with incomplete sky coverage one main issue regarding the PCL methods is the effect of the window function. The window function mixes and smears the temperature and polarization modes on the cut sky. Nevertheless, it has turned out that these window function and boundary effects can be corrected for by implementing analytical methods. These generally involve constructing coupling kernels which can be used to deconvolve the effects of the window functions and recover the underlying full-sky bandpowers. Although most of the work which has been done in this area focuses on the temperature pseudo-C_ℓ estimators (see e.g. Hansen et al., 2002; Hivon et al., 2002), there are well-tested methods which provide coupling matrices for polarization as well (see Hansen and Górski, 2003; Challinor and Chon,

2005; Brown et al., 2005).

In this section we propose a semi-analytical method for the calculation of the mode-mode coupling kernels in the flat approximation. Our analysis is most similar to the curved-sky analysis of Brown et al. (2005), however it can be easier to implement in the sense that in flat-sky the spherical harmonics expansion reduces to the Fourier transform. This is especially advantageous over the curved sky method since it can be easily implemented by the Fast Fourier Transform techniques. In the next section we present the results of a novel implementation of this method and we will show that the coupling matrices are invertible and that we can consistently recover the unbiased temperature and E-mode polarization bandpowers from simulated QUaD experiment pseudo-C_ℓ's.

The Cosmic Microwave Background is characterized by its temperature and polarization at any direction $\hat{n}$ of the sky. We are interested in small scale approximation in which case $\hat{n}$ is close to $\hat{z}$. In this limit we can parameterize the anisotropies by the angular vector $\boldsymbol{\theta}$ in a plane perpendicular to the direction of the propagation $\hat{z}$. In flat sky the spherical harmonics expansion reduces to plane wave expansion (Hu, 2000)

$$\sum_{\ell m} a^X_{\ell m} Y_{\ell m}(\hat{n}) \rightarrow \int d^2\ell X(\boldsymbol{\ell}) e^{i\boldsymbol{\ell}\cdot\boldsymbol{\theta}}, \tag{5.3}$$

for X being a spin-0 quantity. In this case we represent the temperature fluctuation $T(\boldsymbol{\theta})$ by the Fourier space expansion

$$T(\boldsymbol{\theta}) = \int \frac{d^2\ell}{(2\pi)^2} T(\boldsymbol{\ell}) e^{i\boldsymbol{\ell}\cdot\boldsymbol{\theta}} \tag{5.4}$$

where the inverse transform is

$$T(\boldsymbol{\ell}) = \int d^2\theta T(\boldsymbol{\theta}) e^{-i\boldsymbol{\ell}\cdot\boldsymbol{\theta}}. \tag{5.5}$$

$Q(\boldsymbol{\theta})$ and $U(\boldsymbol{\theta})$ are also real scalar quantities whose projection on the tangent plane is similar to that of the temperature:

$$Q(\boldsymbol{\ell}) = \int d^2\theta Q(\boldsymbol{\theta}) e^{-i\boldsymbol{\ell}\cdot\boldsymbol{\theta}}, \qquad U(\boldsymbol{\ell}) = \int d^2\theta U(\boldsymbol{\theta}) e^{-i\boldsymbol{\ell}\cdot\boldsymbol{\theta}}. \tag{5.6}$$

The polarization of the CMB is a spin-2 variable which can be represented by a single complex quantity, $P(\boldsymbol{\theta}) \equiv Q(\boldsymbol{\theta}) + iU(\boldsymbol{\theta})$. To find an expression for polarization first note that using the relations (3.34) the spherical harmonics satisfy

$$\begin{aligned}
{}_2Y_{\ell m} &= [(\ell-2)!/(\ell+2)!]^{1/2}\, \eth\, \eth\, Y_{\ell m}, & (5.7)\\
{}_{-2}Y_{\ell m} &= [(\ell-2)!/(\ell+2)!]^{1/2}\, \bar{\eth}\, \bar{\eth}\, Y_{\ell m}, & (5.8)\\
\bar{\eth}\, \bar{\eth}\, \eth\, \eth Y_{\ell m} &= \eth\, \eth\, \bar{\eth}\, \bar{\eth}\, Y_{\ell m} = \frac{(\ell+2)!}{(\ell-2)!} Y_{\ell m}. & (5.9)
\end{aligned}$$

Substituting Eqs. (5.7) and (5.8) into Eq. (3.35) it is easy to show that

$$\begin{aligned}
Q + iU = \eth\, \eth\, (\psi_E + i\psi_B) \quad &; \quad Q - iU = \bar{\eth}\, \bar{\eth}\, (\psi_E - i\psi_B)\\
\psi_E = \sum_{\ell m} \Big[\frac{(\ell-2)!}{(\ell+2)!}\Big]^{1/2} E_{\ell m} Y_{\ell m} \quad &; \quad \psi_B = \sum_{\ell m} \Big[\frac{(\ell-2)!}{(\ell+2)!}\Big]^{1/2} B_{\ell m} Y_{\ell m}.
\end{aligned} \tag{5.10}$$

The above relations are analogous to the fact that we can decompose a vector field into gradient and curl components. The potentials ψ_E and ψ_B transform under parity operation as scalar and pseudoscalar quantities respectively. They are directly related to E and B modes through

$$E \equiv \eth\,\bar{\eth}\,\psi_E, \tag{5.11}$$

$$B \equiv \eth\,\bar{\eth}\,\psi_B. \tag{5.12}$$

Now substituting Eqs. (5.11) and (5.12) into Eqs. (5.10) the polarization will take the form

$$(Q+iU)(\boldsymbol{\theta}) = \eth\,\eth\,\eth^{-2}(E+iB)(\boldsymbol{\theta}), \tag{5.13}$$

where $\eth^2 \equiv \eth\,\bar{\eth}$. We can use this relation to express the electric and magnetic modes of the polarization in terms of the Stokes parameters in the flat sky

$$E(\boldsymbol{\theta}) + iB(\boldsymbol{\theta}) \equiv \bar{\eth}\,\bar{\eth}\,\eth^{-2}(Q+iU)(\boldsymbol{\theta}), \tag{5.14}$$

Therefore the rotationally invariant quantities E and B have common power spectra with Q and U on small angle limit. In 2D Euclidean space the raising and lowering operators become complex gradients (Castro et al., 2005)

$$\partial = \partial_x + i\partial_y, \qquad \partial^* = \partial_x - i\partial_y, \tag{5.15}$$

with $\partial^2 = \partial\partial^*$ being the Laplacian operator. We take our global polarization basis to be a coordinate system whose x and y axes form a right-handed coordinate with the radiation propagation direction which defines the z-axis. In Fourier space, the derivatives (5.15) act like

$$\partial e^{i\boldsymbol{\ell}\cdot\boldsymbol{\theta}} = i\ell e^{i\boldsymbol{\ell}\cdot\boldsymbol{\theta}}, \qquad \partial^* e^{i\boldsymbol{\ell}\cdot\boldsymbol{\theta}} = i\ell^* e^{i\boldsymbol{\ell}\cdot\boldsymbol{\theta}}, \tag{5.16}$$

with $\ell = \ell_x + i\ell_y$ and $\ell^* = \ell_x - i\ell_y$. Hence, applying these relations to Eq. (5.14) reduces it in the Fourier space to

$$E(\boldsymbol{\ell}) + iB(\boldsymbol{\ell}) = \ell^*\ell^*|\ell|^{-2}(Q+iU)(\boldsymbol{\ell}). \tag{5.17}$$

We further specify ℓ in terms of polar coordinates where $\ell = |\ell|e^{i\varphi_\ell}$ and φ_ℓ is the angle between $\boldsymbol{\ell}$ and x-axis. Equation (5.17) and its complex conjugate can be written as

$$E(\boldsymbol{\ell}) \pm iB(\boldsymbol{\ell}) = e^{\mp 2i\varphi_\ell}(Q \pm iU)(\boldsymbol{\ell}). \tag{5.18}$$

Equation (5.18) has the simple interpretation that in Fourier space $E \pm iB$ is just a rotation of $Q \pm iU$.

Here we are especially interested in the effect of the limited sky coverage on the measurements of the auto- and cross-correlation power spectra. To relate the observed fields on the cut-sky to the true all-sky fields one usually defines finite window functions which weight the underlying temperature and polarization fluctuations. For a scalar field the effect of the window functions is multiplicative, therefore

$$\tilde{T}(\boldsymbol{\theta}) = W_T(\boldsymbol{\theta})T(\boldsymbol{\theta}), \qquad \tilde{Q}(\boldsymbol{\theta}) = W_P(\boldsymbol{\theta})Q(\boldsymbol{\theta}), \qquad \tilde{U}(\boldsymbol{\theta}) = W_P(\boldsymbol{\theta})U(\boldsymbol{\theta}), \tag{5.19}$$

where we have taken the window functions to be different for temperature and Stokes parameters. Here tilde refers to fluctuations observed on the cut-sky. The Fourier transform of the cut-sky temperature field is given by the convolution

$$\begin{aligned}\tilde{T}(\boldsymbol{\ell}) &= \int d^2\theta W_T(\boldsymbol{\theta})T(\boldsymbol{\theta})e^{-i\boldsymbol{\ell}\cdot\boldsymbol{\theta}} \\ &= \int \frac{d^2\ell'}{(2\pi)^2}W_T(\boldsymbol{\ell}-\boldsymbol{\ell'})T(\boldsymbol{\ell'}),\end{aligned} \tag{5.20}$$

where $W_T(\boldsymbol{\ell})$ is the Fourier transform of the temperature window function $W_T(\boldsymbol{\theta})$. We can obtain similar equations for cut-sky Stokes parameters:

$$\tilde{Q}(\boldsymbol{\ell}) = \int \frac{d^2\ell'}{(2\pi)^2}W_P(\boldsymbol{\ell}-\boldsymbol{\ell'})Q(\boldsymbol{\ell'}), \qquad \tilde{U}(\boldsymbol{\ell}) = \int \frac{d^2\ell'}{(2\pi)^2}W_P(\boldsymbol{\ell}-\boldsymbol{\ell'})U(\boldsymbol{\ell'}). \tag{5.21}$$

Combining these equations and substituting from equation (5.18) we can find an expression for the cut-sky electric and magnetic modes:

$$\tilde{E}(\boldsymbol{\ell}) \pm i\tilde{B}(\boldsymbol{\ell}) = \int \frac{d^2\ell'}{(2\pi)^2}e^{\mp 2i(\varphi_\ell-\varphi_{\ell'})}W_P(\boldsymbol{\ell}-\boldsymbol{\ell'})\Big(E(\boldsymbol{\ell'}) \pm iB(\boldsymbol{\ell'})\Big), \tag{5.22}$$

or equivalently

$$\tilde{E}(\boldsymbol{\ell}) = \int \frac{d^2\ell'}{(2\pi)^2}W_P(\boldsymbol{\ell}-\boldsymbol{\ell'})[\cos 2(\varphi_\ell-\varphi_{\ell'})E(\boldsymbol{\ell'}) + \sin 2(\varphi_\ell-\varphi_{\ell'})B(\boldsymbol{\ell'})], \tag{5.23}$$

$$\tilde{B}(\boldsymbol{\ell}) = \int \frac{d^2\ell'}{(2\pi)^2}W_P(\boldsymbol{\ell}-\boldsymbol{\ell'})[\cos 2(\varphi_\ell-\varphi_{\ell'})B(\boldsymbol{\ell'}) - \sin 2(\varphi_\ell-\varphi_{\ell'})E(\boldsymbol{\ell'})]. \tag{5.24}$$

Equation (5.22) again has the simple interpretation of a rotation of $E+iB$ to $Q+iU$ in Fourier space, then a convolution with the window function, followed by a second rotation back to $\tilde{E}+i\tilde{B}$.

In 2D Fourier space, the auto- and cross-power spectra are defined by

$$\langle X_i(\boldsymbol{\ell})X_j^*(\boldsymbol{\ell'})\rangle = (2\pi)^2 C_\ell^{X_iX_j}\delta_D(\boldsymbol{\ell}-\boldsymbol{\ell'}), \tag{5.25}$$

where X_i represents T, E and B modes, and the angle brackets denote ensemble average. An unbiased estimator of these in the flat sky limit is given by

$$\langle C_\ell^{X_iX_j}\rangle = \int \frac{d\varphi_\ell}{2\pi}\langle X_i(\boldsymbol{\ell})X_j^*(\boldsymbol{\ell})\rangle. \tag{5.26}$$

Note that this is the ensemble average of the the estimators (3.45) which is defined on the continuous plane. To verify that this convention is true and consistent with our definition of the Fourier transform we can note that the variance of the temperature fluctuations is given by

$$\begin{aligned}\sigma^2 &\equiv \int \frac{d^2\ell}{(2\pi)^2}\int \frac{d^2\ell'}{(2\pi)^2}\langle X(\boldsymbol{\ell})X^*(\boldsymbol{\ell'})\rangle e^{i(\boldsymbol{\ell}-\boldsymbol{\ell'})\cdot\boldsymbol{\theta}} \\ &= \int \frac{d\ell}{2\pi}\ell C_\ell \approx \int d(\ln\ell)\Big[\frac{\ell(\ell+1)C_\ell}{2\pi}\Big],\end{aligned} \tag{5.27}$$

which gives the same power per logarithmic interval term of equation (2.217).

We now write the pseudo-C_ℓ's in terms of the full sky power spectra $C_\ell = \langle \hat{C}_\ell \rangle$. The temperature auto-correlation power spectrum can be obtained by substituting equation (5.20) into equation (5.26). We will have

$$\begin{aligned}\langle \tilde{C}_\ell^{TT} \rangle &= \int \frac{d\varphi_\ell}{2\pi} \langle |\tilde{T}(\boldsymbol{\ell})|^2 \rangle \\ &= \int \frac{d\varphi_\ell}{2\pi} \int \frac{d^2\ell'}{(2\pi)^2} \int \frac{d^2\ell''}{(2\pi)^2} W_T(\boldsymbol{\ell}-\boldsymbol{\ell'}) W_T(\boldsymbol{\ell}-\boldsymbol{\ell''}) \langle T(\boldsymbol{\ell'}) T^*(\boldsymbol{\ell''}) \rangle \\ &= \int \frac{d\varphi_\ell}{2\pi} \int \frac{d\ell' \ell' d\varphi_{\ell'}}{(2\pi)^2} |W_T(\boldsymbol{\ell}-\boldsymbol{\ell'})|^2 \langle \hat{C}_{\ell'}^{TT} \rangle. \end{aligned} \tag{5.28}$$

In the above the square of the window function can be written in the form

$$\begin{aligned}|W_T(\boldsymbol{\ell}-\boldsymbol{\ell'})|^2 &= \int d^2L |W_T(\boldsymbol{L})|^2 \delta^2(\boldsymbol{L}-(\boldsymbol{\ell}-\boldsymbol{\ell'})) \\ &= \int d^2L |W_T(\boldsymbol{L})|^2 \int \frac{d^2\theta}{(2\pi)^2} e^{-i\boldsymbol{\theta}\cdot\left(\boldsymbol{L}-(\boldsymbol{\ell}-\boldsymbol{\ell'})\right)}. \end{aligned} \tag{5.29}$$

Substituting this in equation (5.28) we obtain

$$\begin{aligned}\langle \tilde{C}_\ell^{TT} \rangle &= \int dLL \Big[\int \frac{d\varphi_L}{2\pi} |W_T(\boldsymbol{L})|^2 \Big] \\ &\times \Big\{ \int \frac{d\ell' \ell'}{(2\pi)^2} \Big(\int d^2\theta e^{-i\boldsymbol{\theta}\cdot\boldsymbol{L}} \Big) \int \frac{d\varphi_\ell}{2\pi} \int \frac{d\varphi_{\ell'}}{2\pi} e^{i\boldsymbol{\theta}\cdot\boldsymbol{\ell}} e^{-i\boldsymbol{\theta}\cdot\boldsymbol{\ell'}} \Big\} \langle \hat{C}_{\ell'}^{TT} \rangle, \end{aligned} \tag{5.30}$$

where we have also decomposed $d^2L = dLLd\varphi_L$. Inside the curly bracket we can keep $\boldsymbol{L}$ constant. We can therefore integrate the angular part in the parenthesis, which leads to

$$\int d^2\theta e^{-i\boldsymbol{\theta}\cdot\boldsymbol{L}} = 2\pi \int_0^\infty d\theta\theta J_0(L\theta), \tag{5.31}$$

where $J_0(L\theta)$ is the Bessel function of order zero. Substituting equation (5.31) into equation (5.30) we can write the temperature auto-correlation pseudo-power spectrum as

$$\begin{aligned}\langle \tilde{C}_\ell^{TT} \rangle &= \int \frac{d\ell' \ell'}{(2\pi)^2} \int dLL \Big[\int \frac{d\varphi_L}{2\pi} |W_T(\boldsymbol{L})|^2 \Big] \\ &\times \Big\{ 2\pi \int d\theta\theta J_0(L\theta) \int \frac{d\varphi_\ell}{2\pi} \int \frac{d\varphi_{\ell'}}{2\pi} e^{i\boldsymbol{\theta}\cdot\boldsymbol{\ell}} e^{-i\boldsymbol{\theta}\cdot\boldsymbol{\ell'}} \Big\} \langle \hat{C}_{\ell'}^{TT} \rangle. \end{aligned} \tag{5.32}$$

In the same way, we can substitute T, E and B modes from equations (5.20), (5.23) and (5.24) into equation (5.26) to calculate other auto- and cross- power spectra. These can be shown to reduce to

$$\begin{aligned}\langle \tilde{C}_\ell^{TE} \rangle &= \int \frac{d\varphi_\ell}{2\pi} \langle |\tilde{T}(\boldsymbol{\ell}) \tilde{E}^*(\boldsymbol{\ell})| \rangle \\ &= \int \frac{d\ell' \ell'}{2\pi} \int dLL \Big[\int \frac{d\varphi_L}{2\pi} |W_T(\boldsymbol{L}) W_P^*(\boldsymbol{L})| \Big] \Big\{ \int d\theta\theta J_0(L\theta) \int \frac{d\varphi_\ell}{2\pi} \int \frac{d\varphi_{\ell'}}{2\pi} e^{i\boldsymbol{\theta}\cdot\boldsymbol{\ell}} e^{-i\boldsymbol{\theta}\cdot\boldsymbol{\ell'}} \\ &\times \Big[\cos 2(\varphi_\ell - \varphi_{\ell'}) \langle \hat{C}_{\ell'}^{TE} \rangle + \sin 2(\varphi_\ell - \varphi_{\ell'}) \langle \hat{C}_{\ell'}^{TB} \rangle \Big] \Big\}, \end{aligned} \tag{5.33}$$

$$\langle \tilde{C}_\ell^{TB} \rangle = \int \frac{d\varphi_\ell}{2\pi} \langle |\tilde{T}(\boldsymbol{\ell}) \tilde{B}^*(\boldsymbol{\ell})| \rangle$$
$$= \int \frac{d\ell' \ell'}{2\pi} \int dLL \Big[\int \frac{d\varphi_L}{2\pi} |W_T(\boldsymbol{L}) W_P^*(\boldsymbol{L})| \Big] \Big\{ \int d\theta\theta J_0(L\theta) \int \frac{d\varphi_\ell}{2\pi} \int \frac{d\varphi_{\ell'}}{2\pi} e^{i\boldsymbol{\theta}\cdot\boldsymbol{\ell}} e^{-i\boldsymbol{\theta}\cdot\boldsymbol{\ell'}}$$
$$\times \Big[\cos 2(\varphi_\ell - \varphi_{\ell'}) \langle \hat{C}_{\ell'}^{TB} \rangle - \sin 2(\varphi_\ell - \varphi_{\ell'}) \langle \hat{C}_{\ell'}^{TE} \rangle \Big] \Big\}, \tag{5.34}$$

$$\langle \tilde{C}_\ell^{EE} \rangle = \int \frac{d\varphi_\ell}{2\pi} \langle |\tilde{E}(\boldsymbol{\ell})|^2 \rangle$$
$$= \int \int d\ell' \ell' 2\pi \int dLL \Big[\int \frac{d\varphi_L}{2\pi} |W_P(\boldsymbol{L})|^2 \Big] \Big\{ \int d\theta\theta J_0(L\theta) \int \frac{d\varphi_\ell}{2\pi} \int \frac{d\varphi_{\ell'}}{2\pi} e^{i\boldsymbol{\theta}\cdot\boldsymbol{\ell}} e^{-i\boldsymbol{\theta}\cdot\boldsymbol{\ell'}}$$
$$\times \Big[\cos^2 2(\varphi_\ell - \varphi_{\ell'}) \langle \hat{C}_{\ell'}^{EE} \rangle + \sin 4(\varphi_\ell - \varphi_{\ell'}) \langle \hat{C}_{\ell'}^{EB} \rangle + \sin^2 2(\varphi_\ell - \varphi_{\ell'}) \langle \hat{C}_{\ell'}^{BB} \rangle \Big] \Big\}, \tag{5.35}$$

$$\langle \tilde{C}_\ell^{EB} \rangle = \int \frac{d\varphi_\ell}{2\pi} \langle |\tilde{E}(\boldsymbol{\ell}) \tilde{B}^*(\boldsymbol{\ell})| \rangle$$
$$= \int \frac{d\ell' \ell'}{2\pi} \int dLL \Big[\int \frac{d\varphi_L}{2\pi} |W_P(\boldsymbol{L})|^2 \Big] \Big\{ \int d\theta\theta J_0(L\theta) \int \frac{d\varphi_\ell}{2\pi} \int \frac{d\varphi_{\ell'}}{2\pi} e^{i\boldsymbol{\theta}\cdot\boldsymbol{\ell}} e^{-i\boldsymbol{\theta}\cdot\boldsymbol{\ell'}}$$
$$\times \Big[\frac{-1}{2} \sin 4(\varphi_\ell - \varphi_{\ell'}) \langle \hat{C}_{\ell'}^{EE} \rangle + \cos 4(\varphi_\ell - \varphi_{\ell'}) \langle \hat{C}_{\ell'}^{EB} \rangle + \frac{1}{2} \sin 4(\varphi_\ell - \varphi_{\ell'}) \langle \hat{C}_{\ell'}^{BB} \rangle \Big] \Big\}, \tag{5.36}$$

$$\langle \tilde{C}_\ell^{BB} \rangle = \int \frac{d\varphi_\ell}{2\pi} \langle |\tilde{B}(\boldsymbol{\ell})|^2 \rangle$$
$$= \int \frac{d\ell' \ell'}{2\pi} \int dLL \Big[\int \frac{d\varphi_L}{2\pi} |W_P(\boldsymbol{L})|^2 \Big] \Big\{ \int d\theta\theta J_0(L\theta) \int \frac{d\varphi_\ell}{2\pi} \int \frac{d\varphi_{\ell'}}{2\pi} e^{i\boldsymbol{\theta}\cdot\boldsymbol{\ell}} e^{-i\boldsymbol{\theta}\cdot\boldsymbol{\ell'}}$$
$$\times \Big[\sin^2 2(\varphi_\ell - \varphi_{\ell'}) \langle \hat{C}_{\ell'}^{EE} \rangle - \sin 4(\varphi_\ell - \varphi_{\ell'}) \langle \hat{C}_{\ell'}^{EB} \rangle + \cos^2 2(\varphi_\ell - \varphi_{\ell'}) \langle \hat{C}_{\ell'}^{BB} \rangle \Big] \Big\}. \tag{5.37}$$

In these equations we can easily calculate the angular integrals over φ_ℓ and $\varphi_{\ell'}$. These can be expressed in terms of the Bessel functions. The Bessel functions of order n are given by

$$J_n(z) = \frac{1}{2\pi i^n} \int_0^{2\pi} e^{iz\cos\varphi} e^{in\varphi} d\varphi, \tag{5.38}$$

where we also have $J_{-n}(z) = (-1)^n J_n(z)$. Substituting $\cos x = (e^{ix} + e^{-ix})/2$ and $\sin x = (e^{ix} - e^{-ix})/2i$ and using the trigonometric relations $\cos^2 x = (1+\cos 2x)/2$ and $\sin^2 x = (1-\cos 2x)/2$ wherever needed we can show that

$$\int \frac{d\varphi_\ell}{2\pi} \int \frac{d\varphi_{\ell'}}{2\pi} e^{i\theta\ell\cos\varphi_\ell} e^{-i\theta\ell'\cos\varphi_{\ell'}} = J_0(\ell\theta) J_0(\ell'\theta), \tag{5.39}$$

$$\int \frac{d\varphi_\ell}{2\pi} \int \frac{d\varphi_{\ell'}}{2\pi} e^{i\theta\ell\cos\varphi_\ell} e^{-i\theta\ell'\cos\varphi_{\ell'}} \cos 2(\varphi_\ell - \varphi_{\ell'}) = J_2(\ell\theta) J_2(\ell'\theta), \tag{5.40}$$

$$\int \frac{d\varphi_\ell}{2\pi} \int \frac{d\varphi_{\ell'}}{2\pi} e^{i\theta\ell\cos\varphi_\ell} e^{-i\theta\ell'\cos\varphi_{\ell'}} \sin 2(\varphi_\ell - \varphi_{\ell'}) = 0, \tag{5.41}$$

$$\int \frac{d\varphi_\ell}{2\pi} \int \frac{d\varphi_{\ell'}}{2\pi} e^{i\theta\ell\cos\varphi_\ell} e^{-i\theta\ell'\cos\varphi_{\ell'}} \cos^2 2(\varphi_\ell - \varphi_{\ell'}) = \frac{1}{2} \Big[J_0(\ell\theta) J_0(\ell'\theta) + J_4(l\theta) J_4(\ell'\theta) \Big], \tag{5.42}$$

$$\int \frac{d\varphi_\ell}{2\pi}\int \frac{d\varphi_{\ell'}}{2\pi} e^{i\theta\ell\cos\varphi_\ell} e^{-i\theta\ell'\cos\varphi_{\ell'}} \sin^2 2(\varphi_\ell-\varphi_{\ell'}) = \frac{1}{2}\Big[J_0(\ell\theta)J_0(\ell'\theta) - J_4(l\theta)J_4(\ell'\theta)\Big], \tag{5.43}$$

$$\int \frac{d\varphi_\ell}{2\pi}\int \frac{d\varphi_{\ell'}}{2\pi} e^{i\theta\ell\cos\varphi_\ell} e^{-i\theta\ell'\cos\varphi_{\ell'}} \cos 4(\varphi_\ell-\varphi_{\ell'}) = J_4(\ell\theta)J_4(\ell'\theta), \tag{5.44}$$

$$\int \frac{d\varphi_\ell}{2\pi}\int \frac{d\varphi_{\ell'}}{2\pi} e^{i\theta\ell\cos\varphi_\ell} e^{-i\theta\ell'\cos\varphi_{\ell'}} \sin 4(\varphi_\ell-\varphi_{\ell'}) = 0. \tag{5.45}$$

Using these relations in equations (5.32-5.37), the curly brackets can be written in terms of integrals over triple Bessel functions. They will take the form

$$\int_0^\infty d\theta\theta J_0(L\theta)J_n(\ell\theta)J_n(\ell'\theta) = \frac{\cos n\eta}{\pi\ell\ell'\sin\eta}. \tag{5.46}$$

The solutions to the above integrals have been given in formulae 6.578-8 and 6.578-9 of Gradshteyn and Ryzhik (1994). Note that we only take into account the solutions for which case ℓ, ℓ' and L form a triangle ($|\ell-\ell'| < L < \ell+\ell'$). This is because in equation (5.29) we have assumed that $\boldsymbol{L} = \boldsymbol{\ell}-\boldsymbol{\ell'}$. Other solutions are already equal to zero (see Gradshteyn and Ryzhik, 1994). Here the area of the triangle is given by $\frac{1}{2}\ell\ell'\sin\eta$ where $\cos\eta = (\ell^2+\ell'^2-L^2)/2\ell\ell'$ and $\sin\eta = \frac{1}{2\ell\ell'}(2\ell^2\ell'^2+2\ell'^2L^2+2\ell^2L^2-\ell^4-\ell'^4-L^4)^{1/2}$. Now substituting these into equations (5.32-5.37) we will find

$$\langle\tilde{C}_\ell^{TT}\rangle = \int \frac{d\ell'\ell'}{(2\pi)^2}\left[\int dLLW_{TT}(L)\frac{2}{\ell\ell'\sin\eta}\right]\langle\hat{C}_{\ell'}^{TT}\rangle, \tag{5.47}$$

$$\langle\tilde{C}_\ell^{TE}\rangle = \int \frac{d\ell'\ell'}{(2\pi)^2}\left[\int dLLW_{TP}(L)\frac{2\cos 2\eta}{\ell\ell'\sin\eta}\right]\langle\hat{C}_{\ell'}^{TE}\rangle, \tag{5.48}$$

$$\langle\tilde{C}_\ell^{TB}\rangle = \int \frac{d\ell'\ell'}{(2\pi)^2}\left[\int dLLW_{TP}(L)\frac{2\cos 2\eta}{\ell\ell'\sin\eta}\right]\langle\hat{C}_{\ell'}^{TB}\rangle, \tag{5.49}$$

$$\langle\tilde{C}_\ell^{EE}\rangle = \int \frac{d\ell'\ell'}{(2\pi)^2}\left\{\int dLL\frac{W_{PP}(L)}{\ell\ell'\sin\eta}\Big(\big[1+\cos 4\eta\big]\langle\hat{C}_{\ell'}^{EE}\rangle + \big[1-\cos 4\eta\big]\langle\hat{C}_{\ell'}^{BB}\rangle\Big)\right\}, \tag{5.50}$$

$$\langle\tilde{C}_\ell^{EB}\rangle = \int \frac{d\ell'\ell'}{(2\pi)^2}\left[\int dLLW_{PP}(L)\frac{2\cos 4\eta}{\ell\ell'\sin\eta}\right]\langle\hat{C}_{\ell'}^{EB}\rangle, \tag{5.51}$$

$$\langle\tilde{C}_\ell^{BB}\rangle = \int \frac{d\ell'\ell'}{(2\pi)^2}\left\{\int dLL\frac{W_{PP}(L)}{\ell\ell'\sin\eta}\Big(\big[1-\cos 4\eta\big]\langle\hat{C}_{\ell'}^{EE}\rangle + \big[1+\cos 4\eta\big]\langle\hat{C}_{\ell'}^{BB}\rangle\Big)\right\}, \tag{5.52}$$

where W_{TT}, W_{TP} and W_{PP} are the angular averaged spectra of the window functions which are defined by

$$W_{TT}(L) \equiv \int \frac{d\varphi_L}{2\pi}|W_T(\boldsymbol{L})|^2, \tag{5.53}$$

$$W_{TP}(L) \equiv \int \frac{d\varphi_L}{2\pi}|W_T(\boldsymbol{L})W_P^*(\boldsymbol{L})|, \tag{5.54}$$

$$W_{PP}(L) \equiv \int \frac{d\varphi_L}{2\pi}|W_P(\boldsymbol{L})|^2. \tag{5.55}$$

Note that in the flat-sky limit there is no mixing between TE and TB or between EE, BB and EB as there is in the curved sky case (see Brown et al., 2005). For practical purposes we usually invert equations (5.47-5.52) to estimate the true full-sky power spectra from the pseudo-C_ℓ's that are calculated from small patches of the sky.

5.2 Reconstruction of the Unbiased Bandpowers

In this section we employ the method presented in §5.1 to reconstruct the unbiased power spectra from noise-free simulations of QUaD pseudo-C_ℓ's in the flat sky approximation. The approach is to calculate the coupling matrices which connect the pseudo-C_ℓ's to the true power spectra and invert them to reconstruct the all sky band-powers. To clarify the strategy note that in discrete space equations (5.47-5.52) take the form

$$\langle \hat{C}_\ell^{TT} \rangle = \sum_{\ell'} M^{-1}_{TT,\ell\ell'} \langle \tilde{C}_{\ell'}^{TT} \rangle, \tag{5.56}$$

$$\langle \hat{C}_\ell^{TE} \rangle = \sum_{\ell'} M^{-1}_{TP,\ell\ell'} \langle \tilde{C}_{\ell'}^{TE} \rangle, \tag{5.57}$$

$$\langle \hat{C}_\ell^{TB} \rangle = \sum_{\ell'} M^{-1}_{TP,\ell\ell'} \langle \tilde{C}_{\ell'}^{TE} \rangle, \tag{5.58}$$

$$\langle \hat{C}_\ell^{EB} \rangle = \sum_{\ell'} M^{-1}_{EB,\ell\ell'} \langle \tilde{C}_{\ell'}^{EB} \rangle, \tag{5.59}$$

$$\begin{pmatrix} \langle \hat{C}_\ell^{EE} \rangle \\ \langle \hat{C}_\ell^{BB} \rangle \end{pmatrix} = \sum_{\ell'} \begin{pmatrix} M_{EE} & M_{BB} \\ M_{BB} & M_{EE} \end{pmatrix}^{-1}_{,\ell\ell'} \begin{pmatrix} \langle \tilde{C}_{\ell'}^{EE} \rangle \\ \langle \tilde{C}_{\ell'}^{BB} \rangle \end{pmatrix}, \tag{5.60}$$

where the coupling matrices are given by

$$M_{TT,\ell\ell'} \equiv \frac{\Delta\ell'\ell'}{(2\pi)^2} \sum_L \Delta L L W_{TT}(L) \frac{2}{\ell\ell' \sin\eta}, \tag{5.61}$$

$$M_{TP,\ell\ell'} \equiv \frac{\Delta\ell'\ell'}{(2\pi)^2} \sum_L \Delta L L W_{TP}(L) \frac{2\cos\eta}{\ell\ell' \sin\eta}, \tag{5.62}$$

$$M_{EE,\ell\ell'} \equiv \frac{\Delta\ell'\ell'}{(2\pi)^2} \sum_L \Delta L L W_{PP}(L) \frac{1+\cos 4\eta}{\ell\ell' \sin\eta}, \tag{5.63}$$

$$M_{BB,\ell\ell'} \equiv \frac{\Delta\ell'\ell'}{(2\pi)^2} \sum_L \Delta L L W_{PP}(L) \frac{1-\cos 4\eta}{\ell\ell' \sin\eta}, \tag{5.64}$$

$$M_{EB,\ell\ell'} \equiv \frac{\Delta\ell'\ell'}{(2\pi)^2} \sum_L \Delta L L W_{PP}(L) \frac{2\cos 4\eta}{\ell\ell' \sin\eta}. \tag{5.65}$$

Therefore our task is to calculate the mode-mode coupling kernels of Eqs. (5.61-5.65) for QUaD window functions and plug them into equations (5.56-5.60) to recover the true underlying power spectra $\langle \hat{C}_\ell \rangle$ from the simulated PCL's $\langle \tilde{C}_\ell \rangle$ generated for the QUaD experiment. For this purpose I will describe, step by step, an implementation approach and the numerical routines which have been used to test the above semi-analytical method.

The coupling matrices encapsulate the information about window functions. So along with equations (5.56-5.60) they can be utilized to deconvolve the boundary and mode mixing effects from the PCL's. Calculation of the coupling matrices in flat sky is straightforward since they only depend on the power spectra of the window functions in Fourier space. (5.53-5.55) Therefore it is essential to determine these window functions' power spectra over the full range of L which is needed for the calculation.

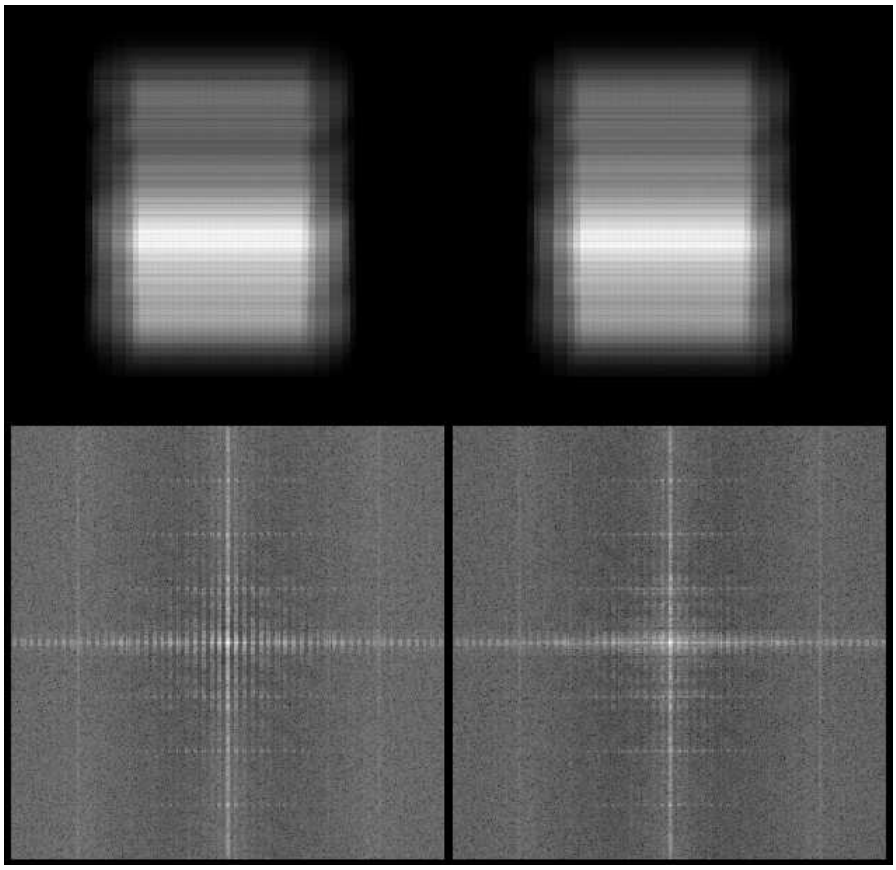

Figure 5.1: The 2006 QUaD temperature (left) and polarization (right) window functions. The top panel shows the masks in real space, while the bottom panel is the logarithm of the square of the amplitude of their 2-D Fourier transforms.

The window functions which we use for the analysis of this section are provided by the QUaD collaboration. These are the inverse variance apodization masks used for the analysis of first year QUaD CMB temperature and polarization maps. (Ade et al., 2008) They represent the expected spatial distribution of the noise in each pixel. Figure 5.1 shows the window functions and the logarithm of their modulus-squared in Fourier space. Here we simply ignore the phase angle information of the Fourier space since our analysis does not depend on it.

The Fast Fourier Transform algorithm which we use is based on a two-dimensional discrete Fourier transform of a bivariate of complex data values $z_{j_1 j_2}$ ($j_1 = 0, \ldots, m-1$, $j_2 = 1, \ldots, n-1$) which is defined by

$$\hat{z}_{k_1 k_2} = \frac{1}{mn} \sum_{j_1=0}^{m-1} \sum_{j_2=0}^{n-1} z_{j_1 j_2} \exp\Big(- 2\pi i \Big(\frac{j_1 k_1}{m} + \frac{j_2 k_2}{n} \Big) \Big), \tag{5.66}$$

where $k_1 = 0, \ldots, m-1$, $k_2 = 1, \ldots, n-1$. The inverse transform is defined by omitting the scale-factor of $1/mn$ and replacing the exponential by $\exp(+2\pi i(\ldots))$ in the above formula. (IDL FFT Function) The definition (5.66) implies periodic boundary conditions for which the

lowest frequency falls in the corners of the 2-D image. Therefore to keep things simple after transformation we always shift the small frequencies to the center (as seen in Figure 5.1). Note that our definition of the Fourier transform (5.5) is different from equation (5.66) in the sense that ours is an expansion in terms of the angular frequency ω, whereas the discrete Fourier transform (5.66) is characterized in terms of the ordinary frequency ζ (with $\zeta = k_1/m$ for 1-D case). As a result the two transformations are related by $\mathcal{F}_{\rm theory}(\omega) = \mathcal{F}_{\rm DFT}\big(\zeta = \frac{\omega}{2\pi}\big)$. This implies that the (i,j)-th pixel in the Fourier space corresponds to the wavenumber on the sky

$$\ell = \sqrt{\Big(\frac{2\pi i}{L_x}\Big)^2 + \Big(\frac{2\pi j}{L_y}\Big)^2}, \tag{5.67}$$

where $i = (-m/2+1, \ldots, m/2)$ and $j = (-n/2+1, \ldots, n/2)$. Here L_x and L_y are the size of the projected image on the sky along x and y axes. Therefore if the angular size of each pixel of the image is equal to $S_{\rm pix}$ we should have $L_x = mS_{\rm pix}$ and $L_y = nS_{\rm pix}$.

To calculate the angle averaged window functions (5.53-5.55) we put the apodization mask in the center of an image (a 2D array) of size (m,n) in real space (see top panel of figure 5.1) and take all other elements of the window matrix equal to zero (black region). We always have the freedom to choose m and n as large or as small as we need. For a fixed apodization mask this freedom only affects the ratio of the observed sky to the full sky, i.e. $f_{\rm mask} = \frac{n_{\rm pix}(W\neq 0)}{mn}$. As we will see this can be particularly important when we want to invert the coupling matrices, however we find that it does not generally have any significant influence on the bandpower recovery. In general, our analysis leads to consistent results for all choices of m and n as long as they are not too small that a large number of wavenumbers (5.67) cannot be constructed from the maps, or too large that the coupling matrices are not invertible.

Equation (5.67) implies that a minimum multipole of $\ell_{\rm min} = \min\{\frac{2\pi}{mS_{\rm pix}}, \frac{2\pi}{nS_{\rm pix}}\}$ and a maximum multipole of $\ell_{\rm max} = \frac{\sqrt{2}\pi}{S_{\rm pix}}$ are recoverable from the window functions. The maximum wavenumber is fixed and determined by the resolution of the experiment. For QUaD the pixel sizes are equal to $S_{\rm pix} = 1.2' = 0.000349$ radians, therefore the maximum integer wavenumber which can be constructed is $\ell = 12730$. This means that the window function power spectra (5.53-5.55) can be calculated up to $L_{\rm max} = 12730$. Recall that equations (5.47-5.52) are valid if the integrals over L are carried out over the multipole range specified by the triangle condition $|\ell - \ell'| < L < \ell + \ell'$. Therefore in order to make full use of all the information in the apodization masks the coupling matrices should be constructed up to $\ell = \ell' = L_{\rm max}/2 + 1 = 6366$. This requires defining coupling matrices of the size 6366×6366 which is not feasible in our Fortran analysis due to the limited memory stack sizes. Therefore to overcome this problem we assume a larger pixel size $S_{\rm pix} = 2.4' = 0.000698$ radians which implies a lower resolution $L_{\rm max} = 2\ell_{\rm max} = 6365$. We further assume $m = n = 2^{10} = 1024$ for both temperature and polarization window functions[1] which leads to the minimum multipole value $\ell_{\rm min} = 9$. We put the angle-averaged spectra for wavenumbers smaller than this minimum multipole equal to $W(\ell_{\rm min})$. Therefore using these options the coupling kernels and the pseudo-C_ℓ's will also be

[1]The DFT algorithm is most optimal if the size of the array is a power of 2.

calculated over multipoles $\ell = (2, 3182)$.

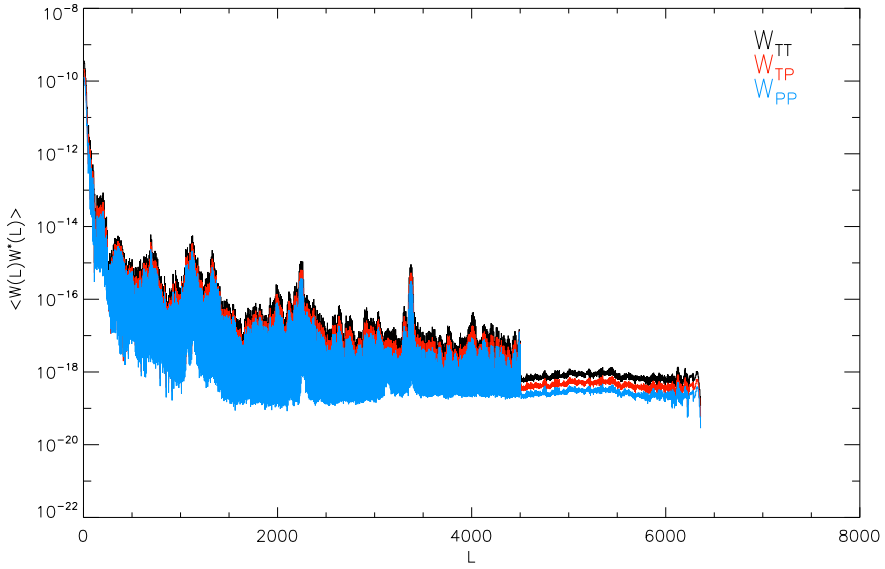

Figure 5.2: The power spectra of the window functions recovered from QUaD apodization masks.

At this stage we calculate the angle averaged window functions (5.53-5.55). Our strategy is to first determine the closest integer wavenumber which corresponds to each pixel of the Fourier transformed window functions, and then average over the square of the amplitudes of the pixels which have the same wavenumbers. The results are shown in Figure 5.2. One thing to notice is that we find that not all of the integer multipoles in the range are recovered this way. However we construct the power spectra for these missing multipoles by performing a cubic spline interpolation. (NAG Fortran Library, Routine E01BAF) Note that we adopt this strategy since it is essential to sum over all possible integer L's in equations (5.61-5.65). Indeed we find that our analysis is most accurate if we take ΔL to be equal to unity. For $\Delta L > 3$ the recovery of the band-powers is not as accurate as the ones which we will present in this section. Using the angle averaged spectra we can immediately determine the coupling kernels of equations (5.61-5.65). Again in these equations we choose $\Delta\ell' = 1$ which will result in coupling matrices of the size $(\ell_{\rm max} - 1) \times (\ell_{\rm max} - 1)$. Note that we do not implement the full binning procedure in Eqs. (5.61-5.65) in order to gain better accuracy. As a result the calculation of the full coupling kernels can be a little time costly, of the order of a couple of hours (depending on $S_{\rm pix}$), however this part of the code has been shared memory parallelized.

For an experiment with a large sky cut the coupling matrices are not always invertible. This is conceptually due to the fact that for large sky cuts the two-point correlations cannot always be determined on all angular scales on the uncut sky. So the recovery of the all-sky power spectra from such PCL's which are themselves highly undetermined is not practically feasible. This effect causes the coupling matrix to be singular for such experiment surveys. For

this reason one often bins the coupling matrix to reduce the correlations and make the matrix invertible. Following the definition of Brown et al. (2005), we define the binned coupling matrix $M_{bb'}$ by

$$M_{bb'} = \sum_{\ell} P_{b\ell} \sum_{\ell'} M_{\ell\ell'} Q_{\ell' b'}, \tag{5.68}$$

where the binning operator $P_{b\ell}$ is defined by

$$P_{b\ell} = \begin{cases} \frac{1}{2\pi} \frac{\ell(\ell+1)}{\ell_{\rm low}^{(b+1)} - \ell_{\rm low}^{(b)}}, & \text{if } 2 \leq \ell_{\rm low}^{(b)} \leq \ell < \ell_{\rm low}^{(b+1)} \\ 0, & \text{otherwise,} \end{cases} \tag{5.69}$$

and its reciprocal operator $Q_{\ell b}$ is

$$Q_{\ell b} = \begin{cases} \frac{2\pi}{\ell(\ell+1)}, & \text{if } 2 \leq \ell_{\rm low}^{(b)} \leq \ell < \ell_{\rm low}^{(b+1)} \\ 0, & \text{otherwise.} \end{cases} \tag{5.70}$$

In the same way to reduce the correlations between measured C_ℓ's one often bins the power spectra. This procedure keeps the total information in the bandpowers unchanged, however breaks the degeneracy and causes the error bars of the measurement to shrink. Therefore we define the full-sky CMB band-powers $\langle P_b \rangle$ by

$$\langle P_b \rangle = \sum_{b'} M^{-1}_{bb'} \sum_{\ell} P_{b'\ell} \langle \tilde{C}_\ell \rangle. \tag{5.71}$$

The band-powers which we obtain this way are already in units of $P_b = \ell(\ell+1)C_\ell/2$. In these definitions we have ignored the noise and the effects of beam and pixelization which can influence the results particularly on small scales. So we do not consider these factors here and leave to investigate them in a future analysis.

The width of the bins is often determined by the size of the sky patch which has been covered by the experiment. The choice of large bands corresponds to exploring the main features such as the mean amplitude of the spectra over a large range, for which details of the acoustic peaks get suppressed in the binning procedure. The choice of small bands correspond to exploring small features which are highly correlated. Since CMB experiments do not have uncorrelated information about bands of width $\Delta\ell \leq 2\pi/\theta$ where θ is the angular extent of the survey, (Bond et al., 1998) we choose the size of the bins to be larger than this value. In our window functions the non-zero elements of the apodization masks comprise a matrix of about 376×450 elements. ($f_{\rm mask} \simeq 0.12$) This corresponds to a minimum bin size of $\Delta\ell = 2\pi/\theta = 2\pi/(0.000698 \times 450) \simeq 20$. We have tested our analysis with various bin sizes. We have found that for bins of width smaller than $\Delta\ell = 15$ the coupling matrices can be singular or the recovered band-powers are scattered all over the place. However, since we see that bins of larger widths are sufficient to show all the features of the power spectra over our large range of multipoles $\ell = (2, 3182)$, we choose to show the bandpowers by 50 bins of width $\Delta\ell = 63$ starting from 34, 98 up to 3150.

Figure 5.3 shows the binned mode-mode coupling matrices from equations (5.61-5.65) and (5.68). The matrices are approximately diagonal since the dominant contribution to each multipole of the bandpower comes from the same multipole of the PCL's. This is also expected

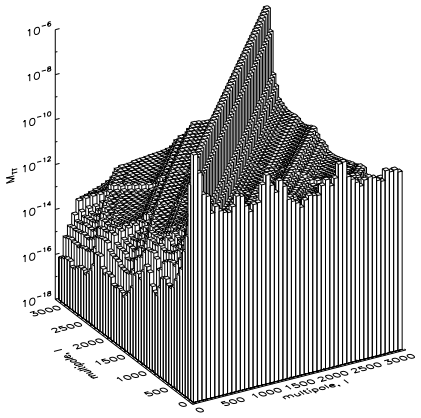

(a) M_{TT}

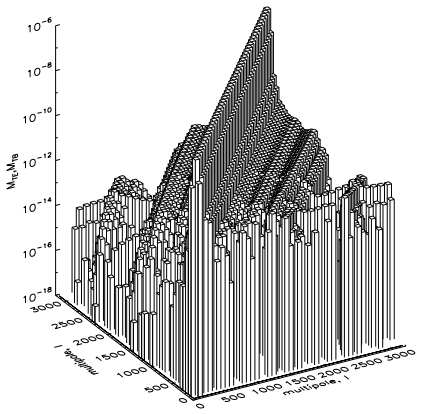

(b) M_{TE}, M_{TB}

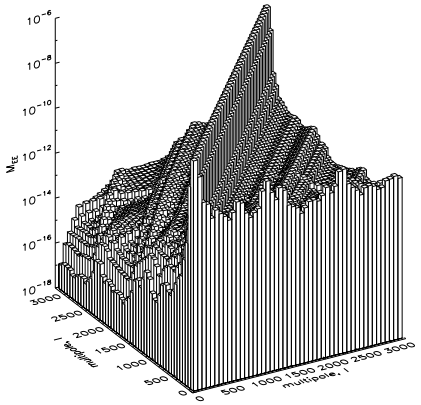

(c) M_{EE}

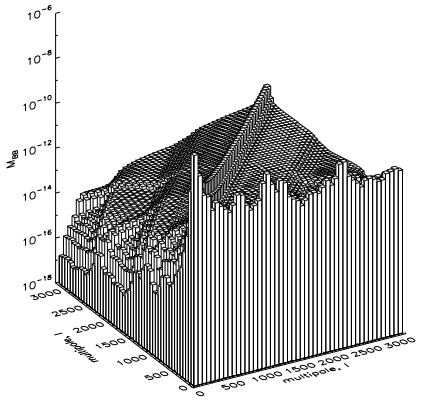

(d) M_{BB}

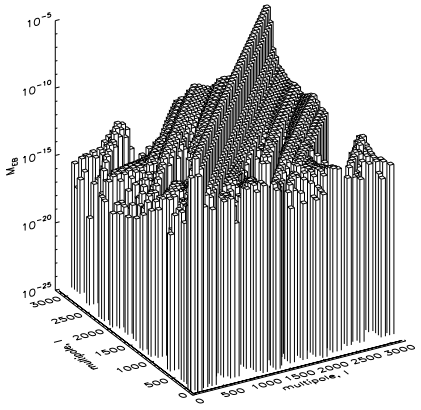

(e) M_{EB}

Figure 5.3: The binned coupling matrices for the window functions of figure 5.1.

from the fact that the coupling matrices M_{TT}, M_{TP}, M_{EE} and M_{EB} should become diagonal if we increase the survey area to match the full sky. Nevertheless, for a full sky survey there is no mode coupling so M_{BB} is expected to be zero. In Fig. 5.3 we also see that the diagonals of M_{BB} have relatively the same low amplitude as its off-diagonals. This is because the polarization modes are very weak so their mixing is relatively small and for the most part swamped by the relative largeness of the E modes. This, as we will see, particularly affects the recovery of the BB band-powers for which the contribution from EE is the dominant factor. (See also Challinor and Chon 2005 for a detailed discussion of the limits of the measurement of the B mode due to the E-B mixing effects on the pseudo-C_ℓ covariances.)

To test our flat sky method we produce simulations of the pseudo-C_ℓ's for QUaD window functions and attempt to recover the cosmological model which has been used to generate the simulations. The Gaussianity of the fluctuations implies that simulated maps of T, E and B modes on the sky can be represented by normally distributed random variables which are correlated to each other. To generate correlated Gaussian fields we adopt the Box-Muller algorithm in combination with the Cholesky decomposition. The Box-Muller transform says that if U_i and V_i, $(i = 0, \cdots n-1)$ are two independent uniform random distributions within the range $(0, 1]$, then random variables

$$X = \sqrt{-2\ln U}\cos(2\pi V), \tag{5.72}$$

$$Y = \sqrt{-2\ln U}\sin(2\pi V), \tag{5.73}$$

are independent and normally distributed with mean zero and variance unity. To make X and Y distributions correlated with a symmetric positive-definite correlation matrix C_{ij} one can carry out a Cholesky decomposition. i.e. find the lower triangular matrix L which satisfies the relation $C_{ij} = \sum_k L_{ik}L_{jk}$. Then correlated versions of X and Y can be constructed by multiplying with L, i.e.

$$x_i = \sum_k L_{ik}X_k \ ; \quad y_i = \sum_k L_{ik}Y_k \tag{5.74}$$

To verify that this gives the expected results we can calculate the correlation function of the new variables

$$\begin{aligned}\langle x_i x_j\rangle &= \langle\sum_k L_{ik}X_k \sum_{k'} L_{jk'}X_{k'}\rangle \\ &= \sum_{k,k'} L_{ik}L_{jk'}\langle X_k X_{k'}\rangle \\ &= \sum_{k,k'} L_{ik}L_{jk'}\delta_{kk'} = C_{ij},\end{aligned} \tag{5.75}$$

and likewise $\langle y_i y_j\rangle = C_{ij}$ and $\langle x_i y_j\rangle = \langle y_i x_j\rangle = 0$, which are what we expected.

With this knowledge in mind we construct simulations for temperature and polarization

CMB maps in the flat sky. For each multipole we define a 3 by 3 correlation matrix as

$$Q_{ij,\ell} = \begin{pmatrix} C_\ell^{TT} & C_\ell^{TE} & 0 \\ C_\ell^{TE} & C_\ell^{EE} & 0 \\ 0 & 0 & C_\ell^{BB} \end{pmatrix}. \tag{5.76}$$

We perform a Cholesky factorization (NAG Fortran Library, Routine F07FDF) and find the lower triangular matrix which satisfies $L_{,\ell} {L_{,\ell}}^T = Q_{,\ell}$. Then the random variables $T_{1,2}$, $E_{1,2}$ and $B_{1,2}$ defined by

$$\begin{pmatrix} T_1 \\ E_1 \\ B_1 \end{pmatrix} = L_{,\ell} \begin{pmatrix} \sqrt{-\ln U_T}\cos(2\pi V_T) \\ \sqrt{-\ln U_E}\cos(2\pi V_E) \\ \sqrt{-\ln U_B}\cos(2\pi V_B) \end{pmatrix}; \quad \begin{pmatrix} T_2 \\ E_2 \\ B_2 \end{pmatrix} = L_{,\ell} \begin{pmatrix} \sqrt{-\ln U_T}\sin(2\pi V_T) \\ \sqrt{-\ln U_E}\sin(2\pi V_E) \\ \sqrt{-\ln U_B}\sin(2\pi V_B) \end{pmatrix} \tag{5.77}$$

are each normally distributed with mean zero and variance $C_\ell^{TT}/2$, $C_\ell^{EE}/2$ and $C_\ell^{BB}/2$ respectively.[2] Here random variables U_X and V_X (for $X = T, E, B$) are drawn from uniform distributions over $(0, 1)$. (NAG Fortran Library, Routine G05CAF) We construct temperature and polarization maps of size (m, n) in Fourier space by assigning each (i, j)-th pixel of the map corresponding to wavenumber ℓ, a random fluctuation given by the module of $X_{,\ell} = X_1 + iX_2$. In this case we take the mean of the auto-correlation of the resulting T, E and B fields over all pixels with common wavenumber ℓ as an estimate of C_ℓ^{TT}, C_ℓ^{EE} and C_ℓ^{BB}, whereas their cross-correlation should give an estimate of C_ℓ^{TE} and $C_\ell^{TB} = C_\ell^{EB} = 0$.

One can immediately construct simulations of the CMB power spectra by the angle averaging method which we described for the window function power spectrum calculation. Again we do not implement the binning in the maps by dividing the space into annuli; instead we average over the value of all the pixels which correspond to the same wavenumber. We construct C_ℓ's which are not produced this way by a cubic spline interpolation. (NAG Fortran Library, Routine E01BAF) We find that this interpolation leaves very small numerical effects, if at all noticeable. Figure 5.4 shows 10 simulated spectra which are generated by this method (dots). The solid lines represent the theoretical model corresponding to WMAP 5yr mean best fit (table 2 of Dunkley et al. 2008) which has been used in the correlation matrix (5.76). The plots are shown up to $\ell = 2500$ to make the features of the peaks more visible. The sampling distributions are approximately Gaussian for which the variance is enhanced at the peaks of the oscillations.

To generate pseudo-C_ℓ's for QUaD we can convolve the Fourier space window function with the simulated temperature and polarization maps. However such a convolution can give accurate results if the Fourier space maps are extended to infinity. (Recall Eqs. 5.20 and 5.21) Therefore we prefer to carry out the convolution in real space using the relations (5.19). Therefore transforming into the real space and multiplying pixel by pixel by the apodization

[2] One may argue that lower triangular matrices might have asymmetric weighting on different modes. However we have tested this by diagonalizing the matrix Q and using the eigenvalue matrix D and eigenvectors matrix P which satisfy $Q = PDP^{-1}$. (NAG Fortran Library, Routine F08FAF) We have found that if we use $PD^{1/2}$ instead of L in Eq. (5.77) we obtain results similar to the ones that we present in this section.

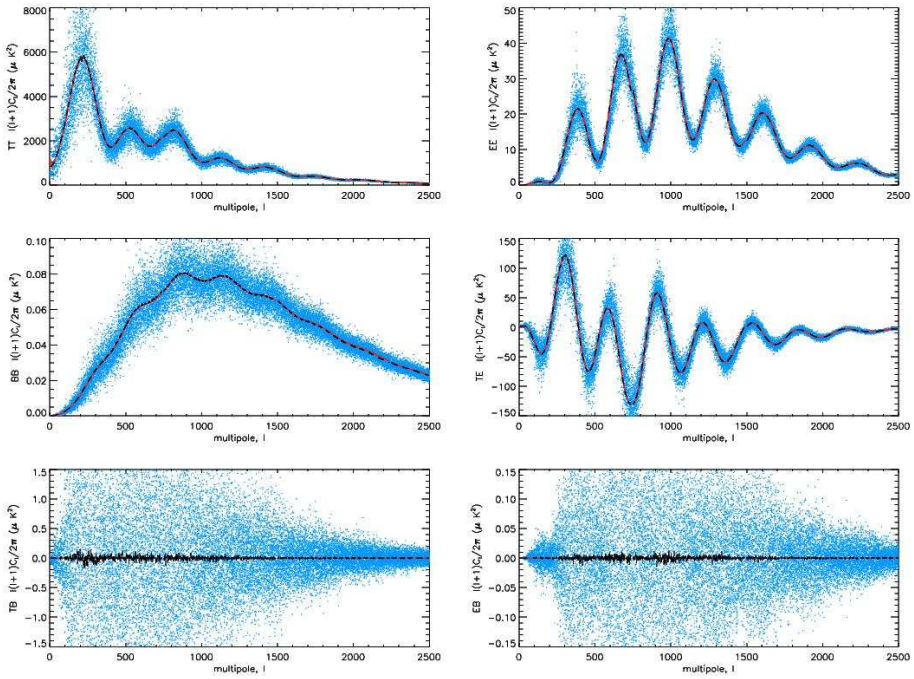

Figure 5.4: Monte Carlo simulations of the temperature and polarization power spectra. The dots represent the scatter of 10 simulations of the full sky power spectra, while the red solid lines are the models which have been used to generate the simulations. The dashed black lines which just lay over red lines represent the mean of 5000 simulations.

mask positioned at the center of the window function, and then Fourier transforming back results in convolved maps which can be used to generate the pseudo-C_ℓ's. Note that the resulting PCL estimators are a factor of $f_{\rm mask}$ smaller in amplitude due to the loss of power caused by the sky cut. They are also smeared and weighted by the window functions which we will deconvolve by applying the inverse coupling matrices.

We now recover the full sky band-powers from Eqs. (5.56-5.60) by inverting the coupling matrices (NAG Fortran Library, Routine F04AEF) and applying them to each individual and mean simulated PCL's. However, note that before projecting the estimated bandpowers on the CMB power spectra one has to re-scale them. We normalize the bandpowers by dividing them by a factor of $L_x L_y = (mS_{\rm pix})(nS_{\rm pix})$. This normalization comes from the Fourier transform definition of equation (5.66) which implies that the power spectrum of the window functions, and in turn the estimated M matrices, are smaller than expected by a factor of mn. This causes the bandpowers to be over-estimated by a factor of mn assuming fixed pseudo-C_ℓ's. The appearance of $S_{\rm pix}$ is intrinsic to our re-definition of the scales on the sky, since now $L_x L_y$ (rather than mn) represents the total area in Fourier space. We have tested the accuracy of this normalization factor by running the analysis for different pixel numbers and sizes and have found that the re-scaling changes appropriately for different choices of m, n and $S_{\rm pix}$.

We have produced an ensemble of 5000 simulated QUaD-like pseudo-C_ℓ's. We bin each of the pseudo-C_ℓ's by the binning operator $P_{b\ell}$ and multiply the binned spectra by the inverse coupling matrices. We re-scale the bandpowers and keep them to use for the calculation of the covariances. Using equations (5.56-5.60) and (5.71) we also calculate the unbiased full sky bandpowers from the ensemble-averaged pseudo-C_ℓ's. The results are shown in figure 5.5. The red dots represent the deconvolved bandpowers $\langle P_b \rangle$, whereas the green dots are the normalized binned ensemble-averaged pseudo-C_ℓ's. In this plot, the PCLs have been normalized to the same maximum as the red points. The horizontal error bars represent the bin sizes, while the vertical errors on TT, TE, EE and BB spectra are the 1-σ errors which represent the scatter of the individual bandpowers due to the sample variance, i.e. they have been calculated by the square root of the variance

$$\sigma_b^2 = \langle \Delta P_b \Delta P_b \rangle = \langle \big(P_b - \langle P_b \rangle\big)\big(P_b - \langle P_b \rangle\big) \rangle. \tag{5.78}$$

However, for TB and EB we have plotted the 1-sigma errors on the 'mean' recovered bandpower values, specifically the standard deviation devided by $\sqrt{5000}$, in order to show that the mean values are generally consistent with zero.

We present the goodness-of-fit of the bandpower recovery in terms of the reduced-χ^2 values defined by $\chi^2 = \sum_b (P_b - P_{b\ell} C_\ell)^2 / \sigma_b^2$ divided by the number of degrees of freedom (dof = 50). They are 11.90, 0.11, 1.18 and 502.90 for TT, TE, EE and BB respectively. We find that the bandpower recovery is not particularly good for BB, as we had anticipated due to the large contribution from EE mixing, and the poorly diagonal polarization coupling matrix M_{BB}. It is curious to see whether the poor BB recovery is due to numerical effects or can be improved by implementing better estimators for the B-mode (see e.g. Smith, 2006). Furthermore, by printing out the contribution from each band-power P_b we see that the poor χ_r^2 value for TT comes from the large multipoles where σ_b is small. For the first 30 bins the reduced-χ^2 value for TT is 0.90 which corresponds to a relatively good recovery for the intermediate-scale bandpowers. We conclude that the proposed flat sky PCL method of section 5.1, potentially with some modifications, can prove to be useful in reconstructing the unbiased temperature and polarization bandpowers for CMB experiments with incomplete sky coverage. However, any practical use of this method also requires the inclusion of noise and beam uncertainty which we have not considered here.

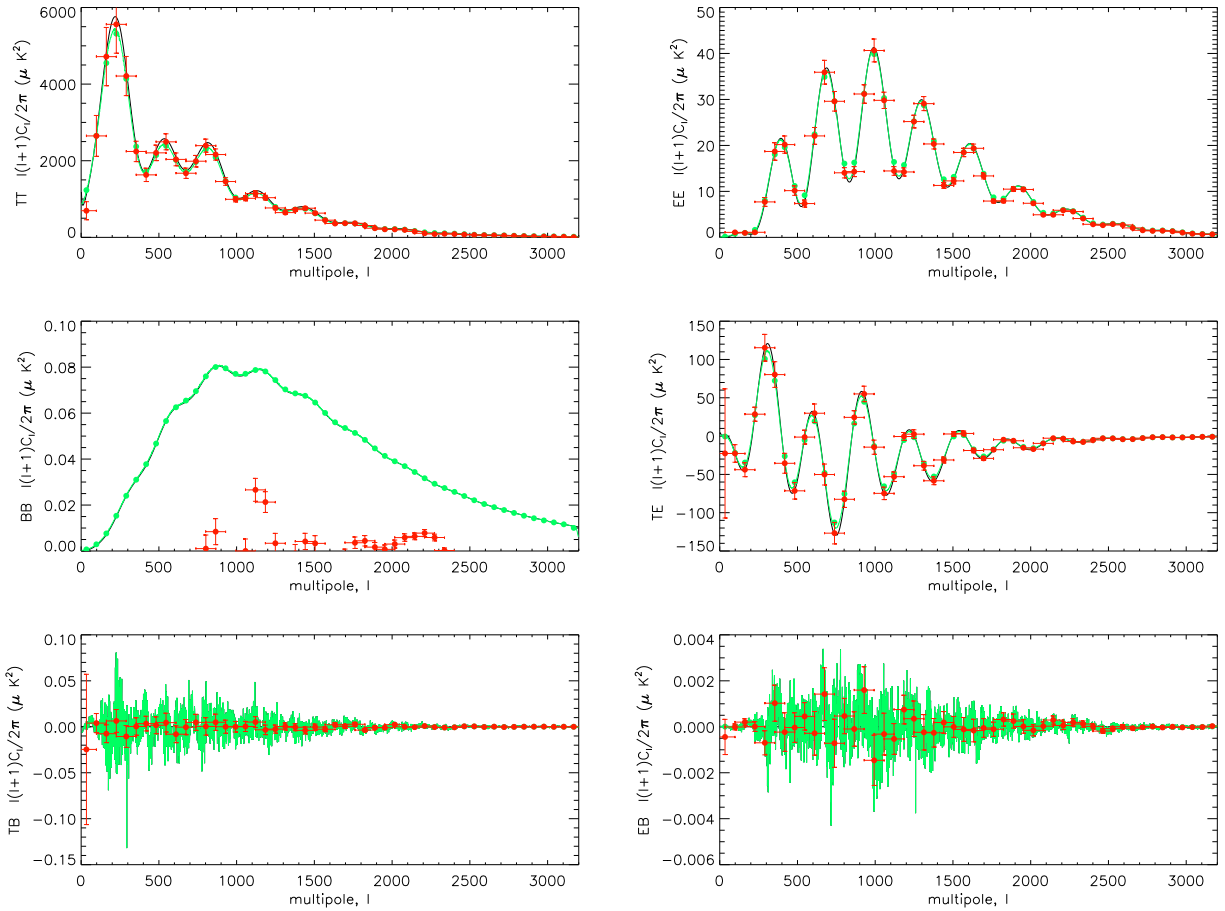

Figure 5.5: The reconstruction of the unbiased estimators in the flat sky approximation. The green dots are the re-scaled binned averaged PCL estimates from 5000 QUaD-like simulations, while the red dots are the deconvolved underlying bandpowers. The solid lines represent the cosmological model which has been used to generate the simulations.

5.3 Covariances of the CMB Pseudo-C_ℓ's

The covariance matrices of the CMB power spectra also provide important information for data analysis. They are particularly important since they provide the error bars of the bandpower measurement, as well as the weighting scheme necessary for the likelihood estimation from each bandpower. For a full sky noise-free experiment covariance matrices are diagonal. We have already derived the cosmic variance term (3.47) which constitutes the diagonals of the covariance matrix of the auto- power spectra. However on the incomplete patches of the sky observed by the experiments, the covariance matrices often contain contaminated non-zero off-diagonals. It is therefore essential to have accurate models of covariance matrix calculation in different limits and approximations. Nevertheless, the exact calculation of the covariance matrices is often extremely CPU time expensive. This is due to the fact that the covariances correspond to 4-point correlations which require a factor of $N_{\rm pix}^2$ more computation than is required by the power spectrum estimation. For this reason it has become conventional to use approximations to accelerate the numerical calculation.

One widely used approach is to construct Monte Carlo simulations for the survey, including the window functions and the noise model in the procedure, and calculate the covariances by ensemble averaging over the simulated spectra (see Hivon et al., 2002). We used this method in section 5.2 when we calculated the 1-sigma error bars of the bandpowers in equation (5.78). Other methods are based on semi-analytical approximations of the bandpowers in order to reduce the number of iterations and loops necessary in the exact numerical calculation. (Challinor, 2004; Brown et al., 2005) Nevertheless, the most practical method to date is the Monte Carlo approach which is also expected to prove efficient for Planck-sized data sets. (Efstathiou, 2006) Hence there has also been some focus on improving the covariance matrix estimation from the simulation approach to construct nearly diagonal matrices from a limited number of simulations. (Pope and Szapudi, 2008) In this section we provide a short analysis of the covariance matrix calculation in the flat sky approximation. The work of this section is an attempt to employ the approach of section 5.1 to the exact calculation of the covariance matrices. However the results of the work turn out to be prohibitively slow to calculate and is not suitable for real purposes.

The full covariance matrices of the CMB power spectra include both auto- and cross- correlation of the temperature and polarization spectra at all possible multipole moments. We construct the general covariances of the estimators (3.45) as

$$\begin{aligned}\langle \Delta\hat{C}_\ell^{XY}\Delta\hat{C}_{\ell'}^{X'Y'}\rangle &= \frac{1}{(2\ell+1)(2\ell'+1)}\sum_{mm'}\langle a_{\ell m}^X a_{\ell m}^{Y*} a_{\ell' m'}^{X'} a_{\ell' m'}^{Y'*}\rangle - \langle\hat{C}_\ell^{XY}\rangle\langle\hat{C}_{\ell'}^{X'Y'}\rangle \\ &= \frac{1}{(2\ell+1)(2\ell'+1)}\Big[\sum_{mm'}\langle a_{\ell m}^X a_{\ell' m'}^{X'*}\rangle\langle a_{\ell m}^Y a_{\ell' m'}^{Y'*}\rangle + \langle a_{\ell m}^X a_{\ell' m'}^{Y'*}\rangle\langle a_{\ell m}^{Y*} a_{\ell' m'}^{X'}\rangle\Big] \\ &= \frac{\delta_{\ell\ell'}}{(2\ell+1)}\Big(\hat{C}_\ell^{XX'}\hat{C}_{\ell'}^{YY'} + \hat{C}_\ell^{XY'}\hat{C}_{\ell'}^{X'Y}\Big), \end{aligned} \tag{5.79}$$

where again we have used the Wick's theorem for Gaussian variables. (Eq. 3.48) To define

covariances for the pseudo-C_ℓ's in the flat sky limit recall the planar approximation of the temperature and polarization modes. These are given by equations (5.20), (5.23) and (5.24) as

$$\tilde{T}(\boldsymbol{\ell}) = \int \frac{d^2\ell'}{(2\pi)^2} W_T(\boldsymbol{\ell}-\boldsymbol{\ell'})T(\boldsymbol{\ell'}), \tag{5.80}$$

$$\tilde{E}(\boldsymbol{\ell}) = \int \frac{d^2\ell'}{(2\pi)^2} W_P(\boldsymbol{\ell}-\boldsymbol{\ell'})[\cos 2(\varphi_\ell - \varphi_{\ell'})E(\boldsymbol{\ell'}) + \sin 2(\varphi_\ell - \varphi_{\ell'})B(\boldsymbol{\ell'})], \tag{5.81}$$

$$\tilde{B}(\boldsymbol{\ell}) = \int \frac{d^2\ell'}{(2\pi)^2} W_P(\boldsymbol{\ell}-\boldsymbol{\ell'})[\cos 2(\varphi_\ell - \varphi_{\ell'})B(\boldsymbol{\ell'}) - \sin 2(\varphi_\ell - \varphi_{\ell'})E(\boldsymbol{\ell'})]. \tag{5.82}$$

We can construct the pseudo-C_ℓ covariance matrices by substituting Eqs. (5.80), (5.81) and (5.82) into the second equality of equation (5.79). Note that as before in the flat sky limit $a^X_{\ell m} \to X(\boldsymbol{\ell})$ and $\frac{1}{(2\ell+1)}\sum_m \to \int \frac{d\varphi_\ell}{2\pi}$, so we are left with

$$\mathrm{cov}(\tilde{C}^{TT}_\ell, \tilde{C}^{TT}_{\ell'}) = 2\int \frac{d\varphi_\ell}{2\pi}\int \frac{d\varphi_{\ell'}}{2\pi} \left|G^{TT}(\boldsymbol{\ell},\boldsymbol{\ell'})\right|^2, \tag{5.83}$$

$$\mathrm{cov}(\tilde{C}^{TT}_\ell, \tilde{C}^{TE}_{\ell'}) = 2\int \frac{d\varphi_\ell}{2\pi}\int \frac{d\varphi_{\ell'}}{2\pi} \left\{G^{TT}(\boldsymbol{\ell},\boldsymbol{\ell'})G^{TE}(\boldsymbol{\ell},\boldsymbol{\ell'})\right\}, \tag{5.84}$$

$$\mathrm{cov}(\tilde{C}^{TT}_\ell, \tilde{C}^{EE}_{\ell'}) = 2\int \frac{d\varphi_\ell}{2\pi}\int \frac{d\varphi_{\ell'}}{2\pi} \left|G^{TE}(\boldsymbol{\ell},\boldsymbol{\ell'})\right|^2, \tag{5.85}$$

$$\mathrm{cov}(\tilde{C}^{TT}_\ell, \tilde{C}^{BB}_{\ell'}) = 2\int \frac{d\varphi_\ell}{2\pi}\int \frac{d\varphi_{\ell'}}{2\pi} \left|G^{TB}(\boldsymbol{\ell},\boldsymbol{\ell'})\right|^2, \tag{5.86}$$

$$\mathrm{cov}(\tilde{C}^{TT}_\ell, \tilde{C}^{TB}_{\ell'}) = 2\int \frac{d\varphi_\ell}{2\pi}\int \frac{d\varphi_{\ell'}}{2\pi} \left\{G^{TT}(\boldsymbol{\ell},\boldsymbol{\ell'})G^{TB}(\boldsymbol{\ell},\boldsymbol{\ell'})\right\}, \tag{5.87}$$

$$\mathrm{cov}(\tilde{C}^{TT}_\ell, \tilde{C}^{EB}_{\ell'}) = 2\int \frac{d\varphi_\ell}{2\pi}\int \frac{d\varphi_{\ell'}}{2\pi} \left\{G^{TE}(\boldsymbol{\ell},\boldsymbol{\ell'})G^{TB}(\boldsymbol{\ell},\boldsymbol{\ell'})\right\}, \tag{5.88}$$

$$\mathrm{cov}(\tilde{C}^{TE}_\ell, \tilde{C}^{TE}_{\ell'}) = \int \frac{d\varphi_\ell}{2\pi}\int \frac{d\varphi_{\ell'}}{2\pi} \left\{G^{TT}(\boldsymbol{\ell},\boldsymbol{\ell'})G^{EE}(\boldsymbol{\ell},\boldsymbol{\ell'}) + \left|G^{TE}(\boldsymbol{\ell},\boldsymbol{\ell'})\right|^2\right\}, \tag{5.89}$$

$$\mathrm{cov}(\tilde{C}^{TE}_\ell, \tilde{C}^{EE}_{\ell'}) = 2\int \frac{d\varphi_\ell}{2\pi}\int \frac{d\varphi_{\ell'}}{2\pi} \left\{G^{TE}(\boldsymbol{\ell},\boldsymbol{\ell'})G^{EE}(\boldsymbol{\ell},\boldsymbol{\ell'})\right\}, \tag{5.90}$$

$$\mathrm{cov}(\tilde{C}^{TE}_\ell, \tilde{C}^{BB}_{\ell'}) = 2\int \frac{d\varphi_\ell}{2\pi}\int \frac{d\varphi_{\ell'}}{2\pi} \left\{G^{TB}(\boldsymbol{\ell},\boldsymbol{\ell'})G^{EB}(\boldsymbol{\ell},\boldsymbol{\ell'})\right\}, \tag{5.91}$$

$$\mathrm{cov}(\tilde{C}^{TE}_\ell, \tilde{C}^{TB}_{\ell'}) = \int \frac{d\varphi_\ell}{2\pi}\int \frac{d\varphi_{\ell'}}{2\pi} \left\{G^{TT}(\boldsymbol{\ell},\boldsymbol{\ell'})G^{EB}(\boldsymbol{\ell},\boldsymbol{\ell'}) + G^{TB}(\boldsymbol{\ell},\boldsymbol{\ell'})G^{TE}(\boldsymbol{\ell},\boldsymbol{\ell'})\right\}, \tag{5.92}$$

$$\mathrm{cov}(\tilde{C}^{TE}_\ell, \tilde{C}^{EB}_{\ell'}) = \int \frac{d\varphi_\ell}{2\pi}\int \frac{d\varphi_{\ell'}}{2\pi} \left\{G^{TE}(\boldsymbol{\ell},\boldsymbol{\ell'})G^{EB}(\boldsymbol{\ell},\boldsymbol{\ell'}) + G^{TB}(\boldsymbol{\ell},\boldsymbol{\ell'})G^{EE}(\boldsymbol{\ell},\boldsymbol{\ell'})\right\}, \tag{5.93}$$

$$\mathrm{cov}(\tilde{C}^{EE}_\ell, \tilde{C}^{EE}_{\ell'}) = 2\int \frac{d\varphi_\ell}{2\pi}\int \frac{d\varphi_{\ell'}}{2\pi} \left|G^{EE}(\boldsymbol{\ell},\boldsymbol{\ell'})\right|^2, \tag{5.94}$$

$$\mathrm{cov}(\tilde{C}^{EE}_\ell, \tilde{C}^{BB}_{\ell'}) = 2\int \frac{d\varphi_\ell}{2\pi}\int \frac{d\varphi_{\ell'}}{2\pi} \left|G^{EB}(\boldsymbol{\ell},\boldsymbol{\ell'})\right|^2, \tag{5.95}$$

$$\mathrm{cov}(\tilde{C}^{EE}_\ell, \tilde{C}^{TB}_{\ell'}) = 2\int \frac{d\varphi_\ell}{2\pi}\int \frac{d\varphi_{\ell'}}{2\pi} \left\{G^{TE}(\boldsymbol{\ell},\boldsymbol{\ell'})G^{EB}(\boldsymbol{\ell},\boldsymbol{\ell'})\right\}, \tag{5.96}$$

$$\mathrm{cov}(\tilde{C}^{EE}_\ell, \tilde{C}^{EB}_{\ell'}) = 2\int \frac{d\varphi_\ell}{2\pi}\int \frac{d\varphi_{\ell'}}{2\pi} \left\{G^{EE}(\boldsymbol{\ell},\boldsymbol{\ell'})G^{EB}(\boldsymbol{\ell},\boldsymbol{\ell'})\right\}, \tag{5.97}$$

$$\mathrm{cov}(\tilde{C}_\ell^{BB}, \tilde{C}_{\ell'}^{BB}) = 2\int \frac{d\varphi_\ell}{2\pi}\int \frac{d\varphi_{\ell'}}{2\pi}\left|G^{BB}(\boldsymbol{\ell},\boldsymbol{\ell'})\right|^2, \tag{5.98}$$

$$\mathrm{cov}(\tilde{C}_\ell^{BB}, \tilde{C}_{\ell'}^{TB}) = 2\int \frac{d\varphi_\ell}{2\pi}\int \frac{d\varphi_{\ell'}}{2\pi}\left\{G^{TB}(\boldsymbol{\ell},\boldsymbol{\ell'})G^{BB}(\boldsymbol{\ell},\boldsymbol{\ell'})\right\}, \tag{5.99}$$

$$\mathrm{cov}(\tilde{C}_\ell^{BB}, \tilde{C}_{\ell'}^{EB}) = 2\int \frac{d\varphi_\ell}{2\pi}\int \frac{d\varphi_{\ell'}}{2\pi}\left\{G^{EB}(\boldsymbol{\ell},\boldsymbol{\ell'})G^{BB}(\boldsymbol{\ell},\boldsymbol{\ell'})\right\}, \tag{5.100}$$

$$\mathrm{cov}(\tilde{C}_\ell^{TB}, \tilde{C}_{\ell'}^{TB}) = \int \frac{d\varphi_\ell}{2\pi}\int \frac{d\varphi_{\ell'}}{2\pi}\left\{G^{TT}(\boldsymbol{\ell},\boldsymbol{\ell'})G^{BB}(\boldsymbol{\ell},\boldsymbol{\ell'}) + \left|G^{TB}(\boldsymbol{\ell},\boldsymbol{\ell'})\right|^2\right\}, \tag{5.101}$$

$$\mathrm{cov}(\tilde{C}_\ell^{TB}, \tilde{C}_{\ell'}^{EB}) = \int \frac{d\varphi_\ell}{2\pi}\int \frac{d\varphi_{\ell'}}{2\pi}\left\{G^{TE}(\boldsymbol{\ell},\boldsymbol{\ell'})G^{BB}(\boldsymbol{\ell},\boldsymbol{\ell'}) + G^{TB}(\boldsymbol{\ell},\boldsymbol{\ell'})G^{EB}(\boldsymbol{\ell},\boldsymbol{\ell'})\right\}, \tag{5.102}$$

$$\mathrm{cov}(\tilde{C}_\ell^{EB}, \tilde{C}_{\ell'}^{EB}) = \int \frac{d\varphi_\ell}{2\pi}\int \frac{d\varphi_{\ell'}}{2\pi}\left\{G^{EE}(\boldsymbol{\ell},\boldsymbol{\ell'})G^{BB}(\boldsymbol{\ell},\boldsymbol{\ell'}) + \left|G^{EB}(\boldsymbol{\ell},\boldsymbol{\ell'})\right|^2\right\}, \tag{5.103}$$

where $G^{XX'}(\boldsymbol{\ell},\boldsymbol{\ell'}) \equiv \langle \tilde{X}(\boldsymbol{\ell})\tilde{X}'^*(\boldsymbol{\ell'})\rangle$. These functions are determined by

$$G^{TT}(\boldsymbol{\ell},\boldsymbol{\ell'}) = \int \frac{d^2\ell''}{(2\pi)^2} W_T(\boldsymbol{\ell}-\boldsymbol{\ell''})W_T(\boldsymbol{\ell'}-\boldsymbol{\ell''})C_{\ell''}^{TT}, \tag{5.104}$$

$$\begin{aligned} G^{TE}(\boldsymbol{\ell},\boldsymbol{\ell'}) &= \int \frac{d^2\ell''}{(2\pi)^2} W_T(\boldsymbol{\ell}-\boldsymbol{\ell''})W_P(\boldsymbol{\ell'}-\boldsymbol{\ell''}) \\ &\quad \times \left[\cos 2(\varphi_{\ell'}-\varphi_{\ell''})C_{\ell''}^{TE} + \sin 2(\varphi_{\ell'}-\varphi_{\ell''})C_{\ell''}^{TB}\right], \end{aligned} \tag{5.105}$$

$$\begin{aligned} G^{TB}(\boldsymbol{\ell},\boldsymbol{\ell'}) &= \int \frac{d^2\ell''}{(2\pi)^2} W_T(\boldsymbol{\ell}-\boldsymbol{\ell''})W_P(\boldsymbol{\ell'}-\boldsymbol{\ell''}) \\ &\quad \times \left[\cos 2(\varphi_{\ell'}-\varphi_{\ell''})C_{\ell''}^{TB} - \sin 2(\varphi_{\ell'}-\varphi_{\ell''})C_{\ell''}^{TE}\right], \end{aligned} \tag{5.106}$$

$$\begin{aligned} G^{EE}(\boldsymbol{\ell},\boldsymbol{\ell'}) &= \int \frac{d^2\ell''}{(2\pi)^2} W_P(\boldsymbol{\ell}-\boldsymbol{\ell''})W_P(\boldsymbol{\ell'}-\boldsymbol{\ell''}) \\ &\quad \times \big[\cos 2(\varphi_\ell-\varphi_{\ell''})\cos 2(\varphi_{\ell'}-\varphi_{\ell''})C_{\ell''}^{EE} \\ &\quad + \cos 2(\varphi_\ell-\varphi_{\ell''})\sin 2(\varphi_{\ell'}-\varphi_{\ell''})C_{\ell''}^{EB} \\ &\quad + \sin 2(\varphi_\ell-\varphi_{\ell''})\cos 2(\varphi_{\ell'}-\varphi_{\ell''})C_{\ell''}^{EB} \\ &\quad + \sin 2(\varphi_\ell-\varphi_{\ell''})\sin 2(\varphi_{\ell'}-\varphi_{\ell''})C_{\ell''}^{BB}\big], \end{aligned} \tag{5.107}$$

$$\begin{aligned} G^{EB}(\boldsymbol{\ell},\boldsymbol{\ell'}) &= \int \frac{d^2\ell''}{(2\pi)^2} W_P(\boldsymbol{\ell}-\boldsymbol{\ell''})W_P(\boldsymbol{\ell'}-\boldsymbol{\ell''}) \\ &\quad \times \big[\cos 2(\varphi_\ell-\varphi_{\ell''})\cos 2(\varphi_{\ell'}-\varphi_{\ell''})C_{\ell''}^{EB} \\ &\quad - \cos 2(\varphi_\ell-\varphi_{\ell''})\sin 2(\varphi_{\ell'}-\varphi_{\ell''})C_{\ell''}^{EE} \\ &\quad + \sin 2(\varphi_\ell-\varphi_{\ell''})\cos 2(\varphi_{\ell'}-\varphi_{\ell''})C_{\ell''}^{BB} \\ &\quad - \sin 2(\varphi_\ell-\varphi_{\ell''})\sin 2(\varphi_{\ell'}-\varphi_{\ell''})C_{\ell''}^{EE}\big], \end{aligned} \tag{5.108}$$

$$\begin{aligned} G^{BB}(\boldsymbol{\ell},\boldsymbol{\ell'}) &= \int \frac{d^2\ell''}{(2\pi)^2} W_P(\boldsymbol{\ell}-\boldsymbol{\ell''})W_P(\boldsymbol{\ell'}-\boldsymbol{\ell''}) \\ &\quad \times \big[\cos 2(\varphi_\ell-\varphi_{\ell''})\cos 2(\varphi_{\ell'}-\varphi_{\ell''})C_{\ell''}^{BB} \\ &\quad - \cos 2(\varphi_\ell-\varphi_{\ell''})\sin 2(\varphi_{\ell'}-\varphi_{\ell''})C_{\ell''}^{EB} \\ &\quad - \sin 2(\varphi_\ell-\varphi_{\ell''})\cos 2(\varphi_{\ell'}-\varphi_{\ell''})C_{\ell''}^{EB} \\ &\quad + \sin 2(\varphi_\ell-\varphi_{\ell''})\sin 2(\varphi_{\ell'}-\varphi_{\ell''})C_{\ell''}^{EE}\big]. \end{aligned} \tag{5.109}$$

Using these equations, calculation of all 21 auto- and cross- covariances of the PCLs should be straightforward. However the numerical calculation over a large range of multipoles is computationally expensive due to the existence of four integrations in the definition of each element of the covariances.

It is therefore reasonable that, in analogy with section 5.1, we try to simplify the equations by applying expressions like Eq. (5.29). Nevertheless, in the simplest case such an attempt leaves us with 14 integrals over several bundles of Bessel functions. For example we can show that auto-covariances of EE will reduce to

$$\begin{aligned}
\mathrm{cov}(\tilde{C}_\ell^{EE}, \tilde{C}_{\ell'}^{EE}) = 2 &\int dL_1 L_1 \int dL_2 L_2 \int L_1' L_1' \int dL_2' L_2' \\
&\times \int \frac{d\varphi_{L_1}}{2\pi} W(L_1) \int \frac{d\varphi_{L_2}}{2\pi} W(L_2) \int \frac{d\varphi_{L_1'}}{2\pi} W(L_1') \int \frac{d\varphi_{L_2'}}{2\pi} W(L_2') \int d\ell_1 \ell_1 \int d\ell_2 \ell_2 \\
&\times \int d\Theta_1 \Theta_1 \int d\Theta_2 \Theta_2 \int d\Theta_1' \Theta_1' \int d\Theta_2' \Theta_2' J_0(\Theta_1 L_1) J_0(\Theta_2 L_2) J_0(\Theta_1' L_1') J_0(\Theta_2' L_2') \\
&\times \frac{1}{8} \Big\{ \Big(J_4\big((\Theta_1 + \Theta_1')\ell\big) J_4\big((\Theta_2 + \Theta_2')\ell'\big) J_4\big((\Theta_1 + \Theta_2)\ell_1\big) J_4\big((\Theta_1' + \Theta_2')\ell_2\big) \\
&+ J_4\big((\Theta_1 + \Theta_1')\ell\big) J_0\big((\Theta_2 + \Theta_2')\ell'\big) J_4\big((\Theta_1 + \Theta_2)\ell_1\big) J_4\big((\Theta_1' + \Theta_2')\ell_2\big) \\
&+ J_0\big((\Theta_1 + \Theta_1')\ell\big) J_4\big((\Theta_2 + \Theta_2')\ell'\big) J_4\big((\Theta_1 + \Theta_2)\ell_1\big) J_0\big((\Theta_1' + \Theta_2')\ell_2\big) \\
&+ \text{all similar terms with permutations of 0 and 4} \Big\} C_{\ell_1}^{EE} C_{\ell_2}^{EE} + \dots
\end{aligned} \tag{5.110}$$

where dots represent the terms coming from $C_{\ell_1}^{EE} C_{\ell_2}^{EB}$, $C_{\ell_1}^{EE} C_{\ell_2}^{BB}$, etc. This makes it infeasible to reach analytical simplifications by this approach.

I have implemented equations (5.83-5.103) and (5.104-5.109) as they are in a MPI parallelized Fortran code to calculate the pseudo-C_ℓ covariances for a 2D top hat window function. For this purpose we use the QUaD 2006 window functions of Fig. 5.1, but we modify the weighting of all observed pixels to be equal to unity (rather than the inverse noise weighting). This time we put m, n equal to $2^{11} = 2048$ in order to have a larger sample of pixels in Fourier space, and we take the pixel sizes to be $S_{\mathrm{pix}} = 1.2' = 0.000349$ radians. (hence $f_{\mathrm{mask}} \simeq 0.03$) Due to the slowness of the calculation we cannot use every single pixel of the window functions for integration. Therefore we approximate the integrals by summing over limited numbers of discrete samplings that we take at each multipole and angular extent. For the choices of 1000 bins for $d\ell''$ integration and 150 bins for the angular integrations over $d\varphi_\ell$, $d\varphi_{\ell'}$ and $d\varphi_{\ell''}$ it takes the program a few hundred CPU hours to calculate the full covariance matrices consisting of 30 bins at $\ell = 44, 127, \dots 2459$. We show the results in terms of the correlation matrix

$$\mathrm{corr}(\tilde{C}_\ell^{XY}, \tilde{C}_{\ell'}^{X'Y'}) = \frac{\langle \Delta\tilde{C}_\ell^{XY} \Delta\tilde{C}_{\ell'}^{X'Y'} \rangle}{\sqrt{\langle \Delta\tilde{C}_\ell^{XY} \Delta\tilde{C}_\ell^{XY} \rangle \langle \Delta\tilde{C}_{\ell'}^{X'Y'} \Delta\tilde{C}_{\ell'}^{X'Y'} \rangle}}. \tag{5.111}$$

The diagonals of the correlation matrix are always unity, while the off-diagonals range from -1 (anti-correlated) to +1 (correlated). Figure 5.6a shows the resulting 180×180 numerical correlation matrix from this analysis. For comparison with Monte Carlo simulations, in Fig.

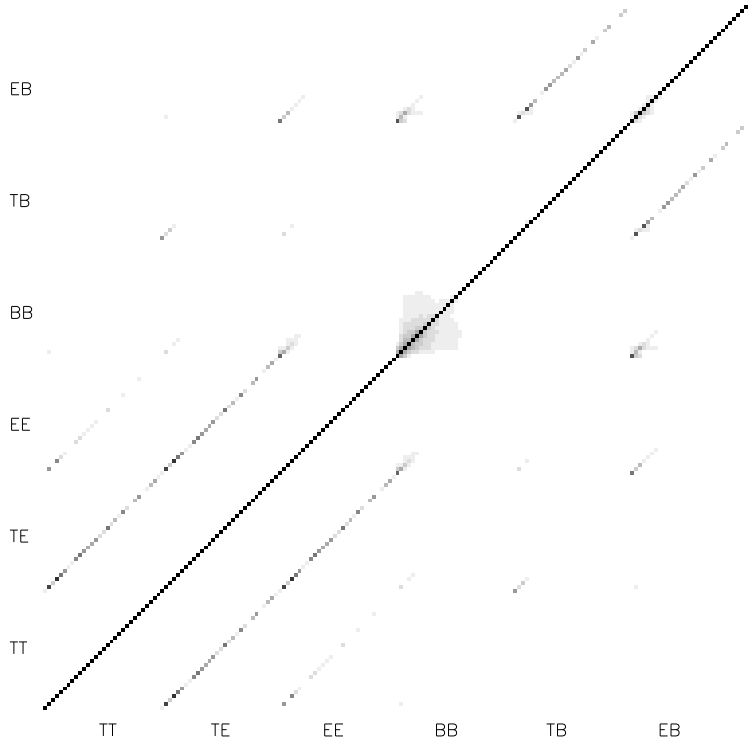

(a) Semi-analytical correlation functions

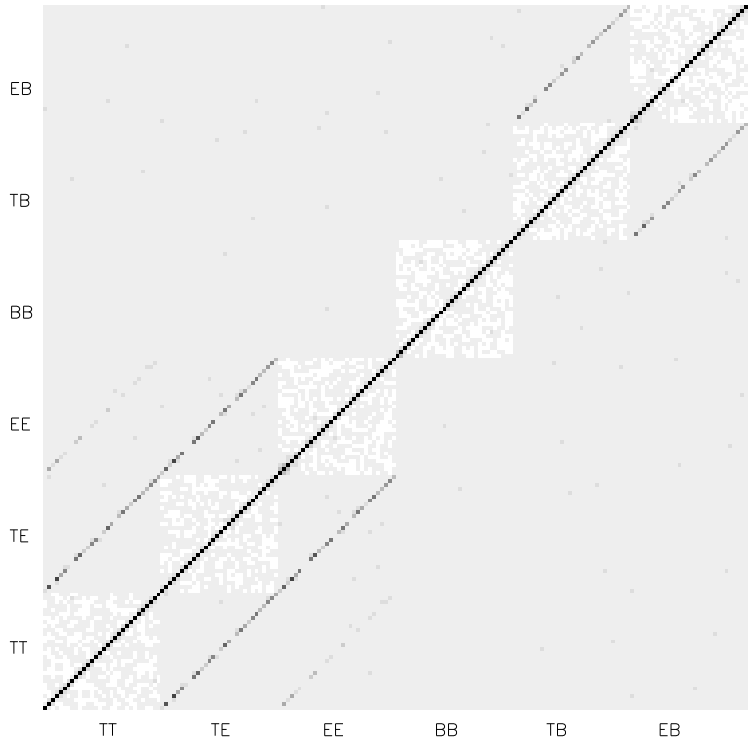

(b) Correlation functions from simulations

Figure 5.6: Comparison between correlation functions of the PCLs constructed from (a) the semi-analytical approach in the flat sky approximation and (b) from 2000 simulations.

5.6b we have plotted the correlation function of the simulations of the flat sky pseudo-C_ℓ's for the same window function. The corresponding simulation covariances are calculated by averaging over an ensemble of 2000 simulations using the relation

$$\mathrm{cov}(P_{b\ell}\tilde{C}_\ell^{XY}, P_{b'\ell}\tilde{C}_\ell^{X'Y'}) = \frac{1}{n_{\mathrm{sims}}-1}\sum_{k=1}^{n_{\mathrm{sims}}}\left(P_{b\ell}\tilde{C}_\ell^{XY} - \overline{P_{b\ell}\tilde{C}_\ell^{XY}}\right)\left(P_{b'\ell}\tilde{C}_\ell^{X'Y'} - \overline{P_{b'\ell}\tilde{C}_\ell^{X'Y'}}\right) \tag{5.112}$$

The covariances calculated from a limited number of simulations usually contain off-diagonal shot noise which is seen in Fig. 5.6b and can be obtimized by running more simulations. It is clear that the semi-analytical approach leads to smaller off-diagonals.

Although the semi-analytical results produce all the significant features of the covariance matrices, to gain good accuracy one has to calculate the integrals with large numbers of bins. Figure 5.7 dotted lines show the square root of the diagonals of the auto-covariances of the pseudo-C_ℓ's calculated by taking the integrations over 2000 and 500 radial and angular bins respectively. It has taken 2400 CPU hours to calculate these diagonal elements over 100 multipoles which are plotted as dots. We compare these results with the analytical expectations from equation (5.79) re-scaled for our window function. Due to the Knox formula (Knox, 1995) for a top hat window function the error bars are scaled by the ratio of the non-zero pixels in the window function. We rescale the covariances from equation (5.79) by dividing by f_{mask} and show their square roots as solid lines in Figure 5.7. Note that these approximated errors do not exactly correspond to true pseudo-C_ℓ covariances since they do not include the geometry of the window functions and the full convolution. In Fig. 5.7 we see that our incomplete numerical calculation provides all the important features of peaks and troughs. It also gives a relatively good approximation in small multipoles, however it diverges on large ℓ's. This mismatch at large ℓ can be rectified by increasing the number of angular bins on larger multipoles.

Figure 5.8 shows a few diagonal elements of the covariance matrices calculated by taking the summations over 2000 and 1000 radial and angular bins respectively. The numerical calculation of each element now takes 8 times longer (due to the presence of three angular loops) amounting to a total of 18000 CPU hours for 34 diagonal elements. The dotted lines now better fit the approximation formula, though the B-mode errors are not so improved. However since the numerical calculation is prohibitively slow we conclude that this analysis is clearly impractical for real purposes, e.g. for parameter estimation where one ideally needs to calculate the full covariances of the spectra at each MCMC iteration in the cosmological parameter space.

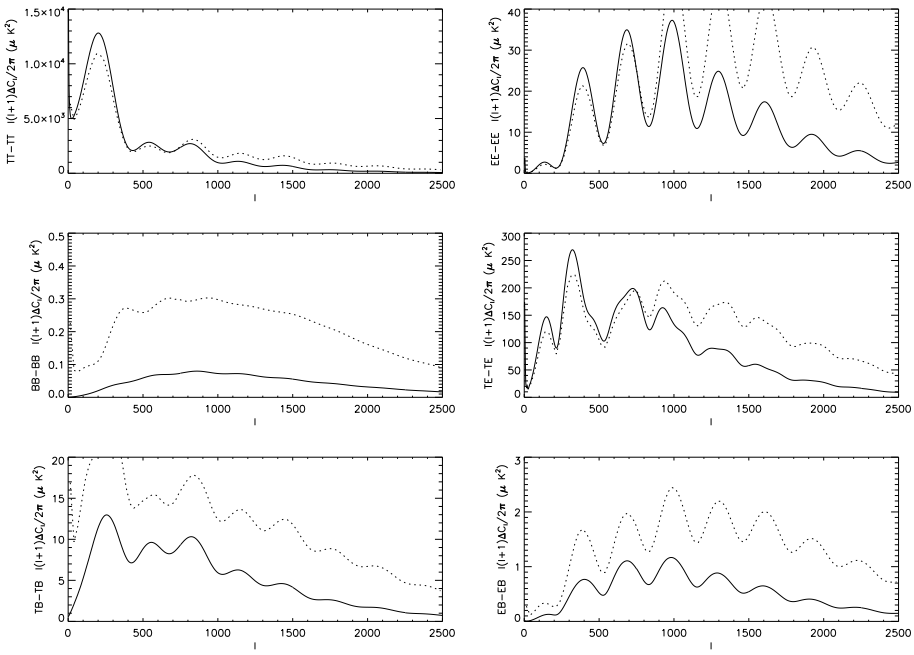

Figure 5.7: The square root of the auto-correlation covariance matrices from approximate Knox formula (solid), and from numerical calculation (dotted) with 2000 bins assumed for $d\ell''$ integration and 500 bins assumed for $d\varphi_\ell$, $d\varphi_{\ell'}$ and $d\varphi_{\ell''}$ integrations.

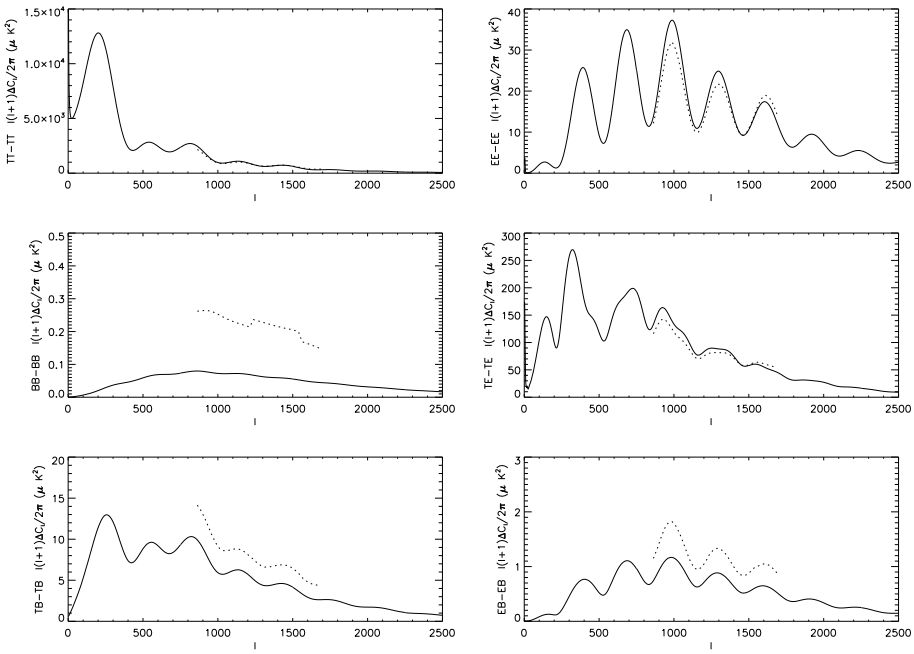

Figure 5.8: The same as figure 5.7, but for summations over 2000 bins for $d\ell''$ and 1000 bins for $d\varphi_\ell$, $d\varphi_{\ell'}$ and $d\varphi_{\ell''}$.

5.4 Conclusions

In this chapter we proposed and tested a semi-analytical approach for the calculation of the CMB pseudo-power spectra in the flat sky approximation. In section 5.1 we defined the coupling matrices which connect the true all-sky power spectra to the flat sky PCLs. Section 5.2 presented the details and the results of the numerical implementation of the pseudo-C_ℓ approach. We found that the bandpowers of the CMB temperature and E-mode polarization power spectra used to generate QUaD-like simulations can be recovered in the flat sky with a reasonable goodness-of-fit. Unfortunately the semi-analytical approach doesn't prove efficient in recovering the B-mode features, which may be due to the B mode signal being too small, and swamped by the E-mode mixing on the patch sky.

In section 5.3 we attempted to extend the flat-sky analytical approach to the numerical calculation of the pseudo-C_ℓ covariances. We have verified that the analytic formula for the covariances is not generally easy to simplify, and that the exact numerical calculation of the pseudo-C_ℓ covariance matrix over a large range of multipoles is impractical due to being extremely CPU time expensive.

Chapter 6

Summary and Future Directions

In this thesis we studied the background science governing the fluctuations of the CMB and utilized the QUaD CMB bandpowers to make predictions for the parameters of the ΛCDM model of cosmology. We further developed a semi-analytical scheme for estimation of the temperature and polarization power spectra from incomplete CMB data.

A comprehensive study of the CMB physics requires adequate knowledge of the theory of the cosmological perturbations which have generated the presently observable power spectrum of matter and radiation fluctuations. For this reason in chapter 2 we provided an analytical overview of the evolution of the perturbations in different constituent species of the universe and their implications for the angular features of the CMB and matter power spectrum. In chapter 3 we then studied the origin of polarization in the CMB and the spin-weighted harmonics formalism which helps to decompose the polarization into the coordinate-independent E-mode and B-mode components, which simplify the polarization characterization.

In section 3.4 we described the QUaD experiment: A CMB polarization survey which for three years collected polarization data from a small patch of the sky, with high signal-to-noise in two different frequency channels unprecedented by other polarization experiments, resulting in high precision determination of multiple acoustic oscillations in the E-mode polarization. QUaD data has successfully passed all the extensive analysis tests, and it has been shown that the level of systematic contamination is low (see QUaD collaboration: C. Pryke et al., 2008). Hence, the QUaD power spectra, with 23 measured bandpowers for TT, TE, EE and BB spectra, given over a large range of scales from $\ell = 164$ to $\ell = 2026$, provide sufficient information for a polarization-only parameter estimation analysis.

In chapter 4 we carried out a maximum likelihood 6-parameter fit to the QUaD combined 100GHz, 150GHz and 100/1500Hz auto and cross-power spectra data set. Our TT power

spectrum shows very good agreement with the results from the WMAP5 analysis. The QUaD TT bandpowers prove to be very likely to arise in a WMAP universe, with the probability to exceed equal to 91.24%. This is non-trivial as most of our data is on smaller scales than WMAP, but also indicates we have good control over the systematics, which is especially supposed to be significant on small scales due to the beam effects.

The 6-parameter analysis of the TE/EE/BB polarization power shows some tension with the ΛCDM model, largely due to a larger baryon density parameter, $\Omega_b h^2 = 0.0319 \pm 0.0046$, compared to $\Omega_b h^2 = 0.02261 \pm 0.00062$ from WMAP5. In the TT-spectrum the effect of an increase in the baryon density would be to enhance the first and third acoustic oscillation, as both the baryon loading and Compton coupling are greater. However, for the TE spectrum animations show that increasing the baryon density would enhance the amplitude of the acoustic peaks on small scales, due to an increase in Thomson scattering on small scales which suppresses the photon diffusion. There would also be a shift in the scale to higher multipoles, resulting in a slight degeneracy with h. The same patterns are seen in the QUaD TE bandpowers whose predicted acoustic peaks seem to be shifted towards large ℓ's compared to the bestfit ΛCDM spectrum. (see Fig. 4.10) It will be interesting to see if this trend persists in future polarization surveys.

We found that the WMAP5 bestfit spectra have a 7.07% chance of being drawn from the same distribution as QUaD TE/EE/BB, whereas the probability of WMAP5 to arise by chance is 11.24% if we compare with QUaD TE alone. Combining our TT, TE, EE and BB power we find an acceptable best fit model with goodness-of-fit 40.26%, and a 11.36% probability that WMAP5 is drawn from the same sample. The decrease of the probability values compared to PTE of TT spectrum means that our polarization data dominates over our temperature data. To test the significance we have analyzed 50 simulated QUaD surveys sampled from the WMAP5 parameters and found only one which lies within the QUaD 1-sigma parameter values. (see Fig. 4.3) This suggests that the probability of measuring the QUaD parameters by chance in a Universe which actually has WMAP5 parameter values can be quite small, provided that our analysis is not overestimating the QUaD constraining powers. Nevertheless, a proper conclusion requires analyzing a larger sample of simulations, and perhaps an improved parameter estimation strategy.

While not wishing to overstate the significance of our parameter estimation results, it is interesting to consider that the discrepancy between QUaD polarization and temperature constraints could indicate that an expansion beyond the standard 6-parameter set might relieve the tensions with ΛCDM model. However QUaD alone does not provide enough constraining power for this purpose, and the WMAP and SDSS data sets which we have used in combination with QUaD to probe the models beyond 6-basic parameters are of such high sensitivity that, for the most part, they dominate over the QUaD constraints.

The new QUaD power spectra from an improved power spectrum estimation pipeline with spherical pseudo-C_ℓ method (Brown et al., 2005) are expected to be published soon. The pa-

rameter analysis presented in this thesis is especially an invaluable preparation for work on the future QUaD data. We will aim to study the new data set with an improved MCMC analysis, incorporating alternative methods of breaking the degeneracy by different choices of parameter space and priors. We shall probe more simulations in order to verify whether the tension seen between QUaD bestfit parameters and those from the simulations persists. We shall include marginalization over SZ effect which is becoming a common practice for the new generation experiments that probe high multipoles. It is also ideal to include correlations between adiabatic and isocurvature perturbations which often significantly improve the isocurvature constraints (see e.g Bean et al., 2006). Here the choice of adding isocurvature modes to the basic 6-parameter model is based on our expectation that the new phase information in the polarization spectra may be helpful in breaking the degeneracy, whereas the choice of tensor-to-scalar ratio is an attempt to constrain primordial gravity waves with the new polarization measurements. However, an extensive analysis of models beyond the accepted standard ΛCDM requires inclusion of the massive neutrinos and particularly the running of the spectral index which may be determined by the large range of multipoles measured by QUaD.

In chapter 5 we proposed a semi-analytical method for the estimation of temperature and polarization pseudo-power spectra in the flat sky. The pseudo-C_ℓ methods have proved to be fast and relatively optimal for CMB parameter estimation, as opposed to the maximum likelihood methods, which although being highly optimal, are extremely slow for large CMB maps. We calculated the flat sky coupling matrices which connect the PCLs to the full sky bandpowers and showed that the semi-analytical method leads to a reasonable recovery of the temperature and E-mode polarization bandpowers from simulated QUaD-like pseudo-Cls, although the features of the low signal BB spectrum cannot be recovered by this method. In the future we shall test the analysis against a wider range of window functions and aim to incorporate noise and the effect of beam pixelization into the formulae. We shall also attempt to modify the method in order to gain a better recovery for BB bandpower. (see e.g. Smith, 2006).

Section 5.3 presents the results of our attempt to develop a semi-analytical method for the exact calculation of the covariance matrices of flat sky PCLs. Using our proposed method we recover all significant features of the covariance matrices with negligible off-diagonal elements, however the exact calculation turns out to be extremely CPU time expensive. Further investigations may be carried out to explore alternative approximation methods, in which case experimental noise should also be introduced in the equations which can substantially complicate the semi-analytical formula.

Bibliography

Ade, P., Bock, J., Bowden, M., Brown, M. L., Cahill, G., Carlstrom, J. E., Castro, P. G., Church, S., Culverhouse, T., Friedman, R., Ganga, K., Gear, W. K., Hinderks, J., Kovac, J., Lange, A. E., Leitch, E., Melhuish, S. J., Murphy, J. A., Orlando, A., Schwarz, R., O'Sullivan, C., Piccirillo, L., Pryke, C., Rajguru, N., Rusholme, B., Taylor, A. N., Thompson, K. L., Wu, E. Y. S., and Zemcov, M.: 2008, ApJ **674**, 22

Amendola, L., Gordon, C., Wands, D., and Sasaki, M.: 2002, *Phys. Rev. Lett.* **88**, 211302

Bardeen, J. M.: 1980, Phys. Rev. D **22**, 1882

Barkats, D., Bischoff, C., Farese, P., Fitzpatrick, L., Gaier, T., Gundersen, J. O., Hedman, M. M., Hyatt, L., McMahon, J. J., Samtleben, D., Staggs, S. T., Vanderlinde, K., and Winstein, B.: 2005, ApJ **619**, L127

Bartolo, N., Komatsu, E., Matarrese, S., and Riotto, A.: 2004, Phys. Rep. **402**, 103

Bartolo, N., Matarrese, S., and Riotto, A.: 2001, Phys. Rev. D **64(12)**, 123504

Bean, R., Dunkley, J., and Pierpaoli, E.: 2006, *Phys. Rev.* **D74**, 063503

Beltran, M., Garcia-Bellido, J., Lesgourgues, J., and Riazuelo, A.: 2004, *Phys. Rev.* **D70**, 103530

Beltran, M., Garcia-Bellido, J., Lesgourgues, J., and Viel, M.: 2005, *Phys. Rev.* **D72**, 103515

Bischoff, C., Hyatt, L., McMahon, J. J., Nixon, G. W., Samtleben, D., Smith, K. M., Vanderlinde, K., Barkats, D., Farese, P., Gaier, T., Gundersen, J. O., Hedman, M. M., Staggs, S. T., and Winstein, B.: 2008, *ArXiv e-prints* 802

Bond, J. R., Jaffe, A. H., and Knox, L.: 1998, Phys. Rev. D **57**, 2117

Bowden, M., Taylor, A. N., Ganga, K. M., Ade, P. A. R., Bock, J. J., Cahill, G., Carlstrom, J. E., Church, S. E., Gear, W. K., Hinderks, J. R., Hu, W., Keating, B. G., Kovac, J., Lange, A. E., Leitch, E. M., Maffei, B., Mallie, O. E., Melhuish, S. J., Murphy, J. A., Pisano, G., Piccirillo, L., Pryke, C., Rusholme, B. A., O'Sullivan, C., and Thompson, K.: 2004, MNRAS **349**, 321

Bridle, S. L., Crittenden, R., Melchiorri, A., Hobson, M. P., Kneissl, R., and Lasenby, A. N.: 2002, MNRAS **335**, 1193

Brown, M. L., Castro, P. G., and Taylor, A. N.: 2005, MNRAS **360**, 1262

Brown, M. L., Taylor, A. N., Bacon, D. J., Gray, M. E., Dye, S., Meisenheimer, K., and Wolf, C.: 2003, MNRAS **341**, 100

Bucher, M., Moodley, K., and Turok, N.: 2000, Phys. Rev. D **62(8)**, 083508

Bunn, E. F., Zaldarriaga, M., Tegmark, M., and de Oliveira-Costa, A.: 2003, Phys. Rev. D **67(2)**, 023501

Carlstrom, J. E., Kovac, J., Leitch, E. M., and Pryke, C.: 2003, *New Astronomy Review* **47**, 953

Castro, P. G., Heavens, A. F., and Kitching, T. D.: 2005, Phys. Rev. D **72(2)**, 023516

Challinor, A.: 2004, *ArXiv Astrophysics e-prints*

Challinor, A. and Chon, G.: 2005, MNRAS **360**, 509

Coc, A., Vangioni-Flam, E., Descouvemont, P., Adahchour, A., and Angulo, C.: 2004, ApJ **600**, 544

Crotty, P., Garcia-Bellido, J., Lesgourgues, J., and Riazuelo, A.: 2003, *Phys. Rev. Lett.* **91**, 171301

Dodelson, S.: 2003, *Modern cosmology*, Modern cosmology / Scott Dodelson. Amsterdam (Netherlands): Academic Press. ISBN 0-12-219141-2, 2003, XIII + 440 p.

Dunkley, J., Bucher, M., Ferreira, P. G., Moodley, K., and Skordis, C.: 2005, MNRAS **356**, 925

Dunkley, J., Komatsu, E., Nolta, M. R., Spergel, D. N., Larson, D., Hinshaw, G., Page, L., Bennett, C. L., Gold, B., Jarosik, N., Weiland, J. L., Halpern, M., Hill, R. S., Kogut, A., Limon, M., Meyer, S. S., Tucker, G. S., Wollack, E., and Wright, E. L.: 2008, *ArXiv e-prints*

Efstathiou, G.: 1990, in J. A. Peacock, A. F. Heavens, and A. T. Davies (eds.), *Physics of the Early Universe*, pp 361–463

Efstathiou, G.: 2004, MNRAS **349**, 603

Efstathiou, G.: 2006, MNRAS **370**, 343

Eisenstein, D. J. and Hu, W.: 1998, ApJ **496**, 605

Eisenstein, D. J. and Hu, W.: 1999, ApJ **511**, 5

Enqvist, K., Kurki-Suonio, H., and Valiviita, J.: 2000, *Phys. Rev.* **D62**, 103003

Francis, C.: 2007, *Ph.D. thesis*, AA(UNIVERSITY OF EDINBURGH, UK.)

Freedman, W. L., Madore, B. F., Gibson, B. K., Ferrarese, L., Kelson, D. D., Sakai, S., Mould, J. R., Kennicutt, Jr., R. C., Ford, H. C., Graham, J. A., Huchra, J. P., Hughes, S. M. G., Illingworth, G. D., Macri, L. M., and Stetson, P. B.: 2001, ApJ **553**, 47

Gelman, A. and Rubin, D. B.: 1992, *Statist. Sci.* **7**, 457

Gilks, W., Richardson, S., and D.J., S.: 1995, *Chapman and Hall, London* 129

Gordon, C., Wands, D., Bassett, B. A., and Maartens, R.: 2001, Phys. Rev. D **63(2)**, 023506

Gradshteyn, I. S. and Ryzhik, I. M.: 1994, *Table of integrals, series and products*, New York: Academic Press, —c1994, 5th ed. completely reset, edited by Jeffrey, Alan

Hansen, F. K. and Górski, K. M.: 2003, MNRAS **343**, 559

Hansen, F. K., Górski, K. M., and Hivon, E.: 2002, MNRAS **336**, 1304

Hivon, E., Górski, K. M., Netterfield, C. B., Crill, B. P., Prunet, S., and Hansen, F.: 2002, ApJ **567**, 2

Hu, W.: 2000, Phys. Rev. D **62(4)**, 043007

Hu, W.: 2001, in K. Sato and M. Kawasaki (eds.), *Birth and Evolution of the Universe*, pp 131–+

Hu, W. and Dodelson, S.: 2002, ARA&A **40**, 171

Hu, W. and Sugiyama, N.: 1995a, ApJ **444**, 489

Hu, W. and Sugiyama, N.: 1995b, Phys. Rev. D **51**, 2599

Hu, W. and Sugiyama, N.: 1996, ApJ **471**, 542

Hu, W., Sugiyama, N., and Silk, J.: 1997, Nature **386**, 37

Hu, W. and White, M.: 1997, *New Astronomy* **2**, 323

Hu, W. T.: 1995, *Ph.D. thesis*, AA(UNIVERSITY OF CALIFORNIA, BERKELEY.)

Jackson, J. D.: 1975, *Classical electrodynamics*, 92/12/31, New York: Wiley, 1975, 2nd ed.

Jaffe, A. H.: 2003, *New Astronomy Review* **47**, 1001

Jimenez, R., Verde, L., Peiris, H., and Kosowsky, A.: 2004, Phys. Rev. D **70(2)**, 023005

Jones, W. C., Bhatia, R., Bock, J. J., and Lange, A. E.: 2003, in T. G. Phillips and J. Zmuidzinas (eds.), *Society of Photo-Optical Instrumentation Engineers (SPIE) Conference Series*, Vol. 4855 of *Society of Photo-Optical Instrumentation Engineers (SPIE) Conference Series*, pp 227–238

Jungman, G., Kamionkowski, M., Kosowsky, A., and Spergel, D. N.: 1996, Phys. Rev. D **54**, 1332

Kaplan, J., Delabrouille, J., Fosalba, P., and Rosset, C.: 2003, *ArXiv Astrophysics e-prints*

Kawasaki, M. and Sekiguchi, T.: 2007, *ArXiv e-prints* 705

Keskitalo, R., Kurki-Suonio, H., Muhonen, V., and Valiviita, J.: 2007, *JCAP* **0709**, 008

Kirkman, D., Tytler, D., Suzuki, N., O'Meara, J. M., and Lubin, D.: 2003, ApJS **149**, 1

Knox, L.: 1995, Phys. Rev. D **52**, 4307

Kodama, H. and Sasaki, M.: 1984, *Progress of Theoretical Physics Supplement* **78**, 1

Kolb, E. W.: 1999, *NASA STI/Recon Technical Report N* **2**, 14556

Kosowsky, A.: 1996, *Annals of Physics* **246**, 49

Kosowsky, A.: 1998, *ArXiv Astrophysics e-prints*

Kosowsky, A.: 1999, *New Astronomy Review* **43**, 157

Kosowsky, A., Milosavljevic, M., and Jimenez, R.: 2002, Phys. Rev. D **66(6)**, 063007

Kovac, J. M., Leitch, E. M., Pryke, C., Carlstrom, J. E., Halverson, N. W., and Holzapfel, W. L.: 2002, *Nature* **420**, 772, astro-ph/0209478

Kurki-Suonio, H., Muhonen, V., and Väliviita, J.: 2005, Phys. Rev. D **71(6)**, 063005

Langlois, D. and Riazuelo, A.: 2000, *Phys. Rev.* **D62**, 043504

Lewis, A. and Bridle, S.: 2002, Phys. Rev. D **66(10)**, 103511

Lewis, A., Challinor, A., and Lasenby, A.: 2000, ApJ **538**, 473

Lewis, A., Challinor, A., and Turok, N.: 2002, Phys. Rev. D **65(2)**, 023505

Liddle, A. R. and Lyth, D. H.: 2000, *Cosmological Inflation and Large-Scale Structure*, Cosmological Inflation and Large-Scale Structure, by Andrew R. Liddle and David H. Lyth, pp. 414. ISBN 052166022X. Cambridge, UK: Cambridge University Press, April 2000.

Lifshitz, E. M.: 1946, *J. Phys. USSR* **10**, 116

Lin, Y.-T. and Wandelt, B. D.: 2006, *Astroparticle Physics* **25**, 151

Lucchin, F. and Matarrese, S.: 1985, Phys. Rev. D **32**, 1316

Ma, C.-P. and Bertschinger, E.: 1995, ApJ **455**, 7

MacTavish, C. J., Ade, P. A. R., Bock, J. J., Bond, J. R., Borrill, J., Boscaleri, A., Cabella, P., Contaldi, C. R., Crill, B. P., de Bernardis, P., De Gasperis, G., de Oliveira-Costa, A., De Troia, G., di Stefano, G., Hivon, E., Jaffe, A. H., Jones, W. C., Kisner, T. S., Lange, A. E., Lewis, A. M., Masi, S., Mauskopf, P. D., Melchiorri, A., Montroy, T. E., Natoli, P., Netterfield, C. B., Pascale, E., Piacentini, F., Pogosyan, D., Polenta, G., Prunet, S., Ricciardi, S., Romeo, G., Ruhl, J. E., Santini, P., Tegmark, M., Veneziani, M., and Vittorio, N.: 2006, ApJ **647**, 799

Masi, S., Ade, P. A. R., Bock, J. J., Bond, J. R., Borrill, J., Boscaleri, A., Cabella, P., Contaldi, C. R., Crill, B. P., de Bernardis, P., de Gasperis, G., de Oliveira-Costa, A., de Troia, G., di Stefano, G., Ehlers, P., Hivon, E., Hristov, V., Iacoangeli, A., Jaffe, A. H., Jones, W. C., Kisner, T. S., Lange, A. E., MacTavish, C. J., Marini Bettolo, C., Mason, P., Mauskopf, P. D., Montroy, T. E., Nati, F., Nati, L., Natoli, P., Netterfield, C. B., Pascale, E., Piacentini, F., Pogosyan, D., Polenta, G., Prunet, S., Ricciardi, S., Romeo, G., Ruhl, J. E., Santini, P., Tegmark, M., Torbet, E., Veneziani, M., and Vittorio, N.: 2006, A&A **458**, 687

Mather, J. C.: 1994, *Infrared Physics and Technology* **35**, 331

Metropolis, N., Rosenbluth, A., Rosenbluth, M. N., and H., T. A.: 1953, *J. Chem. Phys.* **21**, 1087

Milgrom, M. and Bekenstein, J.: 1987, in J. Kormendy and G. R. Knapp (eds.), *Dark matter in the universe*, Vol. 117 of *IAU Symposium*, pp 319–330

Montroy, T. E., Ade, P. A. R., Bock, J. J., Bond, J. R., Borrill, J., Boscaleri, A., Cabella, P., Contaldi, C. R., Crill, B. P., de Bernardis, P., De Gasperis, G., de Oliveira-Costa, A., De Troia, G., di Stefano, G., Hivon, E., Jaffe, A. H., Kisner, T. S., Jones, W. C., Lange, A. E., Masi, S., Mauskopf, P. D., MacTavish, C. J., Melchiorri, A., Natoli, P., Netterfield, C. B., Pascale, E., Piacentini, F., Pogosyan, D., Polenta, G., Prunet, S., Ricciardi, S., Romeo, G., Ruhl, J. E., Santini, P., Tegmark, M., Veneziani, M., and Vittorio, N.: 2006, ApJ **647**, 813

Moodley, K., Bucher, M., Dunkley, J., Ferreira, P. G., and Skordis, C.: 2004, *Phys. Rev.* **D70**, 103520

Neal, R. M.: 1993, *Technical Report CRG-TR-93-1*

Nolta, M. R., Dunkley, J., Hill, R. S., Hinshaw, G., Komatsu, E., Larson, D., Page, L., Spergel, D. N., Bennett, C. L., Gold, B., Jarosik, N., Odegard, N., Weiland, J. L., Wollack, E., Halpern, M., Kogut, A., Limon, M., Meyer, S. S., Tucker, G. S., and Wright, E. L.: 2008, *ArXiv e-prints* 803

Padmanabhan, T.: 1993, *Structure Formation in the Universe*, Structure Formation in the Universe, by T. Padmanabhan, pp. 499. ISBN 0521424860. Cambridge, UK: Cambridge University Press, June 1993.

Page, L., Hinshaw, G., Komatsu, E., Nolta, M. R., Spergel, D. N., Bennett, C. L., Barnes, C., Bean, R., Doré, O., Dunkley, J., Halpern, M., Hill, R. S., Jarosik, N., Kogut, A., Limon, M., Meyer, S. S., Odegard, N., Peiris, H. V., Tucker, G. S., Verde, L., Weiland, J. L., Wollack, E., and Wright, E. L.: 2007, ApJS **170**, 335

Paling, S. M.: 2005, *New Astronomy Review* **49**, 323

Peacock, J.: 2007, *MPhys Advanced Cosmology, Lecture notes*, by John Peacock, 2007 - 2008.

Peacock, J. A.: 1999, *Cosmological Physics*, Cosmological Physics, by John A. Peacock, pp. 704. ISBN 052141072X. Cambridge, UK: Cambridge University Press, January 1999.

Perlmutter, S., Aldering, G., Goldhaber, G., Knop, R. A., Nugent, P., Castro, P. G., Deustua, S., Fabbro, S., Goobar, A., Groom, D. E., Hook, I. M., Kim, A. G., Kim, M. Y., Lee, J. C., Nunes, N. J., Pain, R., Pennypacker, C. R., Quimby, R., Lidman, C., Ellis, R. S., Irwin, M., McMahon, R. G., Ruiz-Lapuente, P., Walton, N., Schaefer, B., Boyle, B. J., Filippenko, A. V., Matheson, T., Fruchter, A. S., Panagia, N., Newberg, H. J. M., Couch, W. J., and The Supernova Cosmology Project: 1999, ApJ **517**, 565

Pope, A. C. and Szapudi, I.: 2008, MNRAS **389**, 766

Press, W. H.: 2002, *Numerical recipes in C++ : the art of scientific computing*, Numerical recipes in C++ : the art of scientific computing by William H. Press. xxviii, 1,002 p. : ill. ; 26 cm. Includes bibliographical references and index. ISBN : 0521750334

QUaD collaboration: C. Pryke, Ade, P., Bock, J., Bowden, M., Brown, M. L., Cahill, G., Castro, P. G., Church, S., Culverhouse, T., Friedman, R., Ganga, K., Gear, W. K., Gupta, S., Hinderks, J., Kovac, J., Lange, A. E., Leitch, E., Melhuish, S. J., Memari, Y., Murphy, J. A., Orlando, A., Schwarz, R., O'Sullivan, C., Piccirillo, L., Rajguru, N., Rusholme, B., Taylor, A. N., Thompson, K. L., Turner, A. H., Wu, E. Y. S., and Zemcov, M.: 2008, *ArXiv e-prints*

QUaD Collaboration: E. Y. S. Wu, Ade, P., Bock, J., Bowden, M., Brown, M. L., Cahill, G., Castro, P. G., Church, S., Culverhouse, T., Friedman, R., Ganga, K., Gear, W. K., Gupta, S., Hinderks, J., Kovac, J., Lange, A. E., Leitch, E., Melhuish, S. J., Memari, Y., Murphy, J. A., Orlando, A., Piccirillo, L., Pryke, C., Rajguru, N., Rusholme, B., Schwarz, R., O'Sullivan, C., Taylor, A. N., Thompson, K. L., Turner, A. H., and Zemcov, M.: 2008, *ArXiv e-prints*

QUaD collaboration: J. Hinderks, Ade, P., Bock, J., Bowden, M., Brown, M. L., Cahill, G., Carlstrom, J. E., Castro, P. G., Church, S., Culverhouse, T., Friedman, R., Ganga, K., Gear, W. K., Gupta, S., Harris, J., Haynes, V., Kovac, J., Kirby, E., Lange, A. E., Leitch, E., Mallie, O. E., Melhuish, S., Murphy, A., Orlando, A., Schwarz, R., O' Sullivan, C., Piccirillo, L., Pryke, C., Rajguru, N., Rusholme, B., Taylor, A. N., Thompson, K. L., Tucker, C., Wu, E. Y. S., and Zemcov, M.: 2008, *ArXiv e-prints*

QUaD collaboration: P. G. Castro, Ade, P., Bock, J., Bowden, M., Brown, M. L., Cahill, G., Church, S., Culverhouse, T., Friedman, R. B., Ganga, K., Gear, W. K., Gupta, S., Hinderks, J., Kovac, J., Lange, A. E., Leitch, E., Melhuish, S. J., Memari, Y., Murphy, J. A., Orlando, A., Pryke, C., Schwarz, R., O'Sullivan, C., Piccirillo, L., Rajguru, N., Rusholme, B., Taylor, A. N., Thompson, K. L., Turner, A. H., Wu, E. Y. S., and Zemcov, M.: 2009, *ArXiv e-prints*

Readhead, A. C. S., Myers, S. T., Pearson, T. J., Sievers, J. L., Mason, B. S., Contaldi, C. R., Bond, J. R., Bustos, R., Altamirano, P., Achermann, C., Bronfman, L., Carlstrom, J. E., Cartwright, J. K., Casassus, S., Dickinson, C., Holzapfel, W. L., Kovac, J. M., Leitch, E. M., May, J., Padin, S., Pogosyan, D., Pospieszalski, M., Pryke, C., Reeves, R., Shepherd, M. C., and Torres, S.: 2004, *Science* **306**, 836

Reichardt, C. L., Ade, P. A. R., Bock, J. J., Bond, J. R., Brevik, J. A., Contaldi, C. R., Daub, M. D., Dempsey, J. T., Goldstein, J. H., Holzapfel, W. L., Kuo, C. L., Lange, A. E., Lueker, M., Newcomb, M., Peterson, J. B., Ruhl, J., Runyan, M. C., and Staniszewski, Z.: 2008, *ArXiv e-prints*

Riess, A. G., Filippenko, A. V., Challis, P., Clocchiatti, A., Diercks, A., Garnavich, P. M., Gilliland, R. L., Hogan, C. J., Jha, S., Kirshner, R. P., Leibundgut, B., Phillips, M. M., Reiss, D., Schmidt, B. P., Schommer, R. A., Smith, R. C., Spyromilio, J., Stubbs, C., Suntzeff, N. B., and Tonry, J.: 1998, AJ **116**, 1009

Riotto, A.: 2002, *ArXiv High Energy Physics - Phenomenology e-prints*

Seljak, U.: 1997, ApJ **482**, 6

Seljak, U. and Zaldarriaga, M.: 1996, ApJ **469**, 437

Seljak, U. and Zaldarriaga, M.: 1997, *Physical Review Letters* **78**, 2054

Seljak, U. and Zaldarriaga, M.: 1998, *ArXiv Astrophysics e-prints*

Sievers, J. L., Achermann, C., Bond, J. R., Bronfman, L., Bustos, R., Contaldi, C. R., Dickinson, C., Ferreira, P. G., Jones, M. E., Lewis, A. M., Mason, B. S., May, J., Myers, S. T., Oyarce, N., Padin, S., Pearson, T. J., Pospieszalski, M., Readhead, A. C. S., Reeves, R., Taylor, A. C., and Torres, S.: 2007, ApJ **660**, 976

Smith, K. M.: 2006, *New Astronomy Review* **50**, 1025

Spergel, D. N., Bean, R., Doré, O., Nolta, M. R., Bennett, C. L., Dunkley, J., Hinshaw, G., Jarosik, N., Komatsu, E., Page, L., Peiris, H. V., Verde, L., Halpern, M., Hill, R. S., Kogut, A., Limon, M., Meyer, S. S., Odegard, N., Tucker, G. S., Weiland, J. L., Wollack, E., and Wright, E. L.: 2007, ApJS **170**, 377

Spergel, D. N., Verde, L., Peiris, H. V., Komatsu, E., Nolta, M. R., Bennett, C. L., Halpern, M., Hinshaw, G., Jarosik, N., Kogut, A., Limon, M., Meyer, S. S., Page, L., Tucker, G. S., Weiland, J. L., Wollack, E., and Wright, E. L.: 2003, ApJS **148**, 175

Springel, V., Frenk, C. S., and White, S. D. M.: 2006, Nature **440**, 1137

Springel, V., White, S. D. M., Jenkins, A., Frenk, C. S., Yoshida, N., Gao, L., Navarro, J., Thacker, R., Croton, D., Helly, J., Peacock, J. A., Cole, S., Thomas, P., Couchman, H., Evrard, A., Colberg, J., and Pearce, F.: 2005, Nature **435**, 629

Stewart, E. D. and Lyth, D. H.: 1993, *Physics Letters B* **302**, 171

Stompor, R., Banday, A. J., and Gorski, Krzysztof, M.: 1996, *Astrophys. J.* **463**, 8

Sunyaev, R. and Zel'dovich, Y. B.: 1972, *Comm. Astrophys. Sp. Phys.* **4**, 173

Taylor, A.: 2004, *Astrophysical Cosmology, Lecture notes 4*, by Andy Taylor, 2004 - 2005.

Taylor, A., Heavens, A., Ballinger, B., and Tegmark, M.: 1997, *ArXiv Astrophysics e-prints*

Tegmark, M., Dodelson, S., Eisenstein, D. J., Narayanan, V., Scoccimarro, R., Scranton, R., Strauss, M. A., Connolly, A., Frieman, J. A., Gunn, J. E., Hui, L., Jain, B., Johnston, D., Kent, S., Loveday, J., Nichol, R. C., O'Connell, L., Sheth, R. K., Stebbins, A., Szalay, A. S., Szapudi, I., Vogeley, M. S., Zehavi, I., Annis, J., Bahcall, N. A., Brinkmann, J., Csabai, I., Doi, M., Fukugita, M., Hennessy, G., Ivezíc, Ž., Knapp, G. R., Lamb, D. Q., Lee, B. C., Lupton, R. H., McKay, T. A., Kunszt, P., Munn, J. A., Peoples, J., Pier, J. R., Richmond, M., Rockosi, C., Schlegel, D., Stoughton, C., Tucker, D. L., Yanny, B., and York, D. G.: 2002, ApJ **571**, 191

Tegmark, M., Eisenstein, D. J., Strauss, M. A., Weinberg, D. H., Blanton, M. R., Frieman, J. A., Fukugita, M., Gunn, J. E., Hamilton, A. J. S., Knapp, G. R., Nichol, R. C., Ostriker, J. P., Padmanabhan, N., Percival, W. J., Schlegel, D. J., Schneider, D. P., Scoccimarro, R., Seljak, U., Seo, H.-J., Swanson, M., Szalay, A. S., Vogeley, M. S., Yoo, J., Zehavi, I., Abazajian, K., Anderson, S. F., Annis, J., Bahcall, N. A., Bassett, B., Berlind, A., Brinkmann, J., Budavari, T., Castander, F., Connolly, A., Csabai, I., Doi, M., Finkbeiner, D. P., Gillespie, B., Glazebrook, K., Hennessy, G. S., Hogg, D. W., Ivezić, Ž., Jain, B., Johnston, D., Kent, S., Lamb, D. Q., Lee, B. C., Lin, H., Loveday, J., Lupton, R. H., Munn, J. A., Pan, K., Park, C., Peoples, J., Pier, J. R., Pope, A., Richmond, M., Rockosi, C., Scranton, R., Sheth, R. K., Stebbins, A., Stoughton, C., Szapudi, I., Tucker, D. L., Berk, D. E. V., Yanny, B., and York, D. G.: 2006, Phys. Rev. D **74(12)**, 123507

Tegmark, M., Strauss, M. A., Blanton, M. R., Abazajian, K., Dodelson, S., Sandvik, H., Wang, X., Weinberg, D. H., Zehavi, I., Bahcall, N. A., Hoyle, F., Schlegel, D., Scoccimarro, R., Vogeley, M. S., Berlind, A., Budavari, T., Connolly, A., Eisenstein, D. J., Finkbeiner, D., Frieman, J. A., Gunn, J. E., Hui, L., Jain, B., Johnston, D., Kent, S., Lin, H., Nakajima, R., Nichol, R. C., Ostriker, J. P., Pope, A., Scranton, R., Seljak, U., Sheth, R. K., Stebbins, A., Szalay, A. S., Szapudi, I., Xu, Y., Annis, J., Brinkmann, J., Burles, S., Castander, F. J., Csabai, I., Loveday, J., Doi, M., Fukugita, M., Gillespie, B., Hennessy, G., Hogg, D. W.,

Ivezić, Ž., Knapp, G. R., Lamb, D. Q., Lee, B. C., Lupton, R. H., McKay, T. A., Kunszt, P., Munn, J. A., O'Connell, L., Peoples, J., Pier, J. R., Richmond, M., Rockosi, C., Schneider, D. P., Stoughton, C., Tucker, D. L., vanden Berk, D. E., Yanny, B., and York, D. G.: 2004, Phys. Rev. D **69(10)**, 103501

Tegmark, M. and Zaldarriaga, M.: 2002, Phys. Rev. D **66(10)**, 103508

Terrero-Escalante, C. A.: 2003, *Physics Letters B* **563**, 15

Terrero-Escalante, C. A., Lidsey, J. E., and García, A. A.: 2002, Phys. Rev. D **65(8)**, 083509

Tojeiro, R.: 2008, *Ph.D. thesis*, AA(UNIVERSITY OF EDINBURGH, UK.)

Valiviita, J.: 1999, *Master's thesis*, AA(UNIVERSITY OF HELSINKI, FINLAND.)

Valiviita, J.: 2005, *Ph.D. thesis*, AA(UNIVERSITY OF HELSINKI, FINLAND.)

van Albada, T. S., Bahcall, J. N., Begeman, K., and Sancisi, R.: 1985, ApJ **295**, 305

Verde, L., Peiris, H. V., Spergel, D. N., Nolta, M. R., Bennett, C. L., Halpern, M., Hinshaw, G., Jarosik, N., Kogut, A., Limon, M., Meyer, S. S., Page, L., Tucker, G. S., Wollack, E., and Wright, E. L.: 2003, ApJS **148**, 195

Wandelt, B. D.: 2004, *ArXiv Astrophysics e-prints*

Wandelt, B. D., Hivon, E., and Gorski, K. M.: 2000, *ArXiv Astrophysics e-prints*

White, M.: 1999, in A. J. Banday, R. K. Sheth, and L. N. da Costa (eds.), *Evolution of Large Scale Structure : From Recombination to Garching*, pp 25–+

White, M. and Hu, W.: 1997, A&A **321**, 8

Zaldarriaga, M. and Seljak, U.: 1997, Phys. Rev. D **55**, 1830

Zaldarriaga, M. and Seljak, U.: 1998, Phys. Rev. D **58(2)**, 023003